The University Of Sheffield.

Health Monitoring Techniques for High Availability Drives

By

Igor Tsyokhla

A thesis submitted for the degree of Doctor of Philosophy

Department of Electronic and Electrical Engineering
Faulty of Engineering
The University of Sheffield

August 2017

Abstract

The growing number and need for high availability drives in the modern world places high importance on reliability and operational availability. Part of the solution to the increased requirements on availability involves monitoring degradation associated with machine failure, diagnosing the mode of failure and predicting into the future to a possible time to failure.

Broad multi-disciplinary knowledge is required to understand drive ageing and implement monitoring systems. This research reviews the failure modes associated with high availability drives, in particular with regards to low voltage random wound permanent magnet inverter driven machines. The main failure modes are presented, with analysis of available literature regarding machine failure. Gaps in literature are identified and the most common failure modes of the low voltage machine, bearing and winding damage are presented.

Currently the area of least understanding in the field of drive health monitoring involves the measurement and analysis of winding insulation failure. The modes of insulation failure are investigated in detail and a new model for ground-wall insulation is developed.

Methods to measure insulation ground-wall insulation have been reviewed, and a new method has been developed to monitor the ground-wall insulation health, during machine operation, using common-mode current inherent in inverter driven machines during operation.

To expand the knowledge of insulation failure, the novel insulation health monitoring method is used to monitor four stators during an accelerated ageing test, representing monitoring of insulation of real machine lifetimes. The results are analysed and additional testing is presented in order to develop the monitoring system for standard industry drives.

The major conclusion from results indicates that insulation degradation progression follows a deterministic trend, with clearly defined threshold of failure, allowing prognosis of lifetime based on monitored parameters. Future work recommendations are made to expand on the findings during the course of research.

Acknowledgement

I would like to thank my supervisor, Prof Jiabin Wang for the opportunities that he has opened and his continual support throughout both my undergraduate work and PhD research. His enthusiasm for drives and drive for the highest standards knows no equal. I would like to thank Dr Antonio Griffo for assistance with formal writing and academic progress. In addition I would like to formally recognise my colleagues who have each contributed in their own way.

I am obliged to all my family, they have raised me in my youth and assured that I would be ready to face whatever lies in the future. I would especially like to thank my close friends and loved ones, they have made life fun and are the reason I am a better person today than when I first met them.

Table of Contents

Introduction

Reliable operation of electric machines, including motors, generators and actuators is crucial to the function of the modern world. Motors are used in a variety of applications ranging from sewage pumps and high value factory production lines to electric vehicle traction, aircraft actuators and propulsion, and many are required to be reliable and available at all times.

One of the means to achieve high availability required to the applications outlined is regular maintenance to ensure guaranteed operation. The work done in this thesis aims to contribute to the emerging field of health monitoring of machines in order to facilitate the diagnosis and prognosis of machine degradation mode and lifetime respectively. The focus of the monitoring is on low voltage random wound inverter driven machines.

The thesis is structured into seven chapters: a preliminary literature review to investigate the gaps of knowledge, an extended review of bearing failure, the most common mode of machine failure, followed by a study of insulation degradation. The study of insulation is covered in four chapters. The first provides an extensive literature review to investigate the insulation and winding modes of failure, followed by a review of insulation monitoring methods, development and testing of a novel insulation monitoring system. Chapter 5 uses the novel system to conduct an accelerated insulation ageing experiment to provide insulation parameter progression information, unobserved in real time until the work done here. Chapter 6 uses the monitoring system to conduct additional experiments, to investigate claims in literature, followed by the conclusions and recommendation for future work. Appendixes contain additional information which would be required to repeat the experiments carried out in this work, as well as an attempt to use a low cost system to implement the same insulation monitoring scheme as used to carry out the main experiments.

The main contributions of the work are the development of a novel insulation monitoring system for inverter driven machines, capable of observing the degradation of insulation in real time, on-line, without interruption of machine operation and the use of this system to monitor previously unobservable insulation ageing until failure. The data obtained shows the degradation of insulation under the most realistic ageing possible. A method has been developed to use this system as the basis for prognosis of remaining useful lifetime of machines, based on insulation health. Industry has been engaged with the research presented here and it is to be hoped that the concept and system developed here will one day be applied in real applications, revolutionising the means to monitor and diagnose winding insulation.

Chapter 1

Literature Review of Machine Faults

Machine failure modes, location of faults and relative frequency of occurrence must be thoroughly understood in order to diagnose machine health condition and to estimate their remaining lifetime. The fault occurrence and state-of-art statistics based methods of lifetime prediction are reviewed. Gaps in knowledge are identified for further study.

1.1 Reliability Studies

Modern drives consist of two basic sections: the inverter delivering controlled power, to a motor which converts electrical power into motion or vice versa. The system can be considered as a combination of four component groups: the motor stator and windings, the rotor, bearings and the inverter. Each of these groups has a number of associated fault mechanisms which are separate from each group. A 1982 survey [1] [2] [3] of industrial plant forms the first comprehensive study of the component failure types, contributing factors to fault and machine failure rates. The 1982 survey compiles responses from 33 companies, operating a total of 1141 motors, expressing reliability per hour of machine operation. The survey used a similar questionnaire style to previous reliability surveys from 1962 [4] and 1973 [5] allowing direct comparison of failure rates, with additional questions to determine the root causes of machine failure. As expected, failure rates have decreased with improvement of machine manufacture and maintenance, however insufficient information is present to compare relative component failure from the 1962 and 1973 studies.

Phase II of the 1982 study was conducted in 1985, adding data for a further 1527 motors [6]. This continuation can be considered a separate study, as the selection of machines were deliberately focused on higher power, higher voltage machines in generation utility sector, with data presented separately for each phase of the study.

The most recent survey on machine reliability comes from 1995 from surveys of faults on motors in the offshore oil industry [7]. To maintain consistency between previous studies, the same methodology was selected by the authors. Majority of the machines in this study were rated at less than 50kW, compared with a minimum rating of 150kW in the 1982 study. In addition, the survey was primarily focused on machines with operating voltage lower than 1kV, compared with the 1982 study where the median operation voltage was between

1-5kV. A large number of machines in the 1995 study also had inverter control, allowing better representation of modern drive failure. The drive failure is lumped together under "other failures" for comparison with previous studies.

An alternate source of component failure is presented in [8], the military handbook used to calculate mean time between failures (MTBF) of complete systems based on a combination of component level failure statistics. In this standard, machine failure is reduced to two components: the bearing and winding, with failure rate constants available for fractional horsepower motors. The MiL standard has numerous criticisms, ranging from inclusion of old components, and over-conservative estimates [9], to poor connection to physics of failure [10], hence the conclusions taken must therefore be carefully limited in scope. Using a combination of available material it is possible to show component failure distribution, and draw conclusions about a wide range of machines.

All surveys agree that majority of failures occur due to bearing fault, with second most important failure modes being in the windings, and a small number of failures in the rotor. This trend can be observed in Figure 1.1, where each survey result is presented separately for comparison. It has been noted from general reviews of condition monitoring methods [11] [12] [13] that there is a disproportionate number of papers covering rotor fault detection.

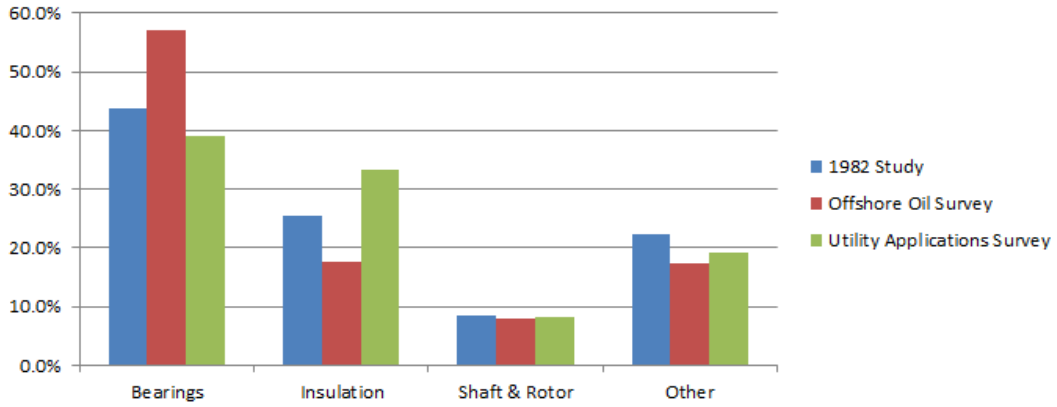

FIGURE 1.1 RELATIVE MACHINE FAULTS ACROSS MULTIPLE STUDIES

It is noticeable that there is a relationship between different motor voltage and power vs the distribution of faults. The machinery with high voltage and high power in [6] in the utility generation sector had the lowest ratio of bearing failures to winding failures, indicating an increase in winding failures in high voltage machines. Whereas the offshore oil survey [7], containing the largest number of low voltage low power machines had the highest bearing to winding failure ratio. Further evidence for this relationship is provided in [7], where data for machines rated 5-15kV also showed the decrease in bearing to winding failure ratio. The MTBF calculation in [8] assumes a 5/1 failure ratio of the bearing to winding, the highest compared to the surveys, for the lowest voltage lowest power machines.

1.2 Maintenance

Maintenance reported in 1982 [1] consisted predominantly of checking the machine during cleaning and lubrication, as well as using a high voltage DC "Megger" test on the windings. The maintenance classed in the survey as "excellent" also contained a significant rate of a bearing inspection. Data in [2] showed that 1/3 of the faults were discovered during maintenance in the 1982 survey, with the rest of the faults occurring during normal operating procedure. Further investigation however identifies that bearing problems were twice as likely to be discovered during maintenance rather than during operation, with very poor winding problem detection lowering the average value of discovery.

The most common repair mechanism reported in [1] was to simply replace the machine with spare. The downtime for this operation was reported at 18.2 hours. This is the best case scenario for quickest repair. For a generation plant in 1973 [5], the downtime cost was roughly $1 per hour per kW of installed capacity. Using the available statistics in [5], a 1MW plant stoppage due to an ancillary 600V induction motor, replaced with spare after a downtime of 6.6 hours would cost $6,600, $35,000 when adjusted for inflation. The downtime of large generation plant averaged 175 hours, due to unavailability of direct component replacement.

For large plant with assets that cannot be quickly repaired, multiple methods of monitoring already exist to mitigate downtime and schedule preventative maintenance. In [14], results for systematic monitoring using partial discharge measurement and insulation power factor measurement on the winding are presented for three large generators over their actual lifetime, up to 27 years on one of the machines. Even for large plant, periodic measurement is generally used due to the cost of measurement. Maintenance has discovered a serious problem in one case study, a detection of slow degradation in the second case study, and an inability to detect failure with one of the methods. Improvements in technology allow more frequent testing and on-line testing of partial discharge [11], however it is evident that this method is not cost effective for small plant.

Focus on monitoring and maintenance has been made mainly on large, irreplaceable plant, and small low voltage machines have been neglected. Modern applications are increasingly reliant on small motors with requirement of high availability in electrification of transport such as more electric, hybrid and fully electric aircraft designs and electric traction and electric ship propulsion. The risk of failure in these fields has generated renewed interest in the study of drive health monitoring. Consensus in the surveys previously mentioned identifies the two most important failure modes, namely bearing failure and winding failure in electrical machines. The focus of research must therefore investigate further into these two fields. Research into rotor and inverter failure has been limited mostly to how the degradation of these two components might affect detection of winding and bearing problems.

1.3 Bearing Failure

Electric motors have intrinsically higher reliability compared to internal combustion engines, due to a much reduced number of moving parts. The output shaft is the only component which would rotate in ideal circumstances. To support the output shaft, most machines use bearings with a contact area between the moving surfaces. For small and medium sized machines, deep groove ball bearings are the most common design choice.

Bearing degradation can come from mechanical fatigue, environmental corrosion and electrical discharge in inverter driven systems. Bearing damage analysis and lifetime prediction is a mature field, where lifetime of the bearing can be predicted by considering metal fatigue as the dominant degradation force. Equation (1.1) is used by bearing manufacturer SKF in their on-line calculator [15], to allow customers to select the correct bearing with required lifetime and load conditions. In Equation (1.1), C is the basic dynamic load rating, P is the equivalent dynamic bearing load and p is a constant exponent which depends on the type of bearing, p has a value of 3 for ball bearings, L_{10} represents the bearing life in revolutions, with 90% confidence.

$$L_{10} = a_{skf}\left(\frac{C}{P}\right)^{p} \tag{1.1}$$

The basic dynamic load rating is provided by the manufacturer for each bearing, and dynamic bearing load is calculated based on the required application. SKF also provides an additional factor a_{skf}, to modify the lifetime due to additional factors of lubrication oil choice and protection from contamination. Degradation with respect to temperature is factored in at this stage, affecting the condition of the lubricant.

Ball bearings contain four major components, inner raceway, outer raceway, ball bearings and bearing cage. Over time, fatigue damage introduces distinct deformations and asperities on the bearing components. The main aim of monitoring bearing health is to track the presence and severity of the damage on these components. Pitting damage on any major component creates an impact when the bearing element rolls over the damaged area. At a set speed, the impact translates to vibration of the bearing, which is transmitted to the rest of the machine. Based on the rotation speed and bearing dimensions, the vibration frequencies can be calculated [16] or obtained directly from the manufacturer when the bearing designation is known [17].

All bearing damage detection methods monitor the change in the vibration characteristic of bearings. The two main methods of measurement are to measure vibration directly with an acoustic transducer, or to measure motor current, based on the assumption that changing the air gap due to vibration will modulate the motor current with harmonics at the bearing frequencies. The main

difficulties in detection of bearing health are separation of bearing health data from changes in machine speed and load, and determination of Remaining Useful Life (RUL) of the bearing based on the measured data. To a large extent, advanced data processing methods such as using statistic spread [18], wavelet decomposition [19] and short time Fourier transform, have ameliorated the problem of actual detection. Combined with an understanding of machine harmonics from other factors such as eccentricity, demagnetisation and turn fault, bearing harmonics can be isolated and tracked over time. Attempts to relate final lifetime of bearings with prediction in Equation (1.1) have mainly involved setting thresholds on monitored parameters [20] and detection of change of trends. More research is required to establish the relationship between monitored parameters and end of life. Currently thresholds are set mostly from experience with similar sized motors.

Multiple commercial systems exist to monitor bearing health [21] [22]. The systems attempt to use the most advanced available data processing methods to learn the harmonics during normal operation and detect anomalies in harmonic magnitudes. Maintenance on safety critical applications is to be carried out by replacing motor bearings when a pre-set threshold is reached. Due to the dominance of bearing failure in all machine failure surveys, it was decided to evaluate an available commercial system to learn more about bearing degradation and health monitoring. Further analysis of bearing degradation as well as results from this experiment can be found in Chapter 2.

Review of bearing monitoring in Chapter 2 shows a gap in literature which requires analysis of monitored real bearing degradation with an attempt to establish a credible link between parameters and end of life. For many applications however this may not be worthwhile and bearings, especially in small motors are cheap and easily replaceable. Once a serious fault is diagnosed it does not make sense to run the bearings to the absolute end of life rather than replacing with new. Windings repair is considerably more difficult and often impossible; in this case the machine lifetime is determined by time of winding failure, even if the bearings fail first. It was decided to focus most of the research on winding health, to develop a novel detection method and link end of life with measure parameters.

1.4 Winding Failure

Winding failure occurs when the insulation layer between conductors, subject to a voltage difference, can no longer support the voltage and breaks down to allow current flow. Fatigue failure of the wire itself has not been reported as a problem in literature; therefore winding degradation can be entirely attributed to the lifetime of the insulation layer separating conductors.

Insulation is subjected to four degradation pressures: Thermal, Electrical, Environmental and Mechanical. Chemical breakdown of the insulation material has been linked to the insulation strength characteristic [23]. Chemical processes are strongly dependent on temperature, and it is currently used as the main predictor of lifetime, based on the temperature classification of the insulation [24]. Air pockets, impurities and other weaknesses internal to the insulation, create localised weakness of the dielectric properties, allowing localised dielectric breakdown when subjected to an electric field. Partial discharges are a significant problem in high voltage machines, where the electrical damage can result in erosion of insulation and decreasing the mechanical strength of the insulation.

Operating environment of the machine can introduce contamination through moisture and dust ingress. In some machines, the effect of radiation and ambient gas such as ozone can greatly reduce the lifetime of the insulation. These environmental variables are usually neglected unless the machine is to be used in a specialised application.

Mechanical damage to the insulation can be caused by stress due to thermal cycling of materials with different coefficients of expansion, conductor vibration due to electromagnetic force and external factors inducing vibration of the machine. Some literature sources claim that little damage results from thermal cycling [25], while others clarify the problem by establishing a relationship between conductor length and mechanical damage [26] [27], showing damage is evident only in long (bar-wound winding longer than 1 meter) machines. Recent renewed interest has aimed to simulate the effect of temperature cycling [28] [29], showing the stress on the insulation, and attempt to use material models to predict end of life, however no conclusion has yet been reached with regard to the effect of mechanical damage to insulation in small and medium size machines.

1.4.1 Failure Prediction

Predicting insulation lifetime is essential in classification of new insulation material and new machine design. As early as 1930 [30], it was recognised that transformer insulation ageing is strongly dependent on operating temperature. Using folding strength as a mechanical strength indicator, a prediction was made for lifetime of insulation paper in [30], correlating the folding strength with breakdown and observing the folding strength over time, an initial lifetime

prediction was made in Equation (1.2), where Y is the lifetime, T is operating temperature and the constants are experimentally derived. The early work on transformer insulation strength is important because the overriding importance of temperature was first realised, and predictions were made for both steady state and varying duty cycle operational lifetime.

$$Y = 7.15 \times 10^{4} e^{-0.088T} \tag{1.2}$$

In 1948, a hypothesis was made to treat insulation degradation explicitly as a chemical phenomenon [23]. It was observed in [23] that the tensile strength of insulating paper seen in Figure 1.2, followed a similar trend to standard chemical reactions described by Equation (1.2).

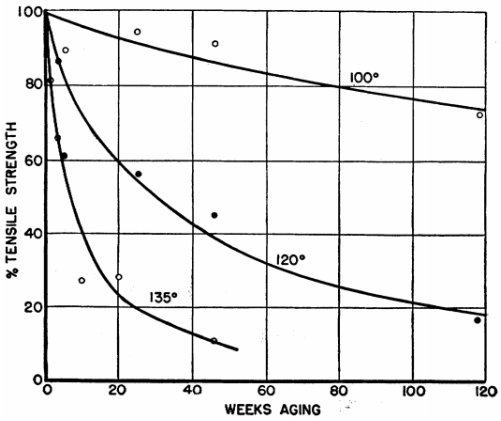

FIGURE 1.2 TENSILE STRENGTH OF AGED TRANSFORMER INSULATION PAPER [23]

Equation (1.4), describes an arbitrary concentration of a chemical constituent and its rate of change over time. The exponent n describes the order of the reaction, for thermal ageing, 1 is most appropriate, and K governs the rate of change of the Equation. Integrating Equation (1.4), one returns Equation (1.5) which describes the behaviour of a physical property P, dependent on the chemical reaction C, seen in Equation (1.3). The exponential progression of property "P", tensile strength can be seen in Figure 1.2.

$$P = f(C) \tag{1.3}$$

$$\frac{dC}{dt} = -KC^{n} \tag{1.4}$$

$$log(C) = -Kt + log(C_0) \tag{1.5}$$

When the degradation of insulation is defined explicitly as a chemical reaction, the rate of change of the reaction can be defined by the Arrhenius Equation (1.6). In Equation (1.6), the reaction rate K is determined by the activation energy of the reaction Ea, the molar gas constant R, the pre-exponential

frequency factor constant A, and the temperature T. The Arrhenius Equation has been derived experimentally from observations of chemical reactions and has been successfully used to predict the rate of chemical reactions with respect to temperature.

$$K = Ae^{-\frac{E_a}{RT}} \tag{1.6}$$

Substituting Equation (1.6) into (1.4), one can use the resulting Equation (1.7) to determine predicted lifetime of the insulation. To set a failure criteria, the relationship between the physical property P and the threshold for breakdown must be established. Defining this threshold requires experimental breakdown data, but for an example mathematical derivation we can define the failure threshold at the time when the value of C reaches 20% of its original value, at time t_{20}.

$$log\left(\frac{C_0}{C}\right) = Ae^{-\frac{E_a}{RT}t} \tag{1.7}$$

$$constant = Ae^{-\frac{B}{T}t_{20}} \tag{1.8}$$

$$\log(L_{end}) = \frac{B}{T} + \log(L_0) \tag{1.9}$$

$$L = L_0 e^{\frac{E_a}{R}\left(\frac{1}{T}-\frac{1}{T_0}\right)} \tag{1.10}$$

When the ratio of C_0/C is given at t20, all factors of Equation (1.7) become constants except temperature, expressed in Equation (1.8) where $B=E_a/R$. Expanding Equation (1.8), combining and redefining the constants, one is able to define an inverse relationship of insulation life with temperature, returning Equation (1.9), where end of life can be related to initial life constant, constant B and temperature.

Equation (1.9) has become the accepted industry standard to predict lifetime of insulation, it is used in IEEE standard 101 [24] to conduct accelerated life tests on insulation to classify endurance of insulation. An alternate formulation of lifetime determination is shown in Equation (1.10), this is commonly used in machine design [31], in this equation the constants in Equation (1.9) have been normalised so that lifetime is referenced to L_0 at temperature T_0.

In IEEE standard 117 [32], samples of insulation are subjected to thermal, electrical moisture and vibration stress cycles to represent ageing, with the temperature stress and number of running hours recorded. Plotting the temperature on an inverse -1/T scale on the X axis and sample life on a log y axis,

fitting parameters to Equation (1.9) becomes a simple straight line fit. The temperature index (TI) of the material is classified as the extrapolation of the fit, indicating at what temperature the sample is expected to last 20,000 hours. To simplify the choice for machine designers, a number of standard insulation classes have been defined, Class A with a TI of 105°, Class F TI of 155° and Class H TI of 180°, with several others covering intermediate ranges.

Accelerated lifetime tests essentially aim to measure the L_0 and E_a constants in Equation 1.10. The activation energy is especially important, as it determines the rate of insulation degradation. A direct method to measure E_a is shown in [33] by using Differential Scanning Calorimetry (DSC) to measure the Oxidation Onset Temperature (OOT) of insulating varnish, the assumption being that the main long term degradation is oxidation. E_a calculation from OOT in [33] of 114kJ/mol compares favourably to E_a of 121kJ/mol, which can be calculated from Equation (1.10) for the same H class of insulation as used in the experiment.

$$Q_{10} = \left(\frac{k_2}{k_1}\right)^{\frac{10}{(T_2 - T_1)}} \tag{1.11}$$

$$k_2 = k_1 Q_{10}^{\frac{(T_2 - T_1)}{10}} \tag{1.12}$$

$$L_{end} = \frac{20{,}000\ hrs}{2^{\frac{(T_2 - 180)}{10}}} \tag{1.13}$$

In chemistry, it is often useful to know the reaction rate change for every 10 degrees of temperature increase. Q10 is a dimensionless quantity defined in Equation (1.11), as the ratio of reaction rates k_1 and k_2 at temperatures T1 and T2. Rearranging Equation 1.11, one can predict the reaction rate k_2 in Equation (1.12), if one knows only the reaction rate at k1, at temperature T1. Most chemical reactions have a Q10 rate of around 2, where the reaction rate doubles for every 10 degree increase in temperature. This assumption is also used in machine insulation lifetime prediction, enabling easy "rule of thumb" prediction of insulation life. The application of this rule is shown in Equation (1.13), where the insulation lifetime is predicted for class H insulation with temperature T_2 in degrees Celsius. The rule of thumb works because the temperature in Equation (1.10) is specified in Kelvin, temperature changes at typical motor operating conditions are high enough so that the reciprocal temperature scale 1/T becomes quasi-linear. At temperatures higher and lower than the 180° specified in Equation (1.13) used to estimate lifetime for Class H insulation, the equation will underestimate final lifetime, giving a conservative safety margin.

In IEEE standard 98 [34], it is assumed that ageing due to thermal degradation is dominant, and the temperature index of the material can be defined as the temperature where it would endure for 20,000 hours. In addition

to thermal ageing, IEEE standard 117 [32] specifies that test motorettes representative of motor winding must undergo exposure to vibration, moisture and electric voltage exposure during the testing, applied in cycles. Interaction between degradation factors can be direct and indirect. Direct effect has a synergy of two degradation modes while both degradation modes are active, if one mode were to decrease or stop, ageing behaviour continues as a single rate effect. An indirect effect creates a memory of both effects, thereby permanently changing the rate of one factor by application of a second, even if afterwards the second factor has decreased.

$$L = cE^{-r} \tag{1.14}$$

$$L = ae^{-wE} \tag{1.15}$$

Common multifactor ageing models reported in [35] [33] consider the interaction between electrical and thermal degradation. There are two basic methods to represent electrical ageing, where data is fitted to either an exponential model in Equation (1.15) or an inverse power model in Equation (1.14). Constants (c and r) or (a and w) are determined from practical tests, most commonly twisted pair wire test, with electrical stress between strands [36].

$$L = L_0 \left[\frac{E}{E_0}\right]^{-(n-bT)} \times e^{-BT} \tag{1.16}$$

$$L = \frac{h}{k_b T} e^{\frac{\Delta G}{kT}} csch^{\frac{e\lambda E}{k_b T}} \tag{1.17}$$

$$L \approx \frac{h}{k_b T} e^{-\frac{e\lambda E}{kT}} \times e^{\frac{\Delta G}{k_b T}} \tag{1.18}$$

Equation (1.16) [37] shows implementation of the most common method of multi-factor ageing, simply multiplying the electrical degradation factor by the thermal degradation factor. Thresholds for degradation onset due to electrical field may be added as shown in [37] for cross-linked polyester (XLPE) undergoing combined electrical and thermal stress. Equation (1.17) uses the Eyring equation [33] to analytically model the lifetime of insulation based on temperature T influenced by electric field strength E. It is interesting to note in Equation (1.17), for high electric field, the hyperbolic cosecant function, csch(x) where x>1 simplifies into Equation (1.18). This equation is effectively a multiplication of Equation (1.15) electrical stress and Equation (1.10) governing thermal degradation, where the change of Gibbs free energy, ΔG is used to represent activation energy and other constants are combined into the 'a' and 'w' constants in Equation (1.15).

1.5 Converter Reliability

The survey on motors used in offshore oil and gas industry [7] includes a significant number of inverter driven machines, using mostly silicon controlled rectifiers. The failure rate of these components has been included in the column 'other' in Figure 1.1 and is comparable to insulation failure prevalence. Inverter component failure rates the details of the "other" column, are important to understand.

An industrial survey carried out in 2011 [38] used a similar methodology as in [1], for the purpose of identifying modern power electronics converter reliability and areas of weakness. The breakdown by component failure was identified and is shown in Figure 1.3. It was found that the most vulnerable component to failure is the semiconductor switching device, followed by capacitor failure and gate drive circuitry.

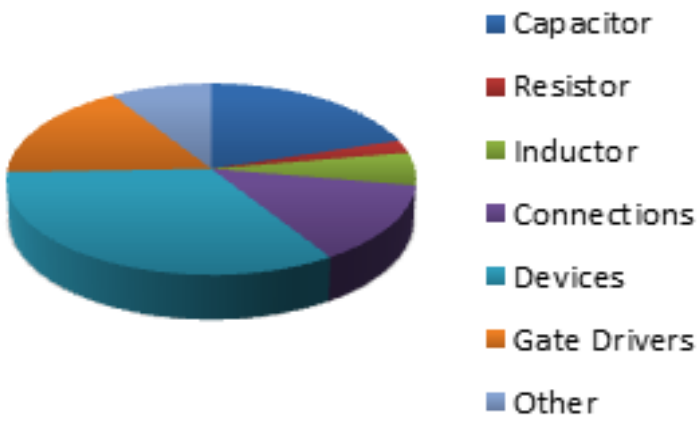

FIGURE 1.3 RELATIVE CONVERTER BREAKDOWN [38]

In the field of motor drives it is evident in [38] that the role of capacitor breakdown decreases, relative to increased device and gate driver failure. Because of the analogy in health monitoring between machine insulation and capacitors, capacitor breakdown has been investigated further.

1.6 Capacitor degradation

Aluminium electrolytic capacitors are widely used in motor drives to maintain the DC bus voltage and to filter out high frequency currents due to converter switching. They experience high voltage stress and hot ambient temperature. The capacitor consists of three key components; the aluminium anode with a thick Al_2O_3 (aluminium oxide, acting as the dielectric) layer, liquid electrolyte and paper insulator. The Al_2O_3 acts layer is added by using electrolysis to build a controlled thickness layer of oxide which is directly proportional to voltage and capacitor voltage rating [39]. The oxide layer is continuously reformed and degrades in quality, resulting in decrease of capacitance and increase of Equivalent Series Resistance (ESR). At the same time the electrolyte slowly evaporates and thickens. At the last stage before failure, the electrolyte is no longer in contact with dielectric, hence the capacitance value decreases sharply.

The effects of oxide layer degradation and electrolyte thickening has been experimentally linked with lifetime, using accelerated life tests [40] [41] and linked with the decreases in capacitance and increase of Equivalent Series Resistance (ESR). The generally accepted definition of end of life for a capacitor is an increase of ESR by 2.8 multiples and around 20% decrease in capacitance [39] [42].

A practical technique to monitor ESR is demonstrated in [43] by directly measuring voltage, current and temperature of a capacitor and calculating the dissipated power. An alternative method to measure ESR is presented in [44] where an FFT analysis is performed on the bus ripple voltage and current and the magnitude components are used. Comparison with an offline test yields good accuracy and phase information, allowing potential for the value of capacitance to be extracted. A Kalman filter with least squares algorithm is proposed for the measurement for ESR and C in [45] concluding this as a viable method. This method is compared against direct online measurement of values in [42]. It is pointed out that the Kalman filter performs well for measuring C while the direct measurement is more suited to ESR. A method which eliminates a direct current sensor on the capacitor is shown in [46] by using conventional phase current sensors for capacitor diagnosis, this method requires good knowledge of the rest of the system, as resistance from semiconductor devices and leads will also contribute to the ESR estimate.

Contrary to the usual assumption that a capacitor is classed as failed when $ESR = 2.8*ESR_0$ or $C = 0.8*C_0$, a maintenance strategy is presented in [42]. The probability of capacitor failure, cost of maintenance and cost of failure is factored in, which can then be used to judge the optimal time to replace a capacitor which may not necessarily be at the accepted failure thresholds.

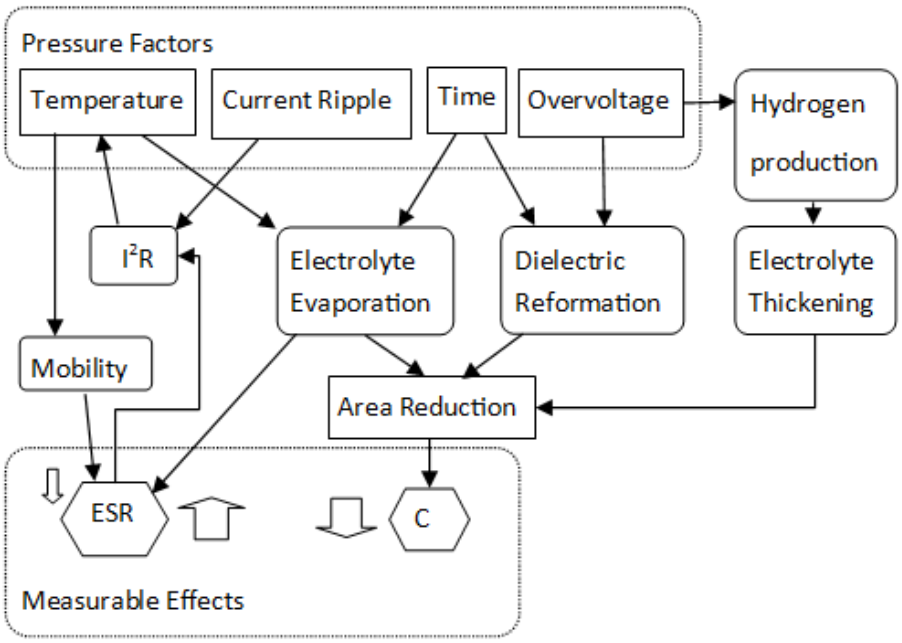

FIGURE 1.4 INTERACTION OF DEGRADATION MECHANISMS AND MEASURED HEALTH INDICATORS

The diagram in Figure 1.4 shows the chemical relationships between pressure factors and measurable outcomes. Standard methods of predicting capacitor degradation use Arrhenius lifetime prediction, which links temperature to mean time to failure. The Arrhenius Equation is sensitive to temperature and requires an accurate estimate or measurement of the internal temperature of a capacitor. A comprehensive heat loss model for capacitors is presented in [47], where the capacitor temperature is estimated based upon calculation of predicted convection and conduction losses. An empirical temperature profile inside a typical capacitor is presented in [39], which could be included in the estimation process using a look up table.

Understanding capacitor failure modes, the mechanisms, physical processes and the impact of these on measurable parameters has allowed the diagnosis of capacitor fault and prediction of failure. The study of capacitor health presents a template for electrical component lifetime prediction. The importance of combining analytic models, physical analysis and practical testing is demonstrated.

1.7 Focus of Research

Reliability studies on machines in industry show that most machine faults are attributable to bearing fault, followed in occurrence by stator faults. Converter faults make up a minor but important part of the drive failure.

Bearing failure is well understood, with industry providing enough information to specify design life of bearings as well as monitoring data. Understanding and monitoring of bearing failure is a mature technology, in addition, bearings can be replaced quickly and cheaply with spare components, reducing maintenance issues. To assess the current state-of-art in bearing health monitoring, further literature review covering failure modes and detection methods is presented in Chapter 2. A commercial bearing monitoring system has been evaluated and the results are discussed.

Capacitor degradation shares several similarities with winding degradation, both processes are assumed to be due to chemical reactions, and both models can be approximated by the Arrhenius law of temperature dependence. Literature shows interest in ability to monitor capacitance state of health over time for maintenance and availability purposes, providing a template for electric component health monitoring.

Monitoring winding insulation degradation, failure and lifetime is an emerging field of study with potential for expansion. It has been decided to make winding failure modes and insulation monitoring methods will be the primary focus of investigation. Chapter 3 is dedicated to understanding insulation degradation investigation of insulation behaviour across multiple frequencies, and development and validation of an improved insulation model. Literature review of insulation monitoring systems is performed in Chapter 4, and a novel monitoring system is developed and tested, implementing on-line characterisation of insulation.

Using the equipment, the assumptions from literature review are tested, with regards to effect of moisture, temperature variation and improved insulation in Chapter 6. The main focus however must be to add to the knowledge of insulation behaviour over time. The equipment designed in Chapter 4 is therefore used to monitor insulation behaviour over an accelerated lifetime in Chapter 5. The findings are noted, discussed and compared to the expectation from literature.

Chapter 2

Bearing Health

Surveys of machine failure consistently rank bearing failure as the most prevalent machine fault, for every machine size, voltage and power. An understanding of bearing failure mechanisms and bearing health monitoring methods is required to establish a full picture of monitoring required for determination of overall machine health status.

As part of the work done in this study, bearing failure modes and bearing monitoring methods have been reviewed in this chapter. A commercial monitoring system has been evaluated. The methodology, results and discussion are presented here.

2.1 Bearing Failure Modes

Bearing degradation originates from multiple sources of damage. Metal fatigue, resulting from bearing element contact is the most common mode of degradation. Other modes present are degradation due to wear, corrosion, plastic deformation and electrical erosion, each of which is briefly discussed.

2.1.1 Fatigue

Metal fatigue is presumed to be the dominant mode of degradation [48] [15] in Section 1.3, where the dynamic load rating of the bearing is determined in laboratory testing. The progression of metal fatigue is shown in Figure 2.1. Early warning of bearing malfunction can be detected by monitoring appearance of small pits, before they grow to cause catastrophic failure.

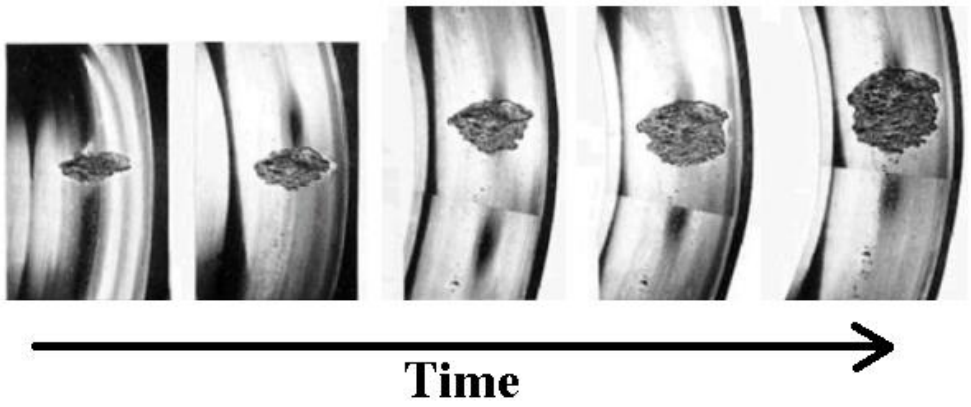

FIGURE 2.1 SUBSURFACE INITIATED FATIGUE DAMAGE PROGRESSION [49]

Pitting creates vibration on every contact during bearing operation, which can be detected and tracked over time to diagnose the number and severity of pitting. Metal fatigue occurs for all bearings during normal operation and is unavoidable in rolling bearings.

2.1.2 Wear Damage

In Figure 2.2, abrasive damage to contamination is shown. External particles have infiltrated into the bearing and created pitting seen in the highlighted area in Figure 2.2, shielded bearings and sealed bearings aim to reduce the amount of contamination which can percolate to reach the bearing races.

FIGURE 2.2 ABRASIVE WEAR DUE TO CONTAMINATION [50]

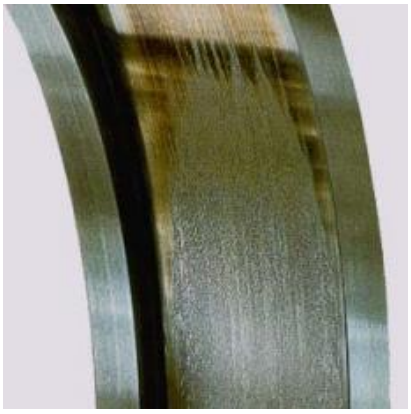

FIGURE 2.3 ADHESIVE WEAR ON OUTER RACEWAY SURFACE [49]

Adhesive wear, the transfer of material from one surface to another is shown in Figure 2.3. The cause of adhesive wear is a combination of poor lubrication and excessive loading. The effect of both adhesive and abrasive wear is to add local weakness in material [49], with potential for cracking affected areas, creating large pits, accelerating bearing degradation.

2.1.3 Bearing Corrosion

Bearing corrosion comes in three types, chemical, friction and fretting corrosion. In Figure 2.4, the effects of moisture ingress, leading to chemical reaction with water are clearly seen. The corrosion forms a rough surface, which can flake off to create contamination. Chemical corrosion can also be initiated through vibrational movement. Fretting damage occurs when the bearing has a loose fit, inter-surface movement flake off metal off the surfaces and create sites for corrosion.

FIGURE 2.4 CHEMICAL CORROSION ON BEARING OUTER RACEWAY [49]

A special case of fretting corrosion is initiated by external vibration. During standstill, external vibration to the bearing can initiate wear in contact points of the bearing. This effect is observed in Figure 2.5, named false brinelling, due to the apparent indentations present due to the wear and corrosion.

FIGURE 2.5 FALSE BRINELLING INDENTATIONS [49]

FIGURE 2.6 TRUE BRINELLING PLASTIC DEFORMATION [49]

2.1.3 Plastic Deformation

True brinelling is the appearance of indentations in the bearing raceways due to mechanical force. Figure 2.6 shows true brinelling due to an overload of the bearing during mounting. Indentations can also be present in the bearing cage and bearing shields due to incorrect handling procedure. Deformation due to transient overload or high static load will also create depressions similar to those seen in Figure 2.6.

Operation with deformation due to transient and static overload is unacceptable [51], and although different standards exist for damage due to initial handling, deformation due to poor handling should be avoided.

2.1.4 Electrical Erosion

Bearing current due to potential difference between rotor and stator has been a well-known phenomenon since 1924 [52]. The potential difference in line-driven machines is caused by magnetic dissymmetry, inducing a shaft potential voltage, leading to bearing current. It is common practice to insulate the non-drive end bearing in large machines to stop this effect.

Inverter-fed drives have inherent Common Mode (CM) voltage present, the voltage harmonics are comprehensively studied in Section 4.4. The common mode voltage induces a current to flow through the machine ground-wall insulation and through the bearings taking the paths shown in Figure 2.7.

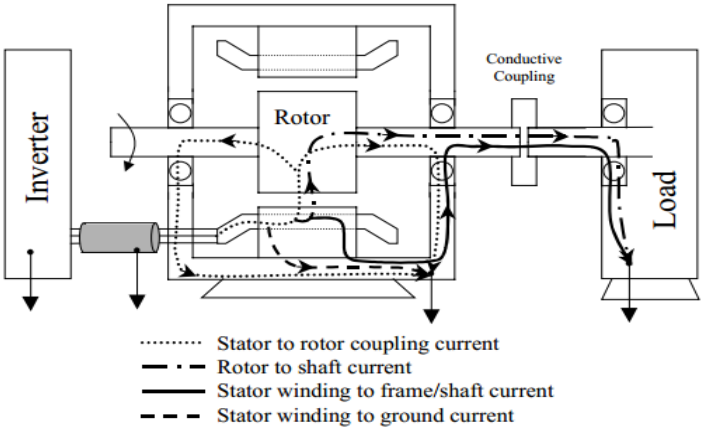

FIGURE 2.7 COMMON MODE CURRENT PATHS IN A MOTOR [53]

To reach the bearings, common mode current is coupled through the winding-rotor capacitance to return to ground, denoted by the dotted path in Figure 2.7. An alternate source of bearing current is formed by the possibility of different load and motor ground voltages, present due to poor grounding. The current takes a path denoted by the solid line in Figure 2.7 to flow through to the load, this path is often ignored due to good grounding practice.

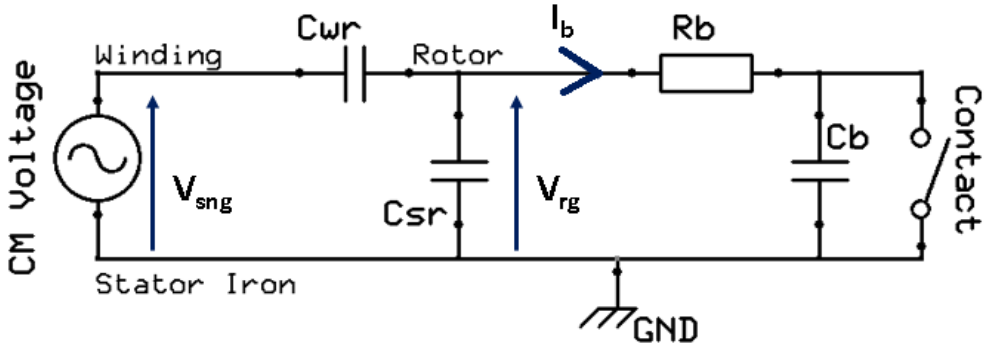

FIGURE 2.8 ELECTRICAL BEARING MODEL

The electrical model for Figure 2.7 is shown in Figure 2.8. The common mode voltage is coupled through the winding to the rotor through capacitance C_{wr}. The voltage present at the bearing is determined by the CM voltage

magnitude and the voltage ratio determined by C_{wr} and C_{sr}, the winding to rotor and rotor to stator iron capacitances respectively.

The bearing itself is represented in Figure 2.8 by the bearing resistance R_b, bearing capacitance C_b and a contact switch. During normal operation, the bearing element is supported by a film of insulating grease. Contact occurs due to occasional bearing contact. The film can also suffer an electrical discharge due to the rotor-ground voltage exceeding the film voltage withstand.

The film thickness which forms C_b depends on load, temperature lubricant viscosity and dielectric properties. In [54] the breakdown voltage on an inverter driven machine is shown to be 30V.

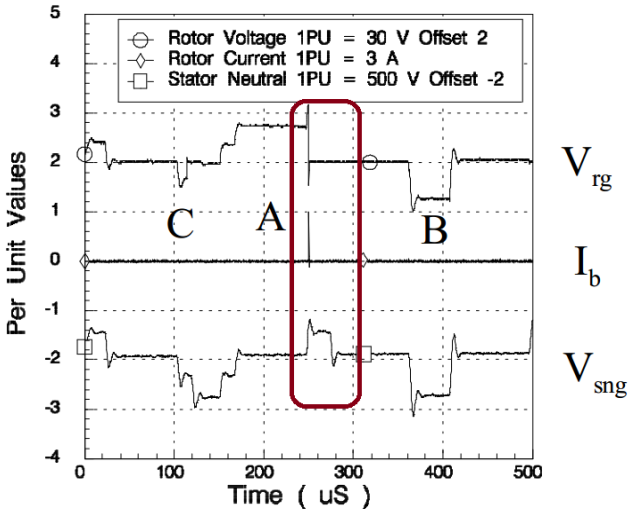

FIGURE 2.9 ROTOR VOLTAGE, BEARING CURRENT AND COMMON MODE VOLTAGE. BEARING CURRENT DISCHARGE EVENT EMPHASIZED [54]

In Figure 2.9, it can be observed, especially at point "B" that the rotor voltage V_{rg} is charged by the common mode voltage V_{sng}. Once the voltage exceeds 30 volts at point "A", a 3A discharge current I_b is observed. Voltages V_{rg}, V_{sng} and current I_b are indicated on the bearing current model in Figure 2.8. At point "C" it is notable that although the V_{sng} decreases, the rotor voltage instead returns to zero. At this point it is highly likely that the bearing makes a contact through normal contact rather than with discharge as at "A", therefore the current I_b is low enough to not be observed.

Damage resulting from bearing current presents two modes: fluting wear due to steady current flow, the effect seen in Figure 2.10, and pitting damage due to discharges when breakdown of the bearing capacitance C_b takes place. The effect can be seen in Figure 2.11.

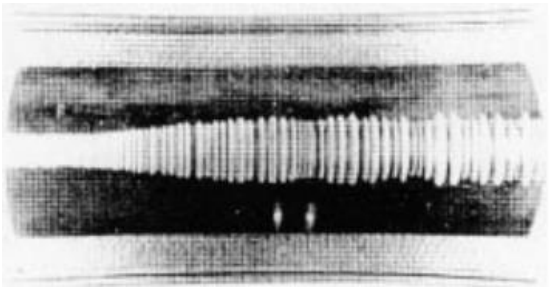

FIGURE 2.10 FLUTING DAMAGE DUE TO BEARING CURRENT [49]

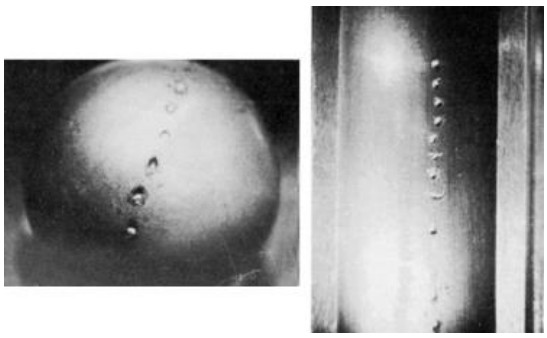

FIGURE 2.11 PITTING DAMAGE DUE TO BEARING CURRENT DISCHARGE [49]

Bearing current damage on sine wave machines, produces fluting damage observed in Figure 2.10. An established current density of 1A/mm^2 is a reasonable level of bearing current [54].

Various methods have been proposed to decrease and eliminate bearing current. Electrostatic shielding of the windings using copper shielding of the rotor-stator gap, has been attempted successfully in [55] [56] to reduce the coupling capacitance C_{wr} in Figure 2.8. Reduction of the dv/dt transient is proposed in [57] via careful cable impedance control and filtering. Applying good quality grounding to the machine and load, combined with insulated bearings has been suggested in [53]. Spalling as seen in Figure 2.11 is not accounted for in the fatigue model currently used in industry. Unlike most other additional wear modes, bearing current cannot be completely eliminated using best practice of bearing application.

2.2 Bearing Health Monitoring

All aforementioned bearing degradation modes will increase vibration present due to bearing contact and changes in the running surfaces. There exists a variety of methods to detect the vibration of bearings, monitor these over time and determine the state of health of the bearing.

2.2.1 Bearing Harmonics

A rolling element bearing in a motor allows the rotation of the output shaft relative to the static stator element. Contact between the two elements is maintained through ball bearing elements, which move over the inner and outer race of the bearing. If there is a fault on one of the bearing components, rolling over the top of this fault would create a shock, which is picked up as vibration. Knowing the bearing element dimensions, it is possible to determine which bearing element contains the fault through analysis of vibration frequencies, and measurement of the severity of the vibration can determine severity of fault.

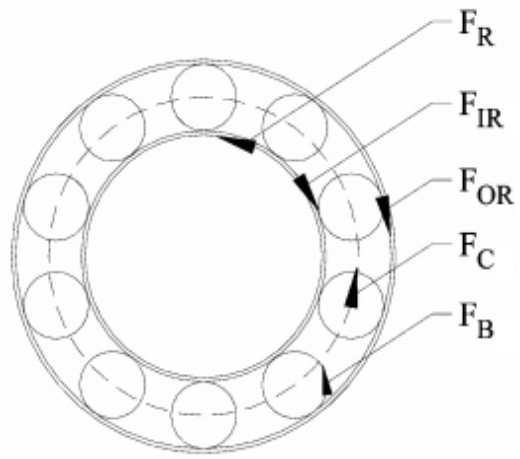

FIGURE 2.12 BEARING ELEMENT FREQUENCIES [16]

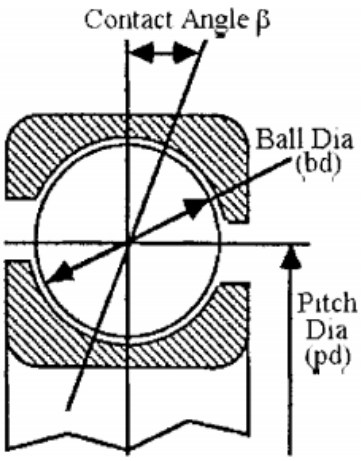

FIGURE 2.13 BEARING CONTACT DIAGRAM [16]

Figure 2.12 shows the rotation directions of the four bearing components: the bearing outer rotor, inner rotor, bearing element and the bearing cage which holds the rolling elements in place relative to each other. The frequencies produced by contact with bearing elements can be calculated for any given rotational speed, expressed as frequency f_r, when parameters n, BD and PD, denoting number of bearing elements, ball diameter and pitch diameter respectively, are available.

$$F_{IR} = \frac{n}{2} f_r \left(1 + \frac{BD}{PD} \cos\beta\right) \tag{2.1}$$

$$F_{OR} = \frac{n}{2} f_r \left(1 - \frac{BD}{PD} \cos\beta\right) \tag{2.2}$$

$$F_C = \frac{1}{2} f_r \left(1 - \frac{BD}{PD} \cos\beta\right) \tag{2.3}$$

$$F_B = \frac{PD}{2BD} f_r \left(1 + \left(\frac{BD}{PD}\right)^2 \cos^2\beta\right) \tag{2.4}$$

The bearing frequencies [19] for faults on the inner rotor, outer rotor, cage and bearing element are expressed in Equations (2.1), (2.2), (2.3) and (2.4) respectively. To calculate the vibration frequencies in Equations (2.1) to (2.4), the bearing dimensions shown in Figure 2.13 are required, alternately the bearing frequencies can be obtained directly from the manufacturer of the bearing [17], requiring only the bearing identification number.

2.2.2 Vibration Monitoring

Vibration resulting from faults in the bearings, at frequencies specified above can be measured directly by placing vibration detection sensors near the bearing. The most common industry accepted sensor uses piezo-electric transducers [58] attached to the motor. Other methods have used acoustic sensors [59] [60] to monitor vibration and more exotic sensing technology such as in [61] where induced resonance with the bearing cage was used to measure vibration.

The difficulty of placing sensors was identified in [62], with a suggestion to use acoustic waveguides to reach the desired location. Due to changing speed conditions expected in drives, a variety of techniques has been developed for discriminating the bearing harmonics. Short time Fourier transform [63], minimum entropy deconvolution [64] and wavelet decomposition [65] have each been used to track harmonics over time, combating problems of noise discrimination and changing speed.

The advantage of vibration monitoring is the vast experience of knowledge available. Industry standards exist which specify the RMS vibration velocity for different classes of bearings and machines [66]. Although bearing harmonics have not specific standards, work is currently being done to determine Remaining Useful Lifetime (RUL) from vibration signature. In [65], harmonics which are tracked for the four bearing frequencies expressed in Section 2.2.1 are used as inputs to a learning algorithm which discriminates the training healthy set from bearings with faults to detect incipient failure. In [67] a database of time domain vibration data from 11 bearings was used to test several RUL estimation methodologies. In [67], both the time domain and frequency domain data were combined to analyse the kurtosis of frequency domain data over time, analysis of anomalies in the frequency data were also analysed. Methods in [67] were judged as a success due to monotonically increasing bearing indicator over life, allowing prediction by setting a threshold for failure, crossing which determines RUL. The paper won the 2012 PHM data challenge, and further such challenges are ongoing, to solve the challenges to analyse vibration data and provide a useful state of health of the bearings.

2.2.3 Motor Current Signature Analysis (MCSA)

Considerable work done in vibration monitoring of bearings shows the way to discriminate harmonics and to use the vibration data to diagnose bearing health and predict the remaining lifetime. Vibration monitoring requires hardware additional to the drive, recently interest has increased in using the current sensors available in drives to monitor bearing vibration.

$$f_{current} = |f_0 \pm n * f_{vibration}| \quad \textbf{(2.5)}$$

Vibrating in the machine rotor alters the flux linkage of the machine, and thus physical vibration is reflected in the current drawn by the machine. Vibration harmonics appear as sidebands of the fundamental frequency f_0, as per Equation (2.5) which shows that the bearing vibration harmonics will be present at integer multiples n around the fundamental. Successful demonstration of measuring bearing damage has been achieved using current measurement, employing wavelet decomposition of current [19], application of the Wiener Filter to cancel noise [68], and using Artificial Neural Network approach [69] to learn the healthy state of machine currents. A MCSA system has been evaluated as part of the project, the operation of which will be covered in the following section.

2.3 Commercial System Evaluation

The field of bearing monitoring has matured to the level where multiple companies produce complete bearing monitoring systems, bearing diagnosis tools, and acceptability standards exist for degradation acceptability, mainly for induction motor drives.

To study the effectiveness of the state of art of bearing monitoring for permanent magnet (PM) drives, in partnership with Artesis Technologies, a commercial MCSA system [21] was evaluated. The system was exposed to a set of new bearings for a requisite learning period, followed by running with degraded bearings inserted into the same machine. System effectiveness, as well as usability of the equipment has been the focus of the evaluation.

2.3.1 Aim

The system used in this experiment claims to be able to detect bearing degradation in low voltage inverter-driven machines. However it has not been used or demonstrated in PM machine drives. The main aim of the experiment conducted was to replicate the most realistic conditions possible for the system to operate the monitoring system as it would be in the field, and detect bearing damage under a variety of conditions.

The bearing damage must be done in a method most representative of reality, allowing the system to detect bearing damage under realistic conditions. For an effective monitoring system, it is important that it reports faults only with damage present. False positive results may completely defeat the usefulness of the monitoring system, requiring more call-outs and work than regular routine maintenance. The secondary aim of the experiment requires the bearing monitoring system to operate normally with no bearing degradation, without presenting false alarms.

An ideal monitoring system would have just two factors available to the user: the mode of failure and the remaining useful lifetime of the system. The overall system usability is evaluated with regards to the possibility of reaching this idea, as well as the ease of installation and use of the system in general.

2.3.2 Equipment

The particular system evaluated from Artesis Ltd, was the Motor Condition Monitoring (MCM) low voltage, inverter grade unit, as seen in Figure 2.14. The unit was designed as a panel mount device to sit alongside inverter drives and other equipment in industrial applications. The system is designed to monitor the phase voltage and current waveforms of inverter driven motors to use MCSA techniques to detect and track bearing characteristic harmonics. Additional harmonics due to unbalance, rotor fault and stator short circuits are also monitored.

FIGURE 2.14 MCM-LV-IN-0005A MODULE FRONT PANEL

The unit contains three hall-effect current sensors, accepting input current up to $5A_{rms}$, and three voltage sensor inputs, accepting line voltage up to $480V_{rms}$. Higher voltage and current ratings are possible through connection of external voltage and current sensors to the device.

The machine selected for operation under monitoring was a 2.83kW inverter driven servo motor, rated at $400V_{rms}$ and $7.5A_{rms}$ at 3000 RPM. To operate the monitoring system without using external current sensors, the maximum current operation was limited to $5A_{rms}$. The monitoring system connection is pictured in Figure 2.15. The unit passes through the current from the drive to the motor. The voltage connection is made directly to the motor terminals to reduce impact of voltage drop due to cable current. Computer connection is made via Ethernet.

The MCM unit functions by monitoring the voltage and current harmonics of the machine in the frequency domain. The calculated harmonic power amplitudes are then used as indicators of problems. For variable speed operation, the acquisition is performed at steady state and harmonics are normalised to the speed during the initial learning period.

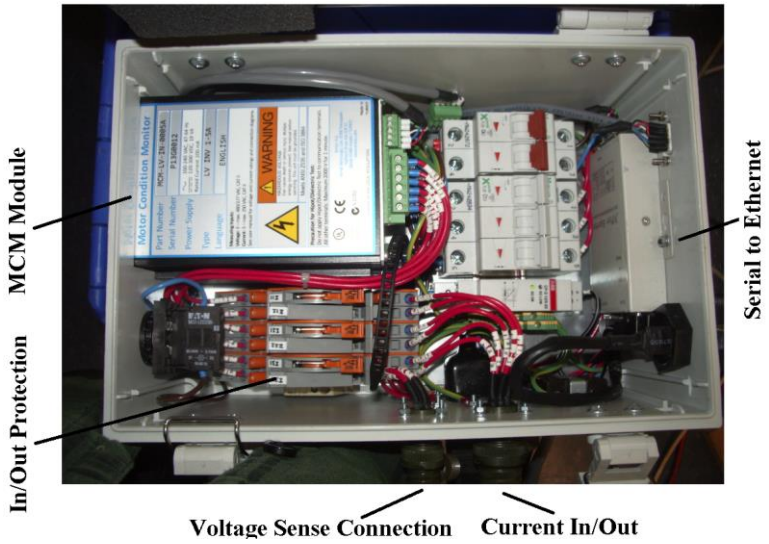

FIGURE 2.15 CONDITION MONITORING SYSTEM CONNECTION

It was shown in Section 2.2.1 that bearings with faults have distinct harmonics which can be calculated from mechanical dimensions, available from the manufacturer. The calculated inner and outer race harmonics are displayed in Figure 2.16, compared to the measured harmonics in the current. It can be observed that strong harmonics are present at the calculated locations. Other harmonics are also present, contributed by the main current and other bearing parameters, however only the harmonics of interest are highlighted.

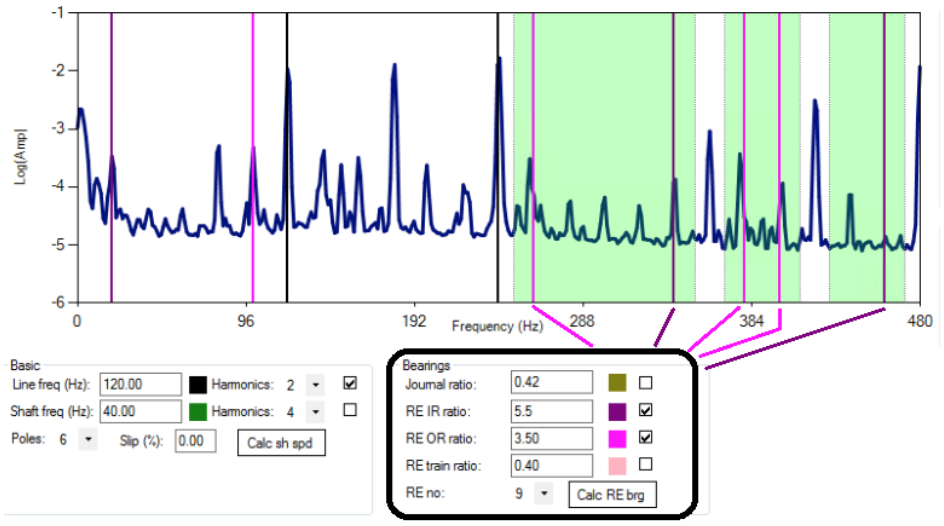

FIGURE 2.16 BEARING HARMONICS CALCULATED VS MEASURED

The MCM system requires a learning period to establish the typical harmonic amplitudes and expected deviation of amplitudes. The machine must operate at a single speed during the 'learn' period. The MCM unit also has an 'improve' mode which allows additional learning information to be updated for multiple speed operation. Majority of the time, the machine operates in the 'monitor' mode, here harmonic amplitudes are measured and the deviation from the mean, obtained during the 'learn' and 'improve' modes are tracked.

The deviation of bearing harmonics in zones highlighted in Figure 2.16 are combined by the Artesis software into a single parameter, visible to the user. This parameter is ultimately used in the results section to determine bearing status.

2.3.3 Methodology

To achieve the aims set out for the experiment, four tests were carried out, designed to most closely follow realistic running of the drive and operating recommendation from Artesis Technologies. The first three experiments replicated the running and monitoring of machines with fixed speed, variable load operation, at three different speeds. The fourth test replicates operation of a drive running at variable speeds and loads, representative of typical inverter driven machine operation.

FIGURE 2.17 SINGLE POINT PROGRESSION FAULT EMULATION [19]

The most commonly used method to test MCSA algorithms and detection equipment is shown in Figure 2.17. Real fatigue damage, as seen in Figure 2.1 is emulated in Figure 2.17 by drilling a hole in the outer race of the bearing, increasing hole size indicating fault progression. Another popular method of fault emulation seeds a fault in a raceway with a scratch, and uses accelerated ageing to enlarge the initial fault. The advantage of both these methods is the modelling of the most important failure mode of the bearing, and the ease of implementation.

The disadvantage of poor representation of reality for the method in Figure 2.17 and the long amount of time required for accelerated ageing. To test the MCSA equipment, it was decided to use a set of old bearings removed from a real machine after 3 years of operation during routine maintenance. This best allows direct comparison of new bearings with the most realistically aged bearings. For all tests, the monitoring equipment implements the 'learn' and 'improve' cycles for healthy bearings. The bearings are removed as in Figure 2.18 and faulty bearings are then inserted in their place.

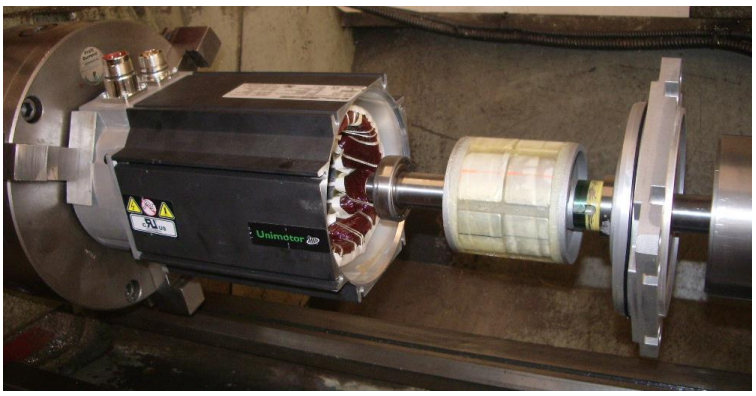

FIGURE 2.18 BEARING REPLACEMENT

FIGURE 2.19 NEW BEARINGS SET

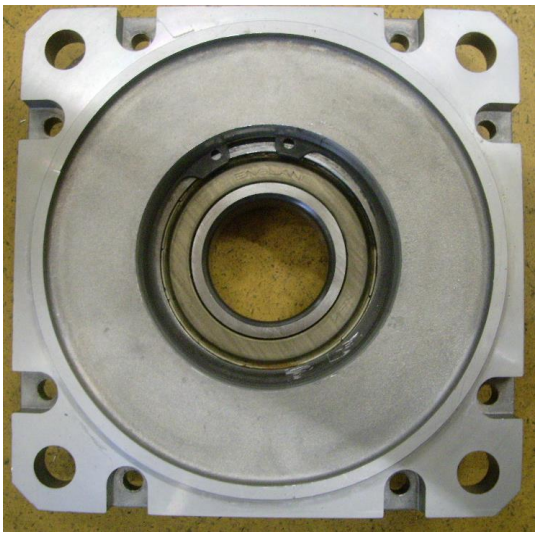

FIGURE 2.20 AGED FRONT END BEARING

The new undamaged bearings are seen in Figure 2.19, with the aged front end bearing shown in Figure 2.20. The discoloration of the aged bearing is clearly visible in Figure 2.20, it is also possible to feel roughness when turning the aged bearing. The biggest disadvantage with replacement of bearings during monitoring is the possibility of inducing eccentricity problems, eccentricity however has its own separate characteristic frequency set which the monitoring system claims to distinguish from bearing signature. The harmonics known to be influenced by eccentricity therefore will not be used to gauge the bearing health state.

Operational Mode	Colour	Duration	
		Iterations	Minutes
Learn		40	60
Improve		20	30
Monitor		20	30

TABLE 2-1 TIME ALLOCATION PER CYCLE

Table 2-1 shows the three operating modes in which the bearing monitoring system operates, the number of acquisition iterations and the

duration of each stage of the process. Each acquisition and processing iteration requires 90 seconds to run.

Healthy Bearings					Faulty Bearings Inserted			
Test 1								
	5A Learn	5A	3A	1A		5A	3A	1A
2400 RPM	1	2	3	4	2400 RPM	5	6	7
Test 2								
	5A Learn	5A	3A	1A		5A	3A	1A
1600 RPM	1	2	3	4	1600 RPM	5	6	7
Test 3								
	5A Learn	5A	3A	1A		5A	3A	1A
800 RPM	1	2	3	4	800 RPM	5	6	7

TABLE 2-2 FIXED SPEED TEST SCHEDULE

Table 2-2 shows the running sequence for the three fixed speed tests. The colours indicate the mode of operation of the bearing monitoring system, as assigned by Table 2-1. The numbering inside the table gives the sequence of measurement.

For the three fixed speed tests, the machine is initially operated in the 'learn' mode for the bearing monitoring system in the motoring mode under constant torque mode, requiring 5A current. Load is applied to the machine through an AVL-102/20 dynamometer, the setup is shown in Figure 2.21. Each learn mode is carried out anew for each experiment. After the initial learning period, the bearing monitoring system switches to the 'improve' mode. In this mode the bearing monitoring data is available, and is used to track the healthy bearing state. The healthy bearings, monitored under 'improve' mode are exposed to three loading conditions, running the motor at 5A, 3A and 1A. When the bearing is replaced, the bearing monitoring system is switched to 'monitor' mode, and the three loading conditions are repeated.

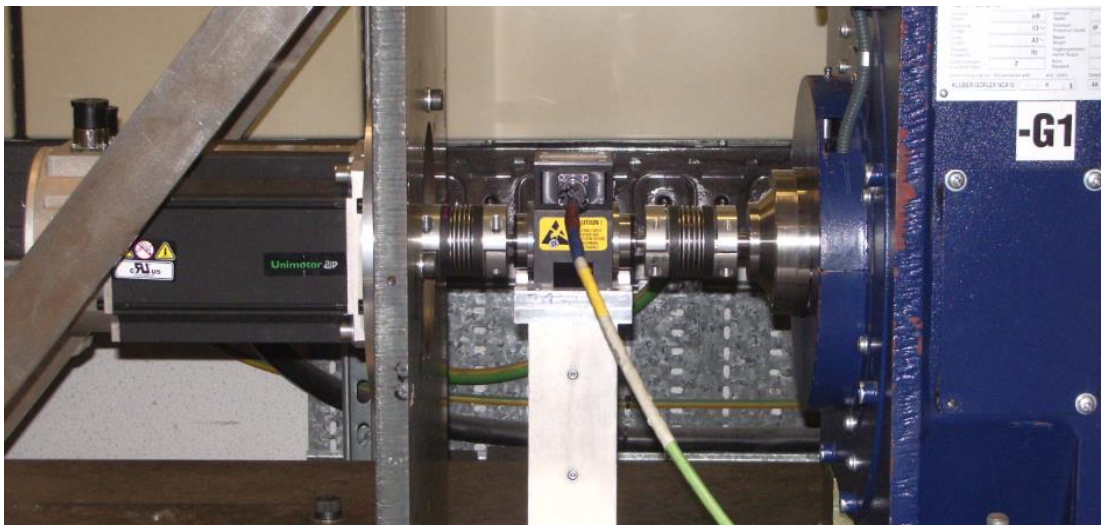

FIGURE 2.21 MACHINE AND DYNAMOMETER CONNECTION

Healthy Bearings					Faulty Bearings Inserted			
Test 4								
	5A Learn	5A	3A	1A		5A	3A	1A
2400 RPM	1	2	3	4	2400 RPM	11	12	13
1600 RPM		5	6	7	1600 RPM	14	15	16
800RPM		8	9	10	800RPM	17	18	19

TABLE 2-3 TEST 4 VARIABLE SPEED TEST SCHEDULE

The bearing parameters monitored with the new bearings and worn bearings are compared for the same loading conditions. The monitoring system must learn typical behaviour during the 'learn' cycle and not present false positives during the 'improve' running or false negatives during the monitoring of the worn bearings.

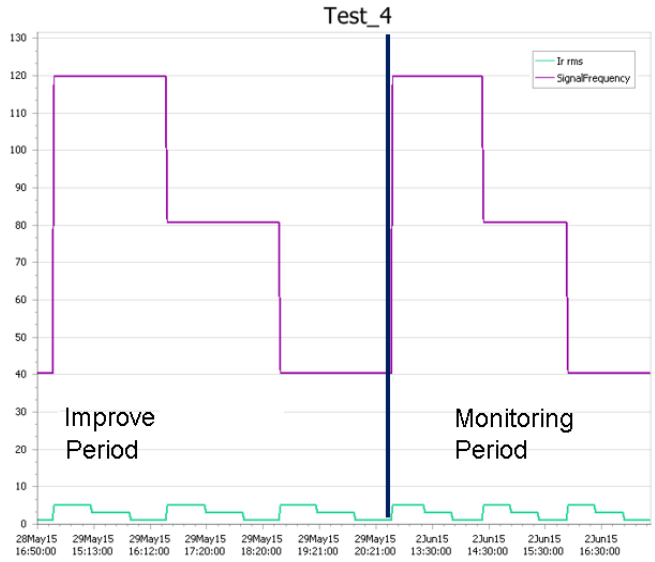

FIGURE 2.22 TEST 4 DRIVE FREQUENCY AND CURRENT COMMAND

Table 2-3 shows the running operation of test 4. The bearing behaviour is learnt at maximum load and then the machine is operated with healthy bearings in the 'improve' mode for each of the three speeds and three loads. In real life operation, an inverter driven motor may expect a change of speed and load. The speeds and loads selected for the four experiments are representative of the conditions that the motor under test is expected to experience.

Figure 2.22 shows the actual measured frequency and current during the test, with frequency (in Hz) indicating the motor speed and load. To reduce effects of 50Hz mains noise, the operational frequency of the machines were deliberately selected to be factors of 40Hz for all tests. For all four experiments it was possible to adhere to the times, speeds and loads specified. It was however observed that the 'monitor' cycles complete in 75 seconds, rather than the 90 seconds expected.

2.3.4 Results

The results for fixed speed experiments 1 to 3 show the bearing parameter output vs input current, with data for healthy and degraded bearings plotted together. The y axis units for the current are amps, the bearing parameter units are not given, due to the opaque nature of commercial equipment. The bearing trend however is clearly visible.

In Figure 2.23, the bearing parameter health indicator together with load current is shown for the fixed speed test at 2400 RPM. With the healthy bearing, at maximum current, there is some deviation from the nominal value of 3, obtained during the learning period, however at 3A and 1A operation, there is no deviation.

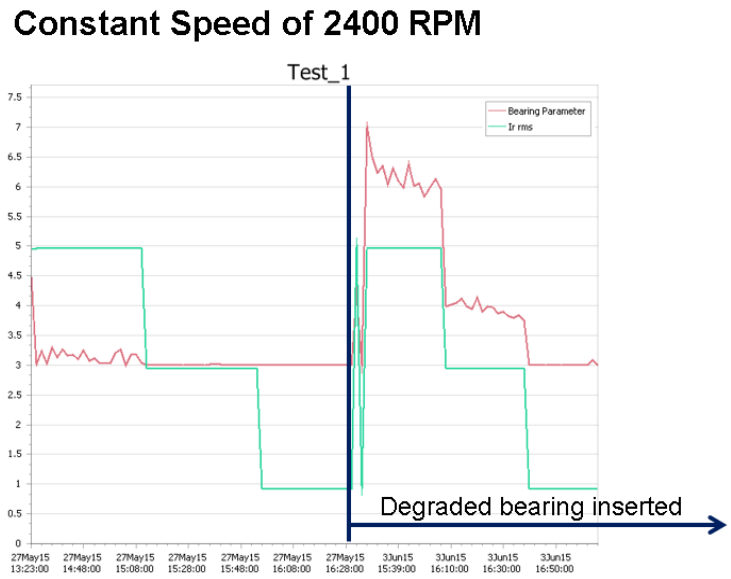

FIGURE 2.23 AGGREGATED BEARING PARAMETER FOR TEST 1

After the insertion of the worn bearings, the bearing parameter increases significantly, compared to its previous value at 5A operation. An initial trend is observed that with decreasing load, the bearing parameter decreases, at the lowest loading operation it is small enough to return the nominal value, despite operation with a worn bearing.

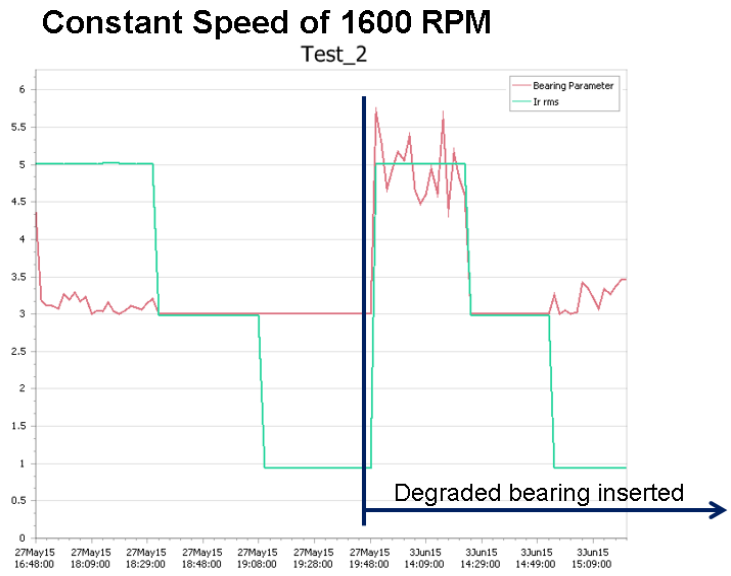

FIGURE 2.24 AGGREGATED BEARING PARAMETER FOR TEST 2

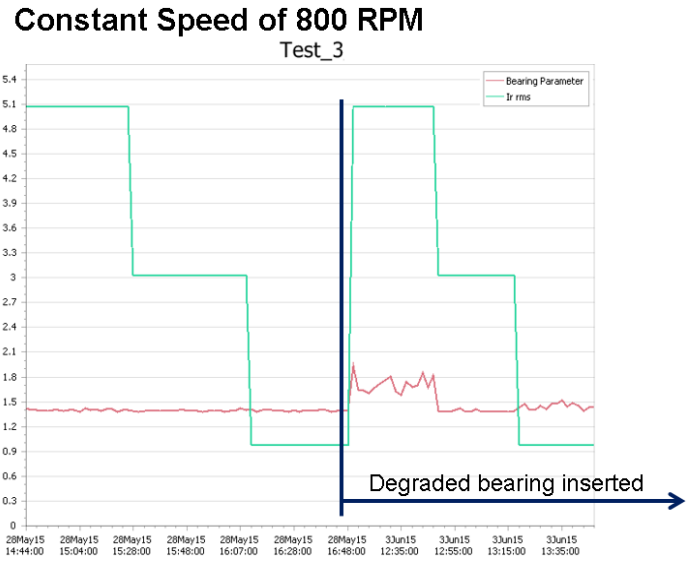

FIGURE 2.25 AGGREGATED BEARING PARAMETER FOR TEST 3

The same initial disturbance for healthy bearings at full load is visible in Figure 2.24 at 1600RPM. At this speed however a false negative reading is returned at medium load of 3A with worn bearings. The magnitude of the bearing parameter is also reduced compared to the first test. The same reduction is also observed at 800RPM operation in Figure 2.25, where there is only minor deviation of the bearing parameter from the nominal with the worn bearing. The nominal value itself is set by Artesis software, and is different in Test 3 compared to Tests 1 and 2.

Results from Tests 1-3 show a clear increase of the bearing parameter at full load operation for all tests. Reduction in load and speed decreases the monitored parameter, at times to a level below the nominal measurement. Because the MCM system measures harmonic power, reduction in signal is expected at lower speed machine operation.

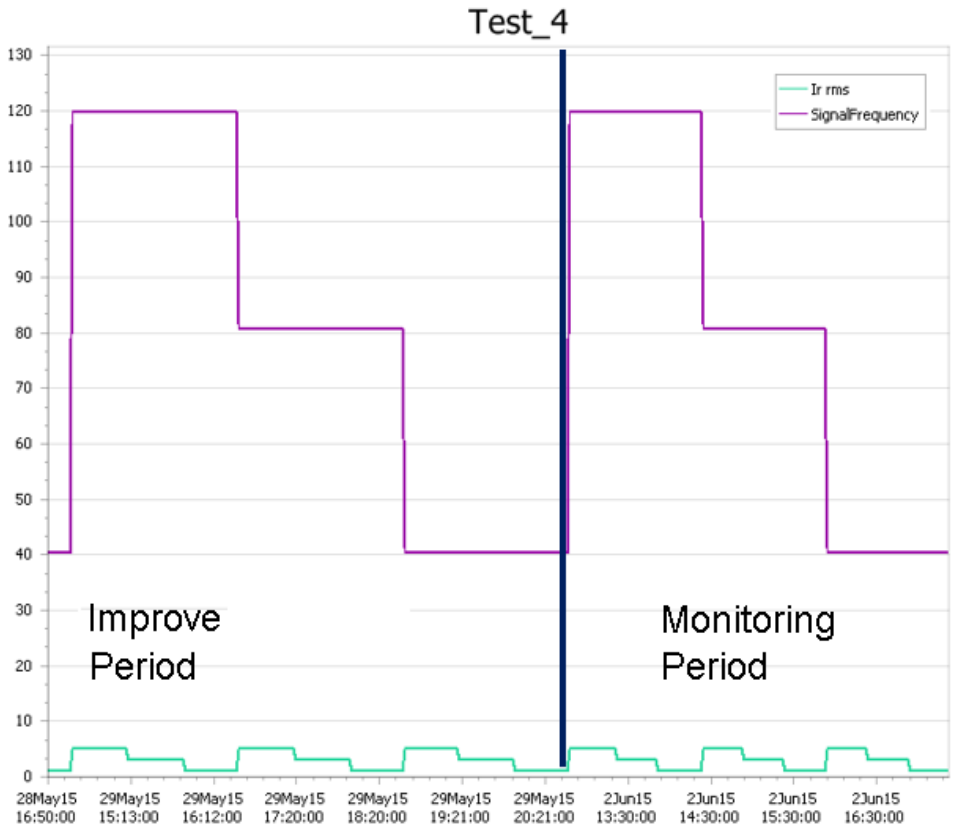

FIGURE 2.26 TEST 4 DRIVE FREQUENCY AND CURRENT COMMAND

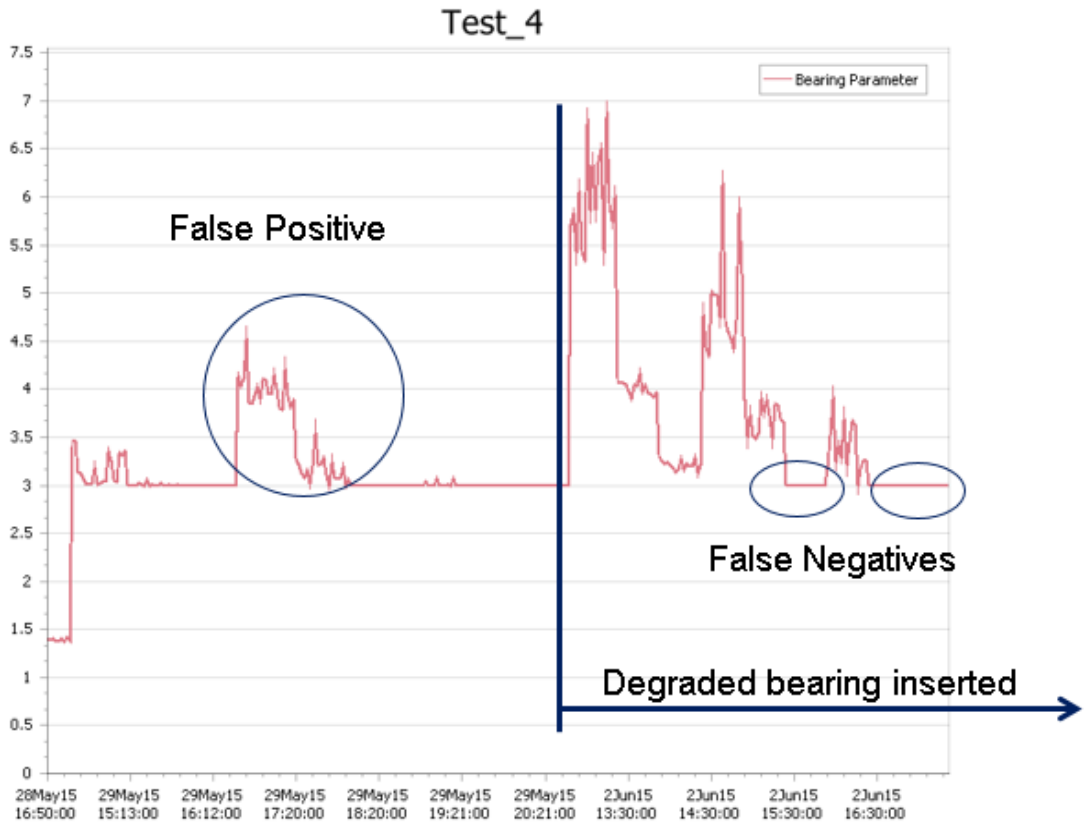

FIGURE 2.27 AGGREGATED BEARING PARAMETER FOR TEST 4

In test 4, where the monitoring system detects the bearing parameter at variable speed and load operation, the trend of parameter reduction is clearly observable in Figure 2.27. Relative to the frequency (which directly relates to speed) and load commands, plotted in sync in Figure 2.26, the bearing parameter decreases with speed and load after replacement with worn bearing. Two false negatives are highlighted in Figure 2.27 when the bearing parameter returns to nominal value.

Ideally in a monitoring system, it would be possible to set a threshold value for the bearing parameter, alerting the user to incipient failure. Due to reduction of parameter, this is not possible and a skilled user must compare machine operation in Figure 2.22 with monitored parameters in Figure 2.27. The false positive highlighted in Figure 2.27 is most likely due to a harmonic appearing at 1600RPM operation, not accounted for by the system when normalisation of frequencies is performed. False positives would also require an experienced user to look at the context of operation. Looking at the full trend, it is clear that overall, the bearing fault parameter increases when the worn bearing is inserted, therefore the monitoring system detection is achieved.

2.3.5 Conclusions

After testing a commercial bearing monitoring system, under the most realistic conditions possible given the limited time, it was determined that the monitoring system is indeed capable of detecting bearing status change. The system was able to successfully return an increased trend for all three fixed speed operation tests at full load. The increased trend was also visible in the variable speed experiment. The system provides easy connection to the machine and drive, and simple one cable Ethernet connection to a network, allowing remote user observation.

Artesis MCM system provides a powerful tool to track change of parameters identified by MCM as representative of the state of bearings. The biggest disadvantage of the system however is the inability to directly access the raw data or the model used to determine the parameters. The abstraction layer designed for general users, culminating with a ‘green’, ‘orange’ and ‘red’ state of health on the front panel in Figure 2.14 makes it harder to understand the true nature of fault progression. Artesis provides guidance with respect to thresholds for parameter trends, obtained from experience, however it is clear from results obtained in this experiment, that the context of the machine operation must also be taken into account to determine the state of health of the bearings. An experienced operator is required to interpret the results to set the threshold and project to a future time of failure based on historic data.

After extensive use of this system, important system level lessons have been learnt. Monitoring system hardware for machines and drives must be easy to modularise and connect to the remote users. The software must also be easy to install and use, requiring a minimum of steps to prevent confusion.

The end user must have a general indication of which mode of failure is occurring, and the progression of degradation. The trend data must be easily accessible to the end user and expert interpretation, as real-life monitored results may require further analysis. Extraction of raw data proved impossible from the MCM system, limiting additional processing by the user. For intellectual property reasons, it is understandable that the processing method of a commercial system may be hidden. In an ideal system however, the monitored data would be open-source, allowing 3rd party processing.

Understanding the philosophy of continuous monitoring has been the most valuable knowledge gained while evaluating a commercial monitoring system. Many of the features of the features identified as advantages and disadvantages in the MCM system have been used and improved on in the monitoring system designed in Chapter 4. It is expected that bearing monitoring will improve over time, as more drives implement such systems. In time it is expected that the short-comings of the system evaluated here will be rectified, based on the observations and experience gained with this experiment.

2.4 Summary

Bearing failure is the most prevalent cause of machine breakdown, especially so in low voltage low power machines. Further literature review has been carried out to familiarise the author with the failure modes of bearings. Special attention has been devoted to faults exacerbated with inverter-driven operation and the electrical common mode model of the bearings.

Bearing monitoring is a mature technology, a literature review of the most common methods has been complimented with a practical investigation of a state-of-art commercially available system. The system was able to distinguish between healthy and worn bearings, albeit with some false positive and false negative events during extreme operation. Experience with the commercial bearing health monitoring system has been invaluable with regards to the design and implementation of a practical insulation health monitoring system.

Chapter 3

Insulation Failure

Motor insulation forms the smallest section of an electric motor, however all energy supplied from the drive to the shaft must pass through this thin layer. The insulation is expected to withstand the applied voltage and the full reaction force of the windings. The insulation layer undergoes degradation from long term chemical degradation, damage from the applied electric field, the damage due to the surrounding environment contaminants and direct mechanical damage. Unlike the bearings in a machine, the machine winding and insulation are not easy to replace, and is not cost effective except for large machines. Due to the inability to replace the insulation, the lifetime of this component effectively sets the maximum lifetime of the machine.

High availability machines required predictable and reliable operation. The modes of insulation failure are studied in this chapter to determine the dominant failure modes and to study the effect of degradation on measurable electrical machine parameters. Models of insulation behaviour are explored and a new physics-based model of ground-wall insulation is presented and verified, using off-line testing.

3.1 Insulation Construction

Typically in Type I low voltage random wound machines there are three layers of insulation material: the wire insulation, ground-wall paper and impregnation material. The physical construction is illustrated in Figure 3.1, with typical insulation materials listed in Table 3-1. For random wound machines, the coils are either wound on the teeth or inserted into the slot, with ground-wall insulation layer in place. The air-gaps between the wires and the stator are then filled with impregnation resin. Several methods for impregnation exist, with options to use dip and bake process, trickle impregnation or Vacuum Pressure Impregnation (VPI) [70]. Air has lower electrical breakdown strength than resin and is a thermal insulator, reducing thermal conductivity [71], Impregnation improves both of these characteristics, as well as adding mechanical stability to the winding.

The insulation material on Type I machines is generally composed of organic material, based on carbon compounds. Organic insulation is made of polymer chains, the material type and construction determines the insulation withstand voltage, mechanical strength and overall lifetime.

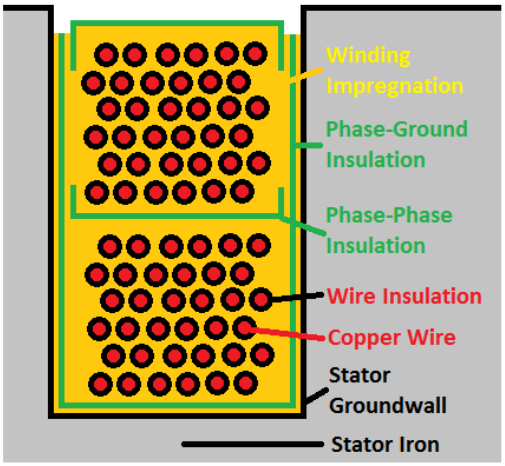

FIGURE 3.1 STATOR SLOT INSULATION

Layer	Material
Turn Insulation	Polyester/Polyurethane
Impregnation Resin	Polyester/Polyesterimide
Groundwall Paper	Aromatic Polyimide

TABLE 3-1 TYPICAL INSULATION MATERIALS

Being constructed from similar materials, the insulation system can be considered to degrade as a single unit, however it will be seen that differences in construction allow one insulation layer to dominate. Inadequate insulation between phase-to-phase windings for example puts an excess stress on the wire insulation layer, thereby insulation lifetime can be set by the weakest insulation component, rather than the system itself.

3.2 Degradation Modes

Insulation is subject to four stress factors: thermal, electrical, environmental and mechanical. Each of these factors are presented separately from the perspective of physics. The degradation cause is identified, with the associated measurable parameter changes. Different machine types have radically different insulation material and degradation modes. The study concerns insulation present in Type I low voltage random wound machines. Degradation modes in high voltage large machines are deliberately not mentioned to maintain focus on the degradation modes specific to Type I machines.

3.2.1 Thermal Degradation

Organic insulation polymers consist of identical chemical blocks which connect together to form inter-twining chains. Figure 3.2 shows a single element of polyester, a common insulation material. The length of the chain is referred to as the degree of polymerisation, and it has been shown for transformer insulation paper that longer chains exhibit stronger mechanical properties [72] [73]. Inter-chain connection or the degree of cross-linking is another important property which determines the withstand voltage. It has been shown that higher levels of cross-linking increases the DC resistance electrical property [74] at the cost of increase in material brittleness. High cross-linking levels are common in high voltage electrical cable.

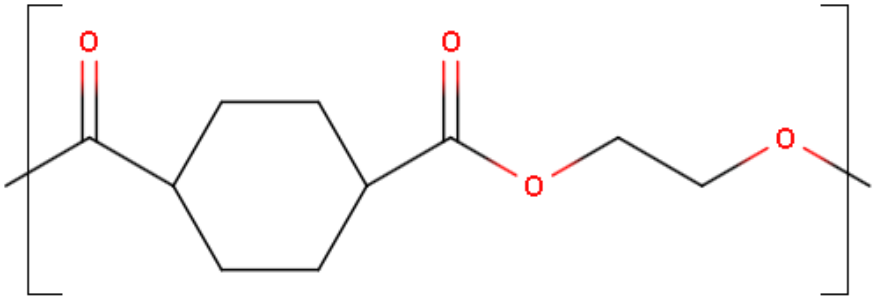

FIGURE 3.2 A SINGLE ELEMENT OF POLYESTER

Over time, polymer chains break down [75], reducing the degree of polymerisation, leading to weaker insulation [72]. Breakdown is accelerated by heat and radiation, leading to eventual failure of the material. After initial breakage of polymer chains, the ends of the polymer must react again to complete the polymer chain. Reaction with oxygen or with other polymer chains leads to oxidation or cross-linking reaction. The two reactions are in competition with each other and will affect the dielectric properties of the insulation material differently, however they will both lead to eventual weakness of the insulation material and failure to withstand applied voltage.

The degradation of chemical structure of the insulation is a long term process, compared to faults caused by contamination or unexpected operating conditions, the degradation is therefore used as a design tool, with the insulation lifetime set by the expected stress for the material and the temperature of operation. In Section 1.4.1, it is possible to predict the insulation lifetime using the Arrhenius equation precisely because of the assumption that insulation degradation rate is due to slow chemical change of the insulation material.

It has been reported that during accelerated ageing tests that the volatile elements of insulation will evaporate [70] [76] over time, affecting the insulation strength. The change of dielectric characteristic is described in detail in Section 3.3, showing the possibility of diagnosis of thermal degradation based on change of insulation model. With ability to track the state of thermal degradation, it is desirable to establish the link between the thermal class of the insulation and the lifetime prognosis based on change of insulation model.

3.2.2 Electrical Damage

In the design of electrical machines, the slot fill factor is an important factor determining how much current carrying copper can be inserted into the slot. To maximise slot fill factor, the insulation layer separating the copper strands from each other and the stator iron, must be minimized, leading to high electric field strength inside the insulating material. To cause damage, the electric field must either overcome the insulating strength of the material, or exploit a local weakness of the material.

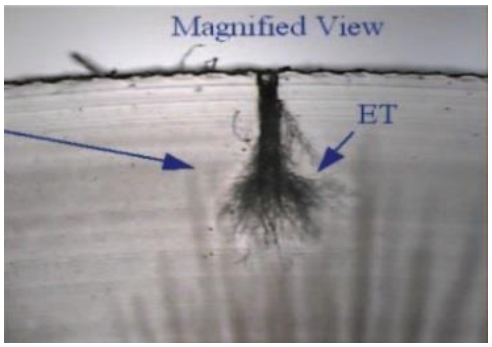

FIGURE 3.3 ELECTRICAL TREEING PHENOMENON IN XLPE CABLE [77]

FIGURE 3.4 TRACKING DUE TO DISCHARGE IN SWITCHGEAR [78]

Weakness in insulation material consists of air pockets in the insulation, trapped space charges and contamination. Partial Discharges (PD) are common in high voltage machines, where the electric field subjected to ground-wall insulation is routinely higher than the breakdown requirement for small air pockets. Figure 3.3 [77] illustrates severe damage by discharges, eroding insulation material leading to mechanical weakness of the bulk. In Figure 3.4 [78], surface discharges through contamination have carbonised the contamination, leading to short circuit, this type of damage is common on the end windings of machines with contamination [79]. Discharges can also lead to production of ozone, reacting with insulation polymer, leading to acceleration of ageing [80].

Insulation systems of medium and high voltage machinery is designed to withstand continuous partial discharges [11] and partial discharge can be used as a tool to measure the state of health of the insulation, as detailed in Section 4.2.1. Type I low voltage machines should not be subject to regular partial discharges, and therefore immune from electrical damage, however recent research has shown that inverter driven machines can indeed be subject to regular PD events [81].

In inverter driven machines insulation is subject to regular fast voltage transients between turns, phases and winding to ground. The winding can be considered as a series of inter-turn inductance and capacitance sections, with capacitance to ground at each section, forming a transmission line. Simulation [82] [83] and measurement [84] of inter-turn and turn-ground voltage shows that the voltage stress on the first few turns is magnitudes more than would be

expected by a line-driven machine. In the extreme in [84], the first inter turn voltage is equal to the full inverter voltage.

Traditionally, line-driven machines have been designed to withstand occasional voltage surges from overvoltage due to cable resonance and lightning strikes [85]. New test standards recommendations [86] have driven developments in insulation, to increase insulation quality of the first few turns for inverter-grade machines [87]. Some evidence exists that voltage transients are damageing without partial discharge present [88], through injection of space charge weakness, however more evidence is required for verification. Drive transient behaviour does not change over time, therefore it is valid to consider inverter damage as a constant.

3.2.3 Environmental Effect

In real world operation, machines may be placed in hostile environments leading to inevitable ingress of the surrounding contamination, resulting in increased failure rate [7] when compared to machines run indoors. For high-availability machines, a decision must be made whether it is safe to run the machine, therefore it is important to diagnose if the machine has experienced environmental ingress.

Moisture Ingress

Moisture can enter the machine in several ways. Direct water contamination, minor leaks from water-cooled stators and condensation due to change of dew point, are all possible methods for moisture to enter into the stator winding.

Moisture can both create faults as well as exacerbate existing degradation mechanisms. It has been identified in reliability studies as a significant contributor to failure in transformers [89] and motors [7]. It would therefore be useful to know when the machine has been exposed to water, what effect this exposure had, and what action if any, is required to service the machine and return it to service. Water contains polar bonds and water ingress can be detected by measuring additional dissipation. Water also has a much higher dielectric constant (~40 compared to 3-5 of organic insulation) [90] therefore a large increase in dissipation accompanied by a large increase in capacitance is most likely caused by water ingress. These two properties allow detection of moisture by measuring an increase in ground-wall insulation parasitic capacitance accompanied with an increase in dielectric dissipation. It has been reported in [91, pp. 249-252] that as much as 5% increase of capacitance is to be expected. A test is carried out in Section 6.1 to validate this claim.

End-Winding Contamination

Open loop air cooled machines are less expensive and have fewer components than closed loop intercooler – radiator machines. The disadvantage

however is that free air could contain conductive particles. Coal dust, salt, oil and aggressive chemicals have all caused contamination problems. Tracking is facilitated by conductive contamination allowing passage of current flow between phase-phase and phase-ground surface of the end-winding.

Tracking phenomenon is seen on machines where an initial hole in insulation allows leakage current through the contaminant between turn-turn, phase-phase and phase-ground [91, pp. 161-165]. The contaminant will carbonise tracks at leakage current, further lowering the resistance. Growth of these tracks will cause partial discharge [79] (due to decreased distance and lower effective breakdown voltage) and finally short circuit.

The tracking phenomenon is easy to detect and emulate, as it effectively forms a resistive path between windings or to ground. The change of resistance is detected as additional insulation power dissipation. It is also possible to detect the resistive tracks by off-line DC resistance measurement [92].

3.2.4 Mechanical Damage

Turn insulation of machine windings consists of a thin fragile layer of plastic, easily damaged by physical contact. Impregnation material and potting of windings exists to protect the turn insulation against the mechanical stress which attempts to move the winding and cause physical damage. Movement of the winding comes from three sources: electrodynamic reaction force, stress due to different coefficient of thermal expansion causes movement during thermal cycles, and vibration due to external disturbance. Standards for classification of insulation stress the winding sample with a shake table to include mechanical damage contribution [32].

Poor Impregnation

Winding impregnation and potting techniques give the winding strength to resist electrodynamic force and some flexibility to prevent brittle cracking. It is shown in [93] through simulation, and confirmed by experiment, that the type of impregnation, and impregnation goodness, as defined by the extent of insulation material proliferation, has significant effect on the maximum hot spot temperature of insulation. This conclusion is supported by [71], where simulation of air gaps inside impregnation showed significant increase in hot-spot temperature.

Poor impregnation quality can lead to delamination and creation of further air pockets. In higher voltage form wound machines this is especially problematic, as the extra air gaps due to delamination lead to increase in partial discharge count [94] and further damage. In low voltage random wound machines, PD and delamination are unlikely. The main effect on low voltage machines is therefore the increased temperature rise required to maintain performance, leading to shortening of lifetime due to thermal degradation.

Thermal Cycling

It is known that for high voltage generators, with long windings, thermal cycling induced stress has the potential for delamination and void creation. In [27] and [26] it is established experimentally, that partial discharge quantity and breakdown voltage correlates to an increase of stress due to thermal cycling. It is also established that the increase effect diminishes with shorter insulation length. In [95] it is shown through simulation that the stress due to normal thermal cycling operation in a MV wind turbine is enough to cause delamination. Traditionally thermal cycling has not been seen as a high priority of study, however with increased deployment of motors in traction and aerospace applications, which are subject to severe load changes and large numbers of high temperature cycles, interest has risen in predicting lifetime of insulation due to changing temperature [96].

To achieve greater performance for traction machines, research in drive application is looking to using dynamic current limit to overload the machine, based on the thermal behaviour of the machine [97]. Application of regular overloading however will induce large temperature cycles on the winding. Simulation of a random wound stator winding slot in [28] and [29] shows that significant stress is present with a modest 50 deg temperature cycle. In [29], the available stress-cycles to fatigue data is used to augment the thermal lifetime estimation, based on the Coffin-Manson fatigue model [98], to predict the lifetime of the winding based on how many cycles of fatigue it has experienced. Currently more evidence is required to link thermal cycling fatigue to a reliable lifetime prediction.

The direct effect of both poor impregnation and thermal cycling is an increase in the number and size of air pockets. Therefore for a given insulation system, the capacitance of the ground-wall and the dissipation factor would both decrease due to the reduction of insulating material.

3.3 Insulation Model

Stator ground-wall insulation can be ideally modelled as a parallel plate capacitor, where the plates are stator iron and copper metals, separated by a layer of insulation dielectric. Energy is stored in the ground-wall capacitance, and is also dissipated due to induced vibration of polar molecules due to changing electrical field [99] [100]. The capacitor model in Figure 3.5 is used in insulation testing standard IEEE 286 [101] to represent ground-wall insulation as an ideal capacitance in parallel with a dissipative resistance element.

All organic insulation materials, polyester, polyimide, polyurethane molecules contain a carbonyl group, shown in Figure 3.6. The carbonyl groups can be clearly seen in polyester in Figure 3.2. An intrinsic property of the carbonyl group is that it is a polar molecule, the electron distribution is not equal and there is a higher probability of encountering electrons near the oxygen atom [102].

When a polar group is exposed to a changing electric field, the molecule starts to vibrate due to electrostatic force, and dissipate energy.

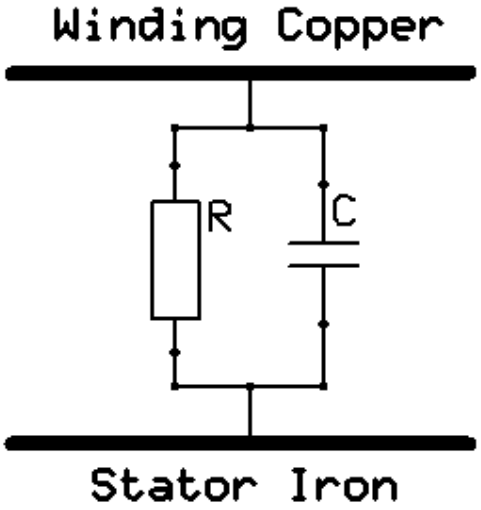

FIGURE 3.5 RC REPRESENTATION OF INSULATION

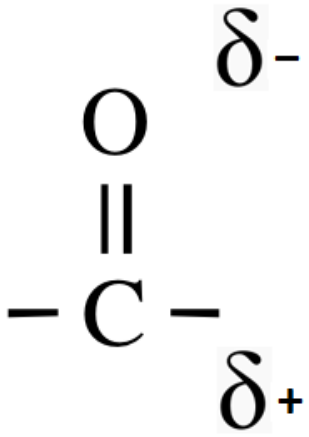

FIGURE 3.6 CARBONYL GROUP CHARGE DISTRIBUTION

During oxidation, polymer chains break up and more carbonyl groups are created with oxygen reacting with new chain ends [75]. Smaller chains are more free to move and can thus dissipate more energy through vibration [90]. In cross linking, the movement of molecules is arrested by the additional links between molecules, and less energy can be dissipated. Tracking the dissipation characteristic can be used to diagnose which chemical process is occurring and estimate the rate of progress.

Capacitance	Dissipation	Diagnosis
↓	↓	Cross-Linking, Insulation loss
↓	↑	Oxidation
↑	↓	Not observed in literature
↑	↑	Moisture ingress, Contamination

TABLE 3-2 INSULATION DEGRADATION DIAGNOSIS

It has been reported in literature that during oxidation and cross-linking, the capacitance of the insulation decreases, from 1%, to a maximum 50% [103] [104], whereas water ingress will increase the capacitance up to 5% [103]. The capacitance change will also be gradual during long term degradation. Tracking the direction of movement of capacitance and dissipation allows four cases to be identified, these are shown in Table 3-2 with their corresponding diagnosis.

3.3.1 Analytical Modelling

The energy storage and dissipation of the insulation material subject to a time-varying electric field, can be described mathematically by considering the dielectric constant as a complex number. The equation for an ideal capacitance is shown in Equation (3.1), where k is a constant representing the machine dimensions, insulation material thickness, ε'_r and ε''_r, the real and imaginary components of the dielectric constant.

$$C = k(\varepsilon'_r - j\varepsilon''_r) \tag{3.1}$$

$$Z = \frac{1}{j\omega k(\varepsilon'_r - j\varepsilon''_r)} \tag{3.2}$$

The voltage subject to the insulation is assumed to be a sinusoidal waveform, and from the perspective of this voltage, the insulation appears as an impedance, Z, shown in Equation (3.2). The current induced by the applied voltage has a complex power $S=V^2/Z^*$ described by Equation (3.4).

$$\frac{1}{Z^*} = -j\omega k(\varepsilon'_r + j\varepsilon''_r) \tag{3.3}$$

$$S = V^2 * \left(-j\omega k(\varepsilon'_r + j\varepsilon''_r)\right) \tag{3.4}$$

$$S = -V^2 j\omega k\varepsilon'_r + V^2\omega k\varepsilon''_r \tag{3.5}$$

Expanding Equation (3.4) in (3.5), it can be seen that the real and imaginary components of the dielectric constant can be considered separately. The real part of the dielectric constant stores energy and can thus be re-written as C_{eq} in Equation (3.6), and the dissipative term can be re-written as R_{eq} in Equation (3.7).

$$C_{eq} = k\varepsilon'_r \tag{3.6}$$

$$R_{eq} = \frac{1}{\omega k\varepsilon''_r} \tag{3.7}$$

It can be seen that the C_{eq} term is the standard equation for a parallel plate capacitor, however the R_{eq} value decreases with increase in frequency. This makes sense from a physical perspective, because with more vibrations per unit of time, molecules can vibrate faster and dissipate energy faster.

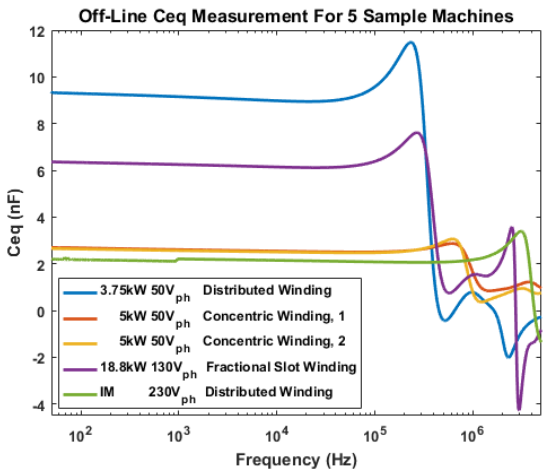

FIGURE 3.7 C_{EQ} MEASUREMENT

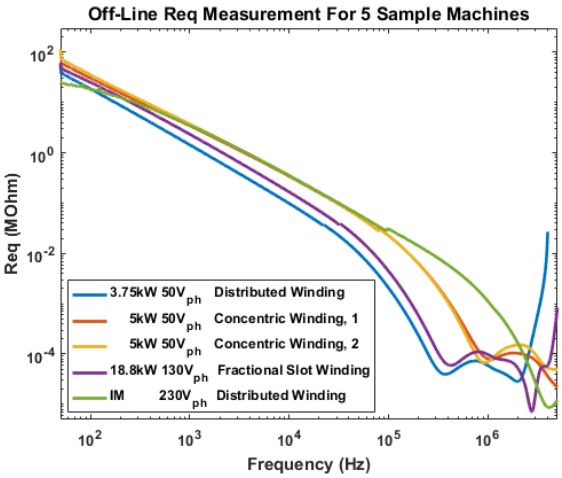

FIGURE 3.8 R_{EQ} MEASUREMENT

The predictions for behaviour of C_{eq} and R_{eq} with frequency were tested initially on 5 sample machines in the laboratory using an IM3570 impedance analyser. In Figure 3.7 and Figure 3.8, at frequencies below 100 kHz, Equations 3.5 and 3.6 are confirmed, with a flat C_{eq}-frequency curve, and decreasing R_{eq} with frequency as predicted. Resonance is observed at high frequency, indicating the limits of Equations (3.6) and (3.7), which neglect the effect of winding inductance in the common mode current path.

3.3.2 EMC Models

Numerous models of machines exist to model electromagnetic noise at high frequencies. Transformers exhibit the same winding parasitic components, modelling techniques used for understanding high frequency transformer behaviour are equally applicable to windings. EMC models and transformer models both explore insulation parasitic behaviour, Figure 3.7 and Figure 3.8 show that above a certain frequency, the resonance behaviour dominates the impedance characteristic. To fully understand insulation health, the low and high frequency behaviour must be considered.

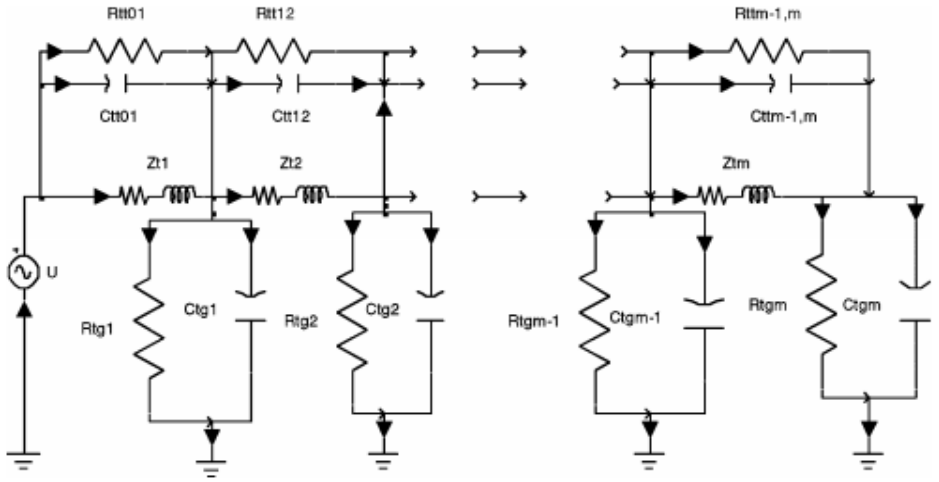

FIGURE 3.9 DISTRIBUTED IMPEDANCE MODEL FOR MACHINE WINDINGS [105]

The most basic method to represent insulation behaviour is shown in Figure 3.9 [105], where the motor winding is represented as a series of LCR pi sections. This method is also used in [105] and [106] to represent transformer parasitic components. In [105], matrix transformation is used to reduce the large number of components for more practical use to model EMC characteristic. Component LCR values can be obtained through analytic modelling [105] or Finite Element (FE) simulation [82] [107]. The biggest problem using simulation results to predict high frequency behaviour is applicability to real life. In [107], the simulation of insulation impedance gives broadly the correct value of common mode capacitance and resonance frequency, however the common mode phase characteristic returns a poor result, especially at frequencies above 1MHz.

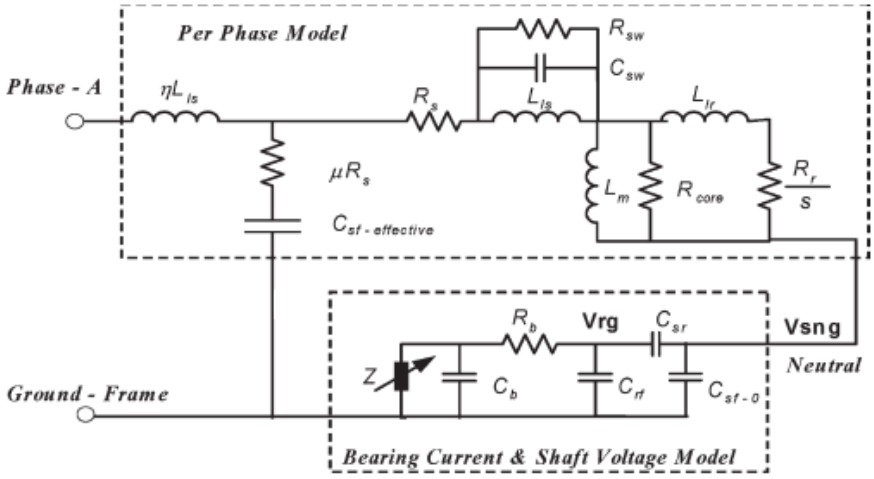

FIGURE 3.10 INDUCTION MACHINE LUMPED PARAMETER EMC MODEL [108]

To model the behaviour of insulation, for the purpose of EMC characterisation, it is suggested in [107] to fit data to a lumped parameter model, rather than attempting to predict insulation behaviour by simulation. A comprehensive model for induction machine stator windings is presented in [108], where a lumped parameter insulation model is added to a standard induction machine model. In Figure 3.10, this model consists of two sections, a per phase model of insulation shows a lumped parameter model, a standard bearing model, used to estimate bearing current in Section 2.1 is attached to the end of this. It is concluded in [109] that a full bearing model is not required, to monitor common mode insulation behaviour up to 10MHz, the model in [108] is simplified further by considering permanent magnet machines [109], eliminating the variable resistance R_r/s in Figure 3.10 which changes with slip.

EMC models are mostly concerned about high frequency behaviour, above 100 kHz range. It is pointed out in [110] and Section 3.3.1 that at low frequencies, the phase behaviour of insulation is best represented by a variable frequency resistance. Although methods exist to model frequency dependent resistance [111] in the time domain, a model has been developed for use in the frequency domain, using lumped parameters to represent physical behaviour.

3.3.3 Insulation Model

The model described in [109] comprehensively represents insulation impedance between 100 kHz to 10MHz. The model simulates the first two resonance peaks of the common mode impedance at 5MHz and 7MHz. During initial testing and simulation, it was discovered that for machines used in the University of Sheffield, the first resonance frequency was in the range of 300 kHz to 1MHz. From simulation of common mode current in Section 4.5.1, performed during development of the insulation model, it was determined that the common mode current was dominated by the 1st resonance point, and that the 2nd resonance point can be ignored.

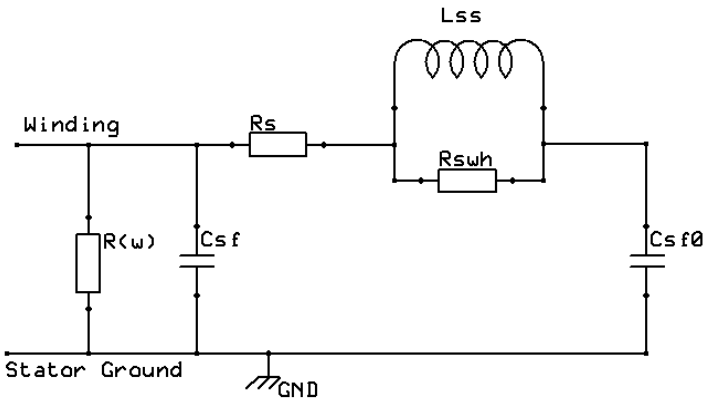

FIGURE 3.11 UNIVERSITY OF SHEFFIELD INSULATION MODEL

The final choice of model is shown in Figure 3.11, where the first resonance behaviour is captured and the capacitance at low and high frequencies are represented by C_{sf0} and C_{sf} respectively. An extra frequency dependent resistance, R_ω was added in parallel to the model to simulate dielectric dissipation of the insulation.

$$C_{sf} + C_{sf0} = C_{eq} = k\varepsilon'_r \quad (3.8)$$

$$R_\omega = R_{eq} = \frac{1}{\omega k \varepsilon''_r} \quad (3.9)$$

Equations (3.8) and (3.9) relate the new model to the analysis in Section 3.3.1, where the value of R_ω is the same as in Equation (3.7), and the overall capacitance is formed by the sum of C_{sf} and C_{sf0}. Each component in the insulation model represents a physical factor:

- C_{sf} represents capacitance at high frequency while C_{sf0} represents the difference between low and high frequency capacitance. The sum of these represents the total equivalent capacitance.
- L_{ss} represents the machine common mode inductance, calculated using common mode capacitances and resonance frequency.
- R_{swh} represents AC losses associated with the resonance. It is observed that this parameter is also sensitive to the inter-phase insulation degradation.

- R_ω represents dielectric losses which vary with frequency.
- R_s is the DC resistance of the winding, this is to be set to a fixed value and is assumed not to change significantly over time

To evaluate these parameters a fitting method was developed. The method works in two stages. First, the measured impedance response is used to determine C_{eq} and R_{eq}. The resonance parameters are subsequently fitted through C_{eq} data. The dissipative values of R_ω and R_{swh} are fitted to R_{eq} data separately. The assumption is that the dissipation is sufficiently low that it does not affect the resonance point significantly. Therefore the parallel C_{eq} and R_{eq} from the parallel RC network can be considered separately.

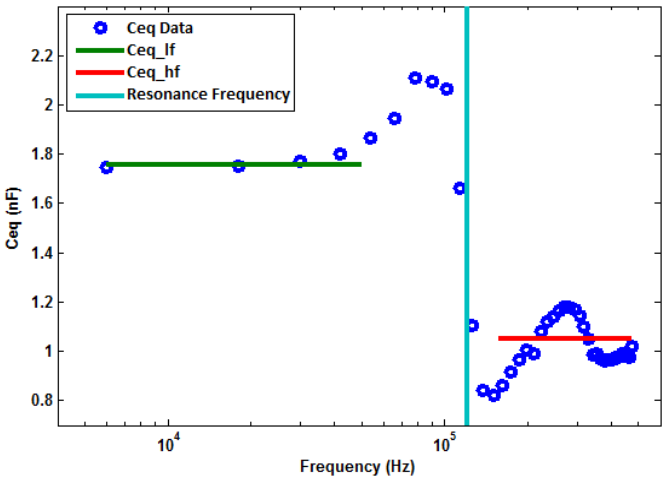

FIGURE 3.12 CAPACITANCE DATA FITTING

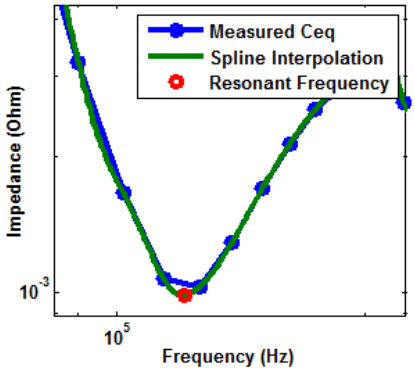

FIGURE 3.13 RESONANCE POINT FITTING

$$C_{sf0} = C_{eq\_lf} - C_{eq\_hf} \quad (3.10)$$

$$C_{sf} = C_{eq\_hf} \quad (3.11)$$

$$L_{ss} = \frac{1}{C_{sf0} * \sqrt{2\pi * f_{res} * k_f}} \quad (3.12)$$

Figure 3.12 shows the fitting of resonance parameters. Impedance measurements up to 50 kHz are defined as low frequency and frequencies above 200 kHz are defined as high frequency. The average values of C_{eq} up to 50 kHz and above 200 kHz are denoted as C_{eq_lf} and C_{eq_hf}. These, together with the resonant frequency f_{res} are used to calculate C_{sf0}, C_{sf} and L_{ss} given in Equations (3.10), (3.11) and (3.12) respectively. To accurately track the resonance point, spline interpolation is used to find the minimum point of resonance as shown in Figure 3.13.

To compensate for a small amount of dissipation, the resonance frequency is adjusted by k_f in Equation 3.11; this value is determined at the start of experiment by trial and error aligning the model impedance to measured impedance, and should not change significantly over time. R_ω and R_{swh} are

calculated in two stages. The Req measurements at low frequencies identified in the red circle of Figure 3.14, are fitted to a linear y=mx+c equation, where m and c represent the gradient and offset of the linear curve, respectively.

R_{swh} is fitted last by least squares method using the full model after all other parameters have been determined. R_{swh} determines the shape of the mid frequency dissipation zone in the green circle of Figure 3.14. This intermediary zone contains dissipation from insulation represented by R_{ω} and apparent dissipation due to resonance.

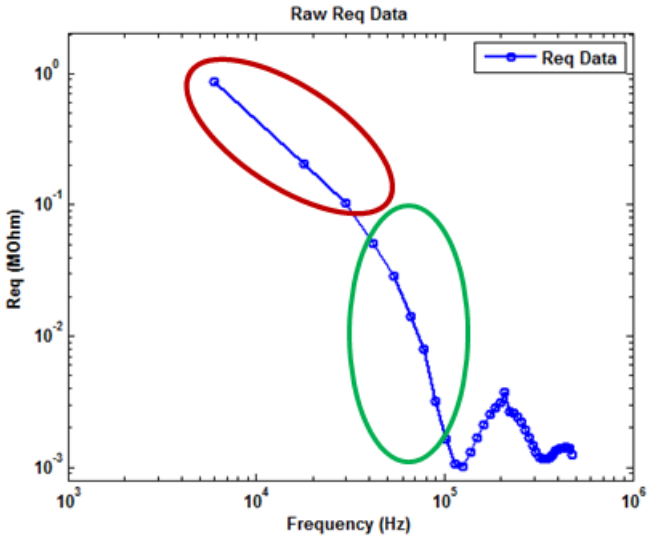

FIGURE 3.14 REQ RESULTS WITH ZONES OF INTEREST HIGHLIGHTED

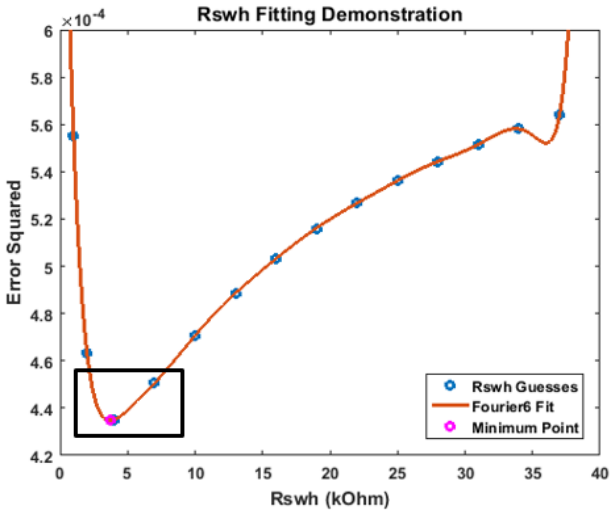

FIGURE 3.15 RSWH FITTING ERROR VS FIXED RSWH VALUE SET

The least-squared algorithm can take many steps to converge to the final result for R_{swh}, the accuracy of the value and time to conversion is directly proportional to the step size. To reduce computation time, an alternate method for fitting R_{swh} was developed. It was found that for a wide range of model values, R_{swh} least squared error formed a predictable pattern. It was decided to calculate the error using a fixed set of representative Rswh values, as shown in Figure 3.15, fit the trend and solve for minimum error value of Rswh.

3.3.4 Model Validation

To validate the model presented in the previous section, raw C_{eq} and R_{eq} data obtained from the experiment in Chapter 5 is used to obtain the model fitted result. The fit result is shown alongside the raw data in Figure 3.16 and Figure 3.17.

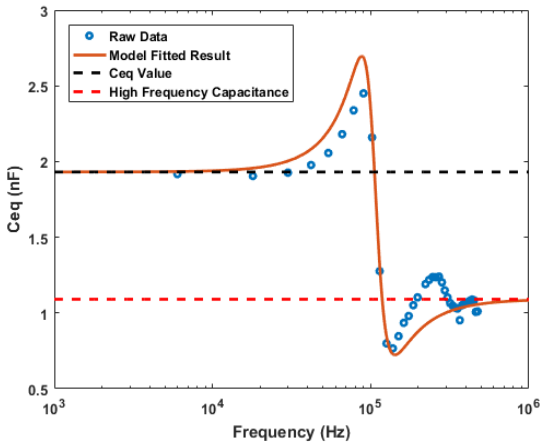

FIGURE 3.16 CEQ FITTING RESULT

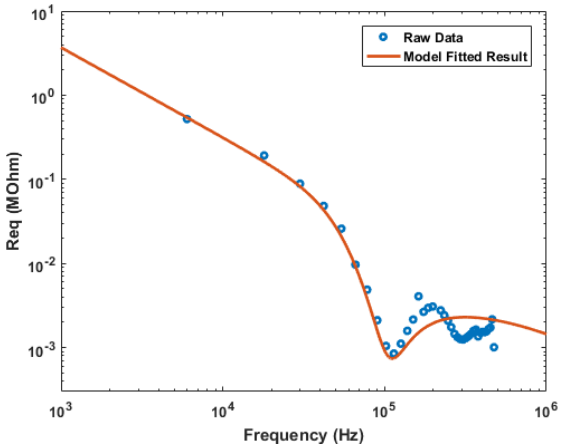

FIGURE 3.17 REQ FITTING RESULT

In Figure 3.16 the capacitance result is shown. The C_{eq} value used to represent low frequency capacitance and the high frequency capacitance used in obtaining the resonance parameters C_{sf} and C_{sf0} is emphasized. It can be seen that the model result trends towards the correct values at high and low frequencies, and the resonance frequency is correct. No value of damping element R_{swh} however would allow the model to follow the raw data values between 70 kHz and 300 kHz. The reason for this is evident in the Req fit in Figure 3.17. Two resonance points are observed, the first near 100 kHz, the second near 300 kHz, whereas the model can only represent one resonance point.

Fitting the data shows the advantages and limits of the model used to fit the results. The capacitance data represents well the high and low frequency capacitance, as well as the first resonance frequency despite deviation of the model value away from the data near the resonance frequency. The R_{eq} fit shows that the model fits the data values well up to the resonance point, however as the R_{ω} and the R_{swh} values are both measured in this range, data above the resonance frequency is not necessary for measurement of dissipative parameters.

3.4 Off-Line Measurements

The Hioki IM3570 used in Section 3.3.1 to measure impedance of a set of machines, uses 5V to inject current through the common mode of the machine to measure ground-wall insulation. Real capacitors have voltage dependency based on the material and quality of dielectric, standards exist for ceramic capacitors with the class specified in part by the voltage dependency. Real drives operate at voltages in excess of 400V compared to the 5V used by the impedance analyser.

To measure any voltage dependency and to verify the applicability of the Hioki instrument to measurement of motor insulation, industry standard equipment was used to conduct off-line capacitance and dissipation factor testing and compared to the Hioki results.

3.4.1 Equipment Setup

The test instrument used for measurement was the MI600, a dedicated instrument for remote measurement of C/DF. The instrument measures the current in the device under test and compares this to the current in a reference capacitor which is subjected to the same test voltage. Any test voltage source can be used and because the current sensor is placed at the ground point, the test voltage can be almost unlimited. The measurement units are battery powered, and the result is sent over fibre optic cable to the operator, allowing as much as 2km distance away from the test equipment.

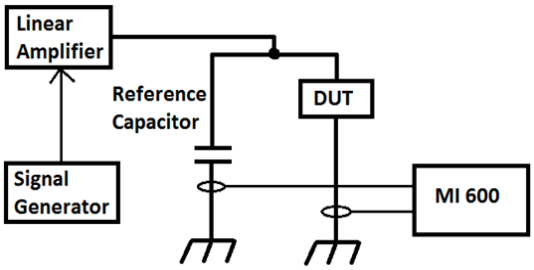

FIGURE 3.18 MI600 SENSOR CONFIGURATION

FIGURE 3.19 PHOTO OF MI600 EQUIPMENT

The experiment configuration is shown in Figure 3.18, the equipment itself can be seen in Figure 3.19. A signal generator provides the sources waveform, boosted by a linear amplifier to the test voltage. The voltage is applied to a reference capacitor and a device under test, a 3.75kW motor with a rated line voltage of 380V. A silver mica reference capacitor is used due to inherently low dissipation of silver mica.

The maximum specification for the linear amplifier limited the test frequency to 30 kHz. Voltages 5V to 120V were applied to the test machine. As with the impedance testing in Section 3.3.1, the machine phases were shorted together to define the common mode voltage, i.e. the same voltage applied between each phase and ground.

3.4.2 Results

Two sets of results are considered: variation of dissipation factor and the absolute values of capacitance of the MI600 instrument compared with the Hioki IM3570. Figure 3.20 shows the dissipation factor of the insulation vs voltage. The discrete measured data points are fitted using MATLAB onto a plane using spline interpolation. It can be observed that the data fit across the voltage axis shows little variation, especially at frequencies above 100Hz. The lack of variation shows that there is little voltage dependency on dissipation, and that measurements at 5V are comparable to those at 100V.

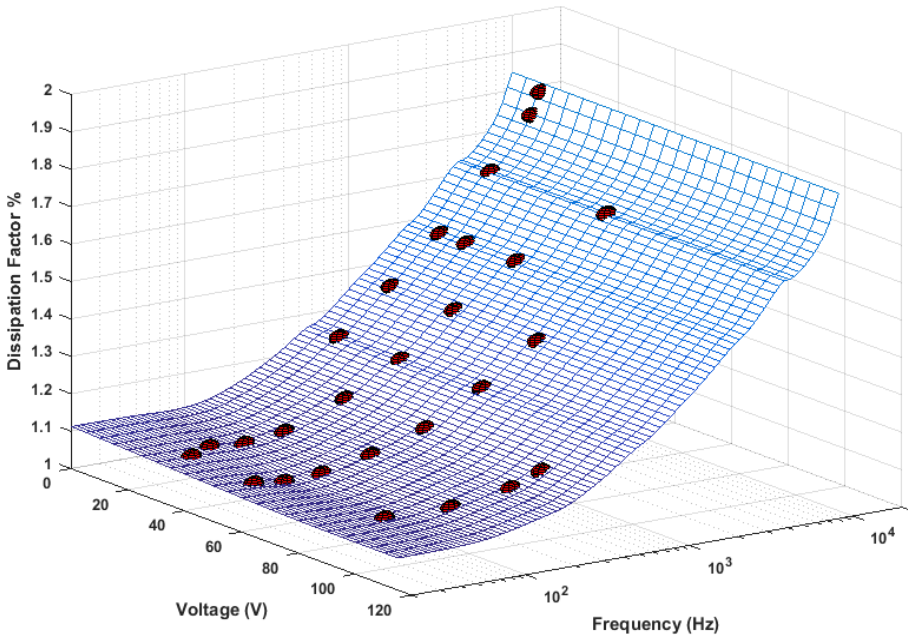

FIGURE 3.20 DISSIPATION FACTOR VS VOLTAGE

The dissipation factor values shown in Figure 3.20 are as separate C_{eq} and R_{eq} measurements in Figure 3.21 and Figure 3.22 respectively. Because it was shown in Figure 3.20 that there is a lack of voltage dependency, all voltage results are plotted together in Figure 3.21 and Figure 3.22.

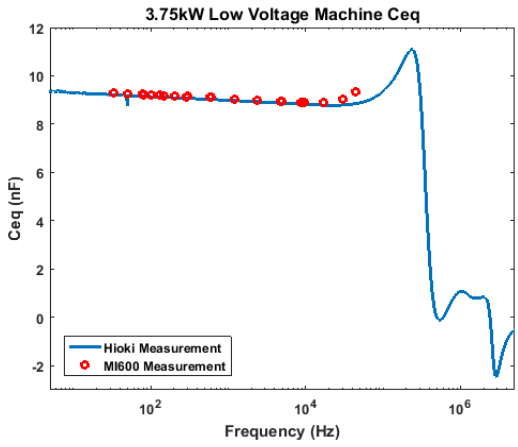

FIGURE 3.21 C_{EQ} MEASUREMENT COMPARISON

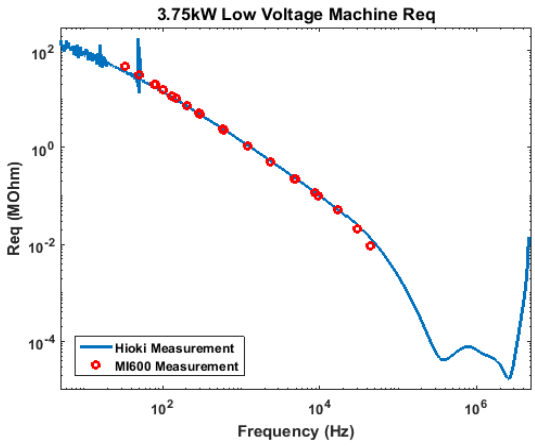

FIGURE 3.22 R_{EQ} MEASUREMENT COMPARISON

Good agreement exists between the two measurement devices for both capacitance and dissipation. The measurement for capacitance is within 1% between the two measurements in Figure 3.21, and within 5% for R_{eq} in Figure 3.22. The consistency of Req measurement is especially important because it only has between 1-2% of the current flow of the capacitance, as per results of dissipation factor in Figure 3.16.

3.4.3 Conclusion

It has been shown that the quality of insulation is associated with two electrical parameters C/DF, and their equivalent model of C_{eq} and R_{eq} in parallel. It has been shown that the Req parameter is a frequency dependant parameter, and model fitting is required to compare parameters obtained at different frequencies. Winding resonance characteristic must also be taken into account when fitting the insulation model at high frequency.

3.5 Summary

Insulation failure mechanisms and their causes are reviewed and discussed in an extension of the literature review. The insulation capacitance and dielectric dissipation are selected as the measurable indicators of degradation.

A model of insulation ground-wall has been developed to incorporate frequency dependent dielectric loss and winding resonance. Insulation impedance characteristic has been speculated from physics and the assumptions have been tested using off-line measurement. A lumped parameter insulation model has been proposed to represent the insulation impedance, with 5 parameters to be tracked which correspond to degradation of the insulation.

The Hioki IM3570 instrument has been compared to an industry standard equipment for measuring C/DF. Due to the unavailability of the MI600 equipment for further testing, it is important to inspect the use of Hioki 3750. The validity of measurement has been verified and confirmed for use in motor insulation common mode measurement. The behaviour of insulation at higher voltages, as would be expected during inverter-driven operation, has been verified as similar to that at low voltage.

Chapter 4

Insulation Monitoring Technology

In this chapter, a thorough review of insulation monitoring methods is presented, and traditional methods are discussed together with state-of-art ideas emerging from the latest research and development. The advantages, disadvantages and applicability of each method is assessed. A new insulation monitoring system is developed to measure ground-wall impedance on-line during machine operation. The new system is tested and verified for use.

The review and final developed method is applicable specifically to low voltage, random wound machines with type I insulation materials. Some methods which may only be applicable to form bar wound or high voltage machines are deliberately not presented to maintain focus on monitoring methods specific to the type of machines studied.

4.1 Off-Line Monitoring Methods

Traditionally, insulation diagnosis is performed at regular intervals on high value machines. The machine is taken out of service during maintenance and accurate diagnosis often requires an experienced operator to judge the state of health of the insulation. The following sections review the three most common off-line insulation monitoring methods and their variations.

4.1.1 DC Insulation Resistance Test

The most common insulation testing applies a fixed DC voltage between winding and ground. Industry names vary for testing, the “Megger Test”, “IR Test” and “HiPot Test”, referring to a popular brand of test equipment used for general testing, a method to extract information from a DC voltage step, and an overvoltage pass/fail test respectively. In all three variations of DC testing, the measured leakage current from windings to stator ground through ground-wall insulation is used as return signal, allowing diagnosis of basic faults.

The equipment to conduct the Insulation Resistance (IR) test, as specified in IEEE standard 43 [92] applies 500V between the winding and ground of the motors rated under 1kV. The leakage current is measured 1 minute and 10 minute marks for diagnosis of steady state DC resistance and the polarization qualities of the insulation.

The IR test assumes a model of insulation in Figure 4.1, where the ground-wall insulation consists of an ideal capacitance representing the inherent parasitic capacitance between winding-ground, an ideal resistor R_I to represent steady

state leakage, and a series R_aC_a pair which adds the decaying current component resulting from polarized insulation molecules aligning to the DC field. Recent research has proposed addition of extra polarisation current branches to accommodate for real life observation of changing time constant of current measurement [112].

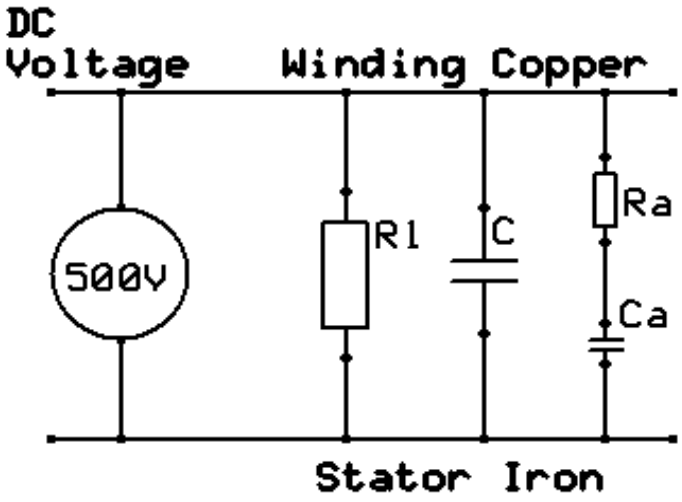

FIGURE 4.1 IR TEST INSULATION MODEL

The current resulting from a DC voltage step to ground-wall insulation is shown in Figure 4.2. The total current consists of three components: an initial surge current I_c, a steady state leakage current I_l and absorption current I_b.

Insulation resistance R_l, is calculated using current value at 10 minutes, where polarisation is assumed complete, and current can only flow through resistive contaminants. The polarization index is a dimensionless ratio of currents at the 1 minute and 10 minute measurement points. The minimum value of R_l specified in the standard is 5MOhm, with a minimum value of polarization index of 1.5 to 2, all values corrected to their value at 40 °C. The initial capacitive current is not used in the IR test and is assumed to diminish before 1 minute measurement for typical machines and IR test equipment output impedance.

Accelerated lifetime test with high humidity and high load is presented in [113], where the polarization index shows a marked decrease from a maximum value of 3.7 to 1.34 at test end. Typical values of healthy polarization index range upwards of 4 [114] [115] however there is currently no universal acceptance of the final value of polarization at end of life of the insulation.

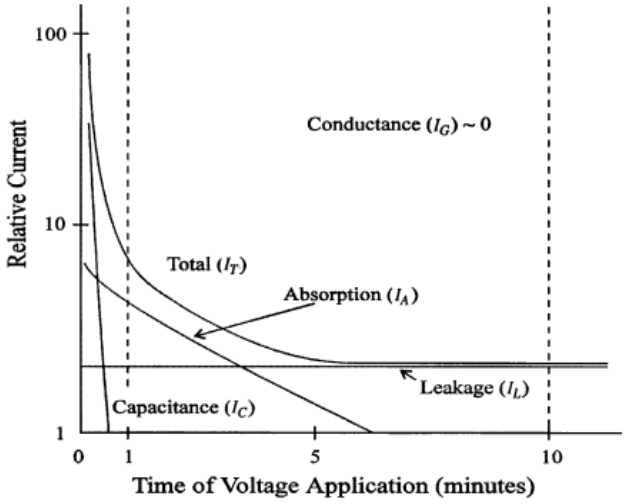

FIGURE 4.2 CURRENTS DURING IR TESTING

The high potential (HiPot) test specified in IEEE standard 95 [116] applies a DC voltage, x1.7 the rated RMS voltage for a time period of at least 1 minute. This test differs from the IR test because it is primarily a pass/fail test, with destructive failure or healthy operation being the only possible states. A similar test using AC overload of 125% to 150% at 50/60 Hz [117] applies a more realistic voltage distribution on the winding insulation. A large amount of power may be required to energise the ground-wall capacitance, especially for large machines, a companion standard [118] specifies application of 0.1Hz voltage to implement the AC over-potential test. None of the over-potential tests provide diagnostic information and are only useful to provide affirmation of machine operation. It is also notable that the standards for over-potential are specified for high voltage machines, the importance of these tests is to illustrate the difference of philosophy of monitoring, pass/fail verification vs incipient fault diagnosis vs prognosis s based on monitored parameters.

The importance of insulation temperature and discharging winding capacitance before test is emphasized in all the standards mentioned above. Standards specify how the insulation resistance values must be corrected to a nominal temperature in addition to the procedure to discharge windings prior to test. Experience in motor testing shows that these two criteria are often ignored when testing new motors using “Megger Testing”. It is notable that some commercial testing equipment also ignores the pre-charge and correction factors [119]. The purpose of the “Megger Test” is best treated as a rudimentary pass/fail test, capable of detection of winding defects, and short circuits to ground.

In [120] it is proposed to use an inverter drive to apply DC link voltage to the stator winding of a low voltage random wound machine to implement the IR test during machine down-time. The concept was successfully tested on a 7.5kW machine with external resistance emulating change of leakage resistance. For

accurate measurement, the machine must be disconnected from the drive through contactors, or the drive IGBT leakage model must be taken into account.

4.1.2 Capacitance and Dissipation Test

The second most commonly used off-line insulation test applies a 50/60Hz voltage from winding to ground to measure the Capacitance and Dissipation Factor (C/DF test) of the insulation. The C/DF test uses a parallel RC model, expanded on in Section 3.3, to represent the energy stored and energy dissipated during the test. Dissipation in literature is expressed as tan(δ), known as the dissipation factor (DF), defines the ratio of energy stored and dissipated in the capacitance and resistance respectively. The relationship to Req and Ceq to DF is shown in Equation (4.1). The ratio is often more important to consider, as it normalises the dissipation to the capacitance and allows easier comparison between similar machines.

$$\tan\delta = \frac{1}{\omega C_{eq} R_{eq}} \tag{4.1}$$

The C/DF test can be performed using any instrument capable of measurement accuracy of better than 0.1% accuracy of capacitance measurement and providing the required reactive power to the capacitance. It is known that capacitance and dissipation factor increase when partial discharge is present. This effect is used on high voltage generators as part of the testing specified by C/DF tests set out in IEEE standard 286 [101], where C and DF is measured at voltages between 20% to 100% of the rated voltage. The increase of parameters with voltage gives an indirect measurement of partial discharge.

In [121], C/DF results over 20 years for three large generators. For two cases, C/DF testing produced inconclusive results, however in one of the generators, indirect detection of partial discharge through tip up of C and DF with voltage showed good agreement with direct partial discharge measurement. Apart from testing high value machinery, the C/DF test is also used to determine the stage of curing during initial impregnation of new machines [122].

A low-cost method to carry out the C/DF test was proposed in [123], where a 60Hz AC voltage was applied by switching between positive and negative DC bus rails during down-times of the machine. Successful measurement of emulated ageing was demonstrated through addition of resistance to increase dissipation, however the requirement to change drive connection during test precludes widespread test of this method.

At present there is not enough long term evidence to interpret C/DF results with defined failure thresholds and confidence levels. Laboratory evidence, combined with an understanding of the insulation material, as detailed in Chapter 3 is required to interpret the insulation degradation mode, the speed of degradation and end of life characteristic.

4.1.3 Surge Test

Both the DC class of tests and the C/DF test measure current flow between winding and ground, and therefore only measure the condition of the ground-wall insulation layer. Similar methodology of test can be applied to obtain information regarding phase-to-phase insulation, by disconnecting the windings at the neutral point and applying the voltage between windings. Insulation structure in Section 3.1 shows that an important insulation system is neglected by both of these tests.

The breakdown of turn-to-turn insulation has potential to create a short circuit in the winding, dissipate power and rapidly cause excessively high local temperature [124], leading to catastrophic failure. Application of steady state voltage will fail to diagnose turn-to-turn insulation issues due to even voltage distribution, treating all winding turns as part of a parallel plate capacitance.

The surge test applies a voltage impulse to the winding, measuring the voltage decay across the winding. The change in inter-turn capacitance and coil resistance, as well as change of magnetic flux due to presence of the turn fault will affect the resonance characteristic of the winding Figure 4.3 shows an example waveform, taken from the IEEE standard 522 [125] for surge test procedure. The change of voltage magnitude and resonance frequency due to presence of a short-circuit turn in one coil can be observed. Surge testing has become an industry standard compliance test during motor manufacture [119].

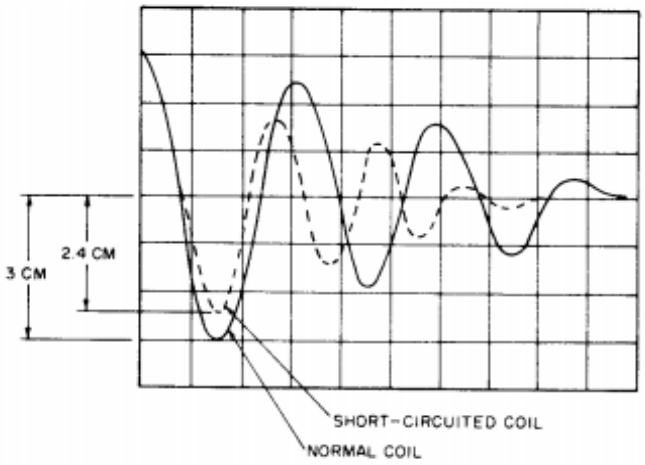

FIGURE 4.3 HEALTHY AND SHORT-CIRCUITED WAVEFORMS DURING SURGE TEST [125]

The surge test allows detection of present turn-to-turn faults, as well as weak turn-to-turn insulation. Due to lack of acceptance standards, an experienced operator is required to judge the deviation of surge test waveform from the master reference, to determine the quality of turn-to-turn insulation.

4.2 On-Line Monitoring Methods

High availability machines and high duty cycle machines must have minimal down-time for maintenance and ideally no running costs associated with the monitoring system. Ideally the state of health of a machine must be continuously tracked during operation of the machine. Problems with the insulation system are to be detected and maintenance scheduled to avoid unplanned outage.

Earliest methods for machine continuous health tracking involved monitoring the operational temperature to use the consumed life [30] as predicted by the chemical reaction in Section 1.3.2. More sophisticated temperature based methods track deviation in the predicted motor temperature due to loading [71] [126], over time, to identify potential problems. Modern methods attempt to track the insulation state directly, by measuring physical parameters while the machine is operating. These are presented here in order of the most established, to the newest methods in development.

4.2.1 Partial Discharge Monitoring

Partial Discharge (PD) phenomenon occurs when electric field between two conductors separated by an insulator exceeds the local insulation material breakdown voltage. A small discharge occurs inside the insulation at local weak spots, caused by air pockets and other features, discussed in Section 3.2.2. Problems such as ground-wall delamination [121] and moisture ingress [79] and poor initial impregnation [127] have been successfully detected through use of partial discharge monitoring.

During a partial discharge event, a small amount of total charge is dissipated inside the weak spot of the insulation, causing a drop in capacitance. Detection of partial discharge operates by either detecting the current inrush flow, or the voltage perturbation which is induced by the current flow [128]. High bandwidth current transducers are mounted on the motor terminals to detect current spikes in current detection systems. Phase voltage can be coupled through capacitive connection to machine terminals to a test instrument to detect voltage perturbation [129]. An alternate method of PD detection measures the microwave radio spectrum to detect the short period voltage pulses [130] [131]. Alternate methods of partial discharge detection include detection of ozone which is released as a by-product of discharge, visual methods to detect discharge corona and acoustic methods which attempt to isolate the sound of discharge from normal machine operation.

Monitoring partial discharge is a mature field, with numerous commercial products available to detect the discharge [132] [133]. Line-fed high voltage machines are tested for partial discharge with respect to IEEE standard 1434 [128], running the machine with a sine wave signal, and observing the discharges.

Figure 4.4 shows the result of PD monitoring, each discharge magnitude expressed in coulombs is plotted against the time of occurrence, relative to the voltage waveform driving the discharge. The number of discharges, the relative ratio between discharges at positive and negative values of input waveform and the shape of the discharge-voltage characteristic have been identified as important parameters which correlate to insulation health [134]. The PD characteristic seen in Figure 4.4, shows an excess of negative polarity pulses, usually taken to indicate an inadequate bond between turn insulation and ground-wall.

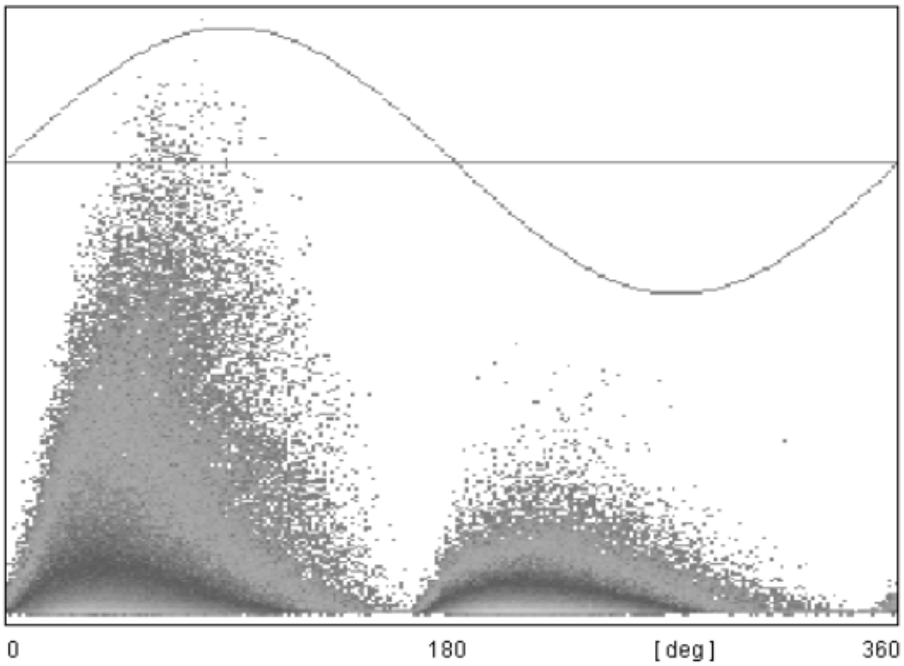

FIGURE 4.4 PARTIAL DISCHARGE MAGNITUDES WITH INPUT REFERENCE WAVEFORM [128]

Currently, the equipment to monitor partial discharge allows display of the raw data, and some statistical parameters regarding the distribution of the discharges seen in Figure 4.4 with respect to time of occurrence. Judgement by an experienced operator however must be made to diagnose degradation of the insulation. Recent research has attempted to correlate the shape of the discharge spectrum in Figure 4.4 with lifetime prediction.

In [135] high voltage rotor bars are subjected to accelerated lifetime testing, showing correlation of time with the skewness and crest factor of PD. It was also shown in [135] that some factors such as kurtosis and maximum discharge have only weak, if not negligible, correlation with lifetime, it was concluded that more data is required to establish a reliable correlation.

Fast voltage transients across motor windings resulting from pulse width modulation (PWM) in modern power electronic drives create uneven voltage distribution, with most voltage concentrated on the first few turns, as described in Section 3.2.2. Although Type I low voltage random wound machines which are

the focus in this study should never undergo regular PD activity [86], state of art inverter drives already exceed the specifications of inverter grade machines. This is evident in [136], where partial discharge has been detected experimentally due to inverter transient effect, despite evidence showing representative Type I motors meeting the required standards in [137].

In [138], a surge injector is used with progressively increased voltage to find the Partial Discharge Inception Voltage (PDIV) of a small random wound stator. The reduction of inter-turn PDIV value over time correlated well with the accelerated ageing test conducted on the 380V 5.5kW Type I test machine, showing the potential for future systems which can monitor partial discharge in machines not usually considered to have discharges occurring. Industry standard equipment to verify new motors also measures partial discharge during surge testing [119] by differentiating the voltage waveform, to observe voltage fluctuations due to discharge.

Novel methods have attempted to take advantage of inverter induced partial discharge, to monitor the PD levels of low voltage random wound machines. The method in [139] uses an antenna combined with broad spectrum analysis to detect PD. The results of an accelerated ageing showed that PD repetition rate can be used as a pre-cursor to failure. In [140], a more conventional approach is taken, employing capacitive coupled sensors used, with mixed results which show the maximum discharge and discharge repetition correlating poorly to motor lifetime for some of the machines. Monitoring PD for machines with Type I insulation operated from an inverter is a promising field of study. However, with anticipated faster switching inverters, forcing higher specifications by new machine standards, partial discharge should not occur frequently on future machines

4.2.2 Sequence Detection

Modern inverter drives contain considerable computing power to implement control algorithms. The most practical method for machine diagnosis and monitoring is therefore to use existing sensors attached to the inverter and use spare computing capacity to run monitoring algorithms.

Most techniques which use on-board current sensors operate on the same principle as Motor Current Signature Monitoring that is used in bearing monitoring in Section 2.2.3. Harmonics associated with each fault are identified and monitored over time, reference [141] for example shows how to derive the harmonics to track rotor eccentricity. In [142] voltage and current asymmetry is used to detect high resistance motor connection. The most commonly used technique for stator windings attempts to detect turn-to-turn contact through monitoring 2^{nd} harmonic current component, as demonstrated in [143] using wavelet tracking of the negative sequence component resulting from the 2^{nd} harmonic, and [144] where fuzzy logic is employed to eliminate false positives.

Regarding inter-turn fault detection, the main problems faced are the speed of detection as required to prevent catastrophic damage and elimination of false flags, caused by other factors which produce similar harmonics to the fault, such as intrinsic magnetic asymmetry, load, applied voltage unbalance and bearing harmonics. However the biggest challenge to diagnostics of future failure rather than detection of fault that has occurred, is the sensitivity of the system.

4.2.3 On-Line Surge Test

The surge test is currently the only known test to diagnose inter-turn insulation condition before final breakdown. Subtle change of winding resonance characteristic due to change of parasitic inter-turn capacitance can be detected by sophisticated off-line equipment, however recent interest has attempted to repeat the test while the machine is operating, using a variety of methods.

The most basic method for conducting regular surge testing is outlined in [145], where charged capacitors are connected to the motor terminals via fast switching IGBT switches to produce a surge voltage at the motor terminals. The machine tested in [145] is line driven, therefore the surge voltage can be connected during machine operation. The Thevenin equivalent of the voltage source feeding the machine can be considered as a short circuit connection, and the surge voltage is subjected to the machine and the shorted cable at the source. It was experimentally demonstrated that with a large enough voltage source impedance, the conventional off-line surge test can be repeated successfully, detecting a 1% inter-turn fault.

The work done in [146] uses an approach where the voltage transients in normal operation of the inverter drive are used as a signal source. A high bandwidth current transformer is used to measure phase currents at the inverter switching transients, the derivative of this current is then used as a reference waveform. The reference waveform contains current harmonics which flow through the winding-ground and turn-to-turn capacitance of the insulation. The root mean square deviation away from this reference in the frequency domain is tracked to indicate change of winding resonance characteristic, and by inference, the change of insulation capacitance.

The method in [146] has been successfully demonstrated using only a single current sensor [147] to measure the common mode leakage current to detect changes in capacitance and work is currently under way to develop the method to compensate for sensor imperfections [148] and degradation of drive IGBTs [149]. The method successfully detects change of parasitic winding capacitance, however the reported accuracy and sensitivity is poor, relative to what is required to carry out a similar off-line capacitance test and only large change can be detected. The biggest advantage of this methodology is that it can be added to high-end drives and tested in the field without extra cost, allowing ease of widespread adoption, despite the drawbacks.

4.2.4 Leakage Current Measurement

On-line surge testing demonstrates the possibility to realise an on-line alternative of a traditional off-line test by employing modern data acquisition, computational power, and inverter drive. This route has likewise been taken with regards to C/DF test. Applied voltage to the windings, whether through injection [150] or using the drive voltage itself [151], with measurement of resulting current, has been used to measure capacitance of motor insulation as well as dissipation factor.

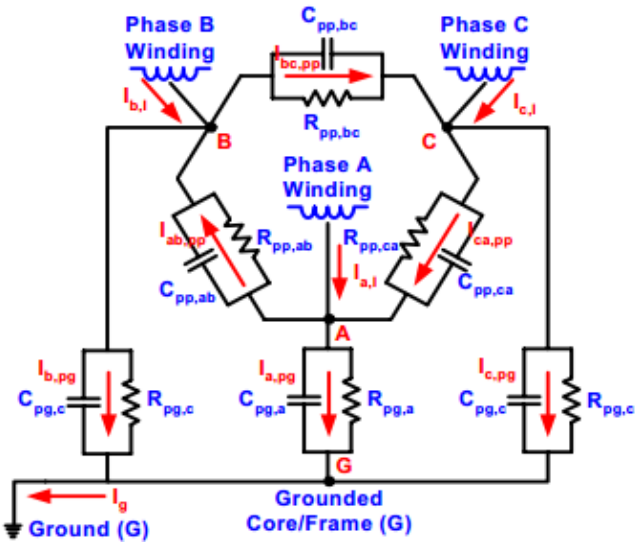

FIGURE 4.5 INSULATION MODEL USED IN [151]

In [151] it was proposed to use residual current from each phase of the winding to measure the phase-to-ground and phase-to-phase insulation impedance. The leakage paths are shown in Figure 4.5, flowing through insulation as represented by $R_{eq}C_{eq}$ pairs. By measuring the phase-to-phase and phase-to-ground voltages, as well as measuring the three residual currents from phases a, b and c, it is possible to measure all of the RC pairs in Figure 4.5.

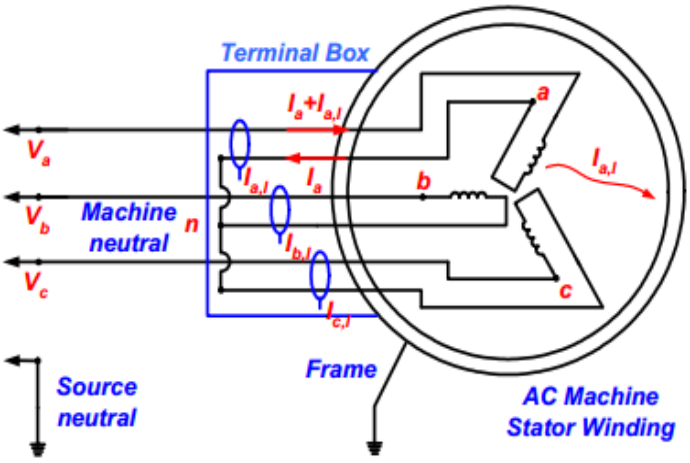

FIGURE 4.6 LEAKAGE CURRENT SENSORS [151]

Current sensors in Figure 4.6 cancel out the fundamental drive current magnetically, measuring only the current which does not return through the phase winding and must therefore leave through winding insulation.

The measurement uses the voltages applied to the machine and resultant leakage currents through insulation between phases and insulation to ground. Because the machine in [151] is line connected, the 50/60Hz driving voltage subjected to the winding is the same frequency and similar magnitude to the off-line C/DF test in Section 4.1.2, the results are directly comparable, and the method achieves the measurement while the machine is operating.

The concept was tested using a line driven 11kW machine, with external resistance to emulate degradation. Residual current is measured as in Figure 4.6. The method showed that it was capable of accurate measurement of phase-to-ground and phase-to-phase insulation impedance. A current sensor, dedicated to this task [152] was developed to measure leakage and is now being used in a commercial application for large motors. The system has demonstrated that it is possible to detect degradation both from end-winding contamination [152] and severe degradation resulting from long-term evaporation of insulation [153]. This method requires three current sensors and an externally connected neutral connection which may not be readily available. Using the fundamental driving harmonic as the signal source, implies the leakage current in the tens of micro-Amperes range, several orders of magnitude smaller than the fundamental current. Hence the, the cost of specialised current sensors required to detect this preclude the use of the method for small machines.

A novel concept was introduced in [154], where it was recognised that the inverter drive intrinsically contains zero sequence voltage components. These components by definition apply the same voltage to all three phases, effectively replicating the C/DF test in section 4.1.2. One current sensor is required, which encircles all three phases, measuring the residual current flowing from the winding to ground through the insulation. The zero sequence voltage and current are used to calculate impedance and thus the combined $R_{eq}C_{eq}$ for all three phases-to-ground, allowing one to track the overall health of the ground-wall insulation. In [154] it is noted that the results from 60Hz & 180Hz harmonics correspond well to offline test, the harmonics at higher frequencies are not used.

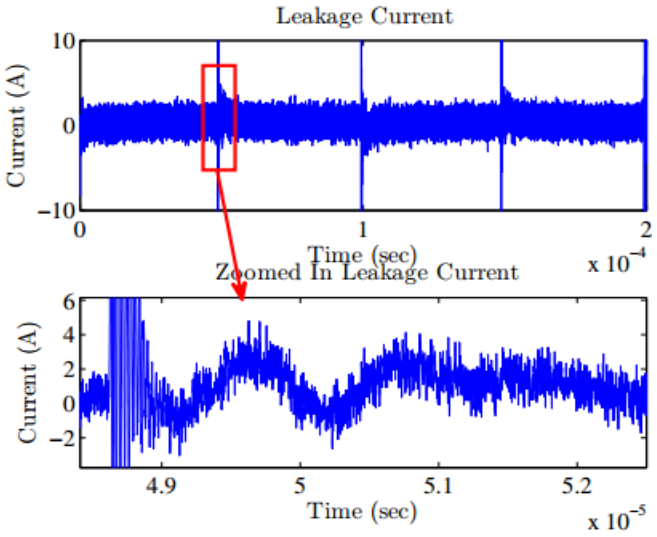

FIGURE 4.7 EXPERIMENTAL LEAKAGE CURRENT MEASUREMENT USING SHUNT RESISTORS [155]

The method described in [155] uses two low cost resistive shunt sensors at the input and output of a phase winding to give a crude measurement of leakage current. The current measured is seen in Figure 4.7, where the spikes associated with the current flowing through ground-wall capacitance due to inverter drive impetus are clearly visible.

Using a high bandwidth acquisition allows the capture of the high frequency leakage current transient in a similar manner as in [146]. However the processing and understanding of the information contained within the current spike transient that is at present lacking. In [146], the information is treated as a macro-parameter which must be monitored for change while in [155] it is proposed that the total leakage current magnitude should be tracked over time. A more sophisticated method of insulation monitoring is required, which recognises the physics of the insulation at high frequency, and provides information to the user that would allow them to diagnose the degradation mechanism and speed of progression based on the measured high frequency leakage currents.

Measurement of leakage current at high frequency shows a promising new avenue of research in the field of insulation diagnosis. Based on understanding of insulation material behaviour at high frequency from Section 3.3, it was proposed to develop a method using leakage current to replicate the C/DF test in Section 4.1.2 with the aim of achieving comparable accuracy and diagnosis capability.

4.3 Monitoring Summary

Monitoring Method	Equipment Required	Applicable Standards	Detected Degradation	State-of-Art Work	Discussion
DC Resistance & IR Test	High voltage DC source with current measurement	IEEE 43	Contamination, Moisture and Tracking	Mature off-line technology. Current work attempts to implement the test during down-time, additional equipment required.	The test can only be carried out off-line and only allows diagnosis of the most prominent faults
DC and AC HiPot Test	DC/AC source rated higher than the machine. If AC, the VA rating must be appropriate	IEEE 95, IEEE 433	Fundamental Defects		This is a pass/fail test, compliance testing of new machines aims to reduce infant mortalities in the field. Regular overload testing may not be appropriate to periodically over-stress the machine
Capacitance and Dissipation Factor Test	Schering bridge or impedance analyser. High voltage source required for tip-up measurement	IEEE 286, IEC 60894	Contamination, Moisture, Tracking, Insulation material change and Partial Discharge	Leakage current has been used successfully to implement the test. Further work is required to develop the monitoring to required standards	Little information exists with regards to acceptability standards and the trajectory to failure. The on-line methods presents the most promising route to monitor machine insulation. More knowledge is required to interpret the results from real machines
Surge Test	High voltage generator with storage oscilloscope	IEEE 522	Turn-to-Turn Insulation Degradation	On-line implementation attempted with limited success. Most promising method involves monitoring resonance behaviour of winding, subject to turn-to-turn degradation	This is the only method to directly test inter-turn insulation. Due to the prevalence of turn-to-turn faults, it is anticipated development of the on-line method would greatly enhance machine failure diagnosis.
Partial Discharge Monitoring	Contact capacitors, high bandwidth current sensors, electric field sensors, acoustic and others	IEEE 1434	Delamination, Contamination, Air Pockets	Both off-line and on-line monitoring is mature technology. Work is being done to automate the analysis and interpretation of data.	The biggest challenges to implementation of PD monitoring is interpretation of data. Most work on PD is performed on high power, high value machines. Recent developments in ultra-fast switching technology introduces PD into low voltage machines.
Sequence Detection	Conventional current sensors		Turn-to-Turn Faults, Eccentricity and Asymmetries	Widely used to implement fault detection, novel uses such as detecting contact quality change are in development.	Differential mode parasitic components are studied in the field of EMC. An understanding of winding behaviour over time can be gained through further research, combining conventional fault monitoring with tracking of high frequency parasitics

TABLE 4-1 SUMMARY OF MONITORING METHODS

4.4 High Frequency Inverter Harmonics

A novel insulation health monitoring method has been developed at the University of Sheffield, which aims to measure C_{eq} and R_{eq} values of ground-wall insulation continuously, while the machine drive is in operation. The system uses the common mode voltage of the drive switching harmonics as the signal source and the resultant leakage current through the insulation, and measures the leakage using a single current sensor. The machine does not require an externally connected neutral, nor does it require perfect magnetic cancellation of the main current, as the measured signals are the switching harmonics at frequencies an order of magnitude higher. The main goal is to diagnose machine insulation degradation at the standard set out by the conventional off-line C/DF test in Section 4.1.2 or better. The common mode voltage and current are measured, to obtain a general overview of ground-wall insulation health.

A typical industrial inverter-fed drive is shown in Figure 4.8 and the paths of the common mode currents resulting from the common mode voltages in the diode rectifier and inverter are shown with arrows. It is important to fully understand the common mode voltages in order to use them for on-line impedance monitoring.

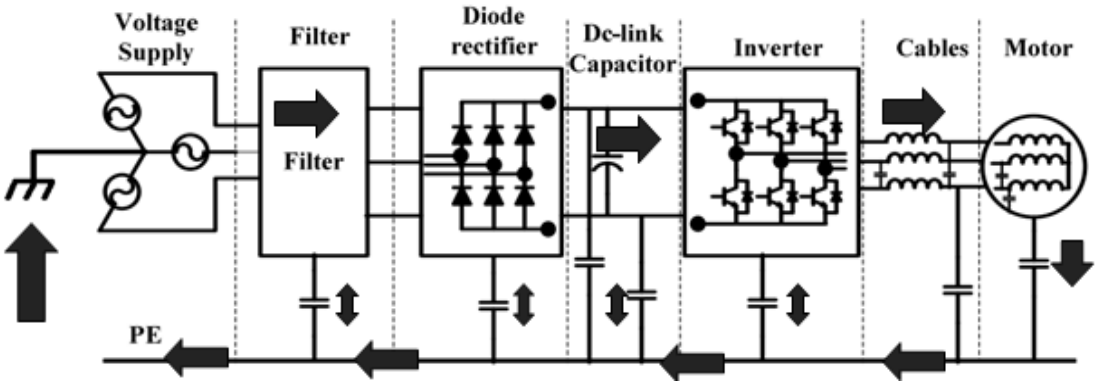

FIGURE 4.8 COMMON MODE CURRENT PATHS IN AN INVERTER DRIVE [156]

The novel aspect of the proposed method is the measurement of a broad frequency range of harmonics in the common mode voltage and current, the use of real-time processing and interpretation of insulation behaviour through a novel model which combines a multitude of harmonics into 5 easy-to-understand parameters. The parameters are based in physics and three of these are directly comparable with standard C/DF measurement. The other parameters illustrate the resonance behaviour of the insulation, showing opportunity to investigate the possibility of tracking inter-turn and inter-phase behaviour of the winding insulation.

4.4.1 Common Mode Voltage

Common mode voltage is defined as the sum total of voltages at machine terminals relative to the motor ground. This can be expressed in Equation (4.2), where the voltage consists of all the phase-to-ground components, V_a , V_b and V_c in a 3-phase system, which do not cancel out.

$$V_{cm} = \frac{V_a + V_b + V_c}{3} \tag{4.2}$$

In the inverter drive shown in Figure 4.8 there are three sources of common mode voltage; diode rectification ripple, space vector harmonic and zero sequence drive voltage. A brief introduction to these sources is included to show how the final choice of harmonics for monitoring purpose was made. The full derivation of the equations in this section can be found in Appendix A.

DC Rectification Ripple

When three phase power is rectified through a diode bridge, the positive and negative rails of the DC link contains ripple, relative to the ground as defined by the grounded centre Y in the D-Y input transformer in Figure 4.8.

$$V_{cm\_rect} = \frac{3V_p\sqrt{3}}{\pi}\left(\sum_{n=1}^{\infty} \frac{1 + (-1)^{(n+1)}}{9n^2 - 1}\cos(3n\omega t)\right) \tag{4.3}$$

The sum of the positive and negative DC bus ripple is shown in Equation (4.3). It can be seen that the first and strongest harmonic is at the third harmonic of the AC mains frequency.

Space Vector Modulation

To raise the effective voltage rating of three phase inverters, it is common practice to inject 3rd harmonic of the drive fundamental phase voltage. The 3rd harmonic superimposed onto the main driving sinusoid lowers the peak value, however does not induce current or torque ripple in the machine. This can be considered as an additional zero sequence components, because the wave will repeat every 120 degrees of the fundamental and all three phases will therefore have identical 3rd harmonic waveforms.

Adding a 3rd harmonic to the phase voltages with a magnitude equal to 1/6th of the fundamental will give an effective 15.5% increase in DC bus utilisation. Similar increase in bus utilisation over sine-PWM is achieved with the commonly used space vector modulation. The harmonics of the space vector contribution are similar to the addition of a triangular wave to a pure sinusoid. The strongest harmonic therefore will be at three times the drive fundamental frequency.

The contributions from space vector modulation and diode rectification harmonics are predominantly at low frequencies, magnitudes of these harmonics fall below 1V after 1 kHz in a typical low voltage (V_{dc} = 600V) servo drive. These

harmonics are used in [154] to measure C/DF similarly to the 50/60 Hz offline measurement method. Capacitive insulation impedance is high at these frequencies resulting in very low current. The method proposed in this project makes use of the wide frequency spectrum of the common mode voltage at the higher frequencies to improve sensitivity.

Zero Sequence Drive Voltage

An inverter drive creates a desired voltage by switching the DC bus voltage on and off, and modulating the duty cycle to produce a rectangular wave whose average equals the desired voltage over time. To generate three phase sinusoidal voltages, offset from each other by 120 degrees for a three phase motor, inverter legs switch in a pattern set out by a modulation scheme such as space vector modulation. The average zero sequence voltage of three sinusoid waveforms offset by 120 degrees is cancelled to zero, however due to the switching pattern an instantaneous zero sequence voltage is present.

Equation (4.4) shows the breakdown of an arbitrary duty square wave signal into frequency components. The fundamental switching frequency ω_s appears at multiples of n, with magnitudes defined by a_n. To calculate the harmonic content of inverter phase voltage, $t_{on}/T = \frac{1}{2} + \frac{1}{2}sin(\omega_m t + \theta_m)$ is inserted into Equation (4.4) to modulate the rectangular waveform with duty of a cosine waveform.

$$V_{rectangle} = a_0 + \sum_{n=1}^{\infty} a_n \cos(n * \omega_s)$$

$$a_n = \frac{2}{n}\frac{V_+}{\pi}\sin\left(\frac{n * \pi * t_{on} * V_+}{T_s}\right) \qquad \textbf{(4.4)}$$

The PWM phase voltage is derived in Appendix A, resulting in Equation (4.5). The first line of the equation represents the DC bus voltage and the desired sinusoidal phase voltage, the second line contains the inverter switching harmonics. The last two lines contain the voltage which constitutes sidebands around the odd and even harmonics respectively.

The common mode voltage is obtained by recreating phase voltages a, b and c obtained using Equation (4.5), where ω_s represents inverter switching frequency, ω_m is the modulating frequency, M is the modulating index, $\beta = \frac{n\pi M}{2}$ and J_x terms are first order Bessel functions. Summing all three phases a, b and c, with voltage phase θ_m= 0, 120 and 240 degrees respectively and dividing by 3 to obtain the definition of zero sequence voltage as expressed in Equation (4.2). The components which do not cancel are the harmonics present in the drive, which can be used as signal sources for insulation health monitoring.

$$V = V_{dc} + V_{dc} * \mathrm{Msin}(\omega_m t + \theta_m) + \frac{4V_{dc}}{\pi}\sum_{n=1}^{\infty}\frac{1}{n}J_0(\beta) * \sin\left(\frac{n\pi}{2}\right) * \cos(n * \omega_s t) + \frac{4V_{dc}}{\pi}\sum_{n=1}^{\infty} 2\sum_{m=1}^{\infty}\frac{1}{n}J_{2m}(\beta)\sin\left(\frac{n\pi}{2}\right)\cos(n * \omega_s t)\cos(2m(\omega_m t + \theta_m)) + \frac{4V_{dc}}{\pi}\sum_{n=1}^{\infty} 2\sum_{m=0}^{\infty}\frac{1}{n}J_{2m+1}(\beta)\cos\left(\frac{n\pi}{2}\right) * \cos(n * \omega_s t)\sin((2m+1)(\omega_m t + \theta_m)) \quad (4.5)$$

The end result of the zero sequence voltage derivation summation shows that the common mode voltage is formed of inverter switching harmonics with sidebands around each harmonic. From the second line of Equation (4.5) it is evident that only odd multiples of ω_s harmonics exist, which are not affected by the modulating waveform.

Sideband harmonics exist at $2*m*\omega_m$ around the odd switching harmonics ω_s for "m" values of m = 3, 6, 9.... Sidebands also exist at $(2*m+1)*\omega_m$ around the even values of ω_s for "m" values of m = 1, 4, 7.....

The full detail of the derivation and implication of the result can be found in Appendix A. For practical purposes it is easier to visualise the harmonics in the frequency domain. An example is therefore included of the voltage in both the time and frequency domains.

Time Domain Illustration

Figure 4.9 shows the measured common mode voltage at the machine terminals of an industrial drive operating with a switching frequency of 2 kHz. The voltage was measured by creating an artificial neutral point at the terminal and acquiring data using an HD6040 LeCroy Oscilloscope through a differential probe ADP100 connected between the centre of the neutral point and ground as in Figure 4.12.

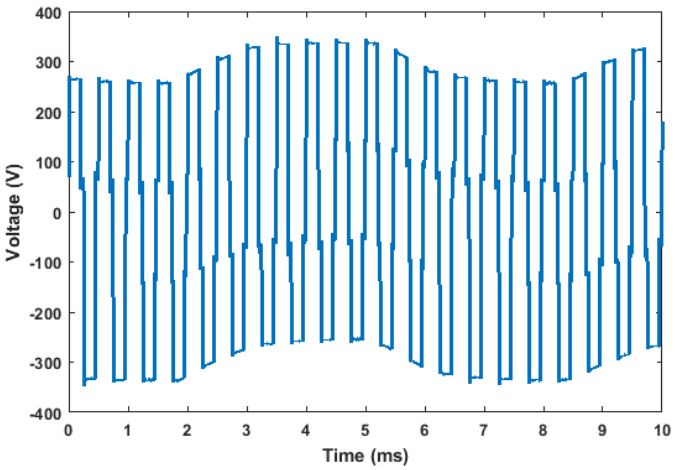

FIGURE 4.9 COMMON-MODE VOLTAGE AT THE MACHINE

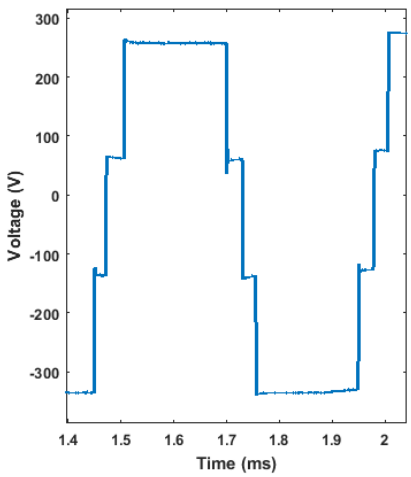

FIGURE 4.10 VCM ZOOMED IN

The ripple on the positive and negative power rails is clearly seen in the envelope of Figure 4.9, showing the diode rectification contribution. In Figure 4.10 the discrete switching steps of each phase leg are seen. There are 6 steps per cycle, corresponding to 3 legs switching on and 3 legs switching off. The contribution from the space vector harmonics is not clearly visible in Fig. 4.9, due to relatively low modulation index used in this illustration.

Frequency Domain Representation

The harmonics described in the derivation are easiest to describe with an example in the frequency domain. Figure 4.11 shows voltage harmonics captured on a drive operating on a 50Hz 3 phase mains AC supply, driving a motor with 200Hz fundamental frequency and using a 6 kHz inverter switching frequency.

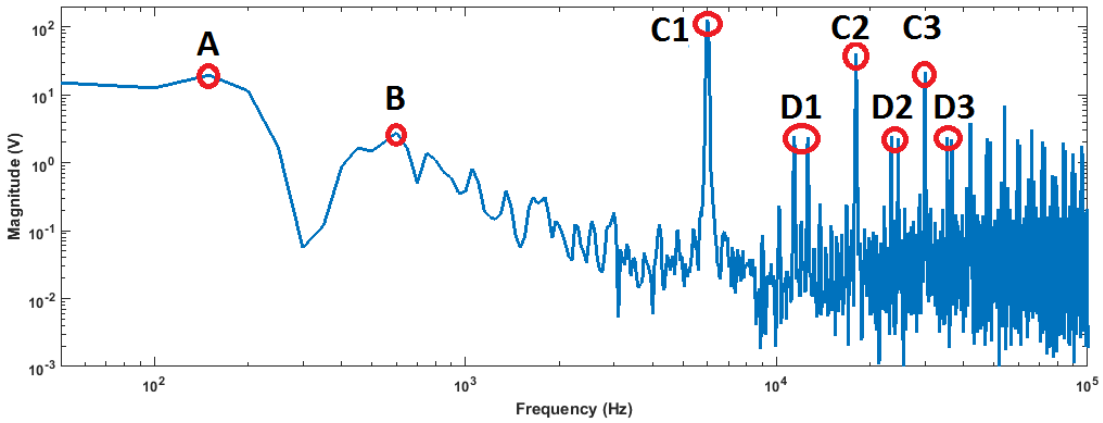

FIGURE 4.11 MEASURED COMMON MODE VOLTAGE HARMONICS

The first harmonic of the diode rectification is indicated by "A" at 150Hz in Figure 4.11. The first harmonic of space vector modulation component is indicated by "B" at three times the modulating frequency i.e. 600Hz.

Harmonics indicated by "C" are the odd multiples of ω_s. Harmonics indicated by D, are sidebands around the even multiples of ω_s, at 12 kHz, at 12 kHz ±600Hz, ±1800Hz... Harmonics also exist around "C" odd multiples of ω_s, at 6 kHz these are at 6 kHz ±1200Hz, ±2400Hz..., however the magnitudes are too low to be observable in Figure 4.11.

4.4.2 Common Mode Voltage Measurement

The common mode voltage is measured using an artificial neutral point. The sum of the phase voltages is achieved by connecting three resistors as shown in Figure 4.12; the sum appears at the centre of the Y point created by the resistors. A differential probe is connected between the Y midpoint and ground to measure the common mode voltage. A differential probe is used to protect the oscilloscope from accidental ground disconnection, as well as providing high voltage step down.

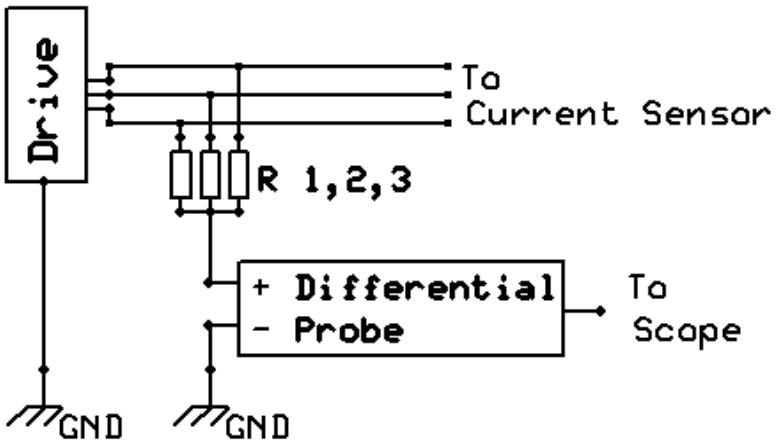

FIGURE 4.12 COMMON MODE VOLTAGE MEASUREMENT SCHEMATIC

For the initial validation experiment, a LeCroy ADP305 probe is used. The datasheet for this probe specifies 8MOhm probe-probe resistance and 12pF inter-probe capacitance. For the long term thermal ageing experiment, a DP-25 probe is used, the resistance of this probe is also 4MOhm and capacitance value is 20pF.

From literature review, the R_{eq} value between 1-10 kHz is expected to be in the same range as the probe parasitic resistance value. The leakage current through the probe will therefore affect measurement. To prevent this, the probe must be connected at the drive terminal, before the current sensor, as shown in Figure 4.12.

4.5 Common Mode Current

Initial measurement of motor common mode impedance in Section 3.3.1 presented the ground-wall as a capacitance of between 2-9nF at frequencies below the resonance point of the winding. In Figure 4.11, the highest magnitude harmonic is at 6 kHz with a magnitude of 100V. Applying 100V to 2nF at 6kHz yields 7.5 mA current harmonic at 6 kHz, a magnitude higher than measured in [151] at line frequencies. To determine the range of useful harmonics and to select the correct current sensor, the common mode current was simulated for a test machine and the simulation verified. The current sensor for the monitoring system was selected and calibrated.

4.5.1 Common Mode Current Simulation

To simulate the expected common mode current, the common mode drive voltage and the common mode impedance of the machine are measured. The impedance of the machine is fitted to the insulation model using the procedure in Section 3.3.3 and is used to represent the impedance of the machine for simulation. Current is obtained by the division of V/Z=I performed in the frequency domain, to give expected current harmonics. The inverse Fourier transform is then used to view the current waveforms in time domain.

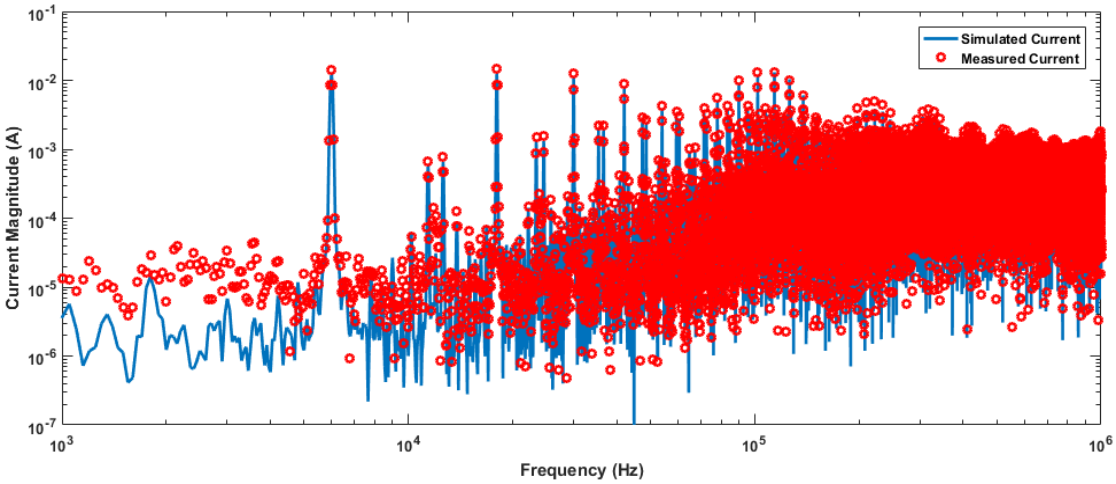

FIGURE 4.13 COMMON MODE CURRENT IN THE FREQUENCY DOMAIN

The strongest harmonic in Figure 4.13 is 12.5 mA at 6 kHz. It is clear that many strong harmonics above 1mA magnitude from 6kHz up to 1MHz. The simulation compares well with measured current except below 10uA, where measured noise is larger than predicted harmonics.

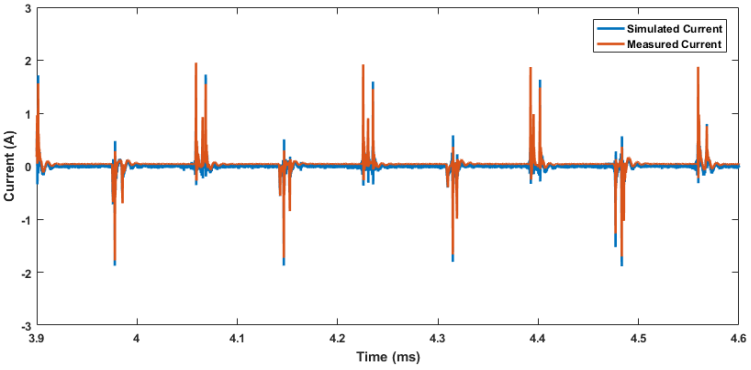

FIGURE 4.14 COMMON MODE CURRENT IN THE TIME DOMAIN

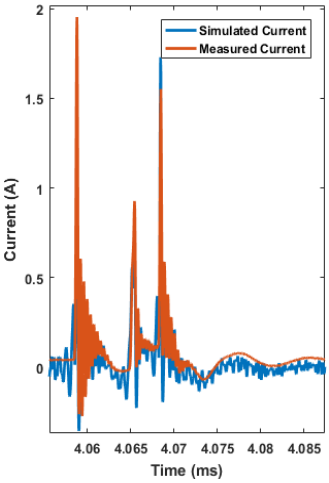

FIGURE 4.15 CURRENT MAGNIFIED

The time domain current waveform in Figure 4.14 shows good agreement between simulation and measurement. The same resonance frequency and decay constants are visible in the magnification in Figure 4.15. The peak current of the simulation is 2A. Simulation of current, using measured impedance and drive voltage allows selection of the current sensor. The sensor specified for the machine under investigation must have minimum ±2A current rating, with bandwidth ideally up to 1MHz to capture strong high frequency harmonics.

4.5.2 Common Mode Current Sensor

Common mode current of a three phase motor is defined by the sum of the phase currents in Equation (4.6). All phase currents will go through the windings, and any current leaking out will travel through the insulation to ground.

$$I_{cm} = I_a + I_b + I_c \tag{4.6}$$

$$\oint H.dl = I_{cm} \tag{4.7}$$

To measure the common mode current, the differential currents must be cancelled magnetically. Equation (4.7) states that integration of the magnetic field density, H, in a closed loop encircling the three conductors, gives the total current going through the surface enclosed by the integration loop. As shown in Figure 4.16, currents I_a, I_b and I_c traveling through machine windings will return and cancel out to zero. Any current returning outside of the integration loop in Figure 4.16, the leakage current returning through ground, will be measured by the calculation.

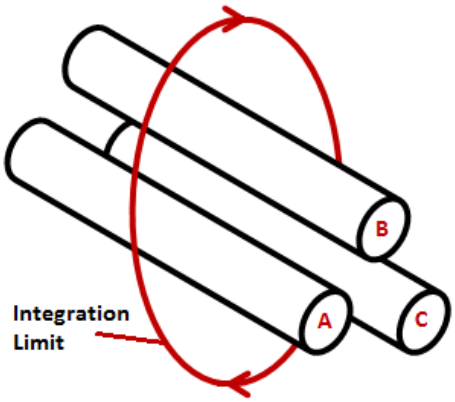

FIGURE 4.16 INTEGRATION OF RESIDUAL CURRENT AROUND THREE PHASE MOTOR CABLE

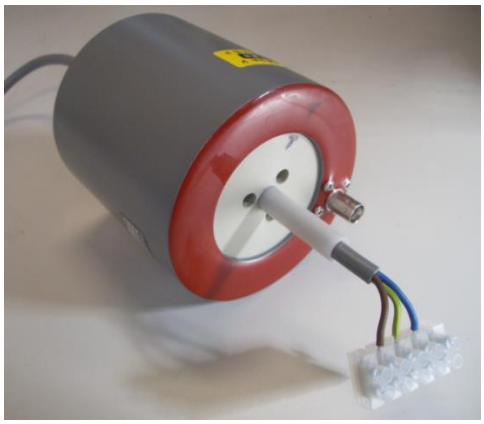

FIGURE 4.17 BERGOZ CURRENT SENSOR

Practical implementation of the integral in Equation (4.7) can be obtained using a high sensitivity current transformer, where the core forms the integration path, summing all current flowing through the core by a sensing coil. The phase current (differential mode) flowing into A must return as a sum of the phase currents in B and C. Ideally, therefore, if all three cables are located at the centre of the current transformer, the resultant magnetic field in the core will be completely cancelled and the sensing coil only measures the common mode (leakage) current. In reality, however, the three cables cannot be located exactly at the centre due to cable size. Consequently, the effect of differential mode currents may not be completely cancelled, leading to local saturation of the current transformer and non-linear response. To increase symmetry and improve quality of cancellation, three factors must be maximised in the sensor

construction: the centring of conductors, distance of conductors from each other and the sensor aperture size. The aperture, centring jig and close positioning of conductors can all be seen in the final sensor build in Figure 4.17.

Current sensor transformers pose a fundamental problem of physical size vs bandwidth, the larger the diameter of the sensor, the larger the sensor inductance, increasing the time constant of the transformer inductance. The sensor must also have a low noise figure and large dynamic range to capture mA range harmonics without saturation from 1A peak currents.

A closed loop current transformer from Bergoz Electronics was chosen for its large aperture, high bandwidth, high accuracy and low noise characteristics. The -3dB bandwidth of the sensor is at 1MHz with a 2A peak current capability.

4.5.3 Current Sensor Calibration

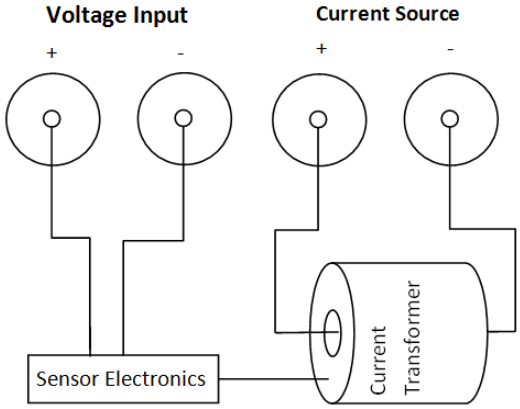

FIGURE 4.18 CALIBRATION SETUP

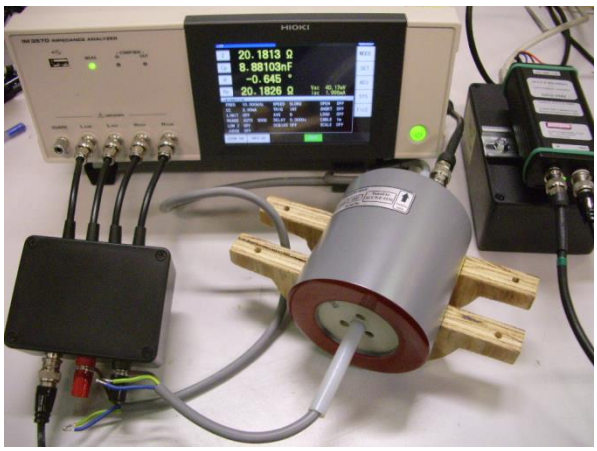

FIGURE 4.19 CALIBRATION IN PROGRESS

Current sensor gain and phase relationship, including the sensor electronics was measured using an impedance analyser as shown in Figure 4.19. The analyser was configured to inject a constant current through the sensor and measure the output voltage from the sensor electronics as shown in Figure 4.18. The voltage/current characteristic can then be interpreted as gain.

According to the datasheet, the gain of the sensor is 5 V/A with zero degree phase response. It is seen in Figure 4.20 that the gain fulfils the specification of at least 1MHz -3db bandwidth; however the phase relationship in Figure 4.21 changes by 65 deg at 1 MHz

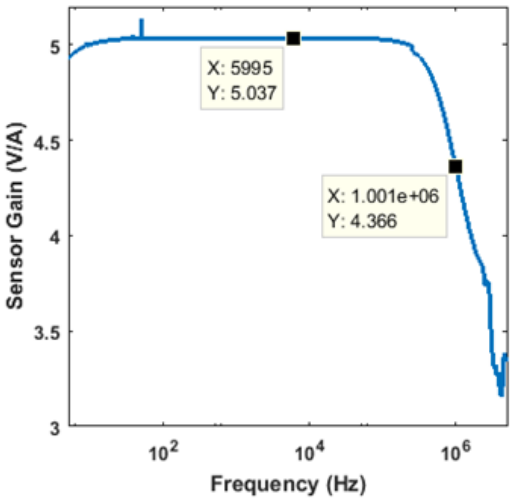

FIGURE 4.20 CURRENT SENSOR GAIN

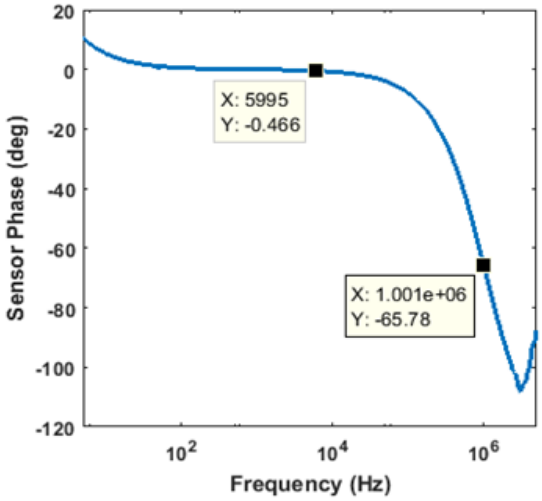

FIGURE 4.21 CURRENT SENSOR PHASE

The measured curves for gain and phase response are used in the data processing stage to offset measured current harmonics to compensate for the response of the current sensor. The limit for compensation is set by the signal/noise ratio which falls with decreasing sensor gain.

4.6 Automated Monitoring System

Recent developments in embedded computing have greatly increased computing power and reduced size, price and power consumption of modern electronic systems. A modern single board computer is more than capable of data processing and controlling a long term experiment.

4.6.1 Hardware

For preliminary testing, voltage acquisition is taken with an HD6040 oscilloscope at 100MS/S, coupled with a 100MHz differential isolated ADP100 probe. The current sensor is the same as selected in Section 4.5. In real-world monitoring applications, it is not feasible to use an expensive bulky scope as the basis of the system. Due to scope availability and desire to emulate the philosophy of the bearing monitoring system presented in Section 2.3, a compact system was designed to carry out long term insulation monitoring experiments.

It was decided to use the Red Pitaya single board computer based on a Zynq zc7010 SoC chip as the basis of acquisition and processing. Zc7010 SoC chip features a dual ARM Cortex A9 processor with an on-board FPGA unit which handles data from a dual high speed ADC. The ADC has 14 bit resolution at 125MHz, superior to the 12-bit acquisition used in the initial validation experiment in Section 4.7.

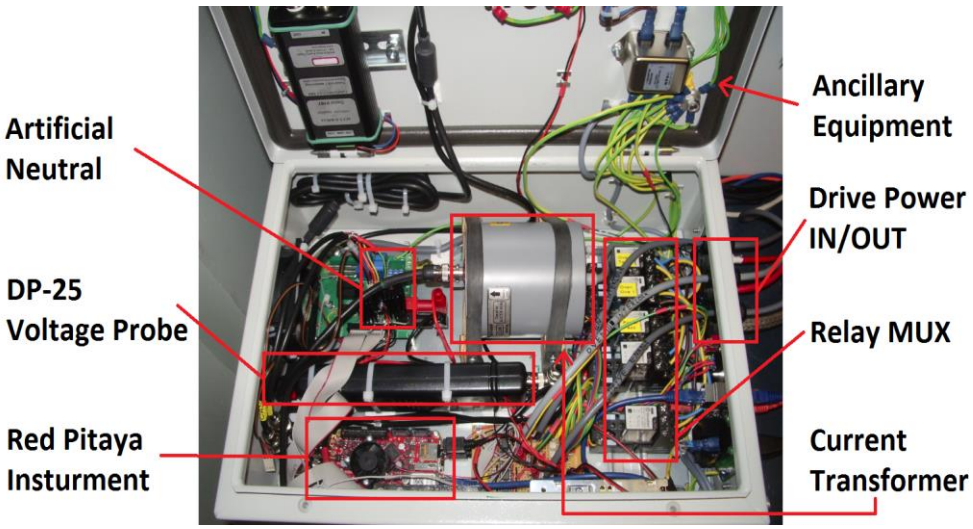

FIGURE 4.22 MONITORING SYSTEM LAYOUT

The major components of the automated acquisition and processing system are labelled in Figure 4.22. To enhance repeatability of acquisition and processing, all the connections must be as short as possible and be subjected to a minimum of movement and temperature variation. Fixing equipment in a rigid enclosure as shown in Figure 4.22 and completely automating the test removes possibility of human induced variations.

4.6.2 Data Processing

The full data processing chain is shown in Figure 4.23, raw voltage and current data is acquired, down sampled and filtered inside the FPGA then passed through shared RAM to the ARM CPU. The ARM CPU implements a transform of the time domain data to the frequency domain, using the FFTW3 library. Impedance calculation Z=V/I and harmonic selection is then performed in the frequency domain by a program written in C code. The output results, together with the raw data for every 100th measurement cycle, are saved and passed to an external computer via Ethernet network..

$$C_{eq} = \frac{1}{2\pi f}\frac{1}{|Z|}\sin(-\theta_z) \tag{4.8}$$

$$R_{eq} = \frac{1}{\frac{1}{|Z|}\cos(\theta_Z)} \tag{4.9}$$

In post processing, the impedance data is transformed to a parallel RC equivalent domain through Equations (4.8) and (4.9) as to be used in the model fitting method in Section 3.3.3. Data backup, graph plotting, model fitting and post processing are performed by a conventional PC in MATLAB. The programming structure of data processing is available in Appendix B.

For the validation experiment in Section 4.7, the first 40 odd switching harmonics were selected, together with the first sidebands around the first 40 even switching harmonics, in total returning 120 harmonics. For the experiment in Chapter 5, the data processing was simplified to discard the sidebands around the even harmonics, therefore returning only the 40 odd switching harmonics at 6 kHz * (2x(1:40)-1). The advantage of discarding the sidebands allows measurement of variable speed drives, because as demonstrated in Section 4.4.1, the sidebands are present at multiples of fundamental frequency, whereas the odd switching harmonics are solely dependent on the inverter switching frequency.

Harmonics with current magnitude of less than 1mA were discarded from further data processing to maintain a minimum signal to noise ratio, therefore the actual number of harmonics varies according to signal strength.

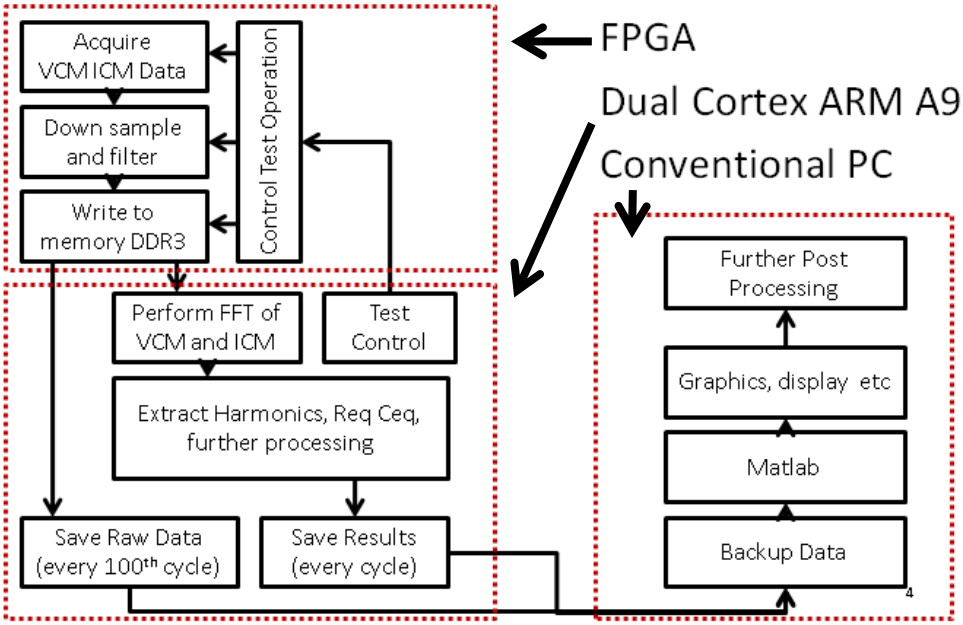

FIGURE 4.23 DATA PROCESSING CHAIN

The data is acquired at 125MHz and down sampled to 25 MHz, 500,001 points are passed to the ARM CPU for the voltage and current channels. The number of points and sampling frequency were selected to capture the repeating period of the fundamental waveform and appropriate frequency resolution to capture the sideband harmonics.

$$\Delta f = \frac{1}{(N-1) * T_s} \qquad (4.10)$$

Equation (4.10) dictates that for a frequency resolution of 50Hz, 500,001 points are required to capture 20ms periods at 25MHz. This gives adequate representation of both the results in Section 4.7 and Chapter 5, where the fundamental frequencies are 50Hz and 200Hz respectively. The whole data acquisition and processing chain repeats at 1 minute intervals.

4.6.3 Error Analysis

To determine the quality and consistency of measurement of the automated on-line monitoring system using automated hardware in Section 4.6.1, 400 insulation impedance results were taken with an automated acquisition setup. The stator was at room temperature and no degradation is presumed to have occurred during the measurement. These measurements allow the quantification of variation expected in further measurements. Combined with a sensitivity analysis, error bars can be defined for all other measurements of C_{eq} and R_{eq}.

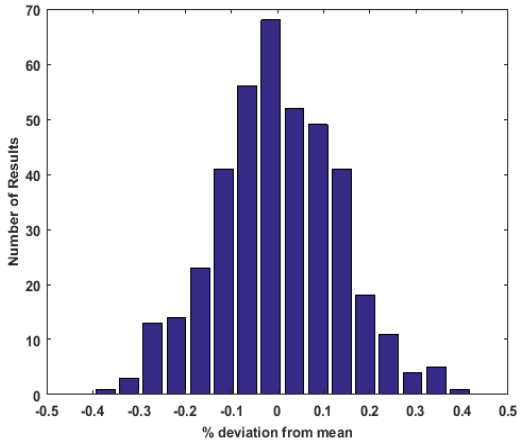

FIGURE 4.24 IMPEDANCE MAGNITUDE DEVIATION FROM MEAN

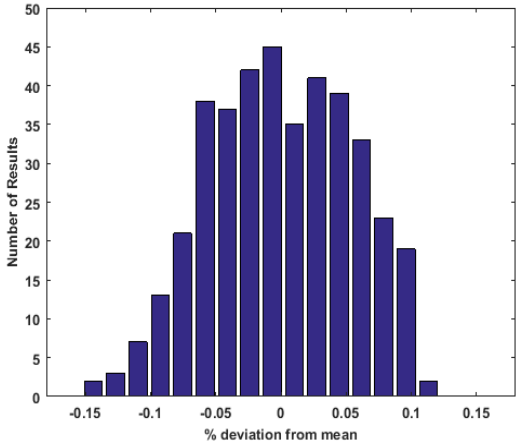

FIGURE 4.25 IMPEDANCE PHASE DEVIATION FROM MEAN

Figure 4.24 and Figure 4.25 show measurement deviations from the mean for the 6 kHz harmonic. Both the magnitude and phase follow a Gaussian distribution. The average RC values measured are 2.128 MOhm and 2.914nF, respectively, with 9.1kOhm impedance and θ_z =-89.7550°. Impedance standard deviation values are 10.9859 Ohms in magnitude and 0.0506 degrees in phase. By defining error for any single point as ± one standard deviation from the local mean, one can spot erroneous data anomalies, or fast impedance degradation trend changes. The sensitivity of R_{eq} and C_{eq} to noise in the common-mode voltage and current can be calculated by partial differentiation of Equations (4.11) and (4.12) with respect to disturbance of measured variable s.

$$\frac{\partial C}{C} = -\frac{\partial |V|}{|V|} + \frac{\partial |I|}{|I|} + \partial\theta_i \cot(\theta_i - \theta_v) - \partial\theta_v \cot(\theta_i - \theta_v) \quad (4.11)$$

$$\frac{\partial R}{R} = \frac{\partial |V|}{|V|} - \frac{\partial |I|}{|I|} + \partial\theta_i \tan(\theta_i - \theta_v) - \partial\theta_v \tan(\theta_i - \theta_v) \quad (4.12)$$

The sensitivity result in Equations (4.11) and (4.12), where $|V|$ and $|I|$are the magnitude of the voltage and current respectively, and (θ_v, θ_i) are the phase angle of the voltage and current, respectively. It is observed that when the impedance angle $\theta_z = (\theta_i - \theta_v)$ is near -90° for a capacitance dominated

insulation system, C_{eq} estimation is predominantly sensitive to voltage and current magnitude variations, which means that C_{eq} noise is dominated by the deviation in impedance magnitude. On the other hand, since $\tan(\theta_i - \theta_v)$ factor will tend towards infinity when the measured impedance angle is near -90°, R_{eq} measurement sensitivity will be dominated by the phase error. Furthermore, the error in R_{eq} estimation will also depend on the absolute value of θ_z.

4.7 On-Line Validation

Initial validation of the current sensor in Section 4.5 for the purpose of on-line measurement of C_{eq} and R_{eq}, was performed with a healthy machine driven at 1000 RPM with no load. Degradation was emulated by adding extra resistance in the machine common mode path.

4.7.1 Aims

The main aims of the experiment were as follows:

- Demonstrate on-line acquisition of machine insulation parameters
- Demonstrate adequate sensitivity to expected parameter variation
- Analyse the measurement errors

4.7.2 Methodology

The machine was set to operate at 1000RPM, at 50Hz electrical frequency. The machine was mounted on a stand as shown in Figure 4.26 and driven by the inverter using closed loop speed control. The machine is a random wound, low voltage servo motor, with H class organic insulation, with overlapped distributed windings. The machine is rated at 2.83kW @3000 RPM, with 380V 7.5A input. This machine is typical of Type I machines.

FIGURE 4.26 HEALTHY MACHINE TEST

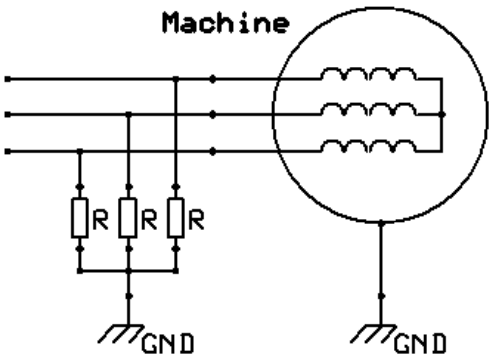

FIGURE 4.27 DEGRADATION EMULATION

Common mode voltage and current was acquired during operation, with a LeCroy 12 bit HD6040 scope, storing 1,000,001 samples each, at 100MS/s. Data was processed off-line using MATLAB to extract zero sequence harmonics. To increase the number of harmonics available, several sets of data were taken with the drive switching frequency at 2, 3 and 6 kHz.

Figure 4.27 shows the use of external resistors to emulation insulation degradation. Three equal resistors are placed in parallel with the insulation to ground path increasing common mode dissipation, emulating the effect of long term oxidation. The capacitance of the winding insulation will not be changed in a short period of testing.

Five emulated degradation scenarios were tested: 4 resistor combinations ranging from 6.2MOhm to 200kOHm, and a scenario without extra resistance loading. The dissipation rises by roughly a factor of 3 in between scenarios. Large R_{eq} variation is expected in real machine degradation, especially towards the end of machine lifetime. It is expected that C_{eq} current dominates, therefore measurement of the minority current through Req component should show the full capability of the system.

4.7.3 Raw Results

Measured impedance magnitude and phase data is shown for the case without extra resistive loading in Figure 4.28 and Figure 4.29. Most of the magnitude and phase points are within 1% of the reference impedance value measured off-line using the impedance analyser. Comparison with an off-line instrument is important to demonstrate the ability of the on-line equipment to measure absolute values of impedance.

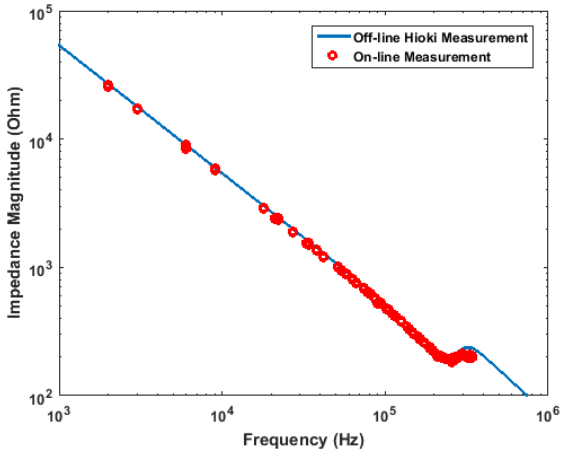

FIGURE 4.28 MACHINE ONLY IMPEDANCE MEASUREMENT

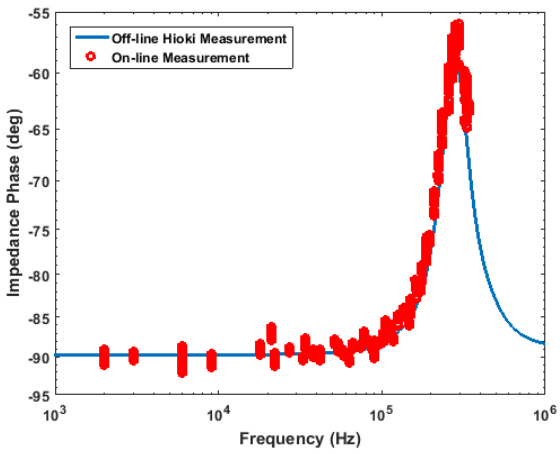

FIGURE 4.29 MACHINE ONLY IMPEDANCE PHASE MEASUREMENT

The raw impedance data is transformed to RC values by assuming a simple parallel RC model described in Section 3.3.1 for further fitting and use. Viewing the data as Req and Ceq can be considered as viewing the impedance data in the Req or Ceq domain. Degradation can be observed visually, by observing the changes in Ceq or Req, changes which would otherwise be unseen by viewing the impedance and phase directly

To transform to R_{eq}, it is required to take the tangent of the phase data in Figure 4.29. It is evident that phase data in Figure 4.29 and Figure 4.30 at values of angle θ_z close to -90°, R_{eq} will tend towards infinity. A new method is proposed to enable the use of all values of phase for calculation of R_{eq} by offsetting the phase data by a small phase angle before transforming the result to the RC domain.

4.7.4 R_{eq} Processing

It was established in the error analysis in Section 4.6.3 that although the noise in both impedance magnitude and phase is Gaussian, the error in R_{eq} will not have the same distribution. At impedance angles close to -90 degrees, the Gaussian distribution would become skewed since negative values of R_{eq} will result when the measured angles containing noise are below -90 degrees. These results are physically incorrect. To circumvent this problem when implementing the model fitting algorithm described in section 3.2.1, a novel method of R_{eq} data processing is devised.

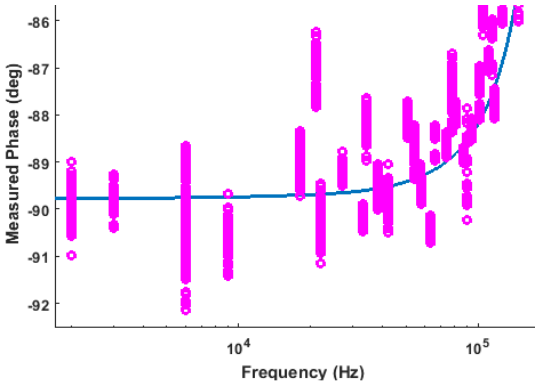

FIGURE 4.30 INSULATION IMPEDANCE PHASE AT LOW FREQUENCIES

It is proposed that in order to yield physically correct R_{eq} data, the insulation impedance phase data in Figure 4.30 must be offset by a fixed angle. The angle must be large enough to shift all measured phase points above -90°, however it must also be small enough to not affect the capacitance measurement. From practical experience it was determined that 5° provides an adequate balance between the two constraints. The offset technique assumes that the measured impedance is mostly capacitive, with only a small dissipative component, this is valid while measuring insulation and other low dissipation capacitance dominated impedances.

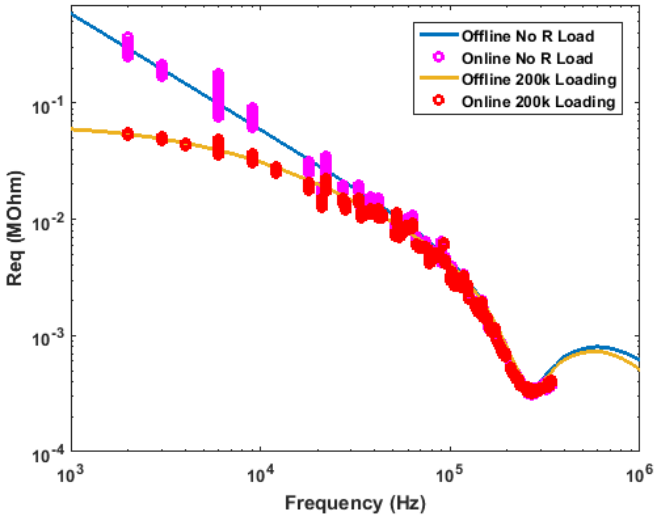

FIGURE 4.31 R_{EQ} MEASUREMENT AT TWO SCENARIOS WITH OFF-LINE COMPARISON

Figure 4.31 shows results of two extreme scenario of insulation health measured in the experiment, after applying the offset technique. Any data processing must be made with the same offset value, to allow consistent comparison of insulation dissipation over time.

4.7.5 R_{eq} Results

To obtain the final R_{eq} results, the impedance data was transformed to the Req domain and the phase offset method used, as described in Section 4.7.4. The measured data for all external resistance loading scenarios is shown in Figure 4.32 in the R_{eq} domain.

Model fitting as described in Section 3.3.3 is used to fit the y=m*x+c parameters of the frequency dependent resistance R_ω for R_{eq} data points between 2 kHz to 30 kHz. The results of this fit are shown in Figure 4.32. The R_ω parameter was selected as the main parameter of interest as addition of extra resistance in the common mode path should not affect capacitance measurement. Due to the decrease of R_{eq} with increase in frequency, most of the change due to parallel resistance in the common mode is expected at low frequencies, the region best represented by the fitted model value R_ω.

The progression of emulated degradation is clearly visible to the naked eye in Figure 4.32 especially at the lower frequencies. In real life operation, changes of insulation may be more subtle over time, noise may also be present. To interpret the data it is suggested to use the fitted values of y=m*x+c for R_ω parameter as monitoring tools.

The results for m and c are shown in Table 4-2, showing clear progression over time. The expected results are obtained by adding the scenario specified resistance in parallel with the initial machine only measurement. It can be seen in Table 4-1 that the measured parameters of scenarios with degradation are broadly in line with the expected values.

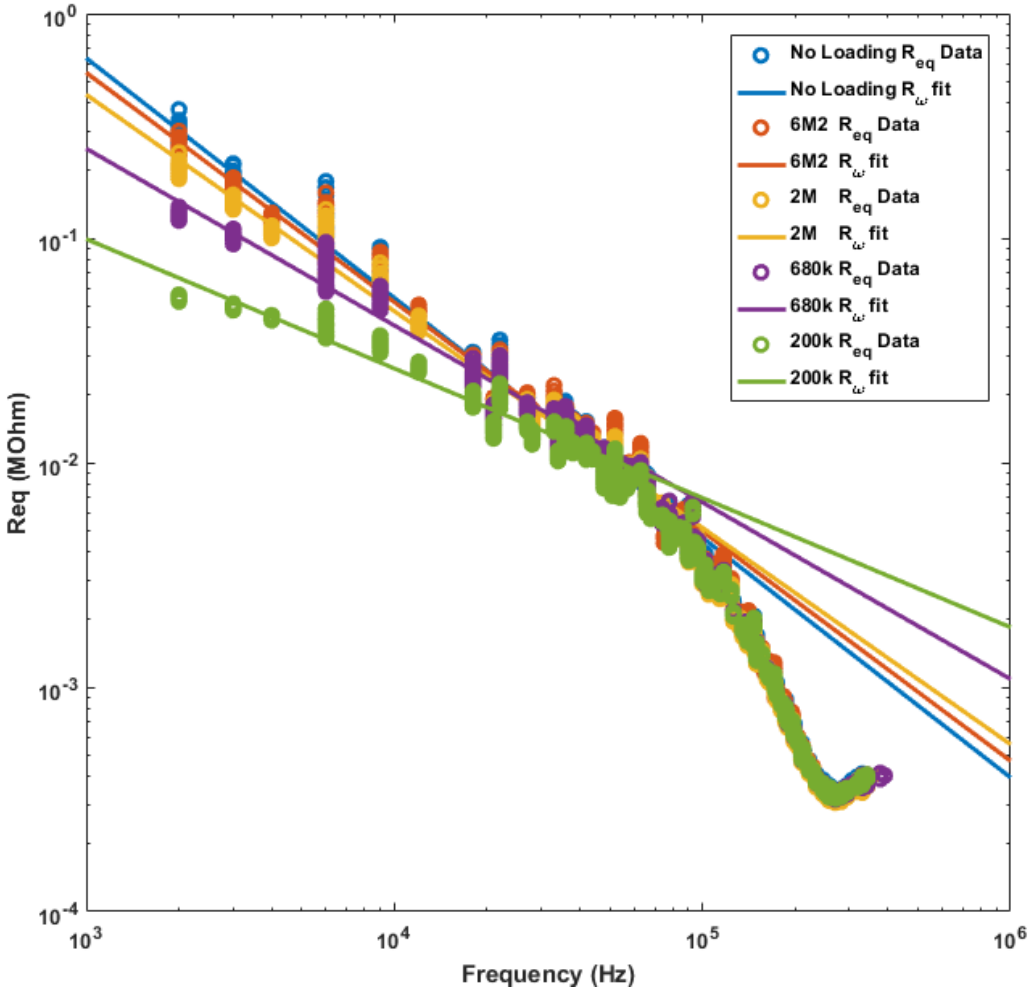

FIGURE 4.32 MEASURED REQ POINTS AFTER PHASE OFFSET TRANSFORMATION

TABLE 4-2 R_W PARAMETERS FOR EACH EMULATED DEGRADATION SCENARIO

Scenario	Measured		Expected	
	m	c	m	c
Machine only measurement	-1.07	3.01	n/a	n/a
2MOhm Resistance CM load	-1.02	2.80	-1.02	2.81
6.2MOhm Resistance CM load	-0.96	2.53	-0.94	2.46
680k Resistance CM load	-0.79	1.76	-0.78	1.75
200k Resistance CM load	-0.58	0.73	-0.51	0.48

With noise present, the parameters “m” and “c” can be filtered over time to establish the trend. The state of insulation can be viewed graphically at any point in time, by using the model parameters to recreate insulation impedance at any time, and viewing the insulation in the C_{eq} and R_{eq} domains.

4.7.6 Ceq Results

It was shown in the error analysis of section 6.4.1 that C_{eq} values is most influenced by V/I impedance when the dissipation is low. Figure 4.33 plots the measured C_{eq} values at the two extreme R_{eq} loading scenarios. It can be seen in Figure 4.33 that the most extreme dissipation scenario with 200kOhm loading on the common mode path, has no effect on measurement of C_{eq} values.

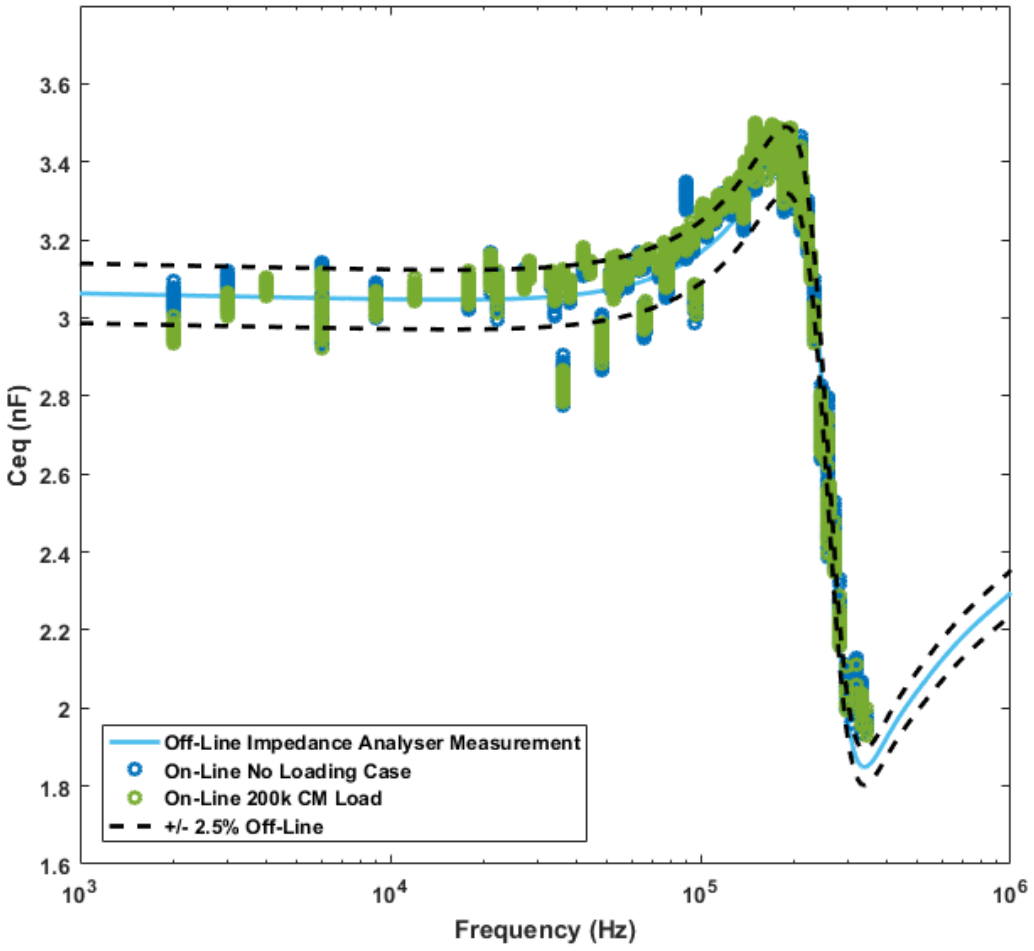

FIGURE 4.33 C_{EQ} RESULTS AT TWO EXTREME R LOADING CONDITIONS

It is seen in Figure 4.33 that 68% of the on-line measured results are within 2.5% of the offline measured result. This experiment has a higher per-harmonic error than the error analysis in Section 4.6.3, for the same 68% spread, the impedance results were within 0.1%. The source of this is in part a lesser specification of acquisition hardware and the temporary hardware arrangement which did not allow for comprehensive shielding and prevention of external disturbance. To improve the accuracy, it is possible to take an average value of all the harmonics acquired. The average value of Ceq between 2-30 kHz using the off-line measurement was 3.0550nF, for the same range the on-line measurement returns 3.0568nF.

4.7.7 Conclusion

Experimental data from the monitoring system has successfully demonstrated measurement of ground-wall insulation impedance during motor operation. The error has been analysed analytically in Section 4.6.3, with practical results for Ceq measurement showing good agreement with off-line reference measurement. Using the automated system in the error analysis, an outright accuracy of 0.1% impedance magnitude shown for on-line impedance magnitude monitoring and therefore Ceq measurement.

The Req measurement requires multiple harmonics fitted to a straight line to measure dielectric dissipation change. An additional data processing stage was required to add a linear phase shift to all data to compensate for non-linearity in the Req vs phase characteristic near -90° phase. Using the methodology it was possible to distinguish reliably between the five dissipation states representative of expected dissipation changes during insulation ageing.

4.8 Summary

An extensive literature review has been carried out to assess the most common current off-line and on-line insulation monitoring methods. Based on the review, it was decided to investigate further the possibility of measuring ground-wall insulation impedance on-line using leakage current. Common mode voltage present during inverter operation has been identified as a signal source for ground-wall insulation current flow.

A novel insulation monitoring method has been proposed based on monitoring the insulation impedance through common mode current measurement due to harmonic present in the common mode voltage due to PWM drives in modern electric drives. Common mode voltage origin and harmonic content is presented. The requirements for a common mode current sensor have been identified through simulation of expected current.

The method for measuring insulation impedance on-line has been tested to detect emulated degradation, as would be expected in real service life of a machine. Detected change is visible outright to the naked eye, however it is also shown how model fitting of low frequency resistance can be a powerful tool to distinguish subtle change over time. The accuracy of the measurement is also compared to an off-line impedance measurement instrument.

The capabilities of the on-line monitoring system are comparable to the requirements of the off-line measurement, therefore on-line measurement has been verified for use as an insulation monitoring system.

Chapter 5

Long Term Ageing Test

A novel on-line insulation monitoring system was demonstrated in the previous chapter, capable of the accuracy required to perform the capacitance and dissipation measurement as would be measured off-line. Literature sources in Chapter 3 reveal that little information is available with regards to experimental evidence of Ceq and dissipation change over time. No data is currently available for on-line real-time monitoring for real long-term ageing.

Accelerated ageing tests on four stator samples were carried out to investigate insulation ageing mechanisms over time, contribute data to the engineering community and validate the developed monitoring system. The samples were aged at four different temperatures, set by elevated ambient temperatures inside test ovens. For the test, the rotors were removed and machines operated with 1/3 rated current, driven by an inverter in open-loop speed control at 200Hz.

Monitored dissipation values revealed a complex behaviour of insulation material over time. Diagnoses of material degradation modes have been proposed based on available literature and measured data. Resonance behaviour change of the samples has been simulated and observed, revealing the possibility to diagnose degradation modes other than insulation material degradation.

A link between capacitance progression and sample lifetime has been established, and a method for sample remaining lifetime has been proposed. Further work to improve the quality of prediction, and ability to diagnose modes of degradation is discussed.

5.1 Aims of the Experiment

In order to link the end of life of insulation to measured parameters, the requisite parameters must be monitored over time and the final value at sample breakdown recorded. Currently there is no information in literature or in IEEE standards linking capacitance and dissipation to end of life. The key aim of this accelerated ageing experiment is therefore to observe the progression of capacitance and dissipation during ageing. The pattern of progression and final values are to be noted.

Accelerated ageing must be performed to emulate the lifetime of the machine in a realistic timeframe. With regards to the ageing, two factors must be maintained: an ageing mechanism representative of normal operation and a consistent representation of all stators of similar machines. The experiment must

be designed to comply with best practice of ageing representation. The quality of conduct of the experiment will reflect how representative the samples are of the general population, and how close the failure times are to calculation.

The accelerated ageing test allows validation of the monitoring system developed. The practical challenges overcome are documented, for development of a future commercial system.

Parameter progression rates which are expected to correspond to the sample accelerated ageing rate are to be monitored. Monitoring the trajectory of progression and the final value threshold allows extrapolation of measured data into the future to final failure. A system for prognosis of remaining lifetime is to be proposed, and the quality of prediction to be quantified.

5.2 Accelerated Ageing Method

An ideal experiment to achieve the aims set out would fit thousands of insulation monitoring systems to thousands of similar samples, operating in the field, over the lifetime of the machines, potentially between 3 to 25 years. A database of monitored parameters and the failure times, failure modes and insulation parameter trajectories would be established. For the purpose of this experiment however, the ideal scenario must instead be replicated with a minimal number of machine samples, and on a much reduced timescale, necessitating accelerated lifetime testing. The approximations and assumptions to realise this are outlined in the method, illustrating the limits of the testing.

5.2.1 Thermal Ageing

Typical lifetime of electrical machines can be between 3 to 25 years, depending on the application and design. To demonstrate ageing in the laboratory, the methodology from IEEE standard 117 [32] for classification of insulation is used as a starting point to conduct the accelerated ageing test.

The IEEE standard assumes that the ageing of insulation is dominated by thermal breakdown, and the insulation breakdown can be treated as a chemical phenomenon. Motorette samples are aged at elevated temperatures with failure time plotted against temperature, the failure threshold may be a number of factors, from tensile strength of material, to breakdown voltage to a loss of mass [34]. Time of failure vs temperature Arrhenius plot is extrapolated to return the temperature at which the samples would survive 20,000 hours, quantifying the temperature index (TI) of the material. The extrapolation is demonstrated in Figure 5.1. Standard insulation classes have been established based on the temperature index, the most common of these are shown in Table 5-1.

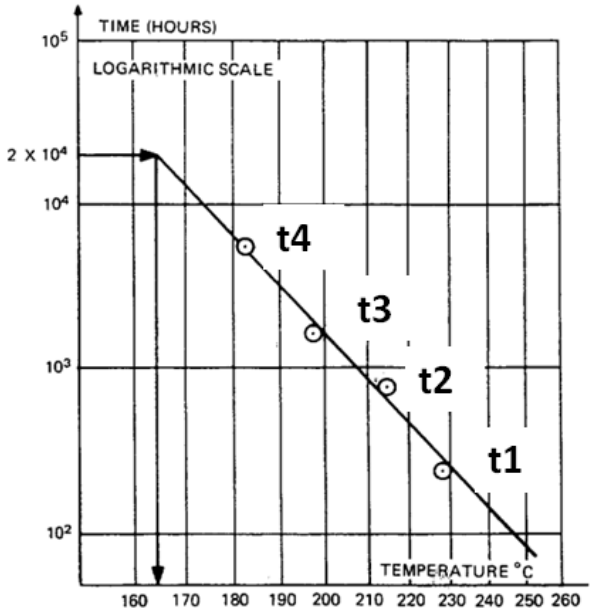

FIGURE 5.1 TIME TO FAILURE VS TEMPERATURE CLASSIFICATION [32]

Insulation Class Class	Temperature Index
A	105
B	130
F	155
H	180
N	200
R	220
S,C	240

TABLE 5-1 STANDARD INSULATION CLASSES

An Arrhenius plot as in Figure 5.1 plots the log of sample lifetime vs -1/T temperature in Kelvin. The fitted line allows determination of B and $\log(L_0)$ constants in Equation (5.1), where L_0 is the lifetime at T_0. Equation (5.1) may be rearranged to normalise L_0 to 20,000 hours at T_0, to return Equation (5.2), where E_a and R denote the activation energy of the material and the molar gas constant respectively. Using this, the insulation lifetime can be easily predicted for other samples, once the constants of the equation are determined experimentally by measuring failure times for insulation samples as functions of temperature.

$$\log(L_{end}) = \frac{B}{T} + \log(L_0) \tag{5.1}$$

$$L = L_0 e^{\frac{E_a}{R}\left(\frac{1}{T}-\frac{1}{T_0}\right)} \tag{5.2}$$

$$L_{end} = \frac{20{,}000\ hrs}{2^{\frac{(T_2-180)}{10}}} \tag{5.3}$$

In literature and industry, the rule of thumb that insulation lifetime halves for every 10 degrees temperature increase, as expressed by Equation (5.3) is widely used. Equation (5.3) is an approximation of Equation (5.2), where it is assumed that increments of temperature δT on the 1/T scale are equal for samples operating at high temperatures. Equation (5.3) is used to anticipate the lifetime of samples tested for this experiment. The implications of using Equation (5.3) are explored in the results section.

5.2.2 Machine Samples

To fulfil the aim of the most representative operation, and for ease of inverter-fed operation of the machine during thermal ageing, a full three phase stator winding was selected for test. Four stators of the same machine as used in Chapters 2 and 4 for testing, and the 2.83kW 400V inverter driven servo drive, were employed for the accelerated ageing experiment. The stator sample is shown in Figure 5.2 inside the oven used to provide elevated temperature.

FIGURE 5.2 STATOR SAMPLE INSIDE OVEN 2

To maintain elevated temperatures, one could either dissipate power through the stator windings, or use an oven to raise the ambient temperature. Although internal dissipation is more representative of real world operation, it was decided to provide all the heat from the ambient temperature. The priority in this case is to maintain the most stable operating temperature for the insulation, which may not be possible with required accuracy using winding dissipation due to changing winding parameters over time. Eliminating winding temperature variations also removes mechanical stress as a degradation factor, narrowing the scope of the investigation.

The samples were subjected to 2.5Arms current, dissipating no more than 20W real power into the windings. The temperature deviation was measured to be no more than 1 °C during the experiment, validation of the oven and sample temperatures can be found in Appendix D. The samples were operated until the inverter drive over-current relays were tripped. The failure criteria is therefore well defined, as the time when the machine would no longer operate.

5.2.3 Equipment Setup

To compress the time required for testing, two samples were tested in parallel. The two samples would be located in two separate ovens, subject to their differing respective test temperatures. A relay system would be placed in series with the monitoring system to multiplex the power flow to either of the two samples under test. The full experimental setup is shown in Figure 5.3. The same insulation measurement system as used in Section 4.6 is used in this experiment.

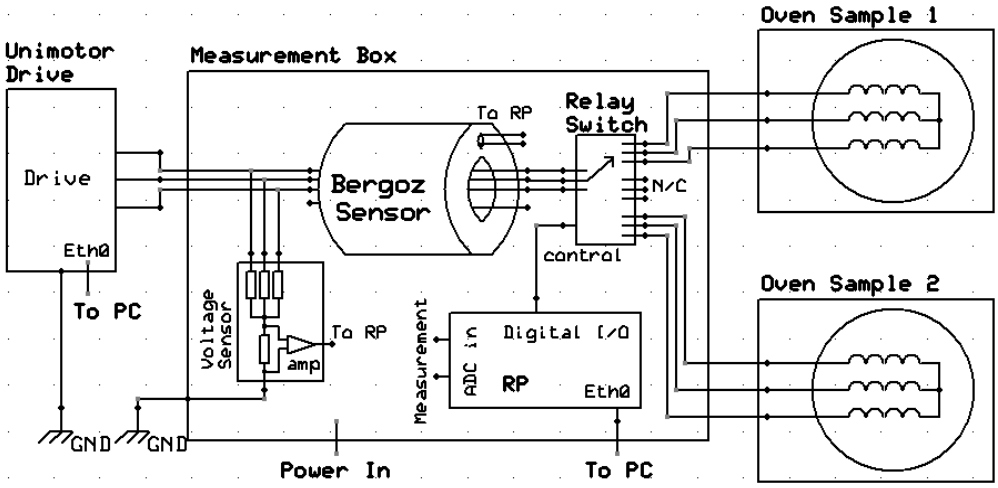

FIGURE 5.3 EXPERIMENT SETUP

The sequence of test would be to connect Sample 1 to the drive power, enable the drive, acquire the insulation impedance while the machine is operating, remove the enable signal and disconnect the sample. Sample 2 would then be connected and the cycle repeated. Measurements of the insulation impedance are made at intervals of 2 minutes, capturing 720 measurements per day per sample. A photograph of the final setup is shown in Figure 5.4.

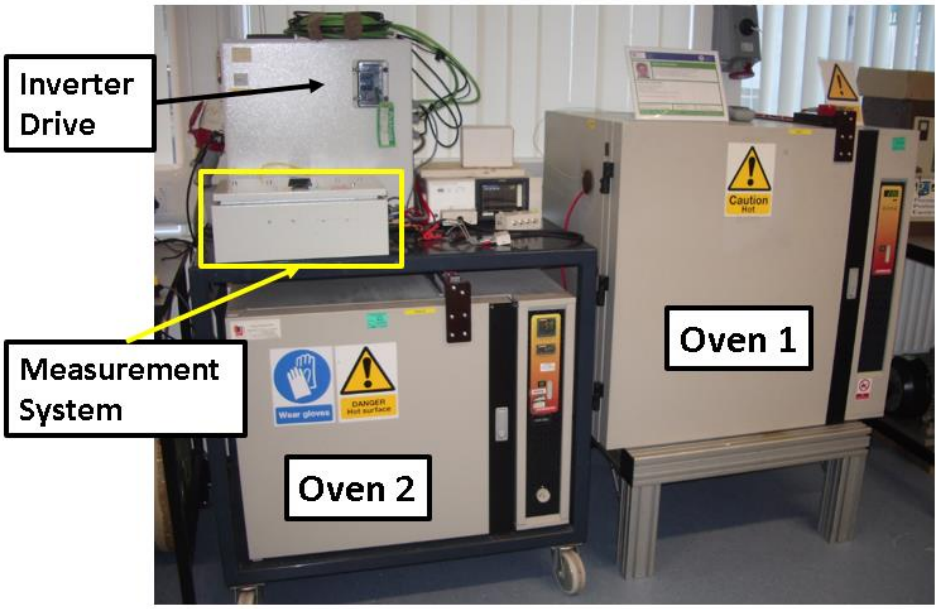

FIGURE 5.4 PHOTOGRAPH OF THE EXPERIMENT SETUP

5.2.4 Test Schedule

The time allocated initially to the experiment was 3 months to finish the accelerated lifetime test, this was then extended to 7.5 months. The temperature of the coldest sample was determined by using Equation (5.3) for Class H material with a TI of 180 degrees to break down within the allotted time. The lowest temperature sample must be no less than 200 °C to not exceed the allotted time.

It is known that insulation degradation at high temperatures may not be representative of real-world degradation and the failure times may differ from those observed in real life. IEEE 117 standard [32] for testing recommends the maximum operating temperature of no more than 250 °C for class H insulation material. The other two temperatures were assigned in 15 °C temperature steps increasing from the lowest temperature sample. The IEEE standard recommends no less than 10 °C difference between samples due to inherent variation of temperature over time inside ovens.

TABLE 5-2 TIME TO FAILURE PREDICTION OF SAMPLES VS TEMPERATURE

Sample Identifier	Temperature (deg)	Predicted Lifetime	
		Days	Weeks
1	200	208.3	30
4	215	73.6	11
2	230	26.0	4
3	250	6.5	1

The expected time to failure for all samples is shown in Table 5-2, together with sample identifiers. The sample identifiers are based on the order of test, for which the timeline is shown in Figure 5.5. Sample 1 operates continuously inside Oven 1, while all other samples expire and are replaced inside Oven 2.

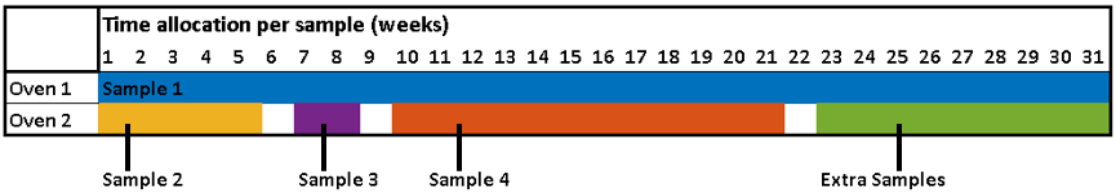

FIGURE 5.5 EXPERIMENT TEST SCHEDULE

One week overrun is allocated per sample, as well as extra time allocated inside Oven 2, to allow for retests, as implemented in testing of Sample 5 in Chapter 6. During the test it was found that Oven 1 maintained a consistent temperature overshoot throughout the test. Setting the temperature demands to 200 °C, returned an operating temperature of 203 °C. The subsequent lifetime prediction calculations account for this by using 203 °C to recalculate Sample 1 predicted lifetime.

5.3 Results and Discussion

The results section starts with a diagnosis of the sample failure mode and the measurement of the thermal index of the insulation material. The complete monitoring parameter results are presented in the following section, and the subsequent results sections discuss the observations. The last results section presents the method and implementation of a prognosis of sample lifetime and evaluates the effectiveness of said method.

5.3.1 Break-Down Mechanism

The insulation monitoring system described in Chapter 4, was designed to monitor insulation ground-wall state of health. It was expected that gradual degradation was to be observed, the progress of degradation being proportional to the oven temperature. Ideally the final failure would happen between through the ground-wall, between the phase-ground impedance, with clear pre-cursors to failure, allowing improved failure prediction.

None of the samples failed through phase-to-ground fault during the experiment. The phase inductance was measured prior to failure for the samples and compared here to the failed phase inductance to diagnose failure mode.

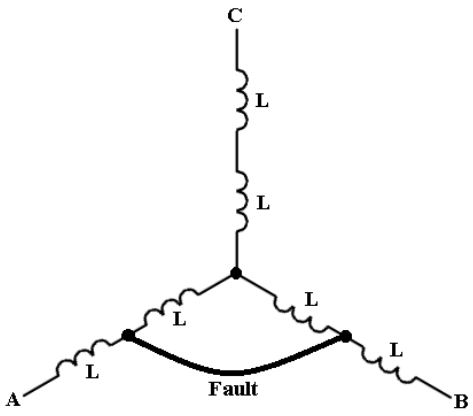

FIGURE 5.6 PHASE-PHASE FAULT VISUALISATION

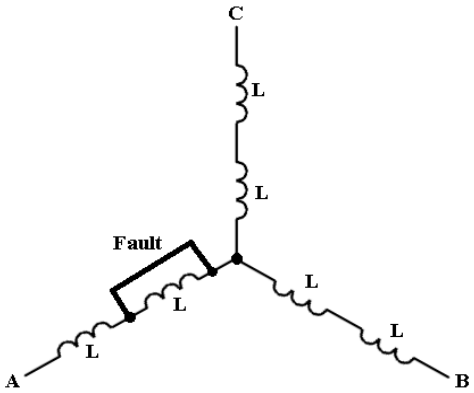

FIGURE 5.7 PHASE-NEUTRAL FAULT VISUALISATION

Two common failure modes on machines are shown in Figure 5.6 and Figure 5.7, where a connection is formed at the end of life between phase-phase and phase to neutral respectively. The two scenarios are compared to measured data. In the event of a phase-to-phase fault, it is expected that all line inductances would decrease, with the faulted phase such as A-B seen in Figure 5.6 decreasing more than the other line inductances. For a turn fault, it is expected that two measured line inductances A-B and A-C in Figure 5.7 would decrease by identical amount and C-B would remain the same as the healthy value. If the neutral is available to measure, diagnosis becomes easier as turn-turn fault would be easy to diagnose with only one phase inductance decreasing.

The healthy line inductances are shown together with results after failure for Sample 3 in Figure 5.8. At 50Hz, the healthy all three line inductances are roughly the same. After the sample has failed, phases B-C and C-A decrease, however phase A-B decreases considerably more, down from 13.8mH to 3mH, indicating clear evidence for the phase-to-phase scenario in Figure 5.6. To verify this analysis, the phase-neutral inductance is measured in Figure 5.9, phase N-C inductance remains at the same healthy value of 6.1mH, however the other two phases decrease as would be expected in the event of phase-to-phase fault.

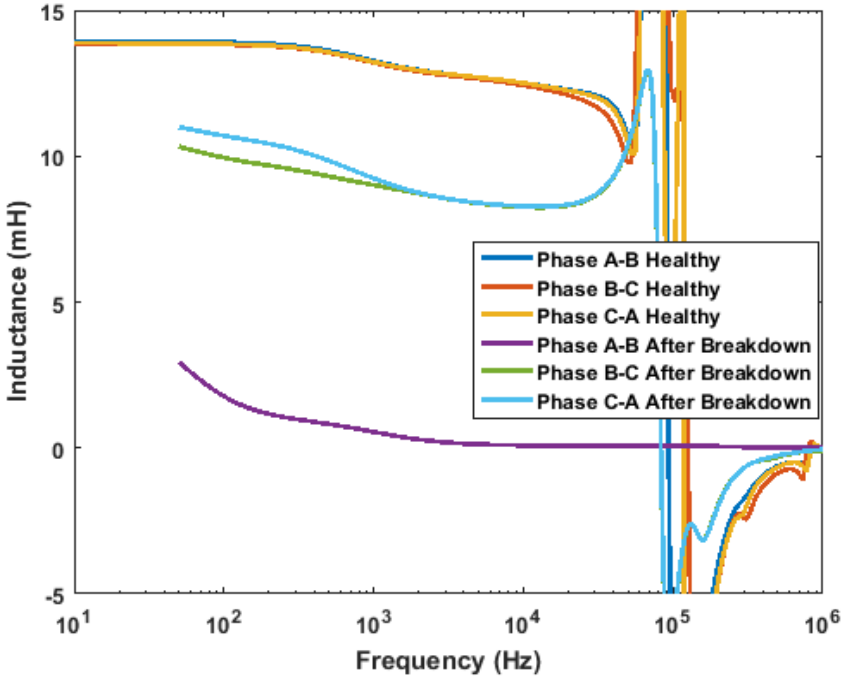

FIGURE 5.8 SAMPLE 3 LINE INDUCTANCES HEALTHY VS AFTER FAILURE

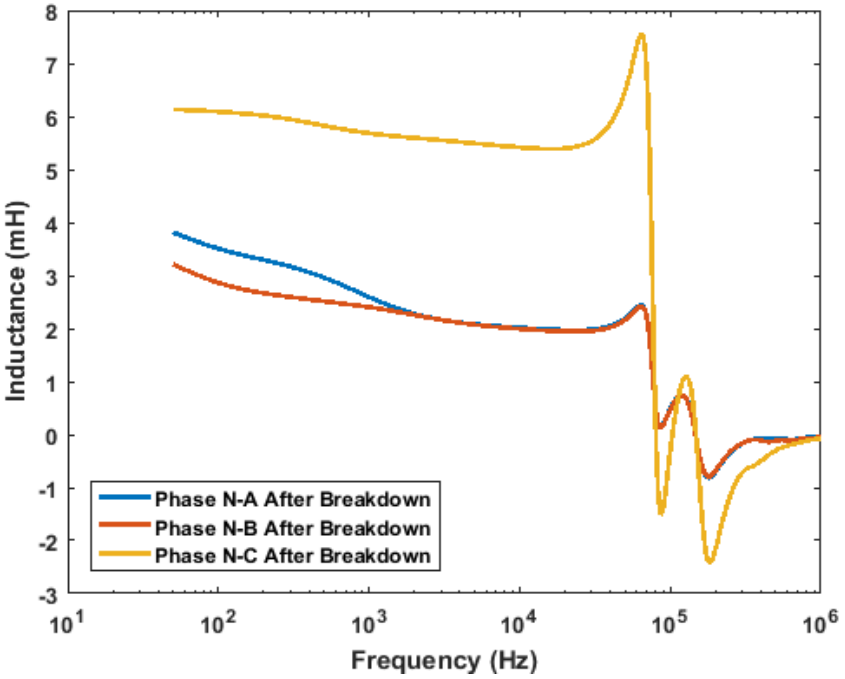

FIGURE 5.9 SAMPLE 3 PHASE TO NEUTRAL INDUCTANCES AFTER FAILURE

The difficulty with the analysis presented above is that this result is only clear for Sample 3. Samples 1 and 4 appear completely healthy when the inductance is measured using the Hioki 3570 impedance analyser, however the fault only appears when the full drive voltage is subject to the samples. The measurement of phase-neutral inductances on Sample 2 reveals that all inductances have decreased significantly, implying that multiple faults are present, therefore it is difficult to diagnose which fault occurred first and which was responsible for the final drive overcurrent that stopped the experiment.

FIGURE 5.10 SAMPLE 4 WINDINGS BEFORE TESTING

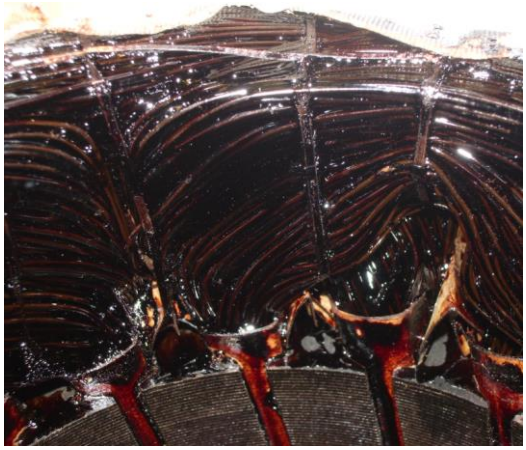

FIGURE 5.11 SAMPLE 2 AFTER FAILURE MAGNIFIED

The stator used in the experiment has a weakness particular to the machine sample used in the experiment. It can be seen in Figure 5.10 that the sample does not have phase-to-phase insulation, the full phase-to-phase voltage is therefore subjected across only the thinnest part of the insulation, the turn insulation of the wire. It can be seen in Figure 5.11 that the turn insulation reduces over time, visible as a lighter colour where it is thinner.

For inverter driven machines, the phase-to-phase voltage is the full DC bus voltage, 600V for this experiment. It makes sense therefore that in this experiment, the weakest part of the insulation, subject to the largest stress, the phase-to-phase turn insulation fails first. The failure times of this experiment therefore represent the strength of the wire insulation used in the samples.

5.3.2 Failure Times

The times of failure between those expected in Section 5.2.4 and the final lifetimes observed are compared in Table 5-3. The lifetime halving is also stated for each measurement. It was found that Samples 1, 4 and 2 conform the closest to the expected value of lifetime. Taking the average value for the halving coefficient, the rule of thumb can be confirmed as valid, to calculate the expected lifetime of insulation.

TABLE 5-3 PREDICTED LIFE VS FAILURE TIME

Sample Identifier	Temperature	Overal Lifetime (days)		Lifetime Halving Coeffient (k)
		Expected	Actual	
1	203	169.2	159.8	9.65
4	215	73.7	83.4	10.54
2	230	26.0	25.2	9.91
3	250	6.5	12.5	11.56
			Average	10.67

IEEE standard 117 [32] is used to calculate the temperature index of the material, as measured in the experiment. The time of failure are plotted on an Arrhenius plot in Figure 5.12. The X axis on an Arrhenius plot represents the absolute temperature -1/(T °C +273), labelled here with the corresponding temperature in °C, the Y axis log scale returns the number of hours of operation. It is expected that for Class H material, the fitted extrapolated straight line must go through 20,000 hours of operation at 180°C temperature.

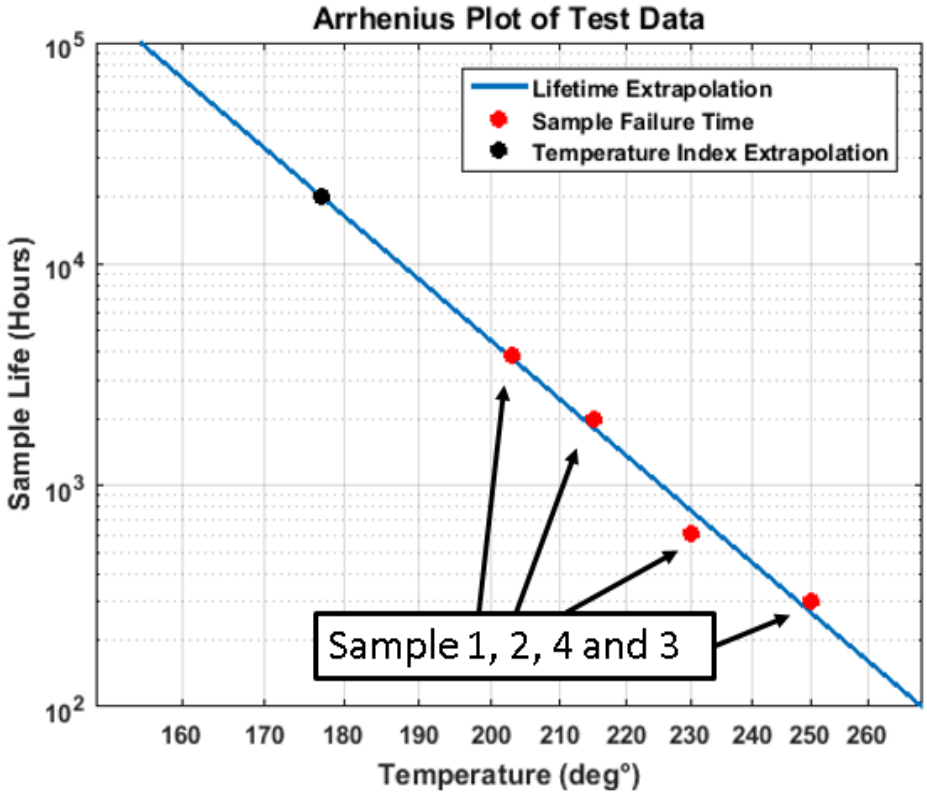

FIGURE 5.12 ARRHENIUS PLOT OF SAMPLE FAILURE TIMES

In Figure 5.12, the measured temperature index of the material is measured at 178 °C. The failure times indicate therefore that the samples tested using the specified methodology well represent class H insulation.

$$L = L_0 e^{\frac{E_a}{R}\left(\frac{1}{T}-\frac{1}{T_0}\right)} \quad (5.4)$$

The justification for using the rule of thumb for expected lifetime is explored in Figure 5.13. The expected lifetime from the Q10 rule of thumb is plotted alongside the measured data, and the lifetime as calculated by Equation (5.4), using the assumption that lifetime halves for every 10°C, near 180°C to calculate the E_a value. The Ea value calculated using this assumption is 121kJ, with the straight line fit of the sample failure data returning Ea value of 123 kJ and other measurements in literature giving Ea value of 119kJ [33].

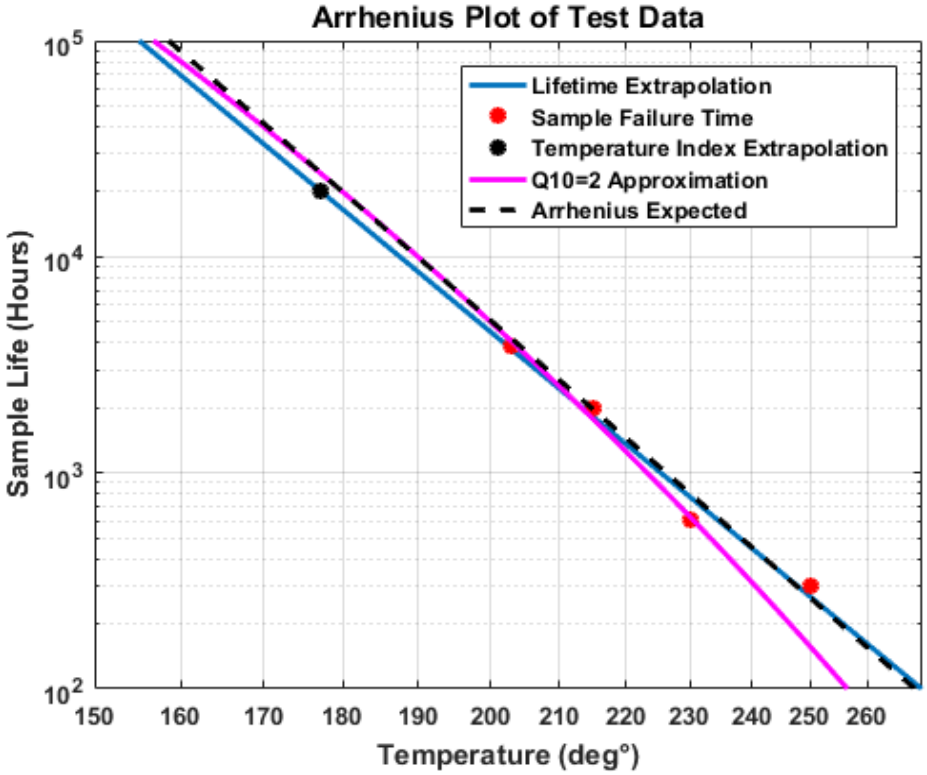

FIGURE 5.13 ARRHENIUS PLOT COMPARISON

The Q10 line correctly tracks the Arrhenius expected lifeline at and near the 180°C, however it underestimates the lifetime at temperatures below and above. The approximation works because although the Arrhenius X axis is given as 1/T, because the absolute temperature is high, the temperature approximates a linear scale. Because the Q10 rule of thumb can only underestimates the lifetime, the error is not critical, as this can be considered as an extra safety factor during machine design.

5.3.3 Raw Results Overview

The following section contains the Ceq, Req and resonance characteristics results as measured over the lifetime of the four test samples. The results are presented together to allow easy comparison between samples. The similarities and differences between parameter trajectories are noted and are to be elaborated on in the following sections. References to these main results will be made by the sections dealing with detailed analysis, with further supporting evidence presented.

Model Fitted C_{eq} Results

The C_{eq} Parameter presented in this section returns the total capacitance of the given sample over time. To obtain C_{eq}, measured impedance data over time is processed as described in Chapter 4. The model in Figure 3.11 is populated and the sum of C_{sf} and C_{sf0} values are used to represent the total capacitance value.

The low frequency capacitance was defined as the first four harmonics, between 6 to 72 kHz, the high frequency capacitance was defined between 360 to 720 kHz for the samples tested. The frequencies between 72 to 360 kHz are defined as the medium frequency, used to extract the resonance frequencies and the R_{swh} value. Contrary to results in Chapter 4, the even sideband harmonics are not used in this experiment.

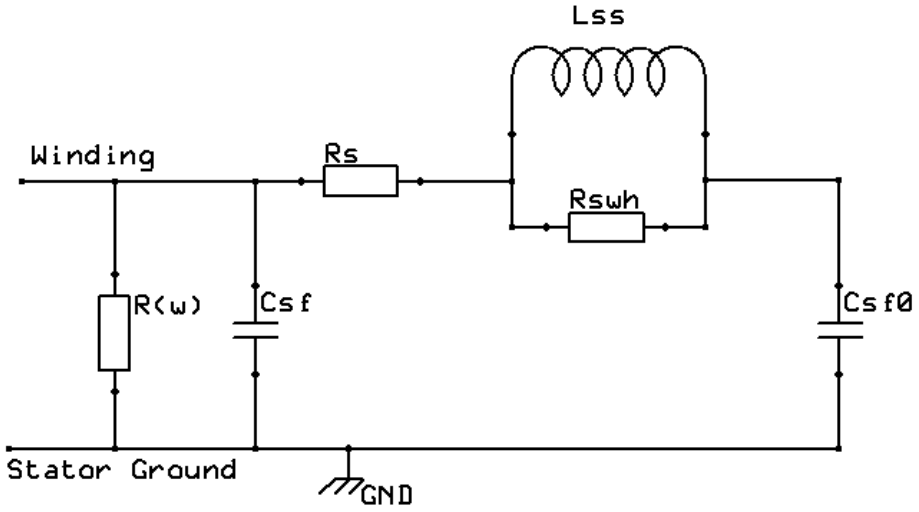

FIGURE 5.14 UNIVERSITY OF SHEFFIELD INSULATION MODEL

The C_{eq} value uses the average value of capacitance measured at the first four harmonics which define the low frequency capacitance. The C_{eq} value is equal to that as obtained if one were to measure the capacitance at a single frequency as is shown in Chapter 3. As shown in Appendix C, the use of multiple harmonics can significantly improve the accuracy of the measurement, surpassing single harmonic detection, by treating each harmonic as a separate signal, with its own random noise figure with a Gaussian distribution.

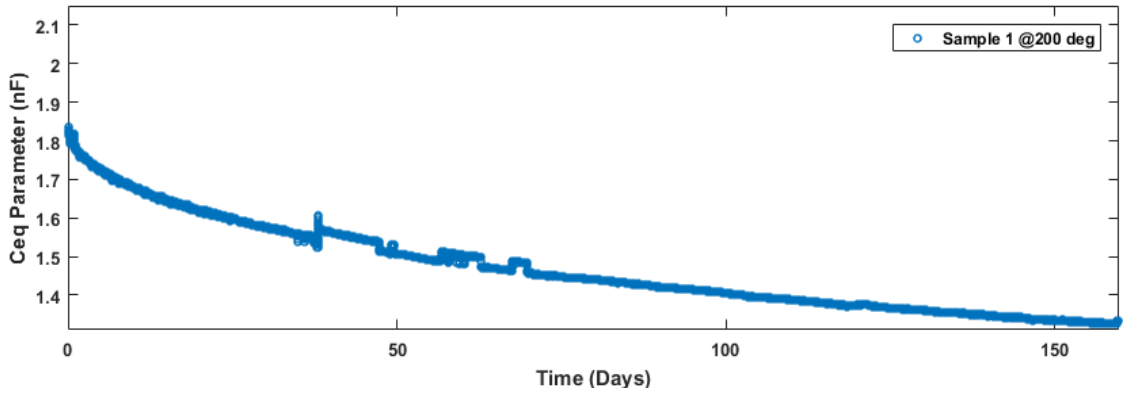

FIGURE 5.15 SAMPLE 1 CEQ PLOT OVER TIME

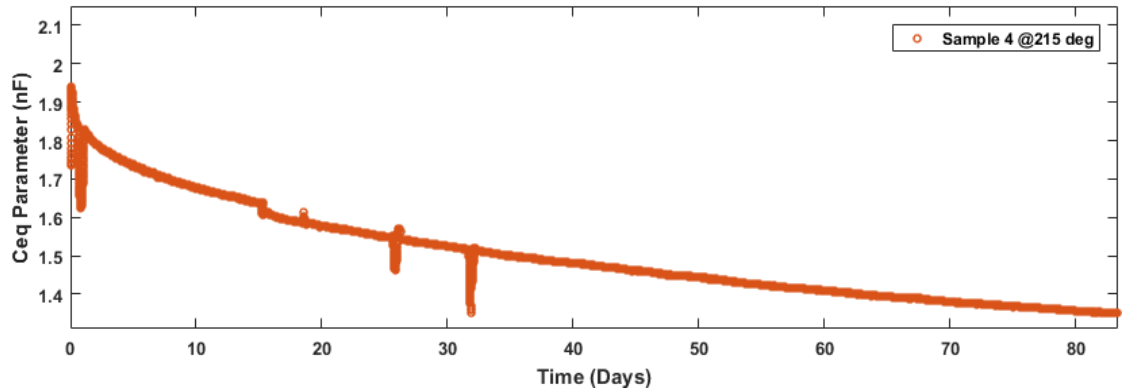

FIGURE 5.16 SAMPLE 4 CEQ PLOT OVER TIME

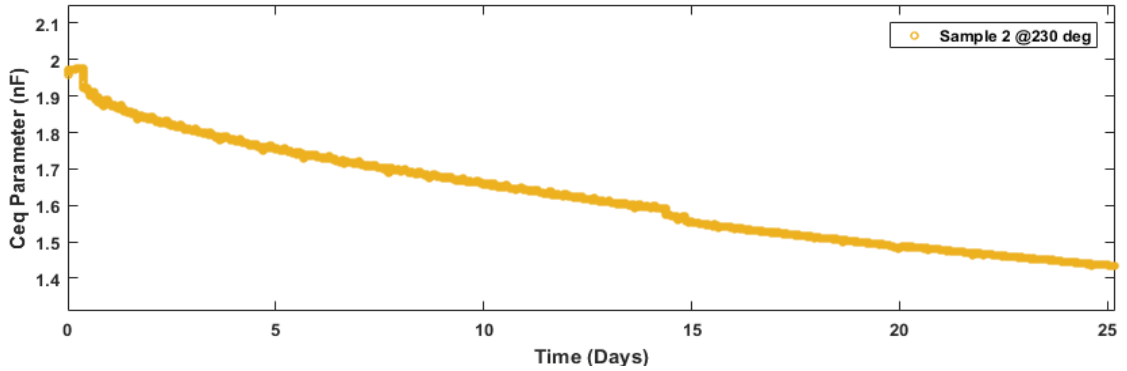

FIGURE 5.17 SAMPLE 2 CEQ PLOT OVER TIME

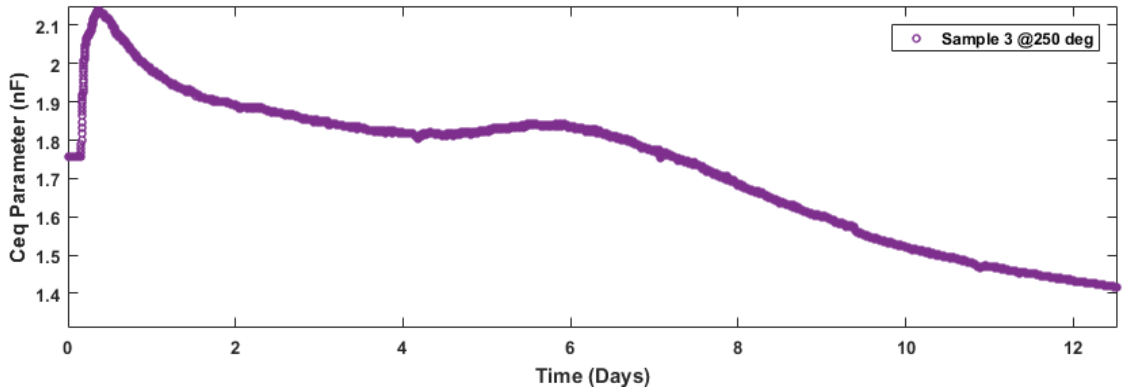

FIGURE 5.18 SAMPLE 3 CEQ PLOT OVER TIME

Ceq for al samples are shown in Figure 5.15, Figure 5.16, Figure 5.17 and Figure 5.18 for samples 1, 4, 2 and 3 respectively. The order is such that the samples are presented in order of increasing temperature. The Ceq results are plotted on an absolute scale, with identical scales on the 'y' axis. The 'x' axis range presents the full experimental timescale, which varies for each sample.

Ceq results presented share several key similarities and differences. Similarities between samples are expected due to the same ageing process acting on the samples, subjected to the ageing in using the same method. The differences are important to analyse, as the emerging field of real-time study of insulation health does not have enough data to build a precedent. The differing responses are noted here, with follow up sections exploring these in detail.

Similarities:

1. All samples show decreased Ceq from maximum starting value, to the end of lifetime.
2. Samples 1, 4 and 2 show clear exponential decrease over time. Sample 3 at 250 °C also shows this initially, however the response veers away from the pattern between days 5 to 7.
3. All samples contain at least one rapid Ceq decrease discontinuity. Possible causes of this phenomenon are explored in Section 5.3.6
4. When one takes the normalised Ceq value to the starting point, for all samples, the degradation rate is highly dependent on the operating temperature, and therefore on the ageing rate.
5. The normalised values also reveal the consistency in Ceq value at the point of sample failure. This threshold value as well as the rate property in '4' are used in Section 5.3.9 to create a framework where the remaining sample lifetime can be determined

Differences:

1. Sample 1 has a distinct Ceq increase discontinuity on day 38 of the experiment. The test was paused due to laboratory relocation. The sample was removed from the oven and remained unpowered for 2 months. The implication for monitoring and prognosis of these types of events are explored in Section 5.3.4
2. The gradual increase of Ceq in Sample 3 observed at day 5 does not occur in other samples. The dissipation information is used to diagnose the possible cause of this event in Section 5.3.8

Model Fitted Req Results

The Rω parameter data is fitted to a straight line y=m*x+c plot at low frequencies on a frequency vs Req log-log plot, as described in Section 3.3, where x and y denote log(f) and log(R) respectively. The data is presented as the 'm' and 'c' parameter variations with time for all Samples. The 'c' parameter effectively shows the dielectric dissipation over time. The 'm' parameter for Rω shows the characteristic of dissipation.

The 'm' parameters are shown in Figure 5.19, Figure 5.20, Figure 5.21 and Figure 5.22 for Samples 1, 4, 2 and 3 respectively, while the 'c' parameters are shown in Figure 5.23, Figure 5.24, Figure 5.25 and Figure 5.26 for Samples 1, 4 2 and 3 respectively, in order of increasing sample temperature.

The dissipation results are more contentious than Ceq data, as the accuracy is inherently lower and there is less literature dealing with dissipation progression over time. The following similarities and differences have been observed.

Similarities:

1. All sample "c" parameters increase towards the end of lifetime, showing decreased dissipation at the later stages of lifetime. Attempts to use this characteristic for prognosis are discussed in Section 5.3.7.
2. Samples 1, 3 and 4 contain clear discontinuities, corresponding to the dates of increase in C_{eq} data.
3. Samples 1, 3 and 4 all exhibit times when the dissipation value returns to its value prior to the discontinuity. The phenomenon is most clearly visible in Sample 1 between days 55 to 72. This is explored in Section 5.3.6.
4. The 'c' parameter for all samples increased initially, until the sample reached its test temperature. This was followed by a decrease in the parameter until discontinuity for all samples except sample 1. The dissipation characteristic changes over time for all samples, this is further explored in Section 5.3.8

Differences

1. Sample 3 experiences a slow ramping increase in the 'c' parameter on day 5, followed by a slow ramp down starting on day 5, reversing again to increase on day 9, until breakdown. The diagnosis of Sample 3 behaviour is explored in Section 5.3.8, where dissipation data, Ceq and resonance parameters are used together to explore the degradation mode.
2. Rates of change of Req are not proportional to temperature. Sample 4 increases very little at the end of its life compared to Sample 1, despite operating at a higher temperature. The effect on possible prognosis using dissipation is explored in Section 5.3.7

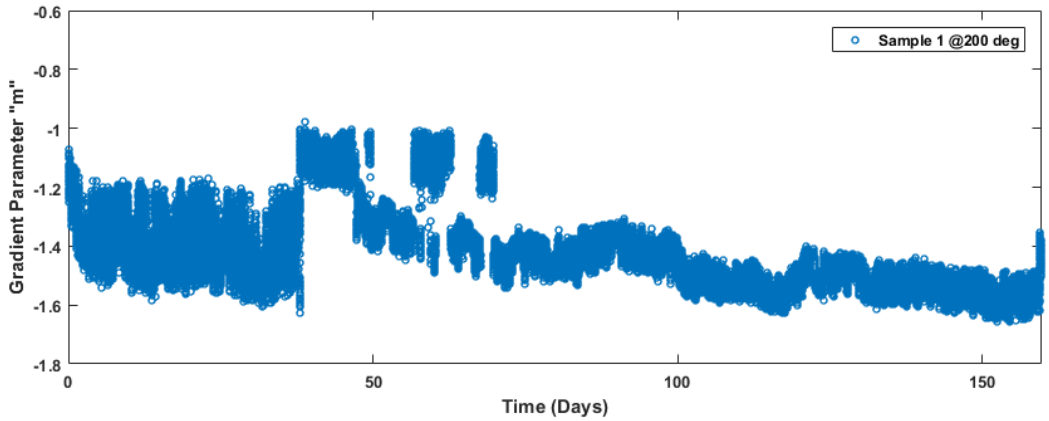

FIGURE 5.19 SAMPLE 1 REQ GRADIENT PARAMETER "M" PLOT OVER TIME

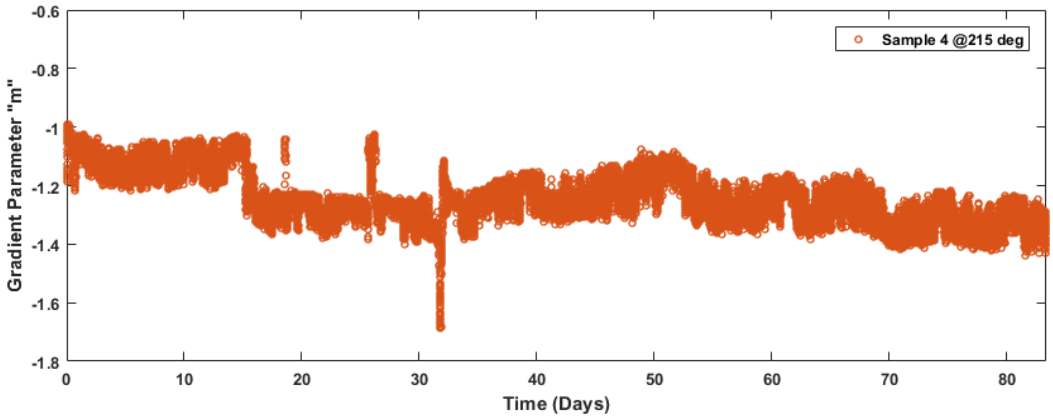

FIGURE 5.20 SAMPLE 4 REQ GRADIENT PARAMETER "M" PLOT OVER TIME

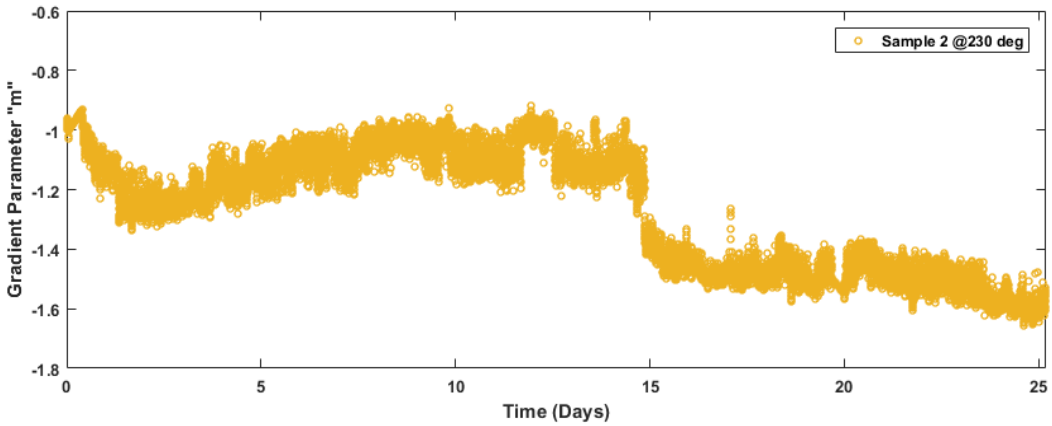

FIGURE 5.21 SAMPLE 2 REQ GRADIENT PARAMETER "M" PLOT OVER TIME

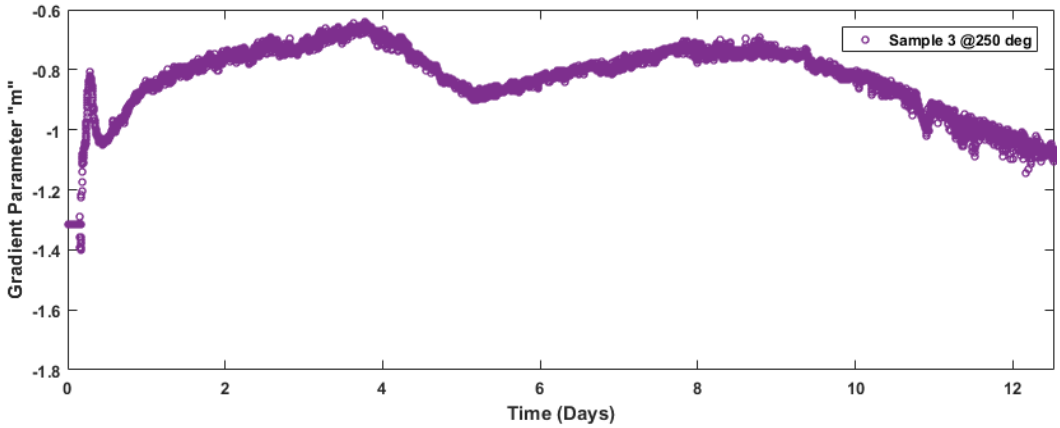

FIGURE 5.22 SAMPLE 3 REQ GRADIENT PARAMETER "M" PLOT OVER TIME

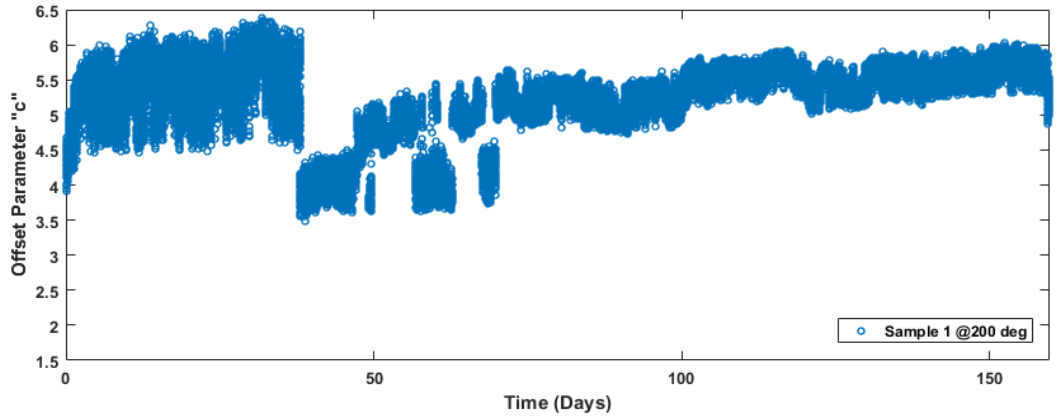

FIGURE 5.23 SAMPLE 1 REQ OFFSET PARAMETER "C" PLOT OVER TIME

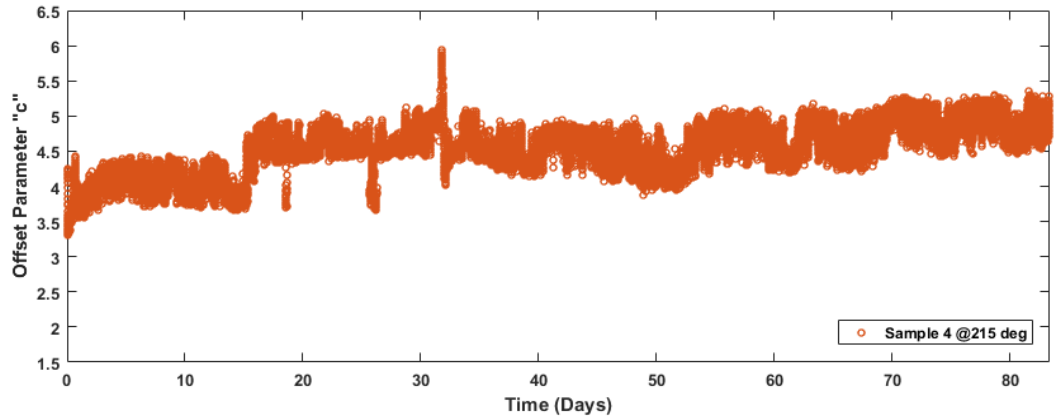

FIGURE 5.24 SAMPLE 4 REQ OFFSET PARAMETER "C" PLOT OVER TIME

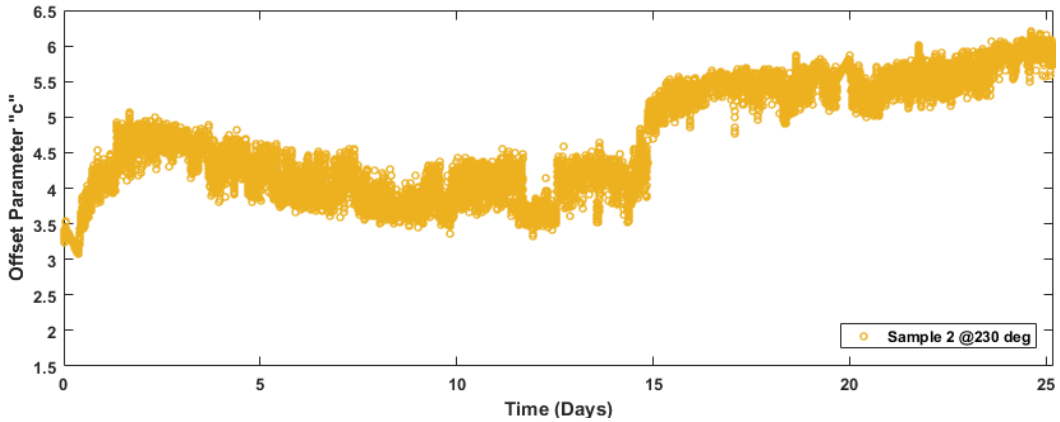

FIGURE 5.25 SAMPLE 2 REQ OFFSET PARAMETER "C" PLOT OVER TIME

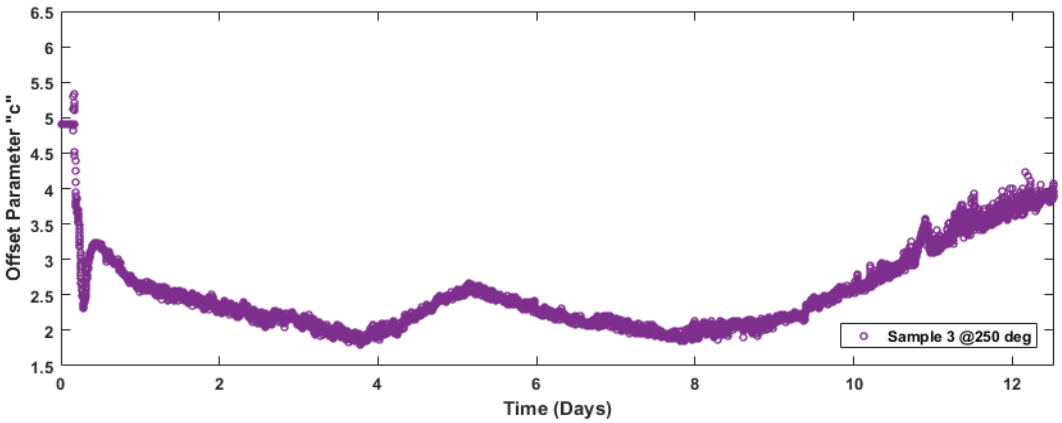

FIGURE 5.26 SAMPLE 3 REQ OFFSET PARAMETER "C" PLOT OVER TIME

Dissipation Factor Results

In Chapter 3, the nature of dielectric dissipation is explored, and it is evident both from literature and practical measurement that dielectric dissipation increases with frequency. It was decided to add a dielectric dissipative term R_ω to represent the dissipation of the dielectric as represented by Equation (5.5).

$$R_\omega = \frac{1}{\omega k \varepsilon_r''} \tag{5.5}$$

$$R_{(f)} = 10^c * f^m \tag{5.6}$$

$$\tan \delta_{(50Hz)} = 100 * \frac{1}{2\pi * 50 * C_{(50Hz)} * R_{(50Hz)}} \tag{5.7}$$

Measuring the R_{eq} figure at several frequencies where the dielectric dissipation, rather than resonance dominates the R_{eq} value, allows tracking of the dissipation line, as expressed in the 'm' and 'c' parameters shown previously. Using the 'm' and 'c' parameters, one can therefore calculate the equivalent resistance at any frequency, using Equation (5.6). As was shown in Chapter 3, the capacitance is a constant at frequencies below machine resonance. As such it is possible to measure the dissipation, at 50Hz, using Equation (5.7) where the dissipation current is represented as a percentage of capacitive current.

The results presented here show the dissipation as it would have been measured by offline dissipation factor measurement. Observing the change of dissipation over time reveals some trends which are not immediately obvious when viewing raw data due to change of capacitance present. The major observations are as follows:

1. Dissipation decreases at the end of lifetime for all samples. This was not expected as oxidation was expected to be the main degradation mechanism, increasing dissipation over time
2. Samples 1, 4 and 2 have a similar amount of dissipation, however Sample 3 has considerably larger dissipation at some points in its life. The 'y' scale has been adjusted for Sample 3 in Figure 5.30 to reflect this.
3. The discontinuities observed in the small Ceq drop and the Req results are again observed in the dissipation characteristic.
4. Dissipation initially starts from a high point falling to a low value after the first day or 2 of the experiment for all samples, this is observed in literature during curing of the insulation impregnation.

The dissipation data is used mostly in Section 5.3.8 for diagnosis of Sample 3, as well as diagnosing the final mode of failure for other samples. The dissipation data underlines how different the trajectory of Sample 3 life was, compared to other samples, despite the expected time of failure.

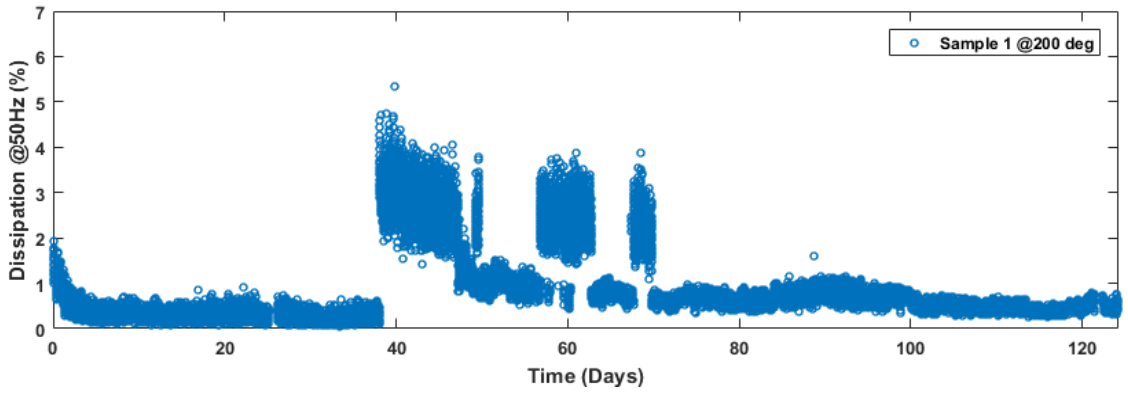

FIGURE 5.27 SAMPLE 1 DISSIPATION FACTOR OVER TIME

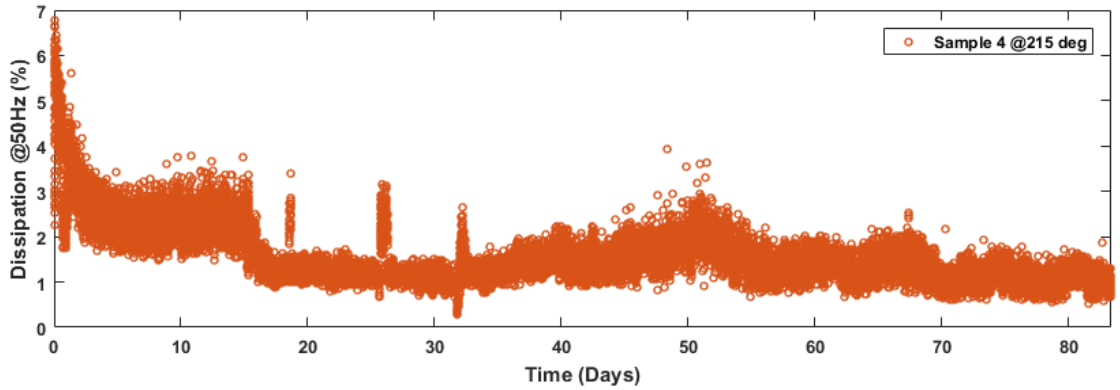

FIGURE 5.28 SAMPLE 4 DISSIPATION FACTOR OVER TIME

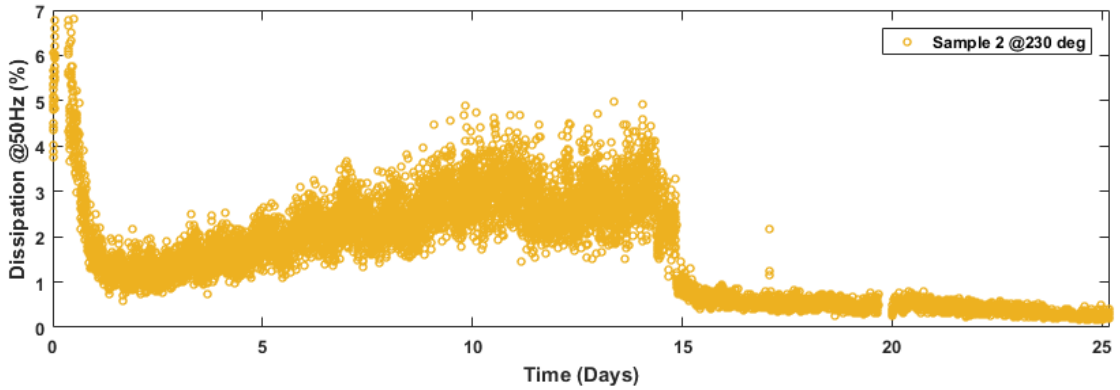

FIGURE 5.29 SAMPLE 2 DISSIPATION FACTOR OVER TIME

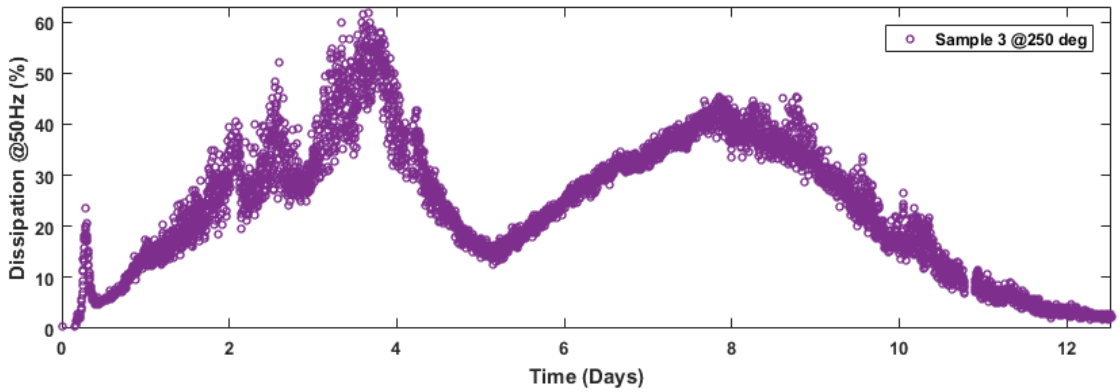

FIGURE 5.30 SAMPLE 3 DISSIPATION FACTOR OVER TIME

C_{sf} and C_{sf0} Parameter Results

Discontinuities have been observed both in the Ceq data and the Req data. To diagnose the behaviour changes, the difference between the high frequency and low frequency response is shown using the Csf and Csf0 parameters. The relationship between capacitance across the frequency range and the parameters is shown in Figure 5.31.

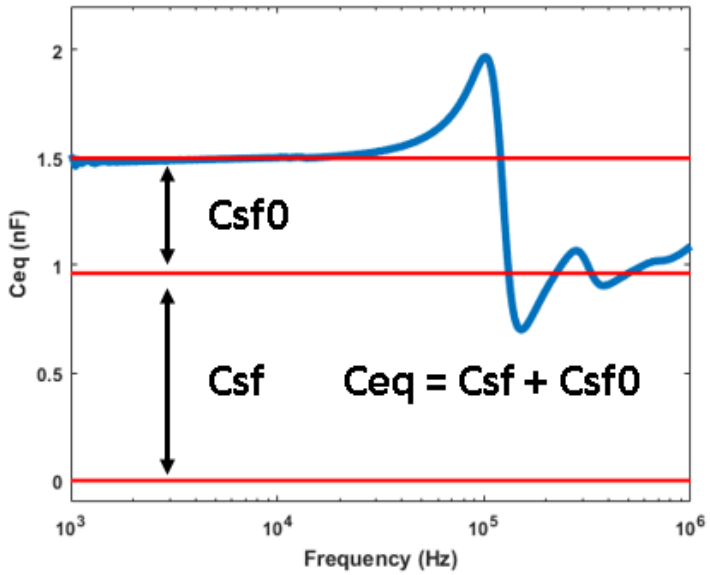

FIGURE 5.31 CSF AND CSF0 RELATIONSHIP TO CAPACITANCE

Similarities:

1. All Csf and Csf0 parameters decrease at the start of lifetime, corresponding to the exponential decrease seen in Ceq results
2. The small drop of Ceq observed earlier is greatly emphasized in the Csf parameter, the change in Sample 3 is now clearly visible on day 9.4
3. The Csf0 results mirror the change in Csf at the discontinuities. This means that the overall Ceq remains almost the same, however the high frequency behaviour changes.
4. The return of parameters back to previous trend as seen best in sample 1 is clearly emphasized in the Csf and Csf0 parameters. This information is used in Section 5.3.6 to detect the change in insulation behaviour.

Differences:

1. Sample 3 Csf trend does not change between days 5-7. The Ceq increase comes entirely from Csf0. This means that the capacitance change behaviour occurs at low frequency.
2. Samples 1, 2 and 3 appear to show a precursor to failure at the end of the sample lifetimes not seen in the Ceq results. This feature is explored in Section 5.3.5

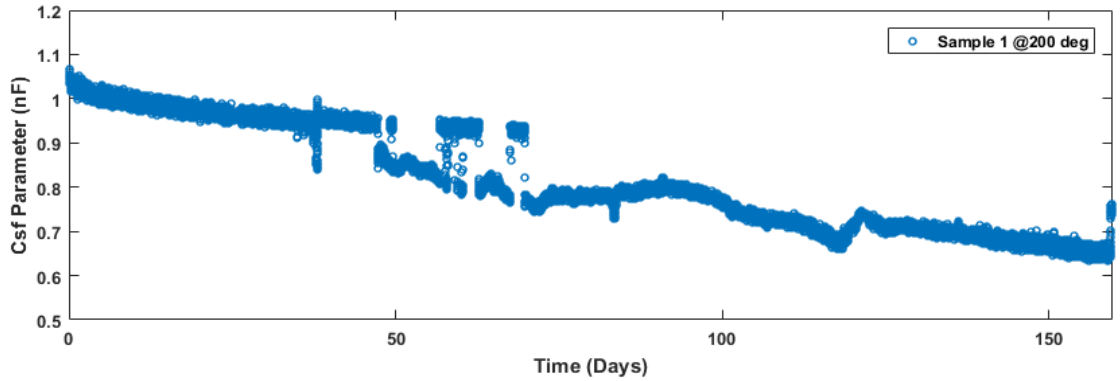

FIGURE 5.32 SAMPLE 1 CSF PARAMETER PLOT OVER TIME

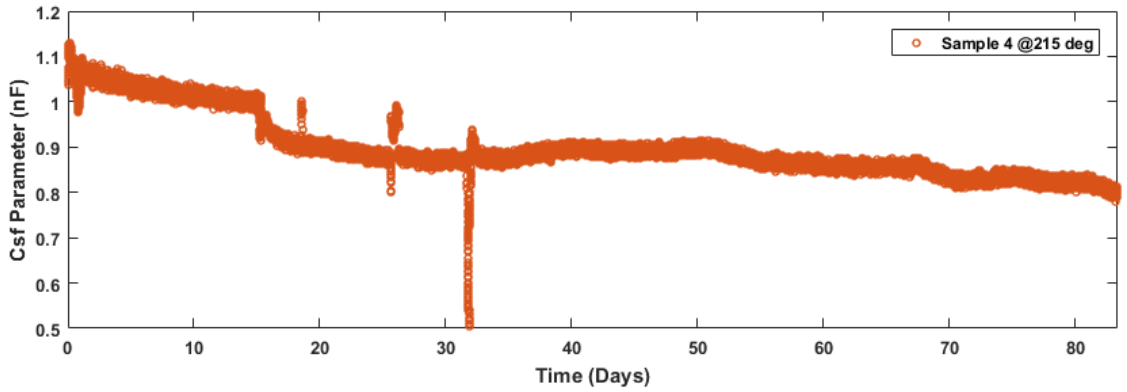

FIGURE 5.33 SAMPLE 4 CSF PARAMETER PLOT OVER TIME

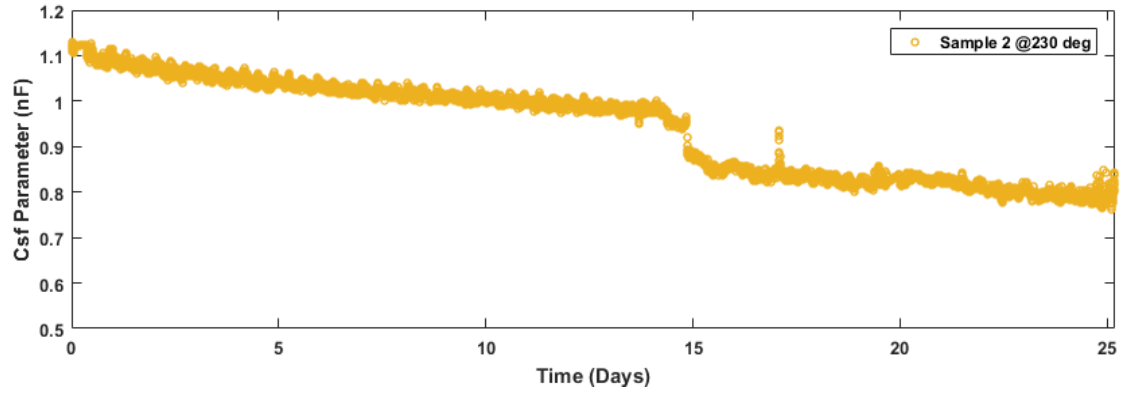

FIGURE 5.34 SAMPLE 2 CSF PARAMETER PLOT OVER TIME

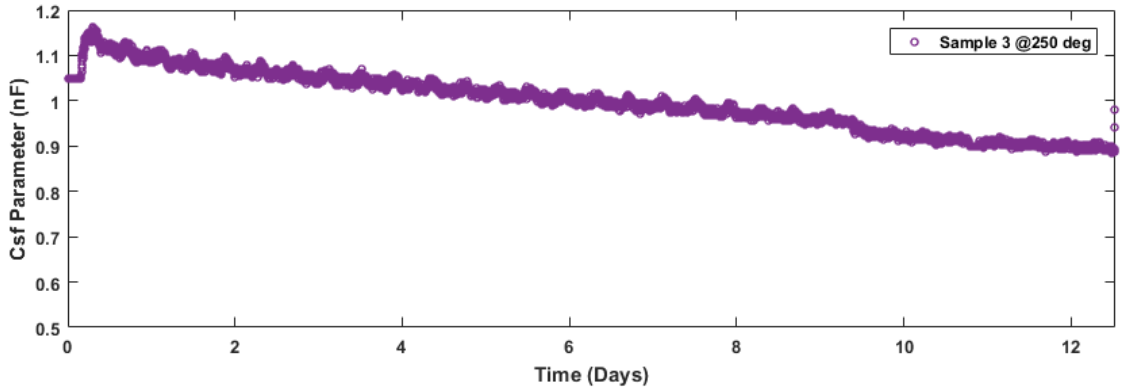

FIGURE 5.35 SAMPLE 3 CSF PARAMETER PLOT OVER TIME

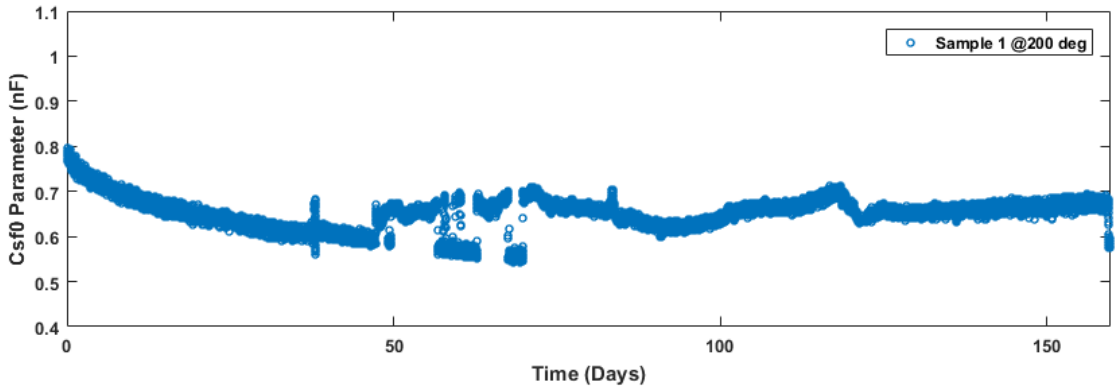

FIGURE 5.36 SAMPLE 1 CSF0 PARAMETER PLOT OVER TIME

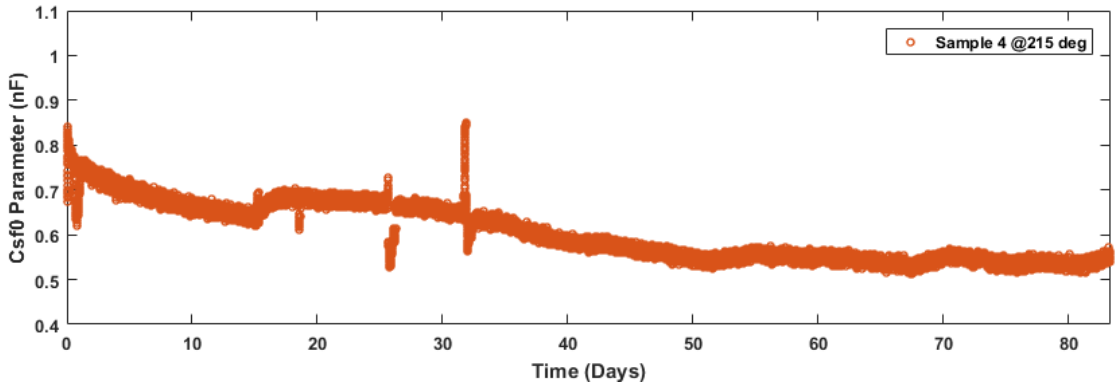

FIGURE 5.37 SAMPLE 4 CSF0 PARAMETER PLOT OVER TIME

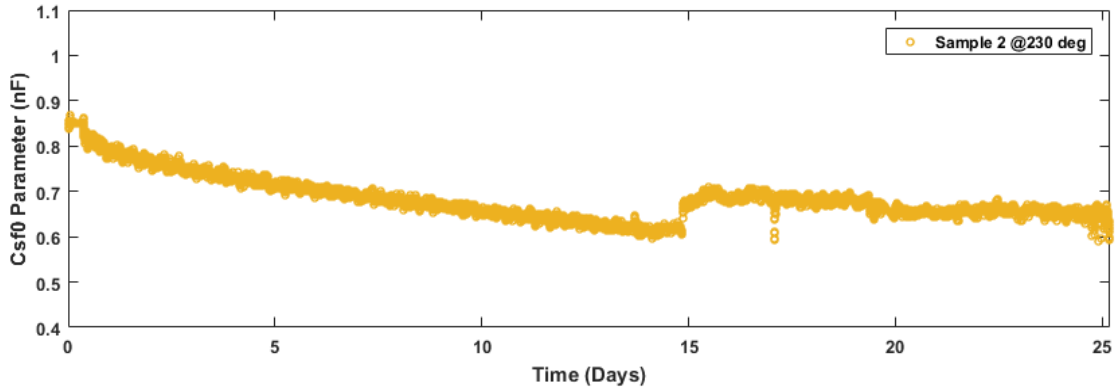

FIGURE 5.38 SAMPLE 2 CSF0 PARAMETER PLOT OVER TIME

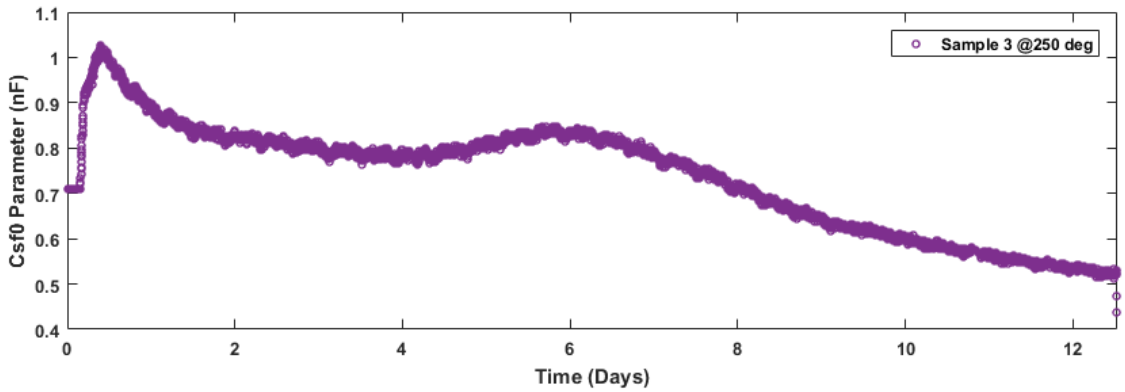

FIGURE 5.39 SAMPLE 3 CSF0 PARAMETER PLOT OVER TIME

5.3.4 Sample 1 Discontinuity

On day 38 of the experiment, it was necessary to remove Sample 1 from its oven and pause the experiment in order to relocate to a new laboratory. The move required two months of downtime, with Sample 1 left in a storage crate for the duration. It was expected that the experiment could be resumed at the new location with parameters returning to their previous state. As it turned out, this was not the case.

After the move, it was found that the Ceq value increased by 1.5%, as highlighted in Figure 5.40 and the dissipation increased from 0.5% up to 3%. As seen in Figure 5.41, the progression in both parameters continued at the same rate.

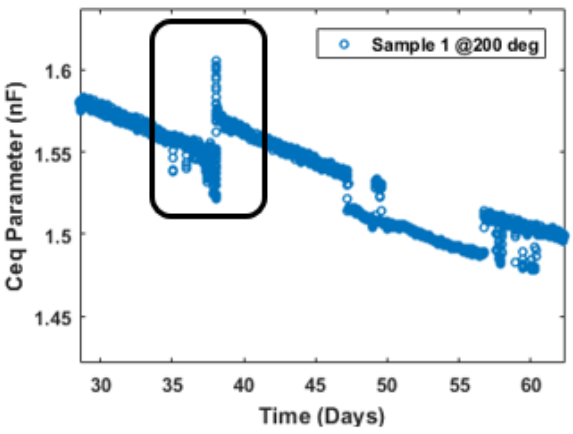

FIGURE 5.40 SAMPLE 1 CEQ AT THE DISCONTINUITY

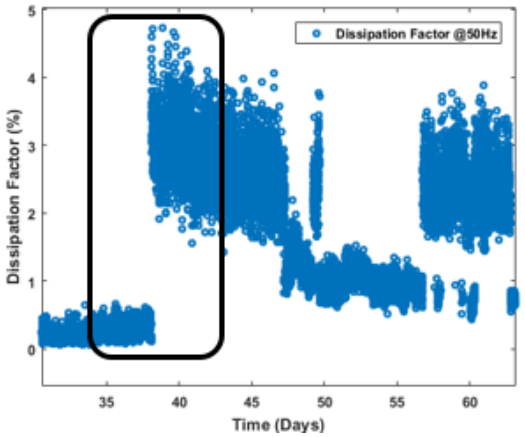

FIGURE 5.41 SAMPLE 1 DIELECTRIC DISSIPATION DURING DISCONTINUITY

It was initially suspected that because the Ceq value returns to the value prior to test on day 47, the discontinuity was due to a resonance change of the winding. This however is not the case, as shown in Figure 5.42 in the Csf0 value. On day 38 there is a transient, however the Csf0 value quickly returns to its previous value. Changes in resonance occurs on day 47 as is shown by the large jumps and temporary return to previous trend in Figure 5.42.

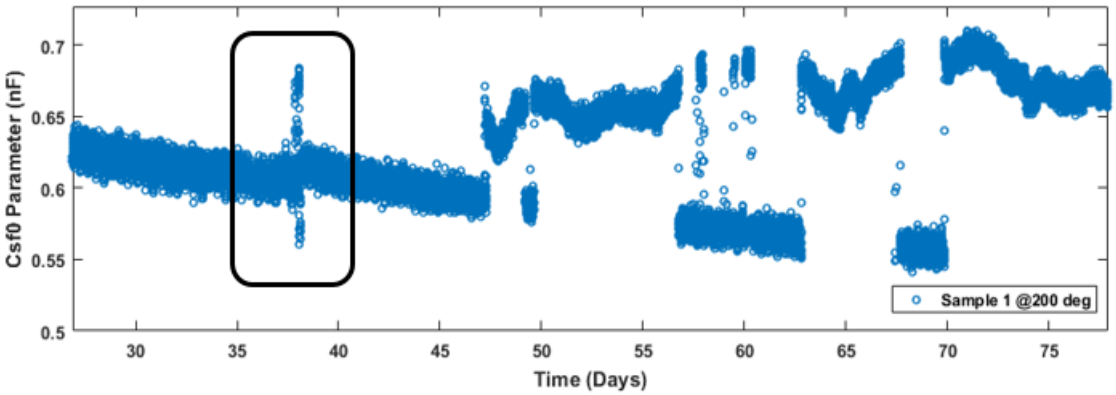

FIGURE 5.42 SAMPLE 1 C_{SF0} PARAMETER DURING DISCONTINUITY

Using literature review from Chapter 3, the measured capacitance and dissipation rise can arise from two known sources, moisture ingress or contamination. It is possible that the end-windings of the machine might be coated with a conductive surface of dust, increasing capacitance with increased surface area and increasing dissipation through an easier path of energy dissipation.

Contamination in this case however is unlikely, as the sample was stored in a sealed container throughout the laboratory move, and never exposed to hostile conditions. Moisture is equally unlikely as the effect of moisture ingress is only temporary until the water can dry out. It is shown in a practical investigation in Section 6.1 that Ceq should return to normal within 6 hours of operation at low humidity. Both the chemical degradation mechanisms that are investigated in Chapter 3 decrease Ceq slowly over time. Hence they would not be responsible for the observed Ceq increase.

For the anomaly observed, it is possible to rule out which mechanisms cannot be responsible for the change. The anomaly itself is far larger than the sensor deviation measured in Chapter 3, and is also measured by the off-line Hioki instrument as can be seen in Figure 5.49. Contamination, moisture ingress, resonance parameter change and the two known chemical degradation methods oxidation and cross-linking have been ruled out as possible causes of the anomaly. Because resonance parameters do not change significantly over the anomaly, mechanical change is ruled out as the cause.

The cause of the change must be chemical changes in the material. As extreme events such as that subjected to Sample 1 of complete cold stoppage and hot restart are seldom seen in normal operation, the effects of this have not been detailed in literature. An experiment may be designed for future work where a sample is aged at temperature, with a regular removal of the sample to ambient. Testing with daily removal cycles at relatively low temperature, 150 °C for class H material for example, would be required to determine if the observed effect presents itself in ordinary operating conditions. Further knowledge of chemistry and chemical degradation of polymers under unusual conditions is required to fully diagnose this problem.

5.3.5 Pre-Cursor Possibility

One of the initial aims of the experiment was to observe any anomalies towards the end of sample lifetime. Close inspection of Samples 1, 2 and 3 show a significant change in the C_{sf} and C_{sf0} parameters. Figure 5.43, Figure 5.44, Figure 5.45 and Figure 5.46 show the C_{sf0} parameter recorded on the last day of experiment for Samples 1, 4, 2 and 3 respectively, in order of increasing temperature.

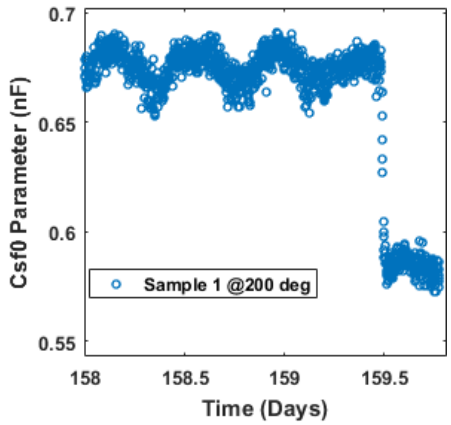

FIGURE 5.43 SAMPLE 1 LAST DAY CSF0

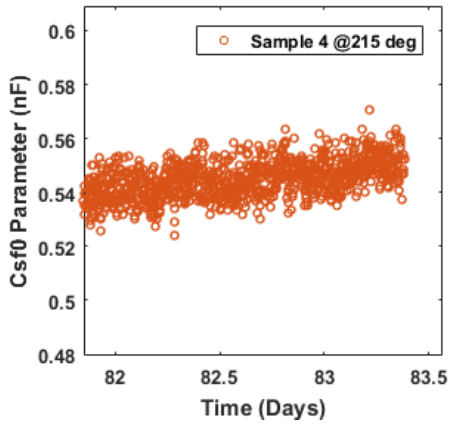

FIGURE 5.44 SAMPLE 4 LAST DAY CSF0

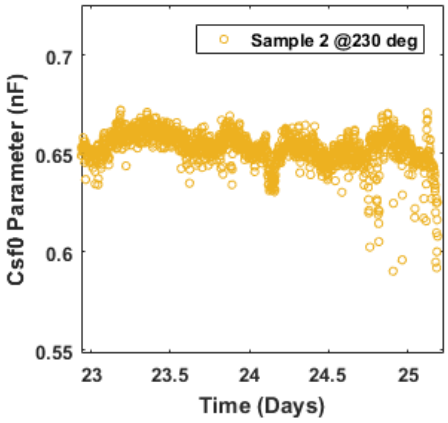

FIGURE 5.45 SAMPLE 2 LAST DAY CSF0

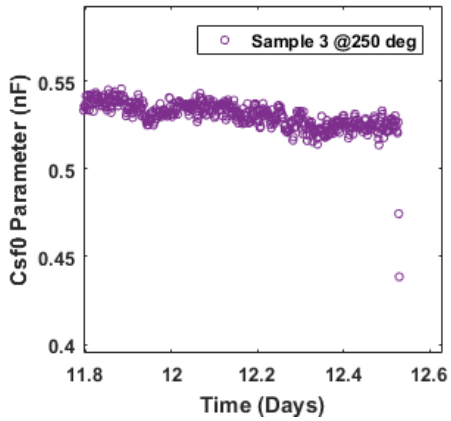

FIGURE 5.46 SAMPLE 3 LAST DAY CSF0

A sharp decrease of Csf0 can be seen most clearly in Sample 1, however many points are also visible with a similar magnitude decrease in Sample 2, Sample 3 only has two points showing the decrease before sample breakdown which does not allow a conclusive decision of the decrease. Sample 4 does not show any points of decrease. The same decrease of Csf0 parameter has been observed in Samples 1 and 2 earlier in their lifetimes, disallowing this step change to be used as a pre-fault indicator.

5.3.6 C_{eq} Decrease Discontinuity

An interesting feature present in all four samples appears as a small decrease of Ceq value. The decrease as seen in the raw results Section 5.3.3 is small compared to the overall trend, however it appears suddenly and is measurable only by using the on-line monitoring equipment. The discontinuity is greatly magnified in the resonance parameters. The possible causes for these events are investigated in this section.

TABLE 5-4 C_{EQ} DECREASE ANOMALY FIGURES

Sample Identifier	Temperature	Sample Lifetime	Day of Anomaly	Life % @Anomaly	Ceq Decrease
1	203	159.8	47.3	29.6%	1.30%
4	215	83.4	15.4	18.4%	1.70%
2	230	25.2	14.4	57.1%	2.00%
3	250	12.5	9.4	75.0%	0.70%

The Ceq decrease observed is stated in Table 5-4, where the decrease ranged from a maximum of 2% in Sample 2, down to 0.7% in Sample 3. The test continued after this observation, and the Ceq trends continued as before, except with an offset. The anomaly appears to have no relation to the sample lifetime, as it appears anywhere between 18% into the life of the sample to 75%, with no relation to operational temperature.

Although the overall Ceq change is small, it can be seen that C_{sf}, C_{sf0} and dissipation parameters change considerably after the anomaly. It was suspected that the stators underwent either an inter-turn or inter-phase fault, however further investigation showed that this could not have been the case. Evidence is presented here to rule out possible causes for the observations and discussion is opened to explore possible explanations.

Catastrophic Fault Investigation

In Section 5.3.1, the final failure mode is diagnosed using phase inductance measurement. For Sample 3, three different line inductance measurements were taken, before the anomaly, after the anomaly and after final breakdown. In Section 5.3.1, there was a clear change of inductance comparing the healthy inductance vs after breakdown. The healthy inductance is compared to inductance measured after the anomaly in Figure 5.47 and Figure 5.48 respectively. The inductance shows less than 0.2% change per phase, a variation expected from measurement uncertainty.

After comparing the line inductance, it was decided to test the integrity of the winding. The normal running current was increased from $2.5A_{rms}$ to $11A_{rms}$, a

150% rated current overload for a short period of time on Sample 1. The sample appeared to operate as normal and fault protection was not activated. The overload was repeated on Sample 4 with the same result. All samples continued operation at $2.5A_{rms}$ after the C_{eq} anomaly until the final end of life.

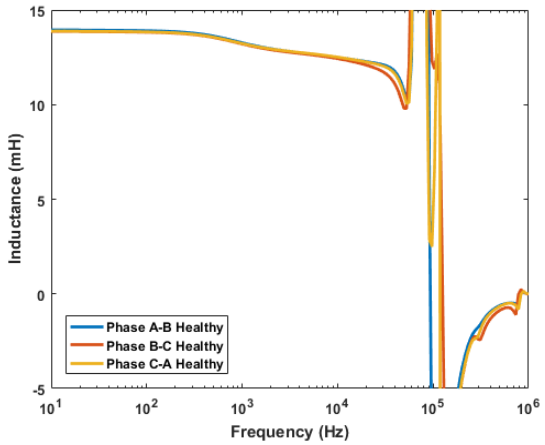

FIGURE 5.47 SAMPLE 3 HEALTHY PHASE INDUCTANCE MEASUREMENT

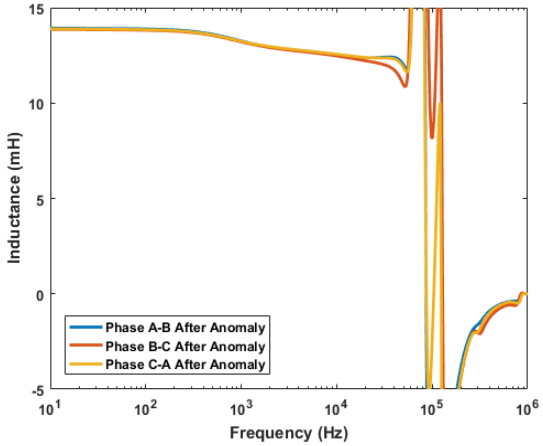

FIGURE 5.48 SAMPLE 3 PHASE INDUCTANCE AFTER ANOMALY

Ceq Investigation

Throughout the on-line testing, measurement was paused daily to conduct an off-line impedance measurement using an IM3570 Hioki impedance analyser. The two most interesting features of the anomaly are shown in Figure 5.49 and Figure 5.50. The C_{eq} decrease is not present when measured off-line, and the C_{eq} value appears to recover. These observations are visible across all samples, except Sample 3, where there appears to be no recovery.

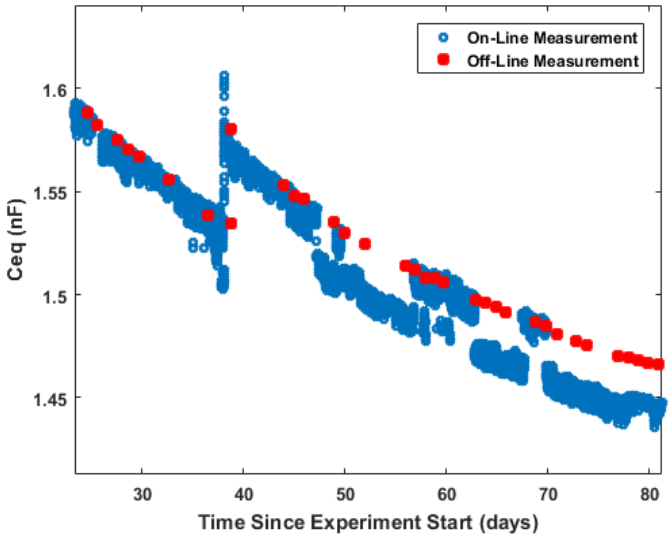

FIGURE 5.49 SAMPLE 1 CEQ RECOVERY

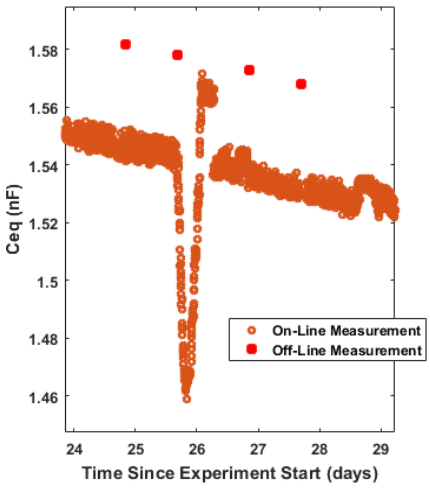

FIGURE 5.50 SAMPLE 4 CEQ RECOVERY

For Sample 4, there were three recovery events, one spontaneous recovery, similar to that seen in Sample 1 and 2, and two recovery events under special circumstances. An experiment was conducted in Sample 4 to determine

C_{eq} variation with temperature, the results of which are shown in Section 6.2. During the experiment, the temperature was cycled from the 215 °C value down to 58 °C. The experiment was conducted once when the machine was healthy, and repeated twice after the C_{eq} anomaly. During the first repeat, shown in Figure 5.50, the C_{eq} value recovered to the off-line measured value. The same recovery was observed in the 2nd repeat. Recovery events suggest that the anomaly may be due to intermittent contact or conductive contamination present in the insulation releasing contact when pressure in the slot is released, either during thermal cycling or ageing.

The difference between the off-line measurement and on-line, is that for off-line measurement, the three phases are short circuited at the terminal, to measure the common mode impedance, whereas the windings on-line are energised, and phase-phase voltage is present. To investigate effects of phase-phase interaction and contact, a simulation of resistive contamination build-up was performed, and the effect was emulated on a test machine.

Simulation Model

The insulation model in Section 3.3 has been modified to enable modelling distributed windings by breaking insulation sections into blocks composed of the full model. A single model block is shown in Figure 5.51 with its input, output and ground connections. The full model connects nine of these blocks together, to simulate three phases, each composed of three chunks of distributed winding.

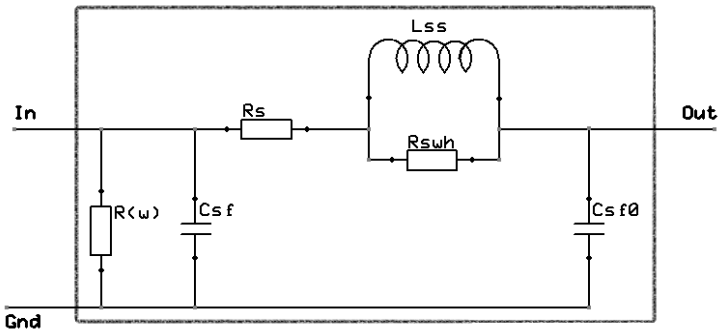

FIGURE 5.51 UNIT OF INSULATION MODEL

The initial measured values for parameters in the full model of insulation are divided by nine to ensure the total capacitance for the full model remains representative of the stator winding. The L_{ss} inductance value is recalculated to maintain the same resonance frequency of the system, based on input values of C_{sf} and C_{sf0}. The blocks are connected in Simulink, using the SimScape library, with impedance result measured output.

For the winding layout for the stators used in the experiment, two modes of insulation degradation, which induce a step change in resonance parameters are considered. A possible turn-fault and single phase faults are simulated.

To simulate the single phase degradation, the insulation chunks are connected as in Figure 5.52, where a resistor was placed in parallel with a full winding to neutral. The neutral point connection was selected because it was possible to test this scenario on a machine stator available in the laboratory.

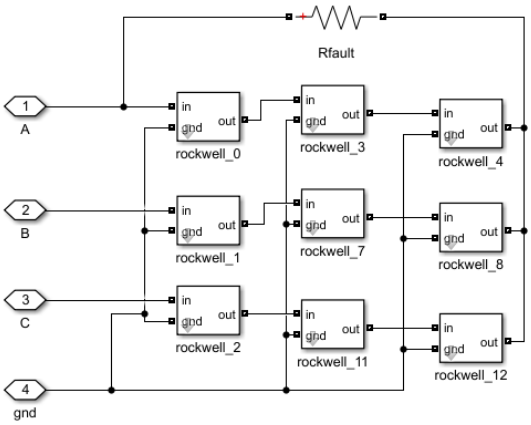

FIGURE 5.52 PHASE FAULT SIMULATION

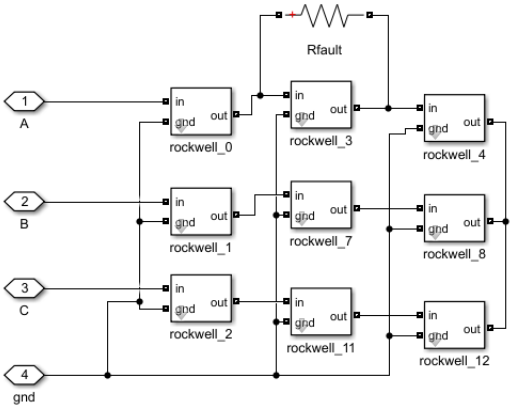

FIGURE 5.53 TURN FAULT SIMULATION

The turn-to-turn fault is modelled in Figure 5.53 as a resistor across a single chunk of insulation within a phase. Although this model is somewhat inadequate for modelling inter-turn effects, building a full distributed model of insulation lies outside the scope of this experiment.

To validate results of the model output, the machine shown in Figure 5.54 is measured using the Hioki IM3570 off-line instrument when subjected to a turn-turn short circuit and a progressively decreasing resistance applied across a phase. The resistance ranges between 100kOhm to a complete short circuit in both the simulation and emulation. In the results, a complete short circuit is represented with 1 Ohm resistance, while no resistance is given the value 1MOhm, to enable plotting on the same graph. The test connections are shown in Figure 5.55. The machine used for fault emulation is a distributed winding IPM machine, rated 3.75kW at 2100RPM [157]. The machine contains a two turn tap at the start of its winding for turn-fault testing.

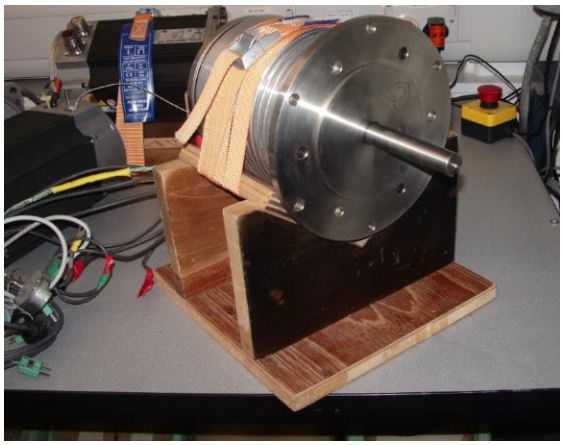

FIGURE 5.54 MACHINE WITH TURN-FAULT WINDING

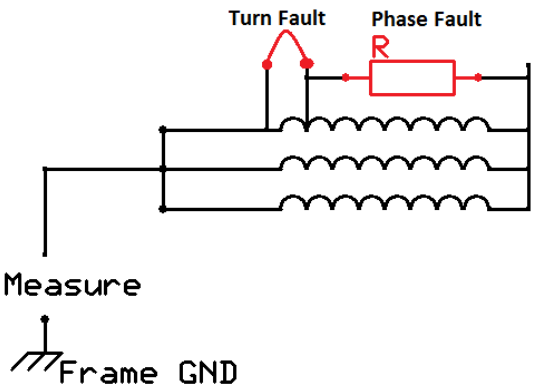

FIGURE 5.55 TURN FAULT AND PHASE FAULT EMULATION

Simulation Results

The simulation and emulation results for the turn fault are presented as movements of three parameters, C_{sf}, C_{sf0} and L_{ss}, responsible for common mode resonance behaviour. The change of parameters between different simulation and emulation scenarios is compared to those observed during the C_{eq} decrease anomaly.

TABLE 5-5 TURN FAULT RESULTS COMPARED TO ANOMALY JUMP

	Parameter Jump		
Parameter	TF Simulation	TF Emulation	@Anomaly
Csf (nF)	--	↑	↓
Csf0 (nF)	--	↓	↑
Lss (uH)	↓	--	↓

The movements of parameters for turn fault simulation and emulation is easy to express as a binary value, either increasing or decreasing as compared to healthy value. Table 5-5 shows the results for the three different parameters, no change or insignificant change is shown as "--".

It is observed that there is little change in parameters in simulation when the turn fault simulation is performed. Little 'Lss' parameter change is also observed in turn fault emulation, despite significant change of C_{sf} and C_{sf0} parameters (C_{sf} change from 1.27nF to 1.58nF before and after the turn fault application respectively) it was observed that these parameters move opposite to the resonance parameter jumps observed in Section 5.3.3.

The measured C_{sf0} and C_{sf} parameters for the single phase fault from the emulation are shown in Figure 5.56 and Figure 5.57 respectively. Two important observations are made: the emulated C parameters move in the same direction as was observed during the ageing test at the C_{eq} decrease discontinuities, it is also observed that only a modest resistance is required to significantly affect the resonance behaviour, only 1 kOhm contact is required to change C parameters by 10% jumps observed in the Csf and Csf0 parameters in Section 5.3.3.

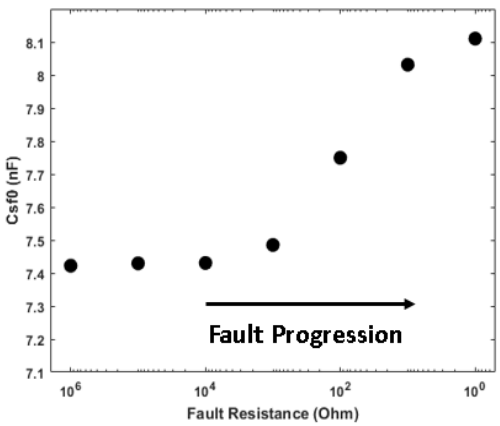

FIGURE 5.56 EMULATED CSF0 VALUE

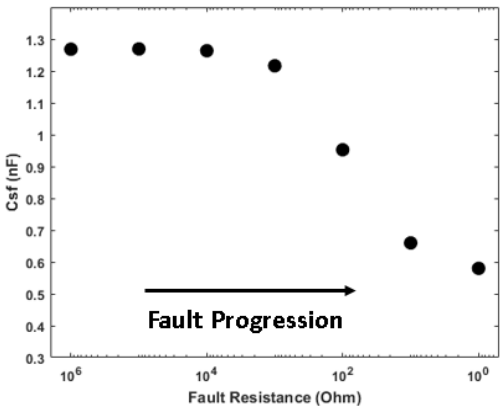

FIGURE 5.57 EMULATED CSF VALUE

L_{ss} inductance parameter is shown in Figure 5.58, the same sensitivity is observed to modest fault resistance values. The L_{ss} parameter for Sample 1 is shown in Figure 5.59, the decrease of Lss is representative of all samples at the C_{eq} discontinuity.

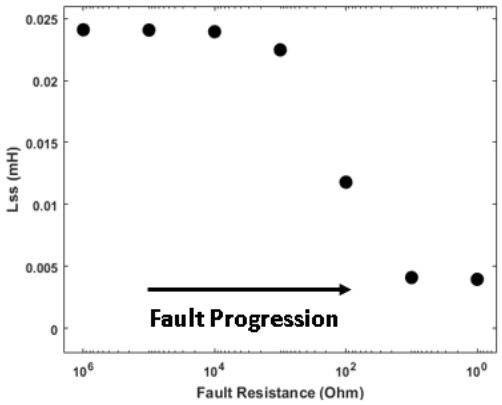

FIGURE 5.58 EMULATED LSS VALUE

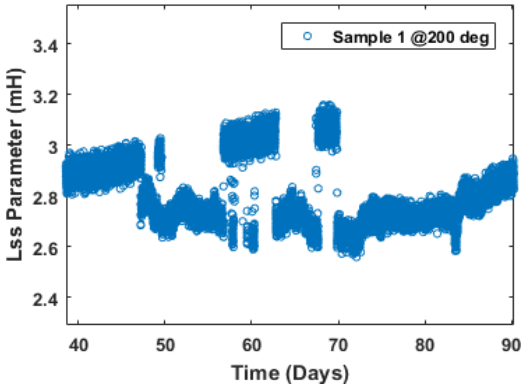

FIGURE 5.59 SAMPLE 1 LSS VALUE

The Lss parameter from simulation shows an even greater sensitivity to phase-neutral resistance, as shown in Figure 5.60, however it was observed that the movement of C_{sf} and C_{sf0} are in the same direction as during the turn fault simulation results in Table 5-5, the C_{sf} simulated parameter is shown for the single phase fault scenario in Figure 5.61.

More work is required on the distributed model, as it seems to represent the insulation behaviour well and shows change of L_{ss} in agreement with the emulation, however distributing C_{sf} and C_{sf0} parameters using the method proposed cannot be validated.

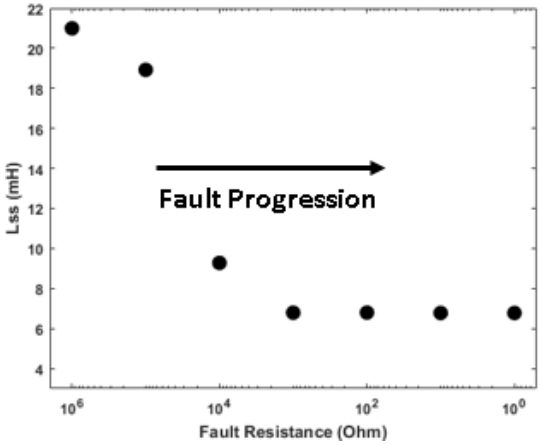

FIGURE 5.60 SIMULATED LSS VALUE

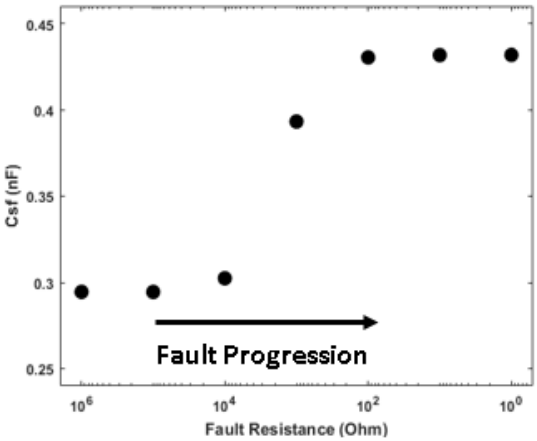

FIGURE 5.61 SIMULATED CSF VALUE

The addition of a resistor in parallel with the model winding inductance has the effect of adding another path for current to flow. The parasitic model simulates behaviour of insulation at frequencies in the 1MHz magnitude. At these frequencies large values of resistance can have significant effect because they have similar magnitude impedance to the model inductance at high frequencies.

In the insulation model in Figure 5.51, the R_{swh} parameter is directly in parallel to the L_{ss} inductance parameter. For Sample 1, the R_{swh} parameter is shown in Figure 5.62.The decrease of R_{swh} is as expected from the emulation and shows that other than during the jumps, the R_{swh} parameter remains constant throughout the lifetime of Sample 1. An additional 8 kOhm of resistance in parallel with a phase in the machine would yield negligible additional current, allowing normal operation to continue.

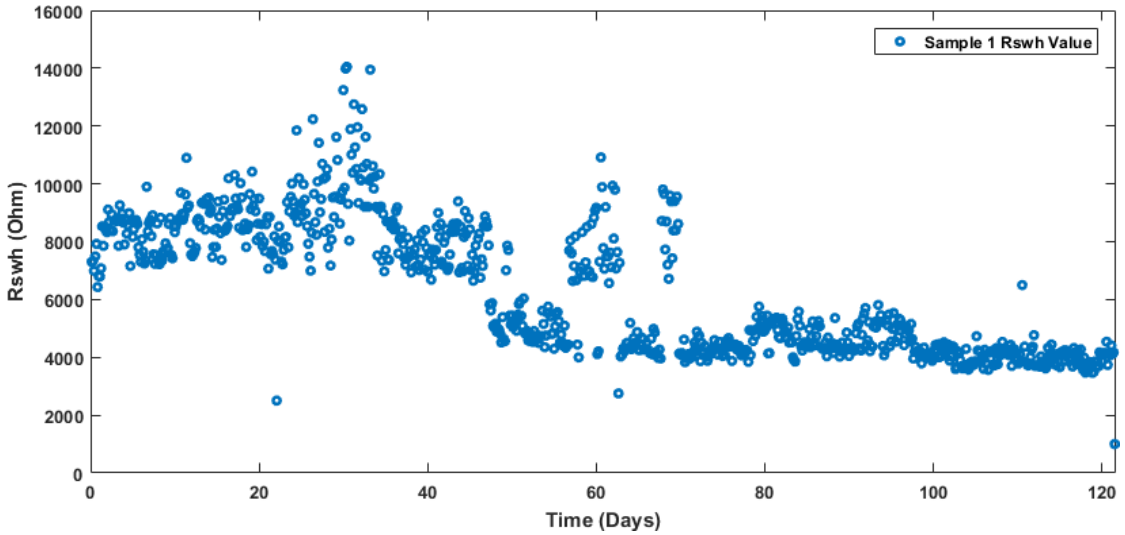

FIGURE 5.62 MEASURED RSWH VALUE FOR SAMPLE 1 OVER TIME

Using the evidence provided it is concluded that the most likely source of resonance parameter discontinuity is a formation of a resistive track, either across a phase connection in the end winding, or between two separate phases. It has been shown both in simulation and emulation that a single turn-turn fault event has a benign signature, however it is feasible that a large section of faulted winding would provide similar signature to a phase-to-phase resistive track. A significant loss of winding inductance and high induced current in the faulted section would lead to rapid failure, making the observed long operation after the event more likely to be a result from a benign resistive phase-to-phase track, rather than a serious winding turn-to-turn fault.

Wire standards allow for miniature holes in insulation, formation of more holes is also expected during ageing, leading to possible tracking phenomenon. Recovery events observed can be explained by spontaneous disconnection/reconnection as the insulation system changes over time due to ageing. To investigate the tracking phenomenon directly, one would design an experiment explicitly replicating the phase-phase emulation on a machine, being monitored on-line, without ageing present. As tracking could occur on any part of the winding, for a complete evaluation of the effect, multiple taps would also be required on the winding, to determine the effect of the position of the fault on measured parameters.

5.3.7 Req Results

In this section, an attempt is made to use the R_{eq} 'c' parameter dissipation as a prognosis tool and the problems associated with this are introduced. The model fitted R_{swh} parameter is shown for Sample 3, with observations that have been made with regards to its usability in insulation health diagnosis.

Rω 'c' Parameter Prognosis

The initial assumption of degradation due to oxidation, assumed that both C_{eq} and dissipation would decrease over time. Although this was observed initially, in samples 2, 3 and 4, after the discontinuity observed in C_{eq} results, the trend of Req 'c' parameter reverses, to increase until end of sample life.

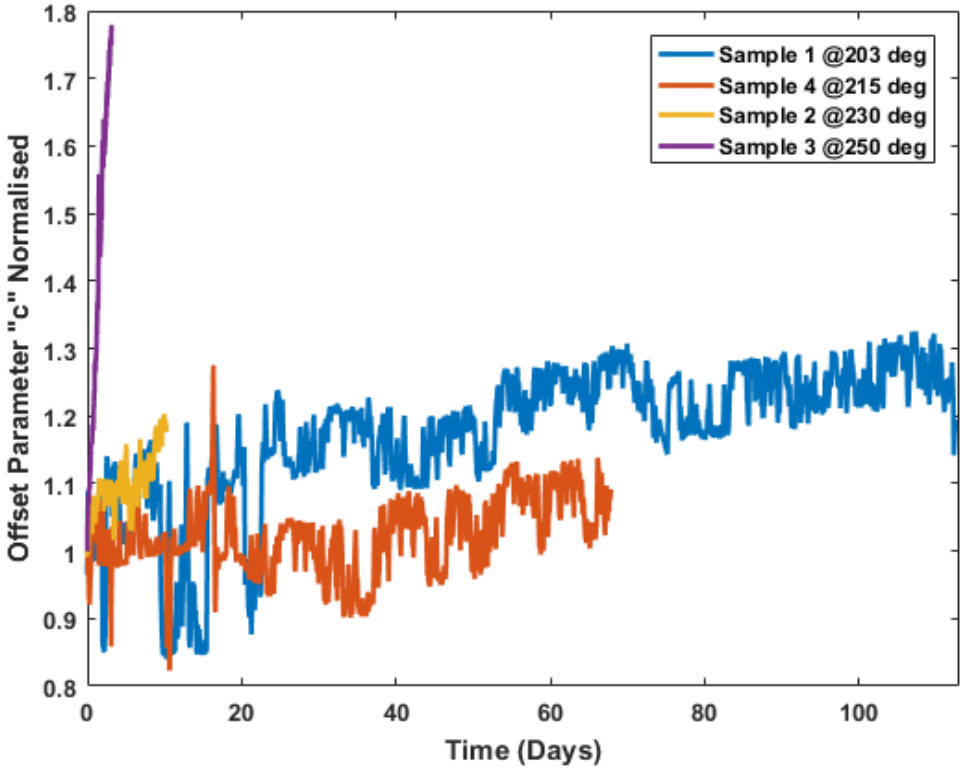

FIGURE 5.63 R_w 'C' PARAMETER OVER TIME NORMALISED TO TIME OF FIRST DISCONTINUITY

It was attempted to use the Req behaviour after the discontinuity to predict the remaining life of the sample based on the progress of the $R_ω$ 'c' parameter.

In Figure 5.63, the 'c' dissipation parameter is shown normalised at the time of discontinuity. Samples 1 & 2 both fail at around 20% increase, with Samples 1, 2 & 3 having a rate of increase proportional to the temperature and therefore the degradation rate. The similarities however end here, Sample 4 might logically be expected to have a rate somewhere between that of Sample 1 and Sample 2, with degradation rates slower and faster than Sample 4 respectively. This however is not observed. During the experiment, Sample 4 exhibits the slowest rate of increase for dissipation.

To enable detection for end of life, a reliable threshold must be established. The observed 78% increase in 'c' parameter for Sample 3 compared with 5% increase for Sample 4 at end of life, the threshold cannot be reliably established, and therefore precludes the possibility of using the dissipation data as a prognosis tool.

R_{swh} Parameter

In Section 3.3, there are two distinct dissipative components in the insulation model, R_ω and R_{swh}. During the experiment, it was discovered that the R_{swh} value contains elements of both the low frequency R_ω response and resonance change behaviour. Rswh for Sample 3 is shown in Figure 5.64 to illustrate the extreme representation of these phenomena.

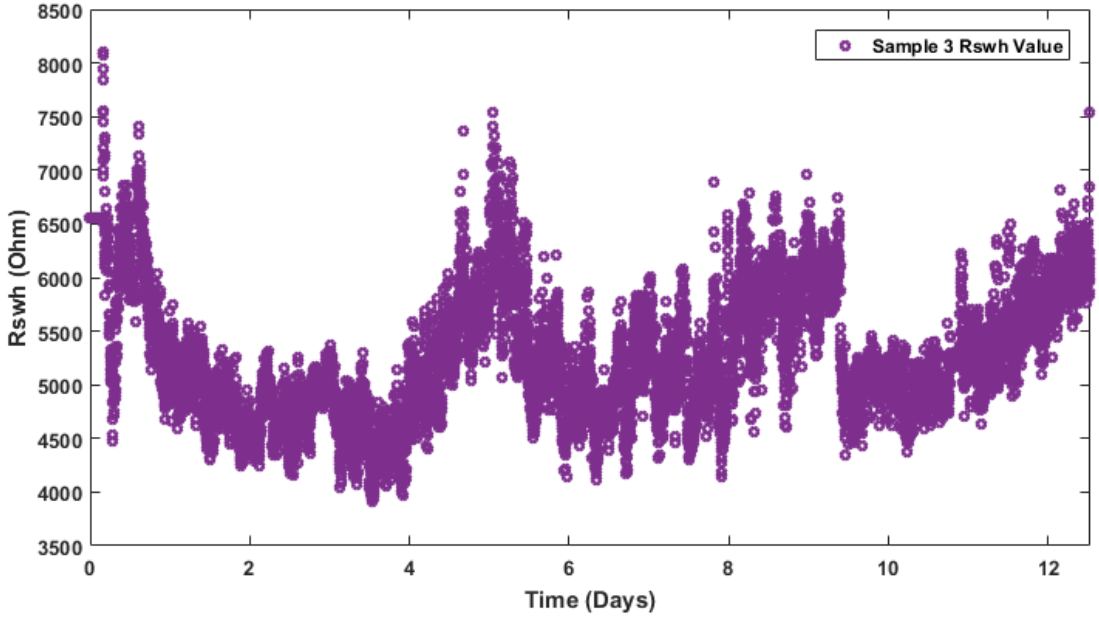

FIGURE 5.64 SAMPLE 3 RSWH RESULT

The data in Figure 5.64 shows the same decrease, increase, decrease and final increase ramps as seen in the dissipation data in Figure 5.26 for Sample 3 R_ω 'c' parameter, however at day 9.4, there is a discontinuity decrease in the final increasing ramp. The discontinuity occurs at the same time as was observed in Section 5.3.3 in the C_{sf} result. It is possible that the same tracking phenomenon is responsible as diagnosed in Section 5.3.6, and a 30kOhm resistive track has formed in parallel with the winding.

To measure the Rswh parameter, many more harmonics are available compared to R_ω, due to a large number of higher frequency harmonics compared to those used to fit R_ω. It is suggested that if the measurement equipment is capable of returning a reliable value for R_ω, this should be the primary dissipation indicator, as dissipation data in the low frequency range is not affected by change of machine resonance parameters in the high frequency region, defined as frequencies above 360 kHz for this machine. Machine resonance itself can be better measured using the C_{sf}, C_{sf0} and resonance frequency instead.

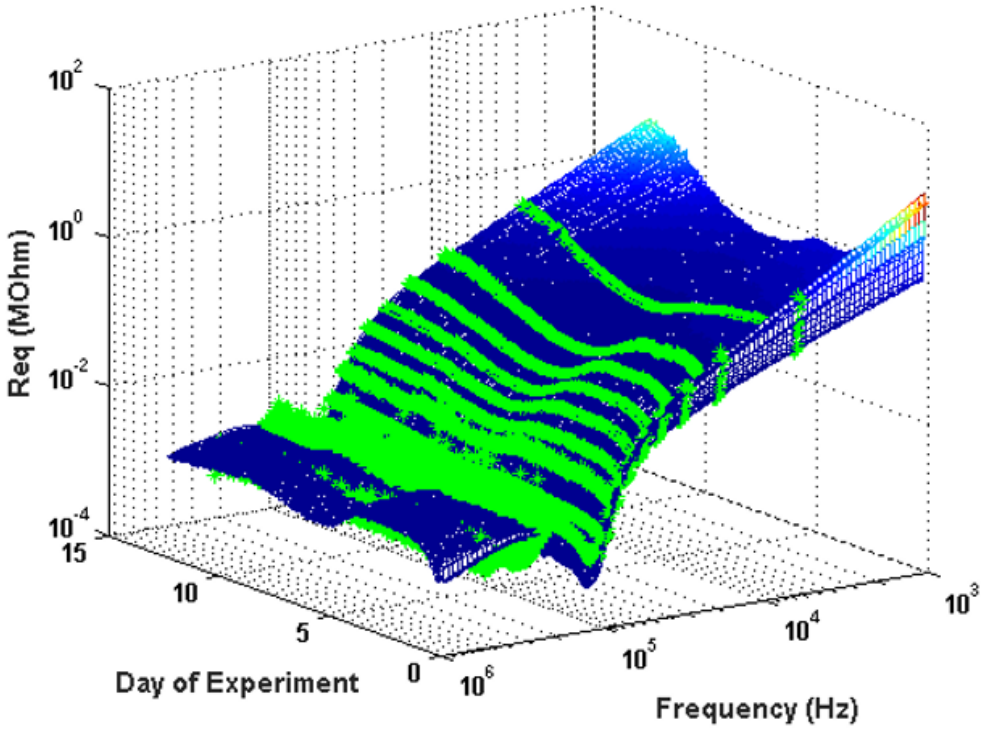

FIGURE 5.65 SAMPLE 3 R_{EQ} OVER TIME, MEASURED DATA VS FITTED DATA PLOT

On-line measurement of R_{swh} value is required for all reconstruction of the full dissipation response over the measured frequency spectrum. Using the insulation model in Section 3.3, one is able to model the whole impedance using 5 values, rather than storing them as raw frequency data. A demonstration of the restoration of the full R_{eq} response is shown in Figure 5.65, where the dissipation response has been reconstructed for data from Sample 3, with original data plotted alongside the fitted surface.

Viewing the data as shown in Figure 5.65 gives little diagnostic information, however it is important to demonstrate the ability of the insulation model to recreate impedance over time. Confidence in the model allows the use of the parameters directly, as health indicators, and it is no longer required to view the raw data values to diagnose the behaviour of insulation. Further study is required to use R_{swh} value as a diagnosis tool for winding dissipation analysis.

5.3.8 Dissipation Diagnosis

Initially it was expected that over time, dissipation for samples would increase, with the rate of ageing proportional to the accelerated ageing rate. The data would be fitted and threshold for failure identified. The results obtained however show significant differences between samples.

Looking at the tanδ dissipation results in Section 5.3.3, at the start of lifetime, all samples have a higher dissipation, quickly decreasing to a lower value. This is as expected observations in industry of the curing process of insulation [122] [158]. Samples 1, 4 and 2 have dissipation @50Hz less than 7% over their lifetimes however Sample 3, the hottest sample, operating at 250 °C dissipates as much as 60% of the insulation current at one point in its life.

Towards the end of life, all samples have decreasing dissipation factor, the opposite of what would be expected from degradation through oxidation. The main degradation mechanism therefore has been concluded to be a loss of volatile elements for all samples, as experienced in the accelerated ageing experiment in [76].

Sample 3 is unusual, as the dissipation is considerably greater than the other samples, the most distinctive feature of the dissipation is also the reversal of dissipation factor trend in Figure 5.30. Although the dissipation factor is affected more significantly by loss of volatiles [76] than the Ceq value, a similar loss of Ceq for Sample 3 to other samples shows that the dissipation for Sample 3 is dominated by oxidation and cross-linking.

It is known that oxidation and cross-linking are competitive reactions, which show the opposite dissipation trends depending on the dominant degradation mode [159]. Only Sample 3 shows significant long term trend reversal. It has been observed in [160] that the dissipation for H class insulation samples decreased at temperatures below 250 °C, however at temperatures higher, an increase was observed. Closer inspection [161] of the samples in [160], revealed that the low temperature samples exhibited a softening of insulation, whereas at temperatures higher than 250 °C, brittle cracking was observed instead. Although the IEEE ageing standard [32] specifies that 250 °C should be an acceptable test temperature. Laboratory evidence, as well as observations on Sample 3, reveal that this temperature a threshold, at which H class insulation degradation starts to deviate from normal degradation modes. Sample 3 is therefore excluded from prognosis, as evidence indicates that multiple ageing modes are present throughout its lifetime.

5.3.9 Ceq Prognosis of Lifetime

In the raw Ceq results, it has been observed that the Ceq parameter decreases for all samples, following an exponential path until end of life. The samples also appear to decrease by the same amount proportional to their starting value, at the end of lifetime. To better compare Ceq change over time, Ceq is plotted as a percentage change over time in Figure 5.66, the breakdown value has been highlighted. All samples have been normalised to their peak value which occurs at the start of the experiment, shortly after experiment start.

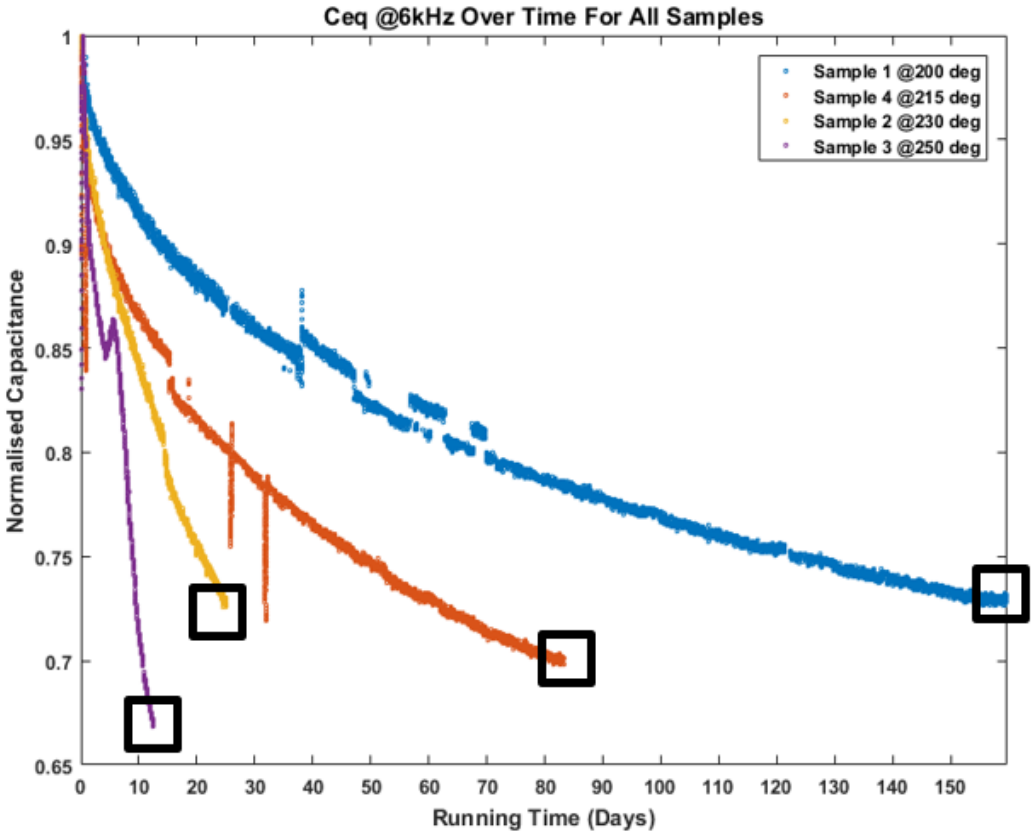

FIGURE 5.66 NORMALISED CEQ PLOT OVER TIME

The normalised plot reveals that all four samples have a similar percentage of Ceq decrease, between 27-33% at their end of life. The decrease figures are listed in Table 5-6 for all samples, with the sample details included. It is preliminarily proposed that the consistent Ceq decrease at end of life can be used as a threshold to indicate insulation degradation and eventual failure.

TABLE 5-6 CEQ REDUCTION FOR ALL SAMPLES

Sample Identifier	Temperature	Overal Lifetime (days)			Ceq Reduction
		Expected	Actual		
1	203	169.2	159.8		27.2%
4	215	73.7	83.4		30.2%
2	230	26.0	25.2		27.4%
3	250	6.5	12.5		33.2%
				Average	29.5%

The most important characteristic common to samples 1, 4 and 2 is the consistent progression behaviour over time. Knowing the expected characteristic, one can use measured data to fit the trend of Ceq, and project into the future. The remaining lifetime can be determined by calculating the time of the Ceq trend to reach a certain threshold obtained from experimental data. It was diagnosed in Section 5.3.8 that Sample 3 undergoes a different ageing process during part of its lifetime, therefore the prognosis in this section uses values and trends from Samples 1, 4 and 2 only, for the purpose of prognosis.

$$C_{eq}(t) = at^b + c \tag{5.8}$$

It was determined through trial and error that the best representation of Ceq over time is fitted by Equation (5.8), where a, b and c are constants which are to be fitted using historic Ceq data. The fitting was performed using the MATLAB 'fit' function. The algorithm outputs the values of the fitted curve, as well as the values of parameters subject to confidence levels of 95%.

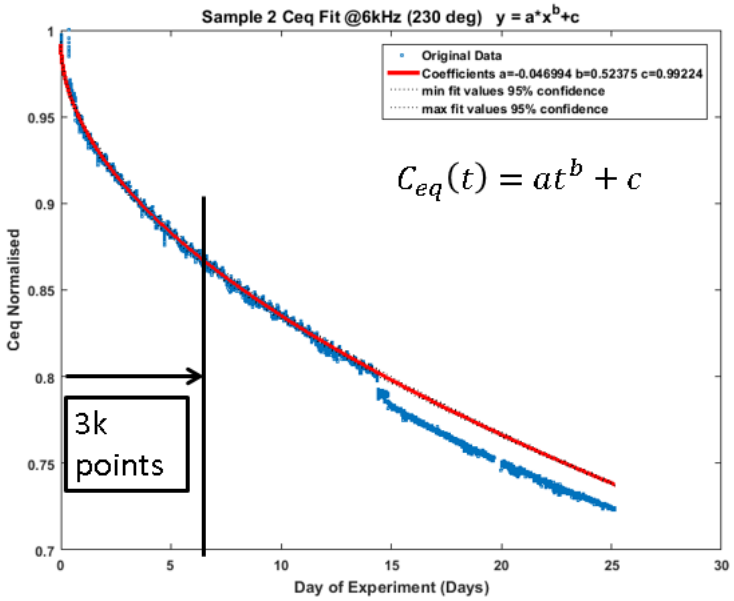

FIGURE 5.67 FITTING CEQ FOR THE FIRST SIX DAYS OF DATA

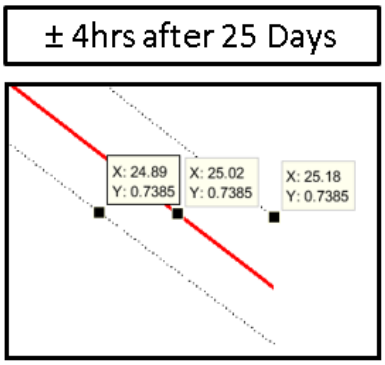

FIGURE 5.68 95% CONFIDENCE FIT

Data fitting is shown for Sample 2 in Figure 5.67, where the first 3,000 points of data, representing the first 6 days of the experiment are used to fit the a, b and c parameters of Equation (5.8). It can be seen that the projection fits the data well up to the discontinuity at day 14.8. After this, the Ceq decrease continues at the same rate, parallel to the prediction.

The fit confidence levels are plotted for the fit alongside the data. At the end of the experiment, the confidence limits can be seen in Figure 5.68. The consistency of Ceq progression and measurement quality is such that the 95% confidence projection places the mean value somewhere between ±4hours after

25 days, effectively a ±0.67% fit error. The same fitting method has been performed for Samples 1 and 4, where it was found through trial and error that the first 25% of C_{eq} data is required to fit the lifetime curve to similar confidence.

An important question in lifetime testing is always "how representative are my samples of the general population?" From testing, the mean value and standard deviation results can be obtained. The calculation of the confidence intervals is required to establish the possible location of the mean. Once a confidence percentage is selected, the mean value in a future experiment results should have a defined probability of being inside the confidence interval values.

$$C_i = \bar{x} \pm Z_i \frac{\sigma}{\sqrt{N}} \tag{5.9}$$

TABLE 5-7 Z PARAMETER FOR TYPICAL CONFIDENCE PERCENTAGES

Confidence	Z
80.0%	1.282
90.0%	1.645
95.0%	1.960
99.0%	2.576
99.9%	3.291

The confidence values for final Ceq value can be calculated using Equation (5.9), where the "Z" parameter for the confidence percentage is selected from Table 5-7. In Equation (5.9) $\bar{x}$, σ and N represent the mean value, standard deviation and number of samples respectively. The commonly used 95% confidence level has been chosen for this experiment. Calculating the mean Ceq value at failure for samples 1, 2 and 4 yields 28.4% mean decrease value, with maximum and minimum levels at 26.3% and 31.8% respectively. The values are shown graphically in Figure 5.69.

In small sample populations, less than N<30, the 'Z_i' value in Equation (5.9) must be replaced with student t factor [24]. For N=3, at 95% confidence, for a single sided confidence interval, Z_i must be replaced with 2.92, significantly increasing the lower bound interval. For an equivalent confidence level for a single sided student t value of 1.96, one must accept a lower confidence value of 90%.

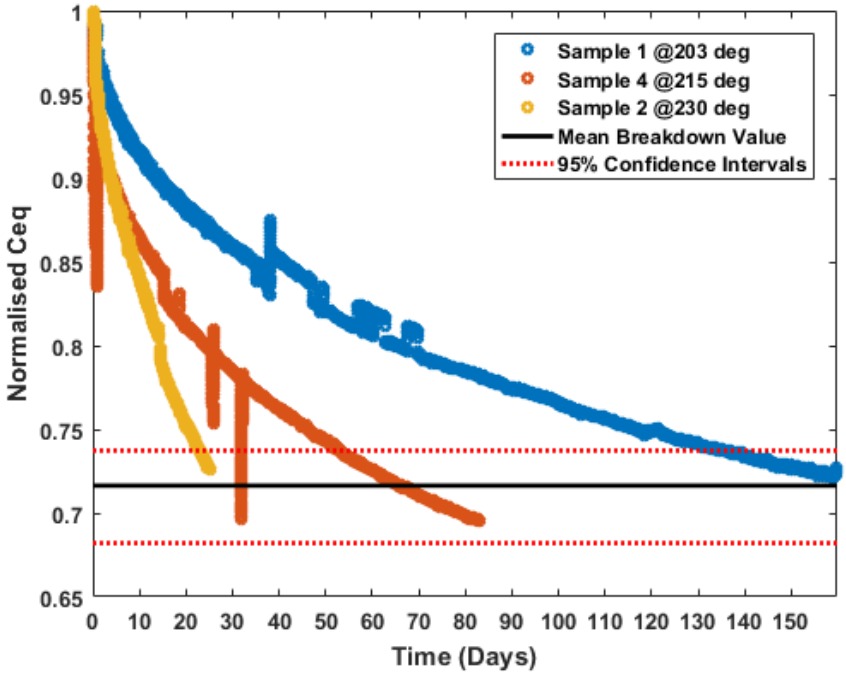

FIGURE 5.69 CONFIDENCE INTERVALS FOR THE LOWEST TEMPERATURE SAMPLES

The effect of the confidence levels on lifetime prediction are shown in Figure 5.70 for the projection of Sample 1 lifetime. The fitting error is exaggerated to show the uncertainty zone. In Figure 5.70, the possible area of sample failure is highlighted, where with a known fitting confidence and a known failure threshold confidence it is possible to say that the sample will fail somewhere in this range with a defined confidence level.

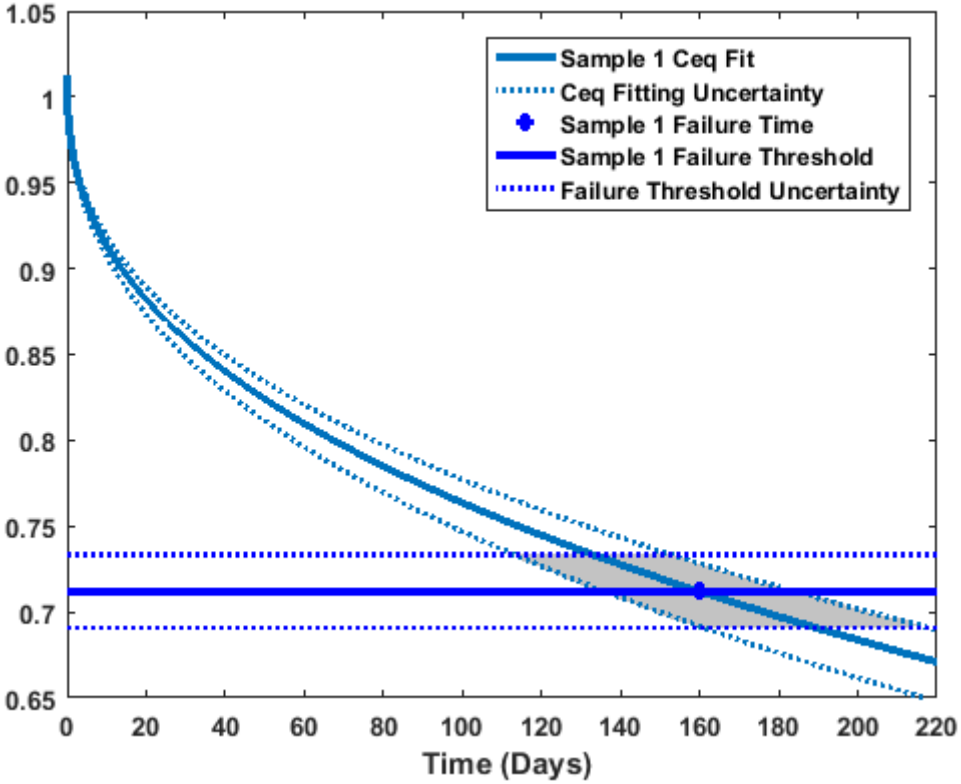

FIGURE 5.70 UNCERTAINTY IN LIFETIME ESTIMATION FOR SAMPLE 1

To reduce the uncertainty zone, the horizontal boundaries require more samples for validating the failure threshold. The fitting quality has been shown to be of superior quality, therefore the uncertainty depends entirely on the failure threshold. There is one more way to reduce the area of the uncertainty zone, which is to accept a lower confidence level, which may be suitable for some applications.

TABLE 5-8 SAMPLE LIFETIME PREDICTION COMPARISON

Sample Identifier	Sample Temperature (°C)	Ceq Reduction (%)	Actual Lifetime (Days)	Predicted Lifetime (Days)	90 % Confidence (using student t) Single Sided Lower Bound	
					(Days to Breakdown)	(Days to Mean Prediction)
1	203	27.2%	159.8	154.1	128.4	25.7
4	215	30.2%	83.4	73.4	59	14.4
2	230	27.4%	25.2	28.6	24.7	3.9

Using the three Ceq thresholds available and the fitting of Samples 1, 4 and 2, a retrospective lifetime prediction has been made. The first 25% of Ceq data for each respective sample has been used to obtain the data fit projection. The predicted lifetime results can be seen in Table 5-8. The predicted lifetime is shown from the mean threshold value for each sample, as well as the implications of the horizontal confidence interval on the earliest expected time to failure It is assumed that the fitting confidence is high enough to make a negligible contribution to the uncertainty zone, therefore the 2D area in Figure 5.70 is approximated with 1D representation for minimum lifetime based on the confidence levels of the Ceq value at failure. It can be seen in Table 5-8 that the predicted value for each sample is reasonably close to the actual lifetime of the machines, with 12% underestimation to Sample 4 and 13.5% overestimation of Sample 2 lifetime, Sample 1 lifetime is within 3.6% of prediction.

In practice the safety limit would be set at the lower bound of confidence level, and the upper limit would be discarded as unnecessary unless it were required to know at what time all of the machines are no longer operational. Because the Ceq progression is exponential, the upper time to fail is correspondingly higher than the lower bound. Selecting the lower bound for Sample 1, it would make sense for it to be taken out of service on day 128 of its operation, underutilising the machine by 25.7 days, by 16.7% compared to the mean prediction value.

To implement real-time remaining lifetime prediction, one would fit the Ceq value over time to Equation (5.8), and project the value of Ceq until it reaches the failure threshold set by the safety limit. Although at present there is not enough data to have an adequate threshold value for the safety limit, the method of prognosis can be established. Results from a practical real-time prognosis can be shown in Figure 5.71. The exponential fitting is performed for Sample 2 with an arbitrary 20% decrease of Ceq set as the safety threshold.

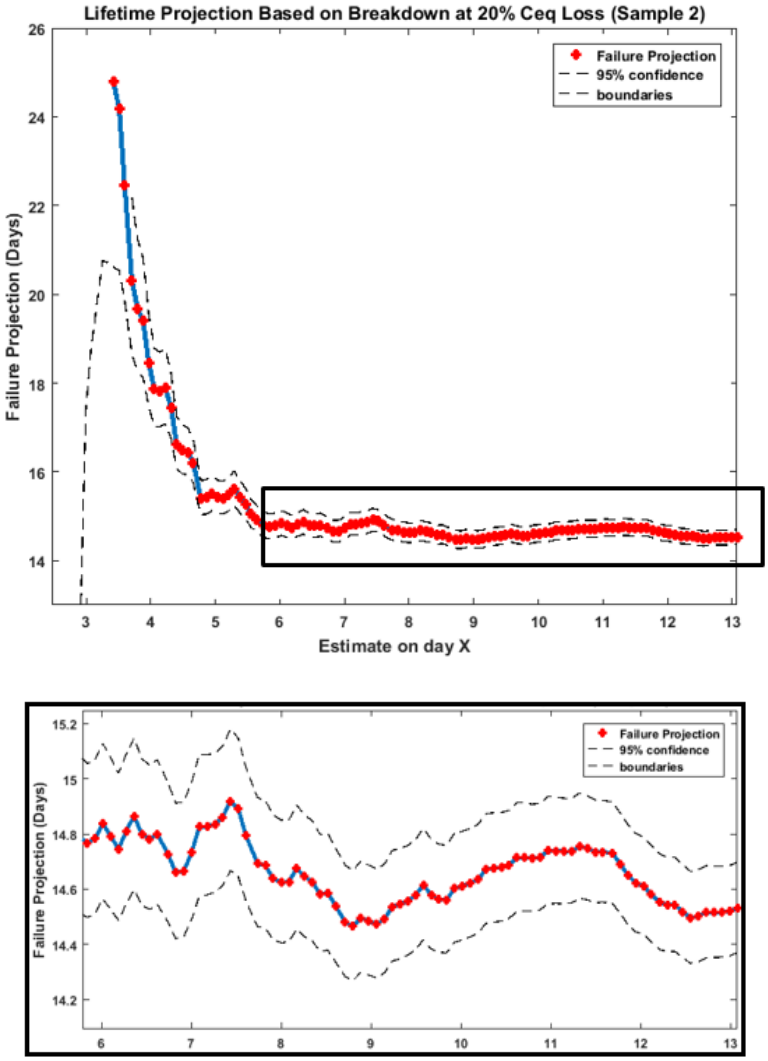

FIGURE 5.71 FITTING DATA OVER TIME

The fitting in Figure 5.71 requires initially at least 3.5 days' worth of data to return a valid prediction value, however as more data becomes available, the failure prediction date converges to a steady state value, with corresponding confidence fit boundaries narrowing. For Sample 2, the convergence requires about 6 days' worth of data. After 6 days, the confidence levels and mean value are defined by variability of data. The fitting in Figure 5.71 projects Sample 2 to reach 20% threshold on day 14.6 ±0.2 days. During testing, Sample 2 actually reached the threshold on day 14.4.

5.4 Summary

The accelerated ageing experiment, for the first time in literature carried out an ageing experiment where the capacitance and dissipation information was tracked over the lifetime of the machine samples. The results have been presented with findings noted.

The quality of data over the long-term monitoring remained as high as that measured in the error analysis in Section 4.6.3. The capacitance data remains within the 0.1% accuracy required by the off-line equivalent test.

All samples tested failed through phase-to-phase insulation breakdown, rather than phase-to-ground, therefore the measurement of phase-to-ground insulation health is used as a global indicator, a proxy for the insulation system degradation. All samples failed at the times expected from H class insulation. It is concluded therefore that the ageing methodology was adequate to age the phase-to-phase turn insulation layer.

Unusual behaviour was observed during the ageing of the highest temperature sample, Sample 3, where both the dissipation data and the capacitance data shows a slow but significant change over time It is concluded that the observations indicate a competition between different insulation degradation mechanisms. Although following existing standards for accelerated ageing returned expected failure times, it is recommended for future experiments that the 250°C maximum temperature for H class samples is to be reduced, to maintain the same degradation mechanism over time.

Parameters measuring the winding common mode resonance characteristic showed unforeseen changes during the life of samples, especially evident in Sample 1, where the sample appears to have numerous fault and recovery events. Further analysis revealed that very minor faults, resulting from resistive tracking in the end-winding, which do not impact the operation of the machine, can nevertheless produce measurable changes of parameters. Further work is suggested to investigate the viability of detecting winding faults, using the method of monitoring common mode insulation impedance over a broad range of frequencies.

The most significant finding during the experiment is the progression of equivalent low frequency capacitance C_{eq} over time during the ageing of samples. The rate of C_{eq} progress was directly related to the ageing rate of the insulation system. It was also found that all samples tested have a very similar Ceq value at failure. Using the consistency and threshold value allowed the development of a prognosis method of future failure.

Chapter 6

Further Testing

Additional testing was implemented to investigate variability of measured parameters with temperature, the effect of moisture ingress and testing of an additional sample with strengthened phase-phase insulation.

Results from humidity experiment and investigation of parameter variation with temperature suggest methods which can be used to diagnose insulation behaviour in real life operation, rather than in controlled laboratory environments.

Results are presented from an additional sample which was designed with improved phase-to-phase insulation. The impact of additional insulation and results over time are discussed.

6.1 Humidity Exposure

Moisture is ever present in the atmosphere and is an ordinary part of our atmosphere. The dew point is defined as the conditions necessary for moisture in air to condense out as water droplets. This is important for machine application because exposed machines operating in low temperature or high humidity areas can have water vapour condense in the windings, seeping into the insulation. Windings can also be exposed to moisture directly, through common faults such as leaks in water cooled machines or unexpected flooding in air cooled machines.

An experiment was devised to mimic a machine operating in high humidity at a representative working temperature. It was predicted in Section 3.2.3 that the capacitance and dissipation of the ground-wall insulation should increase with moisture present.

6.1.1 Aims

The main aim of the humidity exposure experiment is to operate a motor in a realistic scenario, and increase the moisture content of the ambient, up to the dew point. The effects covered in literature review must be verified and viability of on-line measurement to be demonstrated. Detailed aims follow:

- Operate the machine at full voltage inside the humidity chamber at the maximum humidity
- Monitor Ceq and Req parameter with respect to humidity
- Identify problematic moisture ingress

6.1.2 Method

The same machine stator type, as studied in Chapter 5 was used as the test sample to expose to varying levels of humidity. The sample must not undergo any thermal ageing during the experiment and must have minimal variation of temperature, eliminating all variables of parameters except the humidity. The sample was exposed to humidity in the SH-662 benchtop humidity chamber as shown in Figure 6.1. The temperature selected for the test was 80 deg as this is the maximum temperature the chamber is capable of operating at full humidity. The humidity chamber maintains the humidity to within ±3% rh, as per the datasheet.

FIGURE 6.1 SAMPLE INSIDE SH-662 ENVIRONMENTAL CHAMBER

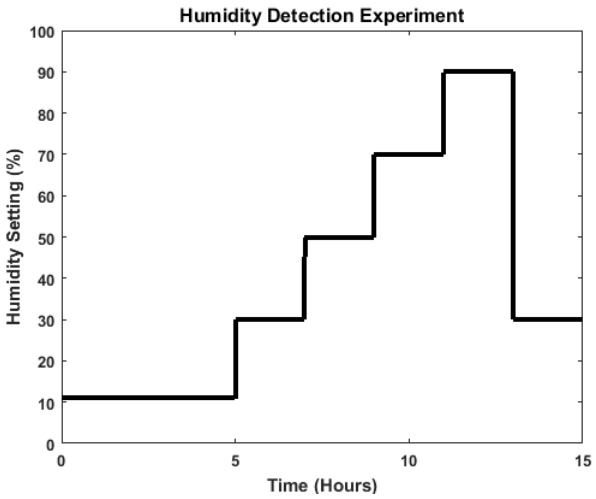

FIGURE 6.2 HUMIDITY COMMAND PROFILE

The humidity test profile is shown in Figure 6.2. Initially the sample was commanded to the lowest humidity level that the chamber can provide, 11% was measured by the chamber, for 5 hours. This allows the sample to dry and heat up to the chamber temperature. After 5 hours it was assumed that the parameters would stabilise and the chamber would be ramped up by 20% relative humidity level ever 2 hours, to allow the moisture ample time to diffuse into the insulation and to obtain at least 60 on-line measured results during the 2 hour window. After exposure at 90%, the moisture would be decreased to 30%, to observe the expected return of the parameters to the levels seen at 30%.

After conducting the humidity cycle as set out in Figure 6.2, it was evident that the parameter change was considerably higher at high levels of humidity. An additional humidity cycle was added to test detection of high moisture ingress. The humidity was increased to the maximum for 8 hours, and afterwards decreased to the minimum.

6.1.3 Results

All data is presented as far as possible on the same y axis scale to allow comparison as well as using the same method of data processing for all graphs. Both the single frequency C_{eq} and R_{eq} data are at 6kHz.

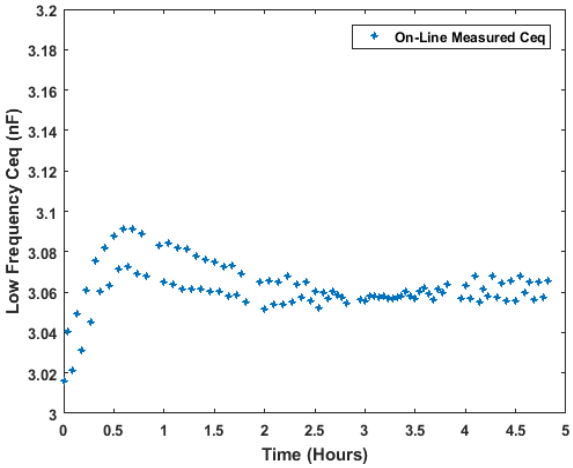

FIGURE 6.3 FIRST 5 HOURS CEQ AVERAGE OF FIRST 5 HARMONICS

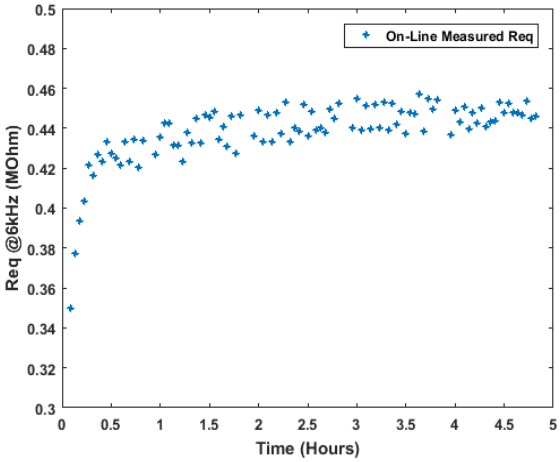

FIGURE 6.4 FIRST 5 HOURS REQ AT 6KHZ BEFORE MOISTURE INTRODUCTION

During the first 5 hours Req shown in Figure 6.4 rapidly increases until it settles to a value of 0.44 MOhm. At the start, Ceq increases as seen in Figure 6.3 and soon stabilises after an overshoot, this is seen at the start of all other samples in Chapter 5. The low frequency Ceq settles down to a steady state after the first 3 hours of the test.

The complete Ceq result is shown in Figure 6.5. The variation of Ceq is plotted alongside the moisture command of the environmental chamber. A distinct change in Ceq is seen immediately after 5 hours, when 30% humidity command was given to the chamber, however relatively little change was observed at humidity levels of 50% and 70%. Between 12 and 14 hour mark, when the humidity command was set to 90%, the Ceq change can be seen to be the same magnitude as the humidity change from 30% to 70%. The change of C_{eq} is even more pronounced when the humidity command was set to maximum on hour 29 of the experiment, increasing by 3.8% before reaching a plateau. The input power to the machine was supplied via a cable with significant capacitance and dissipation. Cable capacitance comprises half of the measured capacitance, therefore the change of Ceq in the stator is actually closer to 8% at maximum humidity.

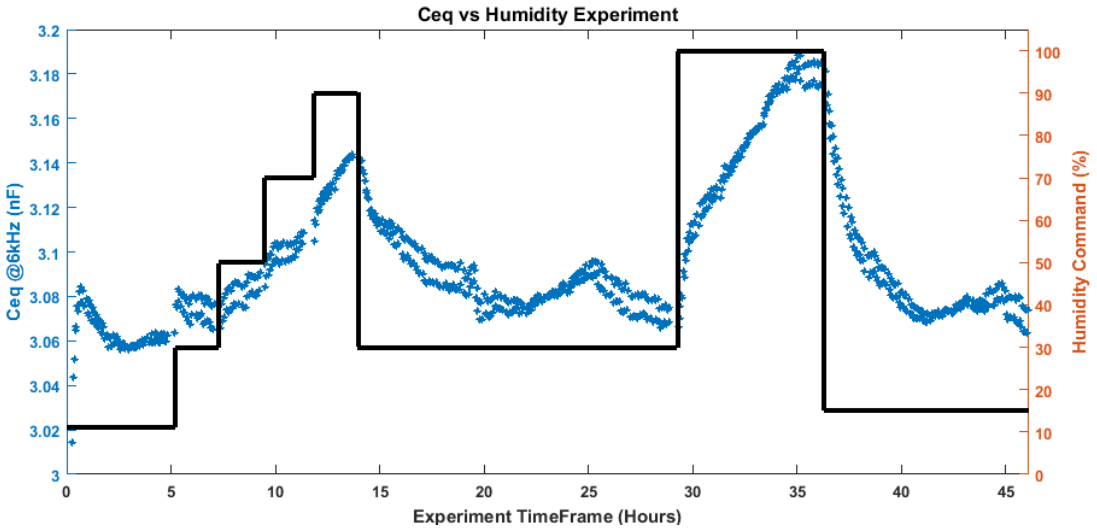

FIGURE 6.5 COMPLETE CEQ RESULTS VS HUMIDITY COMMAND

After the first humidity cycle it was speculated that little humidity change did not result in a significant change of parameters until very high humidity levels were present, resulting in condensation. Results of Req @6kHz shown in Figure 6.6 support this argument, where almost no change was observed with moisture commands between 30% and 70%, while a large decrease is seen with a 90% moisture command.

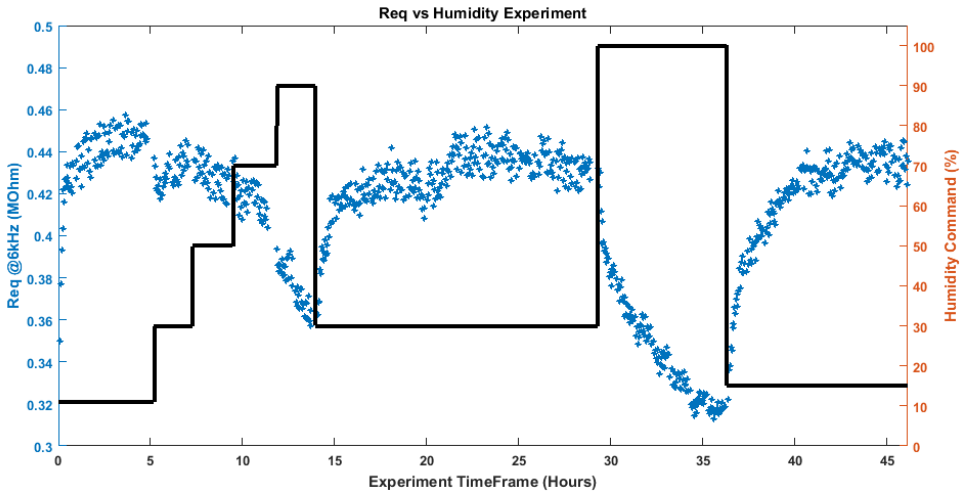

FIGURE 6.6 COMPLETE REQ RESULTS VS HUMIDITY COMMAND

It can be seen that after the moisture was decreased to 30%, the parameters both in Figure 6.5 and Figure 6.6 returned to the state present at the 6hour mark. The Ceq result showed a slight perturbation at the 25 hour mark; however this did not come close to the change observed at 90% humidity. The perturbation illustrates the main problem of health diagnosis and detection; at what threshold can the change be considered abnormal? To answer this question, as well as to investigate the limits of parameter variation with maximal water ingress, The test was repeated at the 29 hour mark, to introduce the maximum moisture level the environmental chamber can provide.

When maximum humidity was applied at hour 29 of the experiment, it was observed that both the Req and Ceq parameters moved in the expected direction and took an exponential path to their final destination. This makes sense considering that initial rapid ingress would go into the most accessible gaps in the insulation, eventually reaching a limit where no more ingress is possible. The parameters reached steady state after about 6 hours of the step at the 35 hour mark. The return of the parameters to previous levels after removal of humidity followed a similar exponential path a similar time constant.

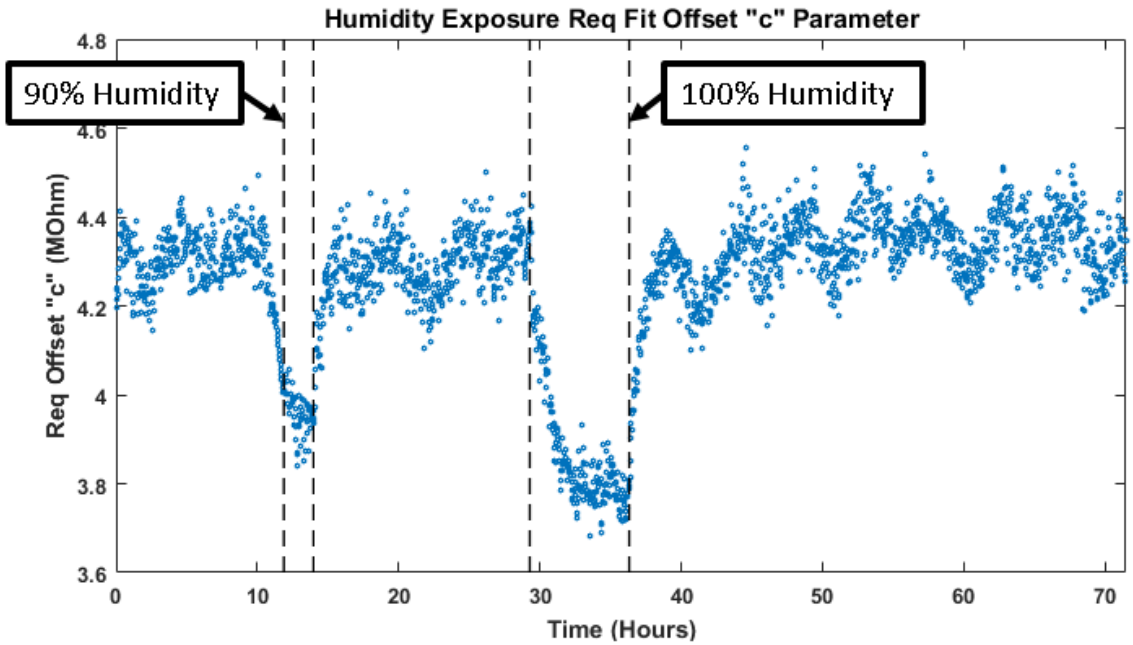

FIGURE 6.7 FITTED R_{EQ} GRADIENT PARAMETER 'C'

To identify moisture ingress, it was found that using the graph fitting described in Section 3.3, the insulation dissipation characteristic Req, as expressed by the gradient and offset of Req vs frequency at low frequencies, showed a remarkable correlation with the humidity level above 90%. Little change is present in either "m" or "c" parameters until the humidity level is above 90%, whereupon a large change is observed. The plot of the "c" parameter is shown in Figure 6.7 with the increased dissipation indicated by drops in "c" plotted alongside the times when the sample is subject to humidity above 90% as set by the environmental chamber command.

6.1.4 Discussion

The parameter change seen in the results section clearly shows that parameter change is non-linear with respect to moisture concentration. It is proposed that this is due to condition above the dew point. When the humidity reaches a level where it can condense out of the air inside the machine, a large amount of water can enter the windings and insulation and produce a measurable effect.

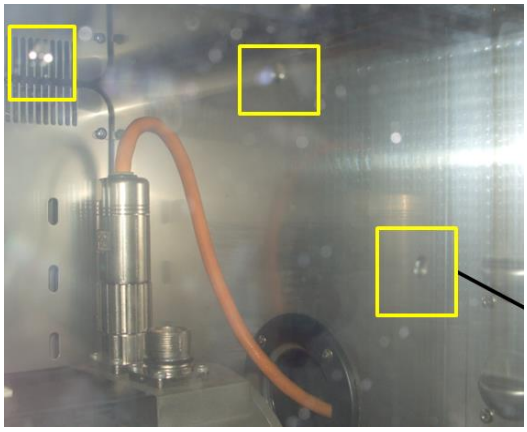

FIGURE 6.8 OBSERVED CONDENSATION INSIDE THE CHAMBER

FIGURE 6.9 CHAMBER FLOOR AT HOUR 37 OF THE EXPERIMENT

Figure 6.8 shows the condensation on the environmental chamber door. Nucleation sites such as dust, dirt and other rough surface would form the centre of the droplets seen. The floor of the chamber is shown in Figure 6.9, covered in water. This picture was taken at hour 35, just before the humidity control was commanded to zero from the maximum value. It is suspected that a similar amount of water would be present inside the machine as inside the chamber in Figure 6.9.

It was shown that the Ceq and dielectric dissipation do indeed rise by 4% and 42% respectively when the humidity level rises from the minimum 11% to the maximum at 100%. The movement is easily detectible and confirms the theory stated in literature with regards to the movement of the parameters.

It was also shown that ordinary change of humidity, up to the point of condensation, can be ignored as part of normal variation of parameters. Further discrimination of humidity can be performed using the fitted parameters of Req as seen in Figure 6.7, showing little to no change until exceptionally high humidity concentrations. This is most useful because it allows easy detection and elimination of false-positives with regards to humidity detection.

6.2 Temperature vs Parameters

It is known from literature [32] that monitored parameters vary with temperature. An additional experiment was performed on Sample 4 by cycling the temperature and observing the change in parameters, using the on-line and off-line monitoring.

The main aim of this experiment is to establish a temperature-parameter ($C_{eq}R_{eq}$) characteristic, and observe how this changes with age. In an industrial setting, variations of temperature are likely and this measurement will show how much effect these variations will have on parameters. If the temperature measurement or estimation is available, the relationship can be used to normalise measured parameters to a single temperature for consistent comparison with historical data.

6.2.1 Experiment Setup

The temperature for Sample 4 was cycled from the test temperature of 215 °C down to 58 °C. The temperature is then stepped in four steps back to test temperature. The parameters are measured both using the on-line equipment during operation, and the Hioki IM3570 instrument when the temperature has reached a plateau.

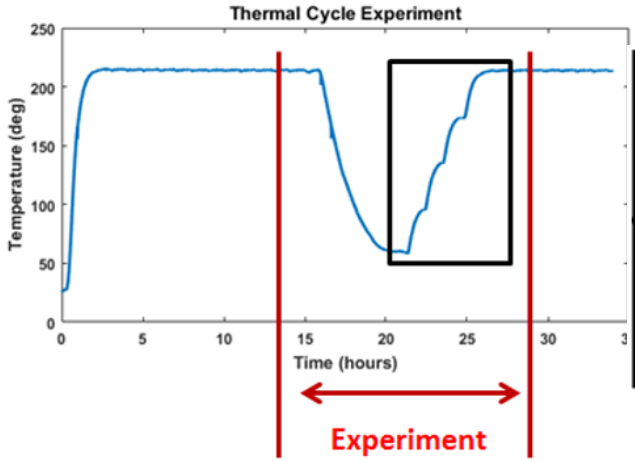

FIGURE 6.10 TEMPERATURE CYCLE EXPERIMENT

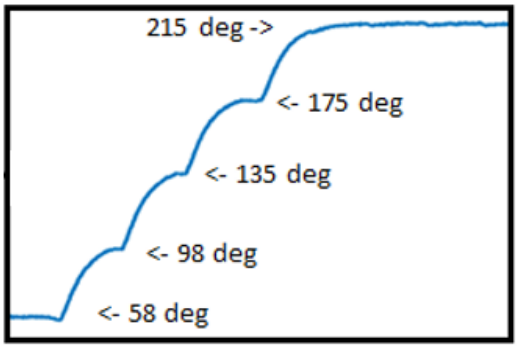

FIGURE 6.11 TEMPERATURE STEPS

The experiment cycle is shown in Figure 6.10, with the steps emphasized in Figure 6.11. The experiment is performed three times, at three different points of sample lifetime. The first experiment occurs after 15 hours after starting operation of Sample 4, the 2nd after 25 days, and the last repeat after 32 days since start. Each experiment requires approximately 12 hours to run the full cycle.

It was judged that a small number of slow cycles would not damage the sample significantly, and therefore the expected time of failure for Sample 4 would not be affected.

FIGURE 6.12 THERMOCOUPLE GLUED TO SAMPLE 4 STATOR

During preparation of Sample 4, high temperature glue was used to attach a K-Type thermocouple to the stator. The location of the temperature sensor is pictured in Figure 6.12, it was not possible to insert the thermocouple directly into the winding. As the oven provides the temperature control, the stator iron temperature should be the same as that of the winding. The thermocouple is connected to the popular MAX6675K cold junction compensated module to send temperature data to a logging device through the SPI bus.

6.2.1 Results and Discussion

The results are presented in two sections, capacitance and equivalent resistance are presented at 6 kHz separately. Results at this single frequency are sufficient to demonstrate the concept of parameter variation, as well as showing the difficulties in practical implementation of compensation.

C_{eq} Result

The capacitance vs temperature result is shown in Figure 6.13 for all three experiments, with on-line data plotted alongside capacitance measured from the off-line instrument. The C_{eq} result shows a clear relationship between temperature and capacitance, with increasing C_{eq} with increased temperature. The root cause of this effect comes from a variety of causes, increased pressure at higher temperatures when the copper conductors and iron core expand, decreased viscosity of resin allowing greater surface area contact and physical property change of impregnation material [162].

The decrease of C_{eq} due to ageing is observed between different experiments. At temperatures below 180 °C, it appears that the same dC/dT

gradient is observed for all samples. In the first experiment however, the characteristic deviates from a straight line fit at temperature above 180 °C.

In the second experiment, a hysteresis loop is observed as the temperature rises back to test temperature. This is an artefact of apparent C_{eq} recovery, and is diagnosed in Section 5.3.6.

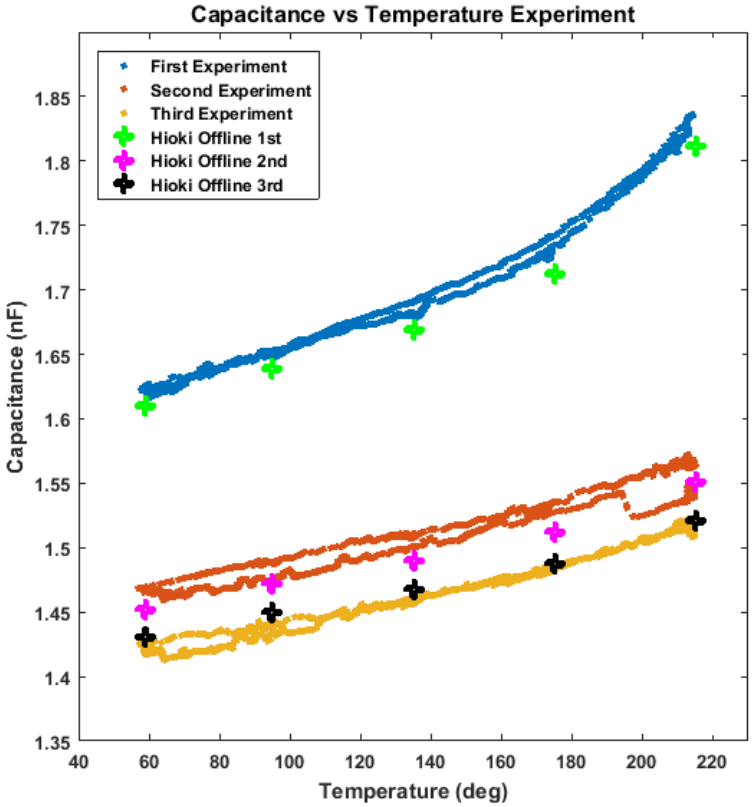

FIGURE 6.13 CEQ VS TEMPERATURE @6KHZ

The consistent gradient dC/dT over time allows measurement of the C vs T characteristic at the start of machine life and using the gradient information to normalise the measured C_{eq} to a nominal temperature. As the normal machine operation for H class insulation is expected to be below 180 °C, it is justifiable to neglect the non-linear portions observed in the first experiment, as operation at these temperatures is unlikely in regular operation.

If temperature sensors are not available, it would be advised to use a thermal model to estimate the machine temperature or a learning algorithm to learn the C_{eq} response to machine losses. Difficulties in the latter would be the long time required to learn the thermal behaviour of the machine, as well as the influence of a varying ambient temperature. Alternately, it has been noted that the value of C_{eq} rise is 7.2% between 60 °C to 180 °C, a value of 0.6% per 10 °C. For machines with predictable small temperature cycles during their life, it may be acceptable to neglect the C_{eq} variation, accepting change of C_{eq} vs temperature as an additional source of noise.

R_{eq} Result

The R_{eq} results with temperature variation are presented in Figure 6.14 and Figure 6.15 where R_{eq} for the first experiment is compared to results for the 2nd and third experiment respectively.

The Req response appears relatively steady for experiment 1 between 60 °C and 150 °C, with a decrease observed at higher temperatures. A wide hysteresis loop is observed, indicating that the R_{eq} characteristic changes, depending on its previous state. In experiment 2, it is observed that the hysteresis characteristic has greatly increased.

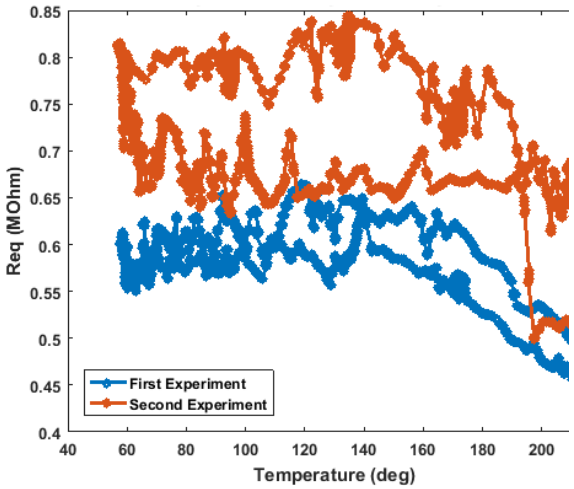

FIGURE 6.14 REQ @6KHZ FOR EXPERIMENTS 1 AND 2

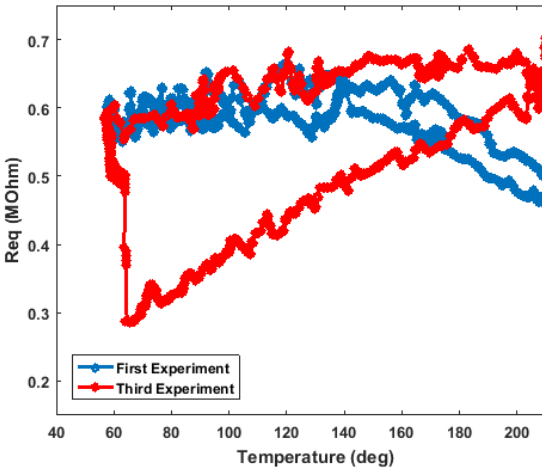

FIGURE 6.15 REQ @6KHZ FOR EXPERIMENTS 1 AND 3

In the third experiment in Figure 6.15, an unusual R_{eq} event has been captured where for a brief time where dissipation increased dramatically after the temperature was lowered to 58 °C. The dissipation returns to its previous value at the end of experiment, however the cause of the event has not been determined. As was observed in Section 5.3.3, the C_{sf} and C_{sf0} parameters show a large change during the third experiment on Sample 4. It is possible that thermal cycling of the sample induced physical contact of the winding, however insufficient evidence is available to fully diagnose the incident.

6.2.3 Conclusion

It was shown that the capacitance during the thermal cycling test presents a consistent characteristic of C vs T. At normal operating temperatures, consistent dC/dT gradient for the three tests allows measurement of initial gradient to achieve compensation required to normalise the measured capacitance value to a nominal temperature. Further research is required to automate the compensation, and ideally remove the need for temperature sensor for temperature feedback.

During normal operation, as shown by results in Figure 6.14 the hysteresis behaviour of R_{eq} will present a serious difficulty of normalising the R_{eq} parameter to a nominal temperature value. At best, when the machine is relatively healthy, at temperature below 150 °C indicated by experiment 1, it may be possible to establish a trend of dR/dT, however as the sample ages, the hysteresis effect cannot be ignored. Alternately it may be possible to monitor the hysteresis characteristic itself as an indicator of machine ageing. More research and practical experience of dissipation during temperature cycling is required to establish a consistent relationship. Further research is also required to enable diagnosis of unusual events, as observed in the third experiment.

6.4 Extra Sample Results

Diagnosis of all failed samples in the experiment in Chapter 5 shows that all samples failed through the weakness in the phase-phase layer, in this case protected only by the wire insulation, caused by the manufacturing practice to not insert a phase-phase insulation layer to reduce manufacture complexity and cost. The weakest link the machine insulation is therefore the phase-phase contact in the machine with distributed winding as it has to withstand the full line-to-line voltage. The ground-wall separation withstood the degradation and acted only as global indicator as to the level of life lost. It was desired to observe a breakdown between phase-ground to complete the study of insulation failure, therefore a special sample with concentrated windings was commissioned for an accelerated ageing test.

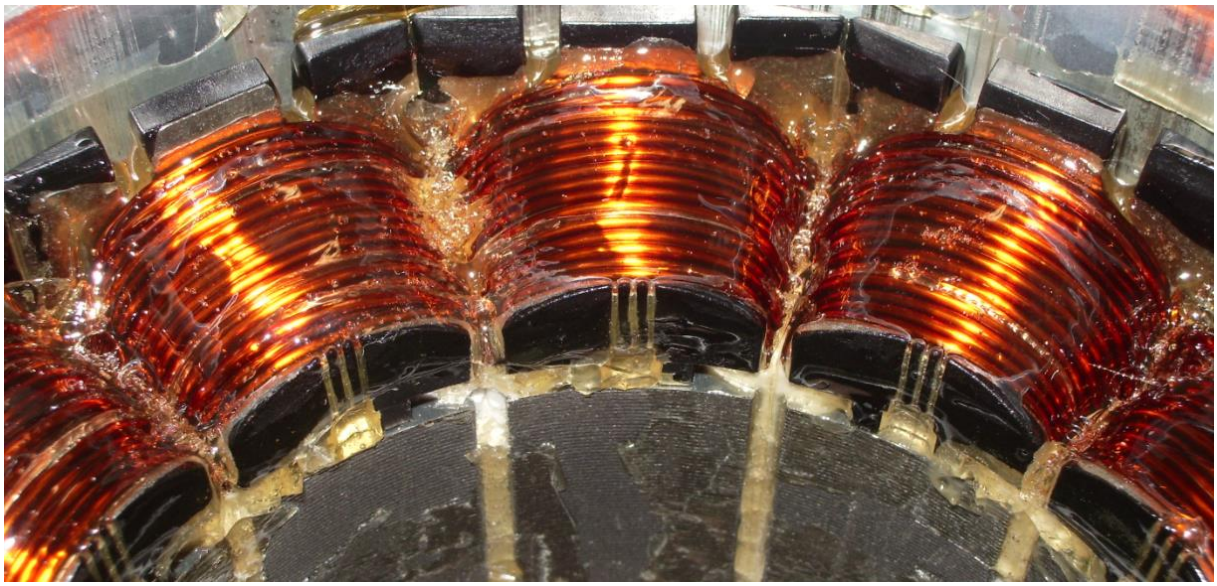

FIGURE 6.16 SAMPLE 5 END WINDINGS

The end-windings for the fifth sample tested are shown in Figure 6.16. The machine is rated at the same power and speed as the other stators used in Chapter 5, however the windings on the special sample are concentrated rather

than distributed. Each coil is tooth wound and separated from adjacent coils with slot liner, and the stator winding is impregnated with the same resin used for the machine with distributed windings. A pre-formed bobbin insulation layer is placed on the teeth to facilitate automatic winding process. Hence the phase-to-ground insulation material is different from the slot liner in the distributed winding machines. Nevertheless it is expected that with additional phase-phase insulation, the failure mode is more likely to be between phase-to-ground.

The additional sample is to be tested during the time allocated in Chapter 5 for additional testing, in parallel with Sample 1. It was decided that Sample 5 was to operate at 230 °C. As the insulation class of Sample 5 is the same Class H as the stators used in Chapter 5, a similar failure time as Sample 2 was expected, also operating at 230 °C, failing after 25 days. The same equipment would be used for monitoring Sample 5 as those used in the test in Chapter 5, and the same ageing methodology would also be applied.

6.4.1 Aims

The main aim of testing the additional sample is to observe the ageing of a sample with high quality end-winding insulation. The difference in time of failure and observations of the failure mode are important to note as this sample represents machines rated for high stress high duty applications.

The phase-to-ground insulation materials used in this sample are different to those used in Chapter 5, however observation of the equivalent capacitance and dissipation are to be noted and compared. Pre-cursors to failure and observations of failure threshold for parameters form the secondary aims.

6.4.2 Results

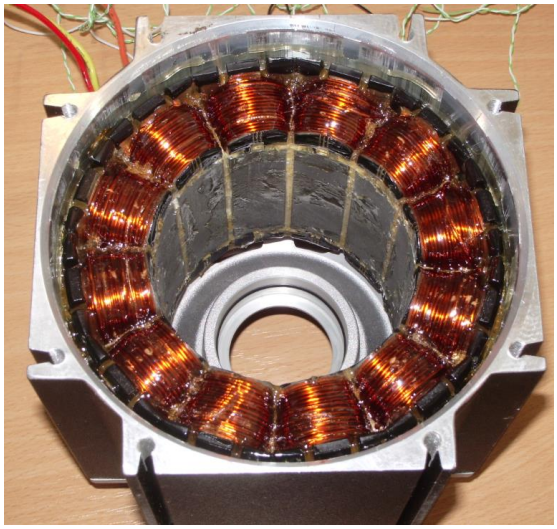

FIGURE 6.17 SAMPLE 5 BEFORE TEST

FIGURE 6.18 SAMPLE 5 AFTER AGEING

The sample before the test and after is shown in Figure 6.17 and Figure 6.18 respectively. The experiment did not go as planned, as the sample failed after a considerably longer time than as was expected from its class H rating and operation initially at 230 °C. Sample 5 failed after 153.9 days of operation compared to 25 days of Sample 2 operating at 230 °C. It was judged necessary to increase the sample temperature to 245 °C on day 111, to increase degradation to a level adequate to cause failure in the time allotted to the experiment.

Factoring in the temperature increase, using the rule of thumb of 10 °C per lifetime halving, the sample life equates to operation of 234 days at 230 °C, or an equivalent temperature index of 212 °C was resultant, rather than 180 °C expected for a Class H insulation system.

The much longer degradation reflects in the colour of the winding impregnation seen in Figure 6.18. Compared to other samples in Chapter 5, insulation colour is considerably darker, and the insulation material itself is brittle to the touch.

Despite the insulation integrity, the extended ageing time and brittle insulation shown in Figure 6.19 which crumbles at the touch of a fingernail, the machine did not fail through phase to ground. The failure is again through phase-phase contact. A DC insulation resistance test is shown on Sample 5 in Figure 6.20, where apparently the sample presents a very large ground-wall DC resistance, passing the off-line Megger test.

FIGURE 6.19 SAMPLE 5 BRITTLE INSULATION ILLUSTRATION

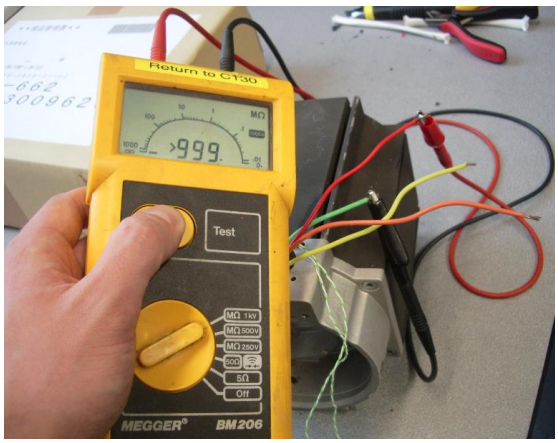

FIGURE 6.20 SAMPLE 5 MEGGER TEST PASS

Failure Diagnosis

The line impedance was measured for Sample 5 at the start of the experiment and after final failure. The starting line inductance is identical per line, value of 10.4mH. Measured inductance after sample failure is shown in Figure 6.21. At low frequencies the machine impedance appears to be very similar to the value measured for the healthy state, however at frequencies above 100Hz, the Y-O line impedance decreases to zero, with other line inductances reducing to ¾ of

original value. Using the analysis from Section 5.3.1, at high frequencies it is possible to suggest that the mechanism of failure is through a phase-to-phase fault.

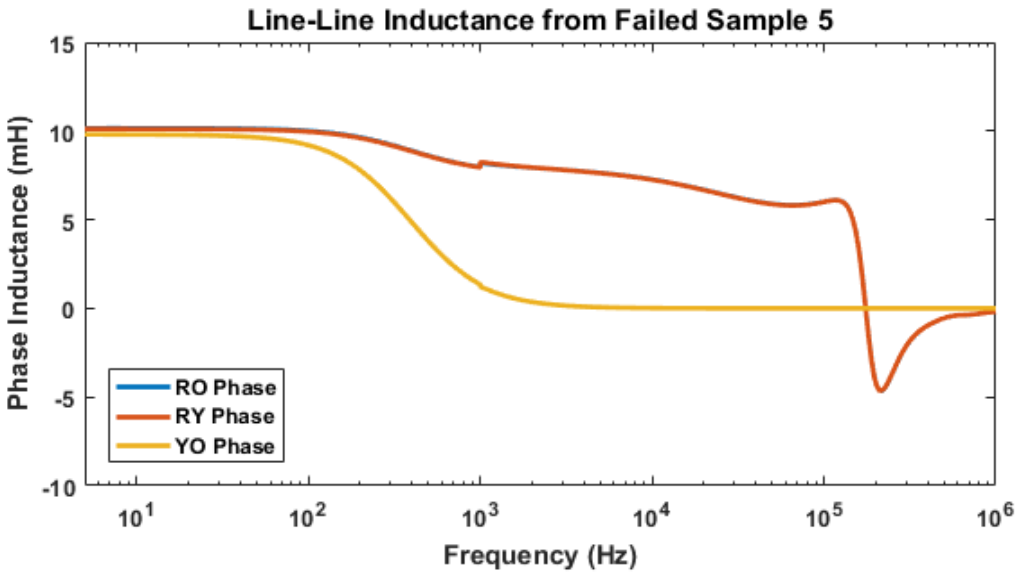

FIGURE 6.21 SAMPLE 5 LINE-LINE INDUCTANCE

To clarify the apparent normal inductance at low frequencies, it is necessary to plot the line resistance at low frequency. In healthy state, the DC line resistance is measured at 0.6 Ohm per line, with resistance increasing at high frequencies due to skin and proximity effect. The failed sample measurement shows similar low frequency resistance, however it is observed in Figure 6.22 that the Y-O line resistance increases to 24.6 Ohm after 100Hz, and remains at this value for all frequencies above 1 kHz.

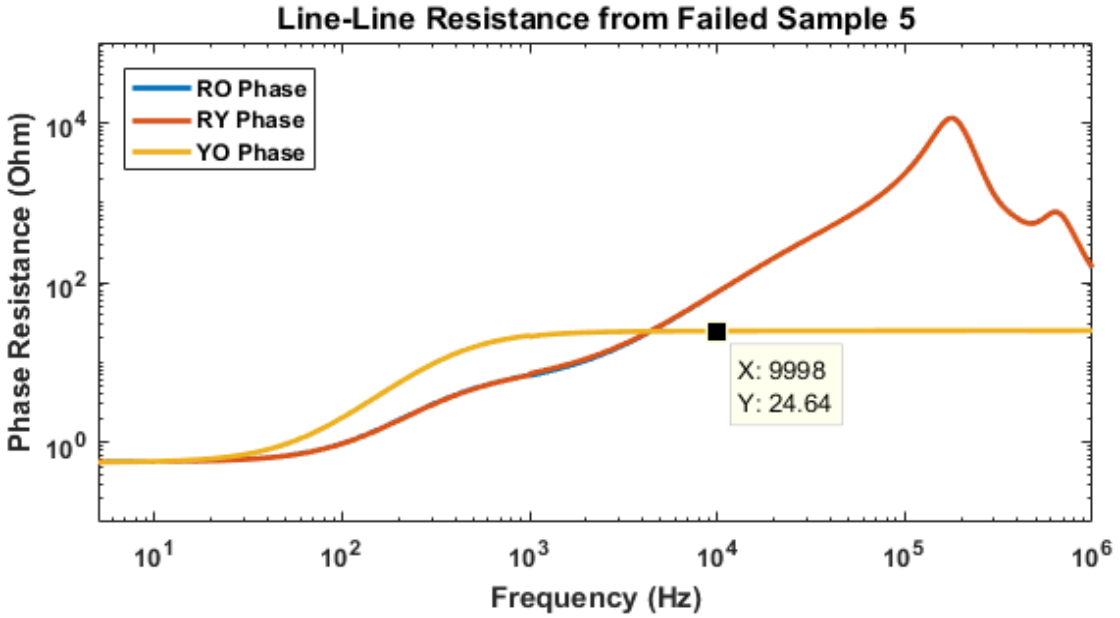

FIGURE 6.22 SAMPLE 5 LINE-LINE RESISTANCE

The most likely fault which can produce the same inductance and resistance as observed for Sample 5 at failure is shown in Figure 6.23. At low frequencies, where the line inductance impedance is lower than the fault resistance, current would flow through the path of least resistance through the inductor. At 400Hz, the line impedance is equal to 24.6 Ohm, and after this point, the fault resistance dominates. The final diagnosis for Sample 5 is failure through a high resistance single phase fault. It is worth noting that the fault resistance may be much lower when the full line-to-line voltage was applied at the point of failure.

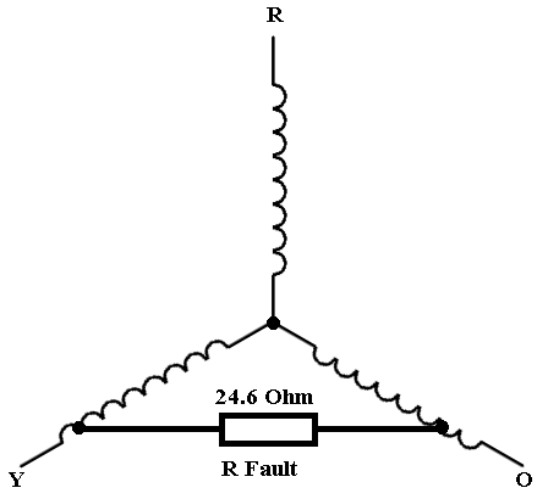

FIGURE 6.23 FAULT DIAGNOSIS FOR SAMPLE 5

Ceq Result

The C_{eq} value throughout the experiment is shown in Figure 6.24. The operational temperature is also noted on the plot. When the temperature increases on day 111, shown in detail in Figure 6.25 the C_{eq} value increases as expected from experiments in Section 6.2. The C_{eq} rate of decrease also increases, as would be expected from a higher temperature operation, inducing higher rate of insulation degradation.

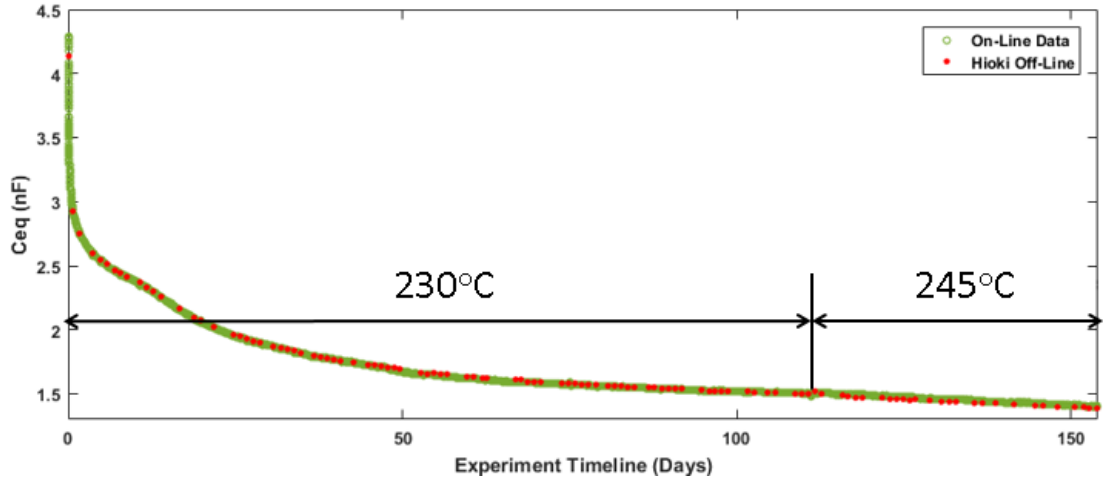

FIGURE 6.24 SAMPLE 5 C_{EQ} OVER TIME

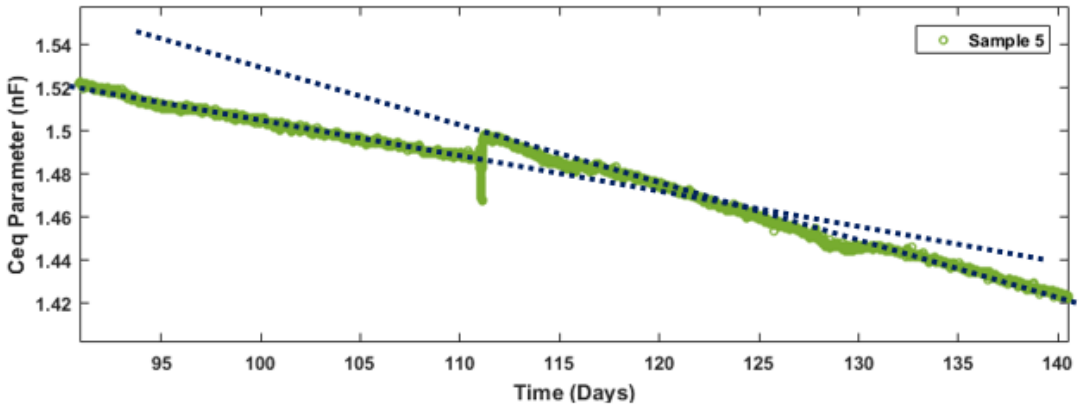

FIGURE 6.25 C_{EQ} RATE OF CHANGE INCREASE

The most unusual feature of Sample 5 C_{eq} results is the progression rate and capacitance decrease over time. At the start of its life, the sample begins with 4.3nF C_{eq} value, which decreases to 1.4nF at the end of the sample lifetime. The C_{eq} value decreases by 30% at the end of day 1 of the experiment, and continues to decrease to a 68% reduction at the end of life compared to the start.

The other unusual quality of Sample 5 is the progression characteristic. Fitting an exponential curve using the method in Section 5.3.9, two trends of capacitance progression are observed, an initial rapid decrease at the start fitted in Figure 6.26, and a long term characteristic which is establishes itself after day 12 of the experiment, shown in Figure 6.27.

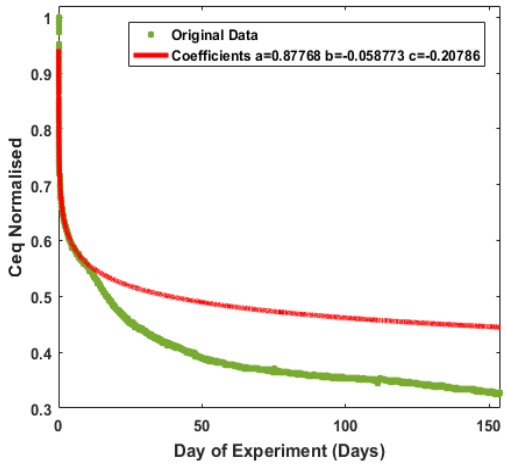

FIGURE 6.26 FIRST 10 DAYS FITTED

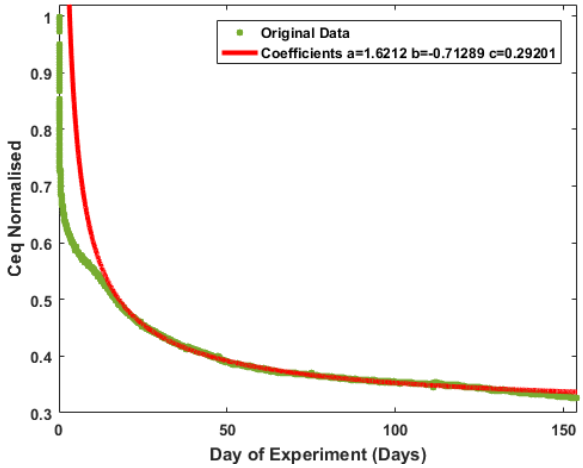

FIGURE 6.27 LONG-TERM TREND FIT

The cause of the extraordinary magnitude of C_{eq} change is explored further using dissipation data. In Figure 6.28, the on-line measurement for dissipation for Sample 5 is shown. In the first day of testing, the dissipation increases to 50%, rapidly decreasing to a value of 15%, after day 12, the dissipation decreases to 7%, and remains between 0.5% to 3% from day 25 until the end of life.

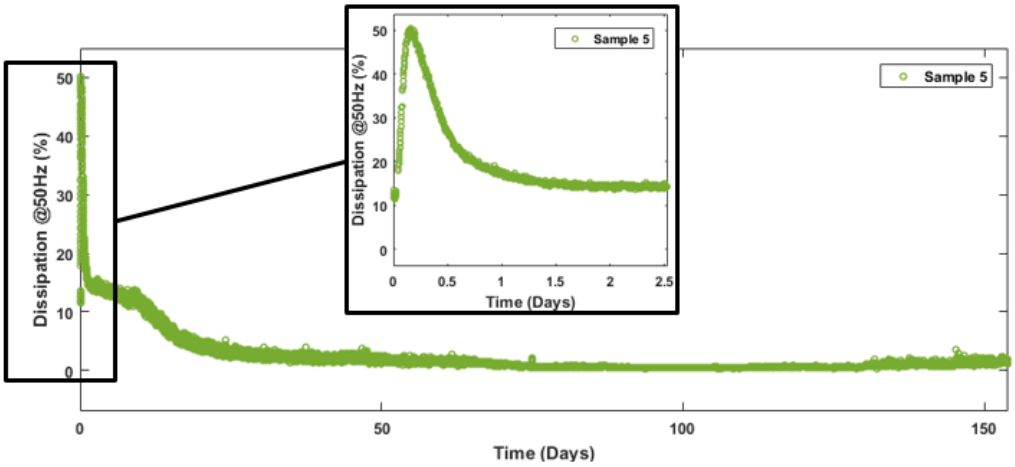

FIGURE 6.28 FAULT DIAGNOSIS FOR SAMPLE 5

Initial spike in dissipation, combined with rapidly dropping C_{eq} is a classic signature of insulation impregnation curing procedure. Uncured insulation consists of short polymer chains, which can dissipate a lot of energy through vibration. Depending on the insulation type, curing process is initiated using a secondary chemical and/or application of heat [163]. When the insulation is cured, short polymer chains start to form longer chains, and start cross linking [158], both processes which decrease dissipation. The shortest polymer chains, the volatiles, boil away reducing the amount of insulation material present, and therefore result in a rapid decrease of C_{eq}. It appears that the sample delivered was not cured prior to delivery. Improper curing would account for the anomalous C_{eq} behaviour at the start of the experiment.

6.4.3 Conclusion and Discussion

In Sample 5, extreme ageing behaviour was observed. After an initial unusual behaviour of Ceq and dissipation caused by improper curing of the sample, the Ceq and dissipation parameters progressed similar to that observed for samples in Chapter 5. It was also observed that the capacitance progression rate changes as expected during a temperature change event, validating the idea of using a final threshold value of Ceq for insulation monitoring purposes.

The sample eventually failed through phase-to-phase fault, same as the Samples in Chapter 5, despite the additional phase-phase insulation. The longevity of this extra sample can be attributed directly to the winding configuration and additional layer of phase-to-phase insulation. To extend the lifetime of machines feedback has been delivered to the stator manufacturer with regards to the effect of including inter-phase insulation on the thermal rating of the machine.

The long effective lifetime of the sample however is under question, as the visual inspection shows high brittleness of the insulation. In standard IEEE117 [32],

it is recommended that a cycle of vibration and moisture exposure is performed during accelerated lifetime testing to induce mechanical stress. Weakness in methodology used in Chapter 5 is illustrated by the results in Sample 5, where a high level of brittleness does not affect the lifetime significantly, as the sample is not subjected to any mechanical stress. It is strongly recommended that further testing includes mechanical stress as part of the methodology, to crack brittle insulation and cause break-down more representative of normal operation.

The aims of this experiment have not been fulfilled, as the phase-to-ground failure was not observed, the pre-cursor to failure have not been identified, and due to the extreme behaviour of parameters at the start of experiment, threshold values for parameters at failure are incomparable to those measured in Chapter 5. Important information however has been obtained regarding insulation characteristics of real machines, improvements to insulation system have been recommended to manufacturers and the importance of correct ageing methodology has been identified.

6.5 Summary

In this chapter, literature assumptions with regards to the effect of moisture and temperature on the capacitance and dissipation parameters have been tested. The humidity dependency results validate the assumptions from literature with regards to expected capacitance and dissipation increase. In addition, model fitting of dielectric dissipation has been shown as a successful tool to detect extreme moisture ingress.

Capacitance variation with temperature has been verified and shown to contain a consistent characteristic which may be used to normalise the capacitance value to a single nominal temperature. Dissipation results show hysteresis, based on either heating or cooling and differing behaviour at different insulation ages. Further work is required to use the dissipation values for diagnosis in machines with large temperature cycles.

Measuring the insulation health of a sample with an improved phase-to-phase insulation showed that the phase-to-phase insulation is the component most stressed under inverter operation. Limitations of the testing methodology have also been identified, with recommendations for more realistic testing suggested.

Chapter 7

Summary and Future Work

This chapter summarises the research carried out in the undertaking of the PhD. Conclusions are listed and future work is suggested to develop the field of health monitoring, diagnosis and prognosis of lifetime of high availability drives.

7.1 Work Summary

Modern drives consist of a machine driven by an inverter system. Increasingly, drive systems have been integrated into both safety critical and cost critical areas, requiring high availability, minimal downtime and high duty cycle operation. Similar requirements from larger machines in the fields of power generation and large equipment have met the standard with increased diagnosis of machine health and pre-emptive action to preclude catastrophic failure. The studies described in the thesis focus on the modes of degradation and failure of smaller inverter driven machines, with emphasis on on-line diagnosis during machine operation.

A literature review revealed that the two most prevalent modes of failure of machines are through bearing and winding failure. To complement knowledge about machine failure, an additional literature review of the most vulnerable component, bearings and the associated bearing monitoring systems was carried out. The system tested is capable of on-line monitoring of bearing status, using a stand-alone unit with minimal effect on the rest of the drive system. The test of the bearing system demonstrated that commercial bearing monitoring technology is relatively mature and was capable of discriminating between new bearings and worn bearings used in the experiments described in Chapter 2.

The gaps in literature have identified the monitoring of long-term insulation breakdown as the main topic of interest for research. An extensive literature review showed that it is possible to link insulation impedance change over time to the chemical and physical degradation of the insulation layer. A common mode model for insulation behaviour was proposed, combining the high frequency response of models used in electromagnetic compatibility validation, and the dissipation expected from dielectric losses of insulation material. Tracking the change of model parameters using the fitting methods presented would allow analysis of winding degradation over time from both physical and chemical damage.

Tracking the ground-wall insulation impedance over time using leakage current has been identified as the most promising method to monitor insulation. In literature there have been successful attempts using leakage current resulting from fundamental frequency excitation for line connected machines to the extent of development of a specialised commercial sensor system. Some attempts have also been made to use the inverter excitation as the source of leakage current. Although initial attempts have been made, the phenomenon of leakage current due to inverter switching has not been fully exploited.

A novel insulation monitoring system has been designed and built to measure ground-wall insulation capacitance and dissipation. The system used the common mode drive switching harmonics as the voltage source across the insulation. Measurement of common mode current allows assessment of the insulation impedance and identification of the parameters of the developed winding insulation model. The measurement is made, by definition, when the drive is operation without any interruption. Testing of the monitoring system has shown that the precision of the instrument constructed is comparable to the requirements for off-line equipment used to conduct routine testing on large machines.

Further testing of the equipment indicated that the measured parameters when the machine stator was subjected to humidity and variation of temperature responded in accordance with literature. The most important testing however involved ageing four samples at four ageing rates to measure the progression of parameters over time. An additional sample was also aged to observe a different failure mode.

During accelerated lifetime testing several discoveries were made about the ageing process of insulation. In the testing, the main insulation degradation mechanism was the loss of insulation through escape of volatile elements, however the two most important chemical changes of real machine ageing – oxidation and cross-linking were also observed. Due to machine construction, the four samples failed through the phase-to-phase insulation, which was composed of only the wire insulation. The failure times recorded adequately represented class H insulation and allowed the monitored phase-to-ground insulation state to be used as a global insulation health indicator. Although a concentrated winding machine with additional insulation between phases was also tested as the 5^{th} extra sample, it too broke through phase-to-phase fault after operation considerably longer than what is to be expected for Class H insulation.

Observations during long term experiments showed unusual intermittent behaviour in capacitance and dissipation. Further inspection of the data, simulation and emulation was carried out to investigate the causes of anomalies. It was determined that the most likely cause of the observations is the formation of benign resistive tracks on the surface of the winding.

The chemical degradation processes anticipated form the literature review were observed, however neither oxidation nor cross-linking was the main cause of failure of the insulation. There is an inherent dilemma between more realistic testing and isolating physical phenomena. Ageing experiments here showed all modes present due to complicated sample construction and operation. Further laboratory testing is required to test for these modes under controlled conditions.

The most important observation from testing the first four samples showed that measured low frequency capacitance trend over time was highly deterministic. The rate of capacitance progression was proportional to the ageing rate with a similar capacitance value observed at the failure of the four samples. The threshold has been quantified to establish the confidence limits of capacitance at sample failure to determine the decrease that would correspond to 90% of the samples failing. A methodology for prognosis of remaining lifetime has been presented based on the capacitance decrease progression and the measured threshold value. It was shown that it is possible to use the capacitance measurements from first quarter of sample life to establish the trend and extrapolate to the time of failure.

7.2 Future Work

During testing of Sample 5, the limitation of the accelerated ageing method was shown, in that real machines would be subjected to multiple sources of stress. Thermal and electric ageing is insufficient and mechanical vibration and thermal cycling is required to correctly represent real machine operation.

Although not explicitly tested for, the results observed in Chapter 5 and further investigation revealed that the proposed insulation monitoring system is capable of detecting faults and degradation of aspects other than the ground-wall insulation. Additional test methodologies require to be devised to investigate the possibility of using the proposed system to monitor other faults possible in machines, such as turn-to-turn fault and tracking. Further research is required to model the effect of faults on the measured insulation common mode model parameters, with practical verification.

The cost of equipment used here to monitor the low voltage low power machine far outweighs the cost of the motor. The current sensor dominates the cost due to the high specifications required to replicate off-line testing. An attempt has been made in Appendix C to push the limits of off-the-shelf low cost sensor technology to implement cost-effective monitoring of small machines. The results show that current sensor stability over time is the limiting factor of the measurement, wiping out the accuracy gains of data processing presented here.

Development work by the current sensor industry is required to develop low-cost current sensors for application in health monitoring.

Practical problems with monitoring, regarding the variation of parameters with temperature, humidity and anomalous offsets require advanced data processing solutions to be useful in industry. The prognosis algorithm presented in Chapter 5 must operate with capacitance data gathered in real world conditions. Effects such as the sharp decrease of C_{eq} due to resistive tracking must be accommodated for in data processing to return consistent measurement of degradation rate. Learning algorithms must be developed which are capable of detecting anomalous data and eliminating false positive alerts by using historic data to establish norms.

Continuous tracking of insulation capacitance and dissipation is a newly emerging sub-section of insulation diagnosis and prognosis. Currently very little information exists about real life progression of capacitance and dissipation parameters over time. Interpreting the results obtained from the experiments performed in Chapters 5 and 6 required using understanding physics and chemistry and limited laboratory insulation ageing experiments to establish the expected movement of parameters. The experiments performed in Chapter 5 show that it is worthwhile to monitor the capacitance of insulation in real time for the purposes of diagnosis and prognosis of future failure.

The next step in this research would involve industrial participation to monitor the capacitance and dissipation parameters during product development and testing. More information is especially required of dissipation, in the testing performed the variation of dissipation trends did not allow a conclusion as to the typical behaviour of dissipation over time. Large scale testing, only possible in industry, would not only improve the confidence in setting a capacitance failure threshold, but also possibly reveal the dissipation trend of machines in real life. The work done here is simply a pre-lude, a demonstration and a chance to make mistakes necessary for development of a better system and methodology.

Appendix A
COMMON MODE INVERTER HARMONICS

There are three sources of common mode inverter harmonics, from the rectifier front end, the space vector modulation and the zero sequence switching voltage. This appendix contains the mathematical derivation of the harmonic content of each of these sources in detail.

A.1 Rectifier Front End

In a typical three phase system, where the building is fed by a D-Y transformer, the ground is defined by the central midpoint of the Y connection. The simulated rectified 3 phase voltages in this system are shown in Figure A.1. In addition to the positive and negative DC bus rails, the sum and difference of the rails are also shown. The difference gives the DC bus voltage and the sum returns the common mode voltage, these are expressed in Equations (A.1) and (A.2). To calculate the harmonic content of the common mode voltage, one needs only the harmonic content of the positive and negative DC bus voltage rails.

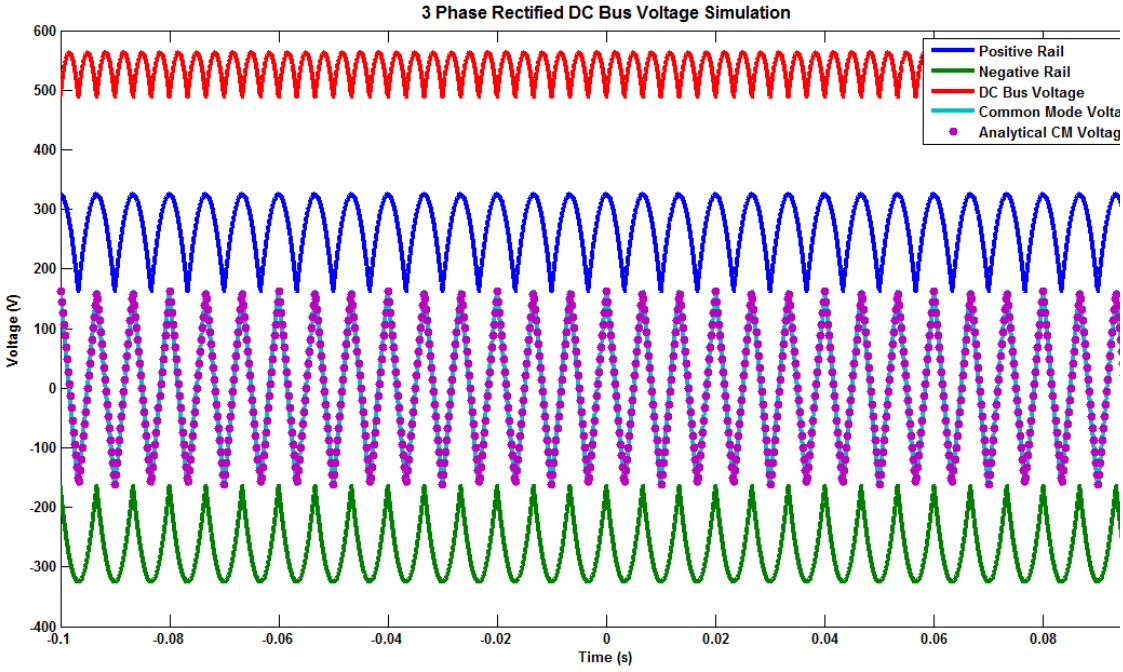

FIGURE A.1 SIMULATED THREE PHASE RECTIFIED VOLTAGES

$$V_{dc\_link} = V_{dc+} - V_{dc-} \quad \text{(A.1)}$$

$$V_{com\_mode} = V_{dc+} + V_{dc-} \quad \text{(A.2)}$$

The positive and negative DC bus rail voltage harmonic content is expressed in Equations (A.3) and (A.4) respectively.

$$V_{+} = \frac{3V_p\sqrt{3}}{\pi}\left(\frac{1}{2} + \sum_{n=1}^{\infty}\frac{(-1)^{(n+1)}}{9n^2-1}\cos(3n\omega t)\right) \quad \textbf{(A.3)}$$

$$V_{-} = \frac{3V_p\sqrt{3}}{\pi}\left(-\frac{1}{2} + \sum_{n=1}^{\infty}\frac{1}{9n^2-1}\cos(3n\omega t)\right) \quad \textbf{(A.4)}$$

Substituting Equations (A.3) and (A.4) into in Equations (A.1) and (A.2), the DC link voltage and the common mode voltage can thus be calculated as in Equations (A.5) and (A.6).

$$V_{dc\_link} = \frac{3V_p\sqrt{3}}{\pi}\left(\sum_{n=1}^{\infty}\frac{1-(-1)^{(n+1)}}{9n^2-1}\cos(3n\omega t)\right) \quad \textbf{(A.5)}$$

$$V_{com\_mode} = \frac{3V_p\sqrt{3}}{\pi}\left(\sum_{n=1}^{\infty}\frac{1+(-1)^{(n+1)}}{9n^2-1}\cos(3n\omega t)\right) \quad \textbf{(A.6)}$$

The common mode voltage resulting from diode rectification is important as the harmonics only depend on the line frequency, and therefore this can be used as a static signal source in variable speed drives. Harmonics resulting from mains rectification and space vector modulation are undoubtedly the harmonics used in [154] to measure insulation capacitance and dissipation at low frequencies. A high sensitivity current sensor is required at these frequencies due to the high capacitance impedance.

A.2 Pulse Width Modulation Harmonics

As the PWM harmonics are the signal sources for monitoring in Chapters 4, 5 and 6, a thorough understanding of the harmonic content is required. In this appendix, the harmonics are derived from basic principles and the harmonic content of the common mode voltage is presented.

Historically, there have been a number of methods used to generate PWM for inverters. To simplify the analysis, sine wave naturally sampled centre aligned modulation is used as the start of analysis. The derivation gives the general case of inverter harmonics, where the modulating cosine waveform can be modified to include the harmonic effects of space vector modulation addition.

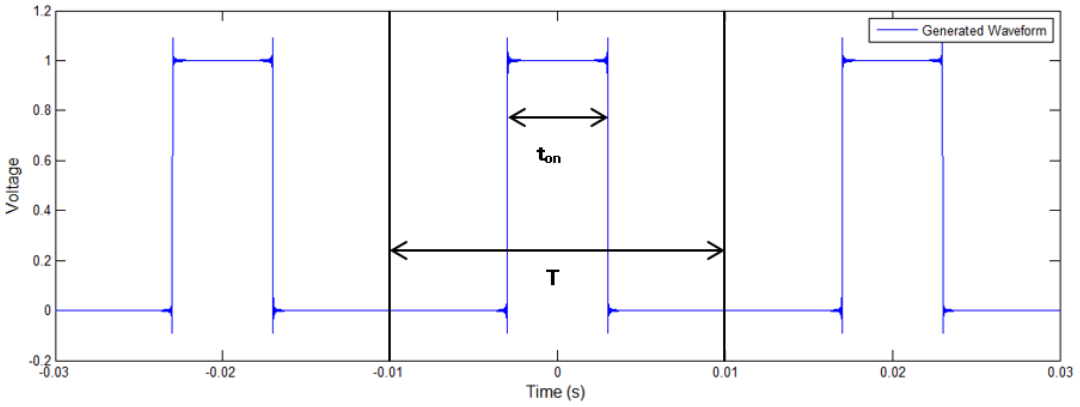

FIGURE A.2 RECTANGULAR VOLTAGE WAVEFORM

The stare of the derivation considers the harmonic content of a rectangular wave in Figure A.2. The voltage consists of a series of harmonics expressed by Equation (A.7), where the average magnitude is defined by the duty cycle in Equation (A.8). The harmonic magnitudes are defined by Equation (A.9).

$$V = a_0 + \sum_{n=1}^{\infty} a_n * \cos(n * \omega_s t) \quad \textbf{(A.7)}$$

$$a_0 = \delta = {}^{T_{on}}/_{T} \quad \textbf{(A.8)}$$

$$a_n = \frac{2}{n\pi}\sin(n\pi\delta) \quad \textbf{(A.9)}$$

In a motor drive, to generate a varying average sine wave, the duty cycle is modulated by a sine waveform as in Equation (A.10). Inserting the sine wave duty cycle into Equation (A.9) returns Equation (A.11) for a_n. To simplify analysis later on, the a_n values are stated as a function of cosine via Equation (A.12) with all terms combined in Equation (A.13).

$$a_0 = \frac{1}{2}(1 + \mathrm{M}\sin(\omega_m t)) \quad \textbf{(A.10)}$$

$$a_n = \frac{2}{n\pi}\sin(n\pi * \frac{1}{2}(1 + \mathrm{M}\sin(\omega_m t))) \quad \textbf{(A.11)}$$

$$a_n = \frac{2}{n\pi}\cos(n\pi * \frac{1}{2}(1 + \mathrm{M}\sin(\omega_m t)) - \frac{\pi}{2}) \quad \textbf{(A.12)}$$

$$a_n = \frac{2}{n\pi}\cos\left[\frac{\pi(n-1)}{2} + \frac{n\pi M}{2}\sin(\omega_m t)\right] \quad \textbf{(A.13)}$$

Using values of a0 and an in Equations (A.10) and (A.13), it is now possible to generate pulse width modulation analytically using Equation (A.7). In Figure A.3, the first 20 "n" harmonics were used to generate a wave with a 50Hz modulation of a 1kHz carrier frequency with a modulation depth of 80%.

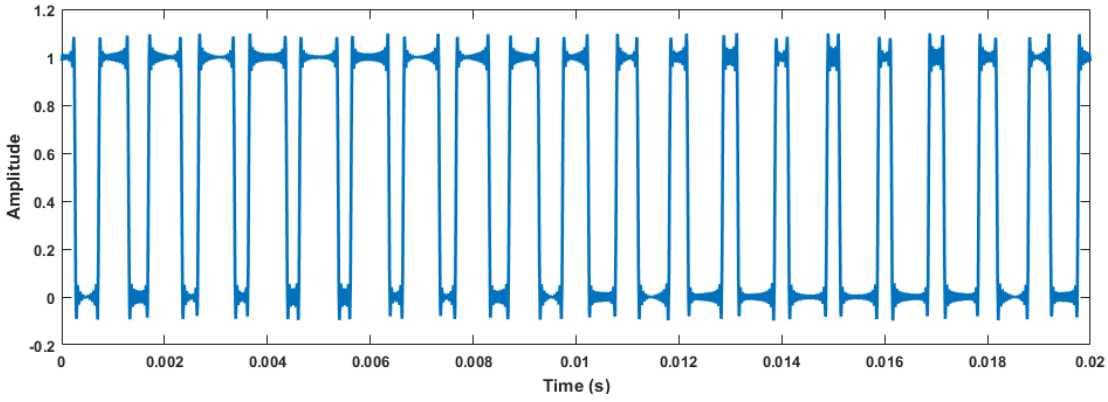

FIGURE A.3 PWM ANALYTICAL GENERATION

For a square waveform, a_n values are 1D values which depend only on the fixed duty cycle and the "n" harmonic. To obtain 1D harmonic values, it is required to expand Equation (A.13) to obtain the position, magnitude and phase of individual PWM harmonics. To perform the expansion, a method used to determine the harmonic content of frequency modulated (FM) waveforms is used.

FM voltage "s" can be written in the time domain as in Equation (A.14). Using trigonometric identities, this can be expanded into Equation (A.15).

$$s(t) = \cos(\omega_c t + \beta \sin(\omega_m t)) \tag{A.14}$$

$$= \cos(\omega_c t)\cos(\beta \sin(\omega_m t)) - \sin(\omega_c t)\sin(\beta \sin(\omega_m t)) \tag{A.15}$$

Equation (A.13) for a_n values can be substituted into Equation (A.15), where $\beta = \frac{n\pi M}{2}$ and $\omega_c t = \frac{\pi(n-1)}{2}$ to produce Equation (A.16). This can be further simplified into Equation (A.17).

$$= \cos\left(\frac{\pi(n-1)}{2}\right)\cos(\beta \sin(\omega_m t)) - \sin\left(\frac{\pi(n-1)}{2}\right)\sin(\beta \sin(\omega_m t)) \tag{A.16}$$

$$= \sin\left(\frac{n\pi}{2}\right)\cos(\beta \sin(\omega_m t)) + \cos\left(\frac{n\pi}{2}\right)\sin(\beta \sin(\omega_m t)) \tag{A.17}$$

It can be seen in Equation (A.17) that for odd integer values of "n", the equation becomes cos(b*sin(x)), and for even values it is sin(b*sin(x)). To expand these factors, Bessel functions of the first order can be used.

$$\cos(\beta \sin(\omega_m t)) = J_0(\beta) + 2\sum_{m=1}^{\infty} J_{2m}(\beta)\cos(2m\omega_m t) \tag{A.18}$$

$$\sin(\beta \sin(\omega_m t)) = 2\sum_{m=0}^{\infty} J_{2m+1}(\beta)\sin((2m+1)\omega_m t) \tag{A.19}$$

Equations (A.18) and (A.19) show the expansion for the two cases that are present in Equation (A.17). In the frequency domain. Substituting Equations (A.18) and (A.19) into Equation (A.17), reinserting the expansion into Equation (A.13) and inserting the a_0 and a_n values into Equation (A.7) results in the full PWM waveform in the time domain in Equation (A.20).

$$
\begin{aligned}
V = V_{dc} + V_{dc} * \mathrm{M}\sin(\omega_m t) \\
+ \frac{4V_{dc}}{\pi} \sum_{n=1}^{\infty} \frac{1}{n} J_0(\beta) * \sin\left(\frac{n\pi}{2}\right) * \cos(n * \omega_s t) \\
+ \frac{4V_{dc}}{\pi} \sum_{n=1}^{\infty} 2 \sum_{m=1}^{\infty} \frac{1}{n} J_{2m}(\beta) \cos(2m\omega_m t) \sin\left(\frac{n\pi}{2}\right) \cos(n * \omega_s t) \\
+ \frac{4V_{dc}}{\pi} \sum_{n=1}^{\infty} 2 \sum_{m=0}^{\infty} \frac{1}{n} J_{2m+1}(\beta) \sin((2m+1)\omega_m t) \cos\left(\frac{n\pi}{2}\right) * \cos(n * \omega_s t)
\end{aligned}
\tag{A.20}
$$

Equation (A.20) for PWM consists of four lines: the first contains the DC bus voltage and the fundamental drive harmonic, the second contains the harmonics resulting only from the switching frequency and the last two lines outline the sidebands around the odd and even switching harmonics "n" respectively. The sidebands can be seen more clearly by expanding the last two lines of Equation (A.20) in (A.21).

$$
\begin{aligned}
V = V_{dc} + V_{dc} * \mathrm{M}\sin(\omega_m t) \\
+ \frac{4V_{dc}}{\pi} \sum_{n=1}^{\infty} \frac{1}{n} J_0(\beta) * \sin\left(\frac{n\pi}{2}\right) * \cos(n * \omega_s t) \\
+ \frac{4V_{dc}}{\pi} \sum_{n=1}^{\infty} 2 \sum_{m=1}^{\infty} \frac{1}{n} J_{2m}(\beta) \sin\left(\frac{n\pi}{2}\right) \begin{bmatrix} \cos((n * \omega_s t) + (2m\omega_m t)) \\ + \cos((n * \omega_s t) - (2m\omega_m t)) \end{bmatrix} \\
+ \frac{4V_{dc}}{\pi} \sum_{n=1}^{\infty} 2 \sum_{m=0}^{\infty} \frac{1}{n} J_{2m+1}(\beta) \cos\left(\frac{n\pi}{2}\right) \begin{bmatrix} \sin(n * \omega_s t + (2m+1)\omega_m t) \\ + \sin(n * \omega_s t - (2m+1)\omega_m t) \end{bmatrix}
\end{aligned}
\tag{A.21}
$$

An alternate method is used to obtain PWM voltage in the time domain in [164], where double Fourier expansion is used to obtain the result in Equation (A.22). The result is the same as derived in Equation (A.21), except that the last two lines have been combined and the phase of the switching and modulating harmonics have been included.

$$
\begin{aligned}
V = V_{dc} + V_{dc} M \cos(\omega_m t + \theta_m) \\
+ \frac{4V_{dc}}{\pi} \sum_{n=1}^{\infty} \frac{1}{n} J_0\left(\frac{n\pi M}{2}\right) \sin\left(\frac{n\pi}{2}\right) \cos(n\omega_s t + \theta_s) \\
+ \frac{4V_{dc}}{\pi} \sum_{n=1}^{\infty} \sum_{\substack{m=-\infty, \\ m \neq 1}}^{\infty} \frac{1}{n} J_m\left(\frac{n\pi M}{2}\right) \sin\left([n+m]\frac{\pi}{2}\right) \cos(n[\omega_s t + \theta_s] + m[\omega_m t + \theta_m])
\end{aligned}
\tag{A.22}
$$

To generate zero sequence voltage, for three phase motors, it is required that θ_m = of 0, 120 and 240 ° is substituted into three equations for voltage and summed together.

$$V = V_{dc} + V_{dc} * M \sin(\omega_m t + \theta_m) + \frac{4V_{dc}}{\pi} \sum_{n=1}^{\infty} \frac{1}{n} J_0(\beta) * \sin\left(\frac{n\pi}{2}\right) * \cos(n * \omega_s t) + \frac{4V_{dc}}{\pi} \sum_{n=1}^{\infty} 2 \sum_{m=1}^{\infty} \frac{1}{n} J_{2m}(\beta) \sin\left(\frac{n\pi}{2}\right) \cos(n * \omega_s t) \cos(2m(\omega_m t + \theta_m)) + \frac{4V_{dc}}{\pi} \sum_{n=1}^{\infty} 2 \sum_{m=0}^{\infty} \frac{1}{n} J_{2m+1}(\beta) \cos\left(\frac{n\pi}{2}\right) * \cos(n * \omega_s t) \sin((2m+1)(\omega_m t + \theta_m)) \quad \text{(A.23)}$$

In Equation (A.23), for the sum of voltages with the three angles, the first line cancels out as expected. The harmonics around the odd values of "n" also cancel, except for values of m = 3, 6, 9.... The harmonics around even values of "n" only exist for values of m = 1, 4, 7.... The second line is not affected, as the switching harmonics are not affected by the phase or frequency of the modulating waveform.

For a waveform therefore with 6 kHz switching frequency, with 200 Hz modulating frequency, it is predicted that harmonics exist at the odd integer values ofω_s, at 6, 18, 30 kHz...

The sidebands around the odd n=1, 6 kHz harmonic are present at 6 kHz ±1200Hz, ±2400Hz...

Sidebands around even n=2, 12 kHz, are at 12 kHz ±600Hz, ±1800Hz...

A.3 Space Vector Modulation

The maximum output phase voltage in inverter drives is limited by the DC link voltage of the drive. It is recognised that for three-phase voltages, where the loads have no zero sequence current, all harmonics with x3 multiples of the main harmonic cancel. It was recognised in literature that addition of 3rd harmonic zero sequence component to the three phase voltages can decrease the effective phase voltage and therefore increase the DC bus utilisation by 15.5%. Generation of PWM using the SVPWM method utilises the same principle. Figure A.4 shows the space vector contribution and the resulting phase voltage, with the voltage reduction compared with the original modulating waveform.

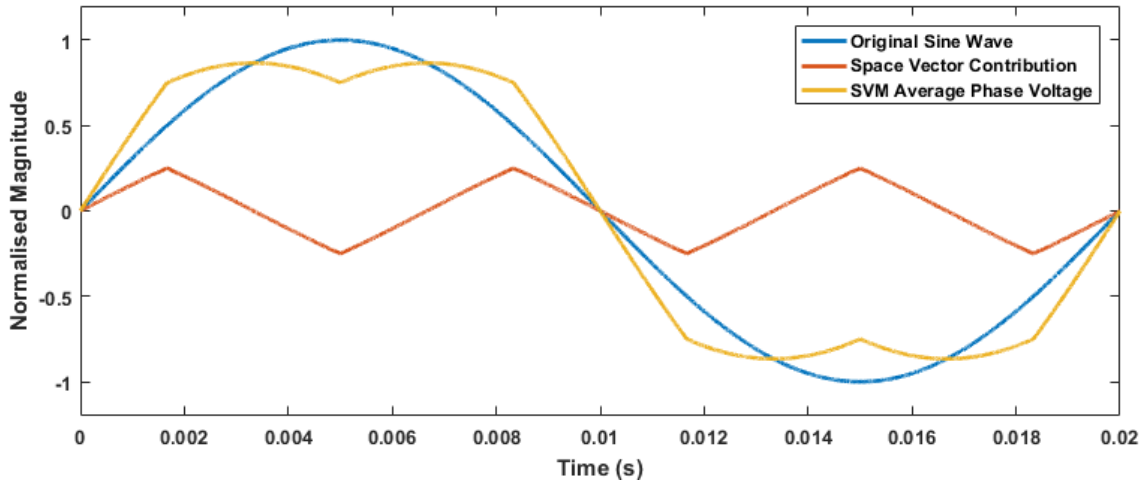

FIGURE A.4 PWM MODULATING WAVEFORMS

It is shown in [164] that the generation of space vector contribution is analogous to the addition of the sum of the positive and negative envelopes of the three phase voltages. The circuit in Figure A.5 shows a practical visualisation of generation of space vector PWM using analogue circuitry to implement the addition of the space vector component to the phase voltages.

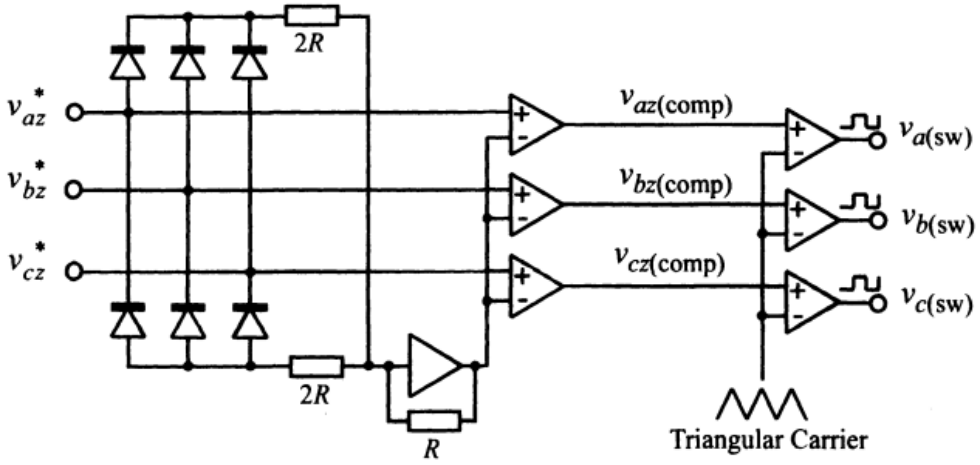

FIGURE A.5 ANALOGUE GENERATION OF SPACE VECTOR PWM [164]

The harmonics due to the space vector are the same as those due to diode rectification, stated in Equation (A.6), where the frequency is that of the modulating wave. To obtain the full drive zero sequence voltage, Equation (A.6) may be substituted into Equation (A.23) to calculate the sidebands due to SVM, however in practice these can be neglected due to their small magnitude. SVM harmonics are only visible in the low frequency part of the spectrum, provided the fundamental drive frequency is low, SVM harmonics should make negligible contribution to the insulation current.

Appendix B

DATA PROCESSING FLOW

This appendix contains all the programming code used in the project to implement the on-line measurement system in Chapter 5 and 6. The FPGA, C and Matlab code are expressed as flow diagram blocks, due to the very large extent of the program code (at least 100 pages altogether).

B.1 C Program

The top level of the software is shown in Figure B.1 where crontab launches the main program once per hour. The main program itself, in Figure B.2 initiates and calibrates the inputs, reads the previous state of the time log "n" and launches the processing run for testing Oven1 and Oven2.

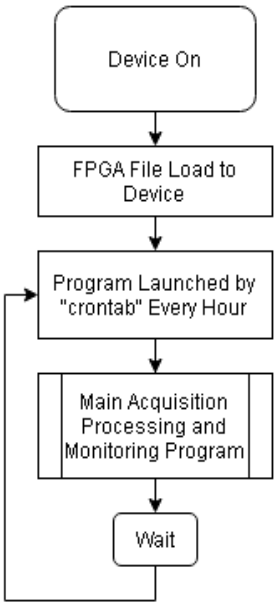

FIGURE B.1 LAUNCH AT TURN-ON

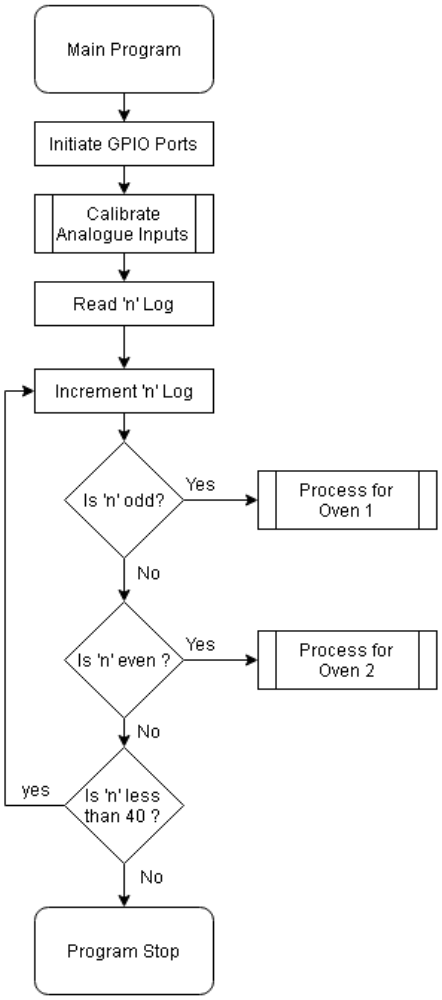

FIGURE B.2 MAIN PROGRAM RUN

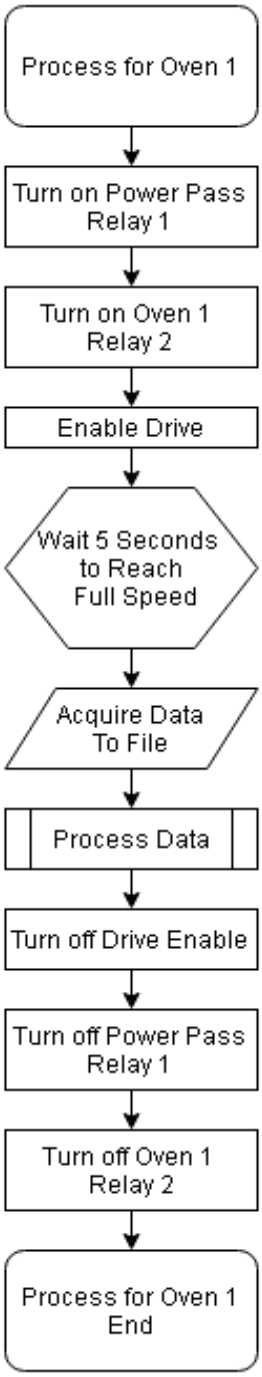

FIGURE B.3 OVEN 1 PROGRAM PROCESS

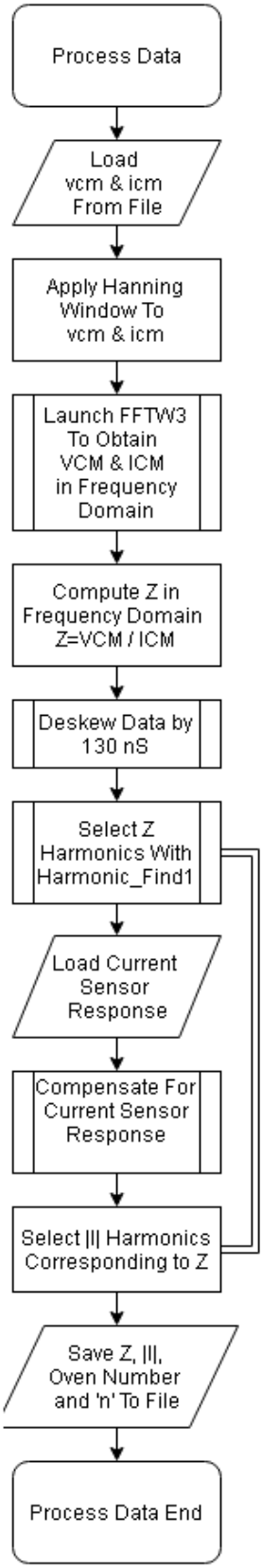

FIGURE B.4 DATA PROCESS CHAIN

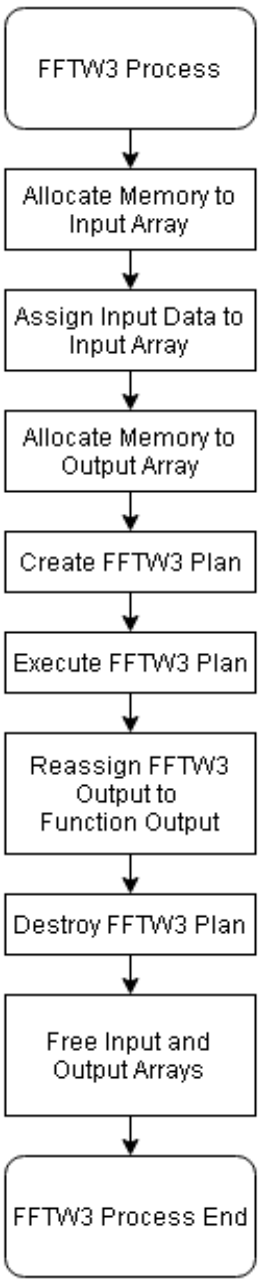

FIGURE B.5 FFTW3 OPERATION

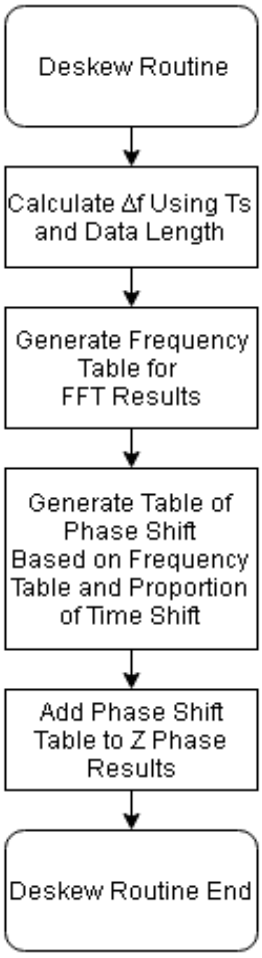

FIGURE B.6 DESKEW ROUTINE

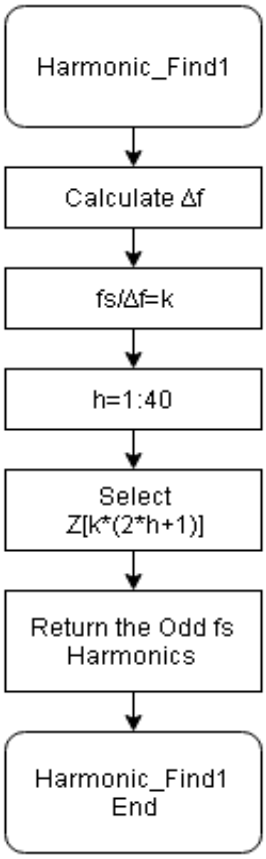

FIGURE B.7 HARMONIC SELECTION

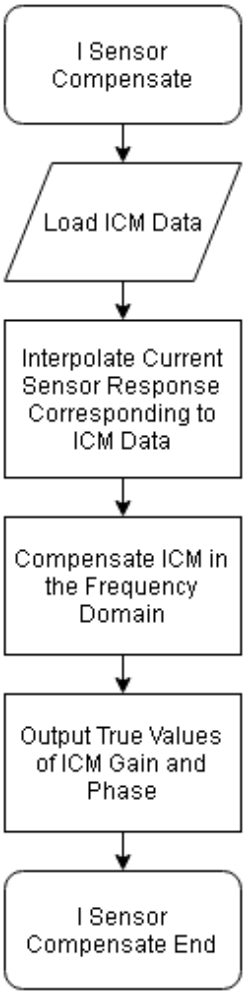

FIGURE B.8 CURRENT SENSOR COMPENSATION

Processing for Oven1 is shown in Figure B.3. The Oven1 and Oven2 programs are identical with activation of relays corresponding to Oven2. The data processing chain is shown in Figure B.4, with the subsections of B.4 expanded on in Figures B.4, B.5, B.6, B.7 and B.8.

B.2 FPGA Program

The FPGA unit was programmed using Vivado software package from Xilinx. The software allows easy programming of the Zynq series of FPGAs by allowing easy conversion of Verilog code into graphical blocks. An example of the process is illustrated. Figure B.9 shows the Verilog code for synchronised buffering of the external ADC used in Section C.2. The buffer stores data ¼ of the clock cycle after start of acquisition. This code is converted into a block structure and used as part of the overall GPIO structure in Figure B.10.

```
//this module adds 1/2 (or 3/2) ADC clock cycle delay after clocking the ADC
//to acquire data once the lines have settled
//__|-----|_____|-----|_____|   clk_1          10MHz
//__|--|__|--|__|--|__|--|__|   clk_2          20MHz
//  ^           ^           ^   ADC sample
//           ^           ^            ADC acquire

module clocked_buffer_igor(
clk_1,
clk_2,
in_data,
buf_out
);

parameter DATA_WIDTH = 16;

input   clk_1;
input   clk_2;
input   [DATA_WIDTH-1:0] in_data;
output  [DATA_WIDTH-1:0] buf_out;

reg     [DATA_WIDTH-1:0] buf_out;
wire    [DATA_WIDTH-1:0] in_data;

always @(posedge clk_2)
begin
if (~clk_1)
        begin
                buf_out=in_data;
        end
end

endmodule
```

FIGURE B.9 VERILOG CODE FOR A CLOCKED BUFFER STAGE

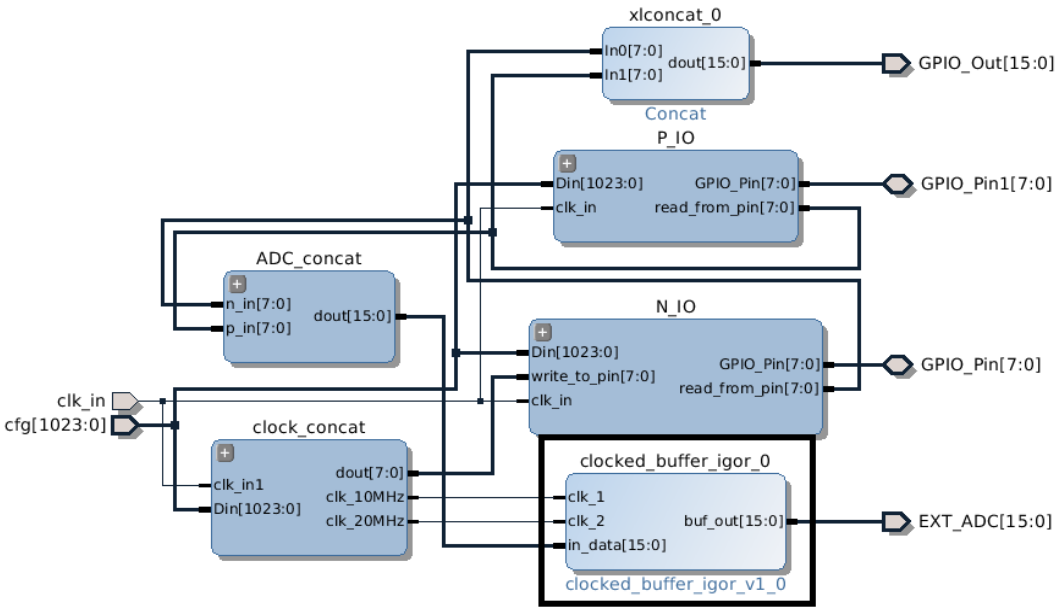

FIGURE B.10 "GPIO GENERAL" BLOCK IN VIVADO WITH CLOCKED BUFFER OUTLINED

The block structure enables easy change of code, automation of inter-block connectivity and use of code from multiple authors. Multiple authorship is most starkly illustrated in the input block which takes the input from the on-board ADC on the Red Pitaya board, conditions this and transfers it to the streaming AXI bus. The blocks to do this are shown in Figure B.11, where the input pins are routed to the AXI bus using a block from Pavel Demin, a Red Pitaya board developer, the signal is converted to an asynchronous signal line using a block written by the author, the input filter compensation is performed by blocks taken from the official Red Pitaya software release, and this is then synchronised to the main system AXI bus. The synchronisation block as well as a library of commonly used blocks such as for concatenation, slicing and constants, are provided by Xilinx.

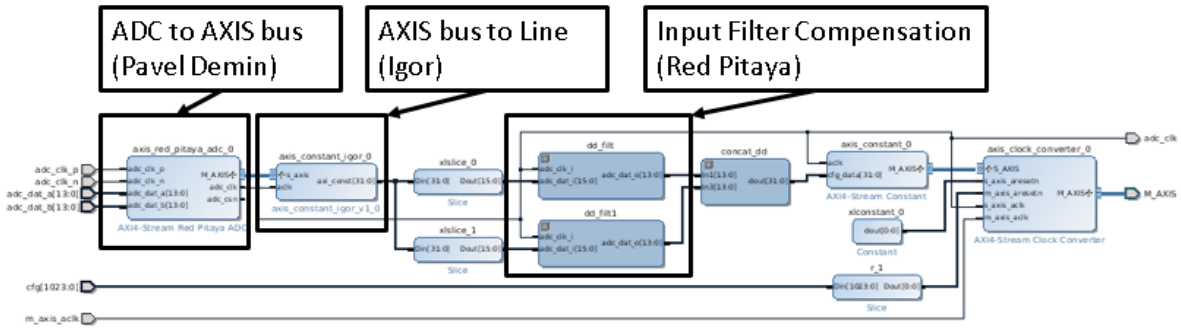

FIGURE B.11 "ADC_IN" INPUT BLOCK CONTENTS

The complete FPGA system is shown in Figure B.12. The input from the two fast ADCs which are used to measure VCM and ICM are acquired and conditioned at 125MS/s, down sampled and filtered down to 25MS/s. The two channels, each 16 bit wide, are written to RAM at the command of the CPU and processed further using C code. The RAM writer block packetizes a pre-programmed number of samples and transfers these to memory, these samples are then available to be accessed from C, through shared RAM. For this experiment 524,288 samples per channel are acquired as 500,001 points at 25MHz equates to 50Hz frequency resolution in the frequency domain.

The RAM writer module can accommodate 4 channels, in this case 2 are used for the fast ADC, and 2 are used for the GPIO, which is used to acquire data from the external ADC in Appendix C as well as controlling the relays used in the experiment in Chapter 5. The on-board DAC unit is configured as a sine wave generator, however this is not used in the experiment.

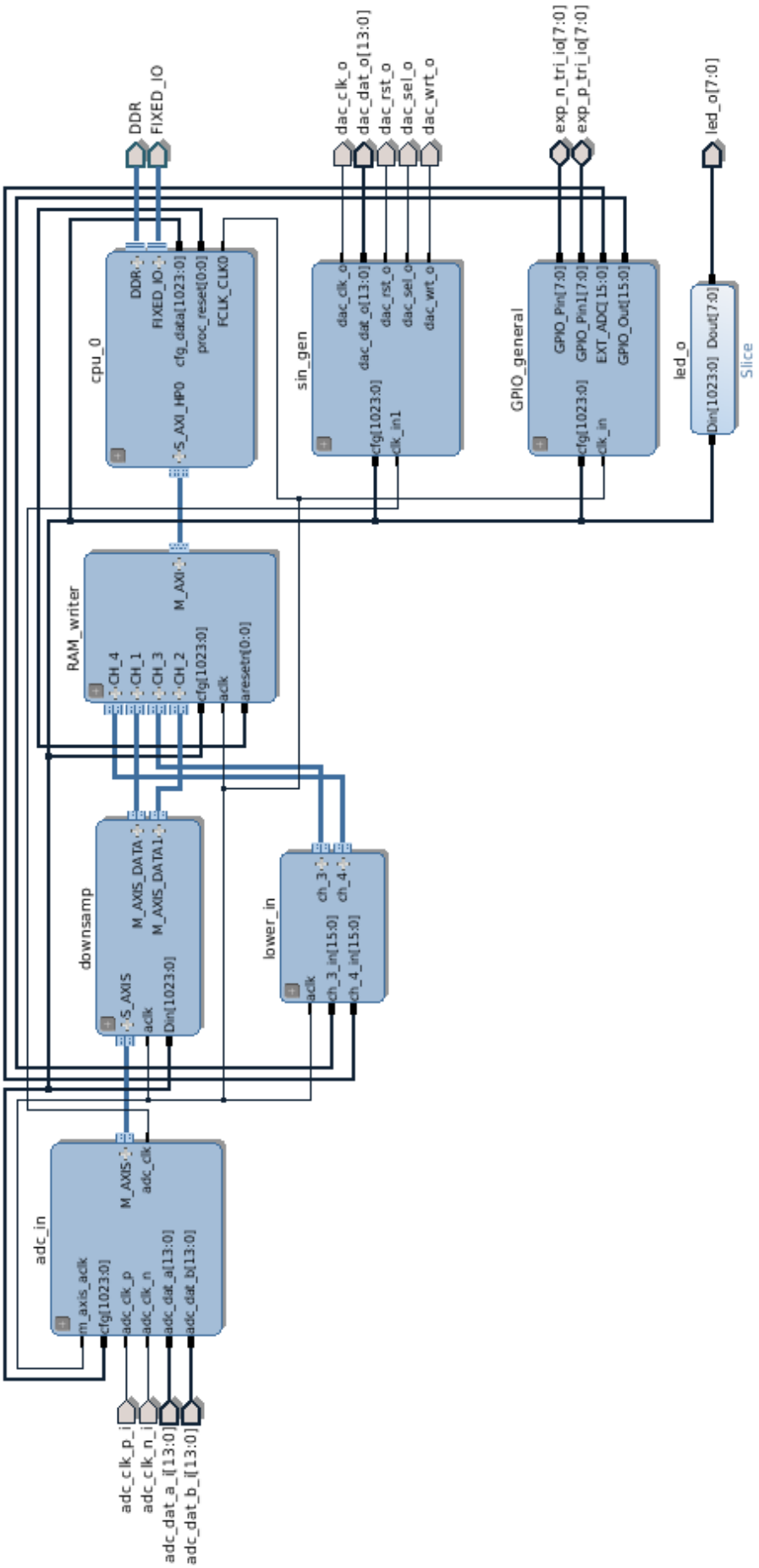

FIGURE B.12 COMPLETE FPGA BLOCK STRUCTURE

Appendix C

LOW COST INSULATION MONITORING

A practical insulation monitoring system would be required to be cost competitive and compact enough to fit into a machine drive. An attempt was made to monitor the insulation parameters using off the shelf low cost hardware, the cost of the sensors and supporting hardware limited to £50. The system was installed in series with the system used in Chapter 5, and operated for the first half of the test, capturing the progression of samples 1, 2 and 3. It is shown that it is possible to obtain useful data to track the progression of degradation using low cost hardware, the limits of the system are also explored.

Tests with Low Cost Hardware

During validation testing in Chapter 4, it was recognised that using the state of art current sensor combined with high speed acquisition it was possible to achieve impedance measurement accuracy comparable to off-line instruments. To make a cost effective system, to allow monitoring of a larger number of non-critical machines, a task was set to evaluate the use of off the shelf current sensors applied to measure common mode accurately. A platform was constructed and put in series with the main experiment in Chapter 5, measuring the Ceq and Req for Samples 2 and 3, as well as half of the life of Sample 1. The results are presented here, together with an evaluation of the system.

C.1 Aims

Long term ageing experiment allows field testing of multiple systems. It was decided that the cheap sensor system was to be placed in series with the main current sensor to monitor the insulation behaviour over time.

The main aims of this experiment were similar to the aims for the initial validation experiment in Chapter 4. The sensor system must evaluated to measure the accuracy of the sensor and analyse the measurement error. Additionally, the stability of the sensor system over time must also be evaluated.

Further aims of this experiment would require the assessment of how close the system comes to replicating the results from ideal sensors presented in Chapter 5, and whether the phenomena identified can be measured using this system.

C.2 Low Cost Sensor Hardware

Reviewing the hardware used to conduct measurement of impedance in Chapters 4 and 5, three requirements are identified: an isolated voltage measurement, a high bandwidth high sensitivity current sensor and a powerful data processing platform. Since the same processing platform previously used is powerful and cost effective, it is also employed for the experiments with low cost hardware. The voltage and current sensors are changed to enable cost effective acquisition.

Voltage Sensor

The voltage sensor used in the main project uses an expensive differential probe to implement the isolation. Inspired by methods used to measure voltage in power electronics, especially islanding detection in grid-connected converters [165], an isolated ADC system is employed.

The system is shown in Figure C.1, the per-phase voltage is reduced with potential divider and buffered, the sum of these is fed to a 10MS/s 12 bit ADC. The ADC signal and clock line are isolated with commonly used Si866x series of chips, which provide 5kV isolation, using a semiconductor-based isolation barrier. The summing stage and ADC conversion is performed entirely on the isolated portion of the board. As all analogue circuitry is referenced to isolated ground, compensation for common mode gain in the analogue stage is not required.

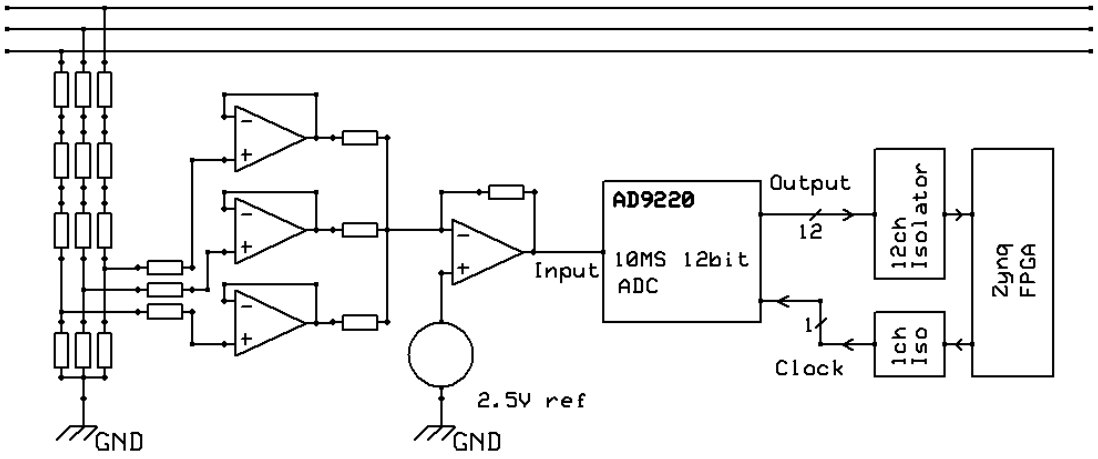

FIGURE C.1 ISOLATED VOLTAGE SENSOR SYSTEM

The biggest advantage of this system over using an isolated probe is the definition of parasitic components. The input resistance network clearly defines the resistance to ground of the voltage sensor, with stray capacitance minimized to negligible levels through PCB layout. Voltage waveforms from this voltage sensor system are compared with differential probe voltages in Figure C.2.

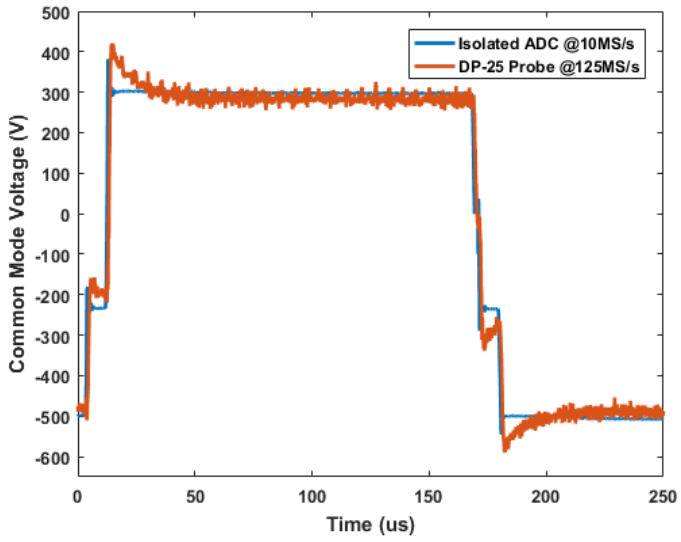

FIGURE C.2 COMMON MODE VOLTAGE COMPARISON

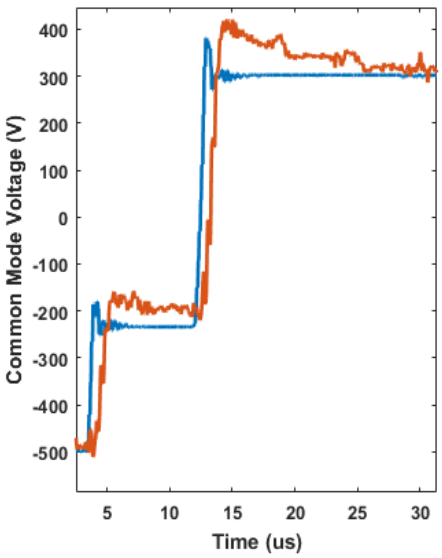

FIGURE C.3 WAVEFORM AT EDGE

Although the claimed bandwidth of the differential probe is 25MHz, compared with Nyquist bandwidth of 5MHz for the isolated ADC system, it is clear in Figure C.2 that the voltage transients are measured better by the isolated ADC system. The true limit on the differential probe is set by the parasitic components on the board. Because the differential probe attempts to measure the full voltage directly with an input impedance of 4MOhm, this is then considerably more vulnerable to parasitic components present than the defined phase-ground resistor ladder in Figure C.1, with an effective common mode impedance to ground of 130 kOhm.

Current sensor

The current sensor used in Chapter 4 dominates both the cost and size of the measurement system. The requirements for high sensitivity and bandwidth are diametrically opposed, with corresponding cost increase of the sensor. The LEM CTSR range of current sensors has been selected as a compromise between these characteristics. The sensor has a decreased bandwidth of 100 kHz vs 1MHz for Bergoz, with sensitivity of 0.8V/A compared to 2V/A for Bergoz. The decrease of bandwidth means that it is no longer possible to populate the high frequency portion of the insulation model used in Chapter 5, however low frequency measurements, below 100 kHz should be feasible.

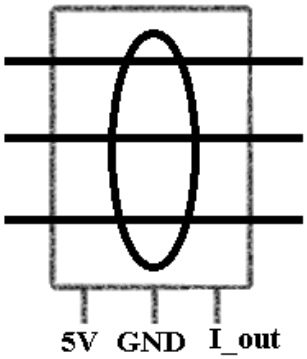

FIGURE C.4 LEM CTSR SENSOR SCHEMATIC

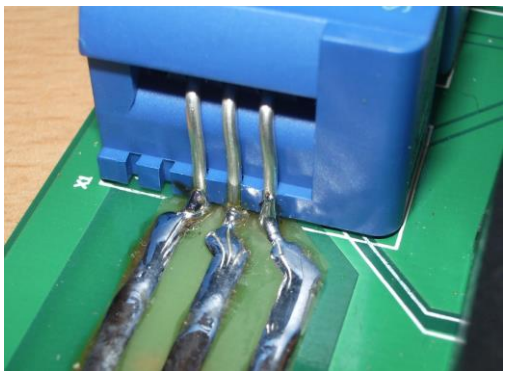

FIGURE C.5 LEM CTSR SENSOR CONNECTION TO MEASURE ICM

The original purpose of the LEM CTSR range of current sensors is designed to enable switching the input current range. Figure C.4 shows the current sensor schematic symbol, where three sense wires go through the sensor, these were originally designed to enable 1 2 or 3 turns to increase sensitivity. In this experiment, a, b, c phase wires are instead routed through the sensor to enable magnetic cancellation of the phase current and measurement of the common mode current. The physical connection of the phase wires is shown in Figure C.5, this connection is only possible due to low voltage operation. At voltages below 1kV the physical separation distance is adequate to prevent breakdown, at higher voltages.

Full System

The full system can be seen in Figure C.6 and Figure C.7, with relevant sensors highlighted and labelled. Further details regarding the design and functionality testing of the sensor system can be found in Appendix C.

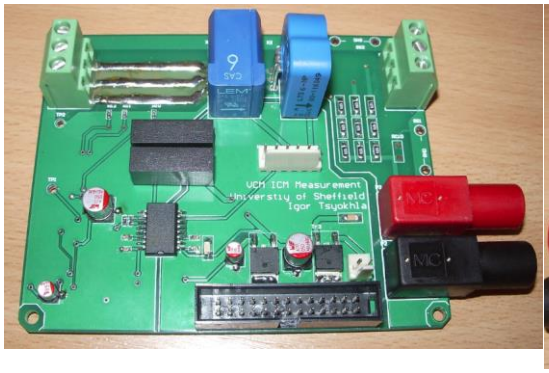

FIGURE C.6 CHEAP SENSOR FRONT

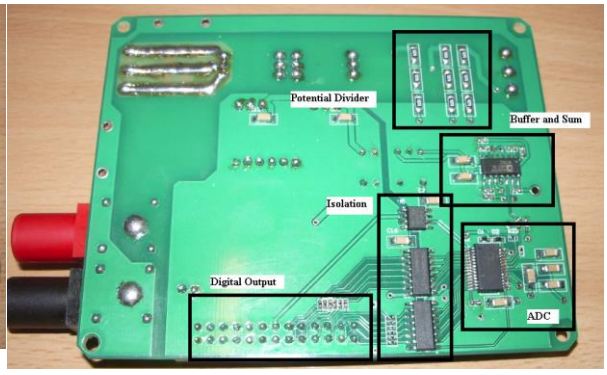

FIGURE C.7 VOLTAGE SENSOR SYSTEM

C.3 Sensor Validation

Initial measurements of C_{eq} and R_{eq} for the low cost sensors are shown in Figure C.8 and Figure C.9 respectively. It can be seen that compared to using the ideal sensors, the absolute capacitance value is wrong, as are the Req values. It also noticeable that the data after 100 kHz does not match well to the ideal sensors. It was not possible to calibrate the low cost sensor using the same

method as used in Section 4.5.1 due to low sensitivity of the sensor, as well as larger noise figure.

Lower sensitivity combined with a lower frequency response renders the high frequency data invalid, therefore only the low frequency C_{eq} and R_{ω} values can be extracted. If the C_{eq} data is to be used as suggested in Section 5.3.9 for prognosis of remaining lifetime, the absolute value of measurement is not important as the relative change over time is required.

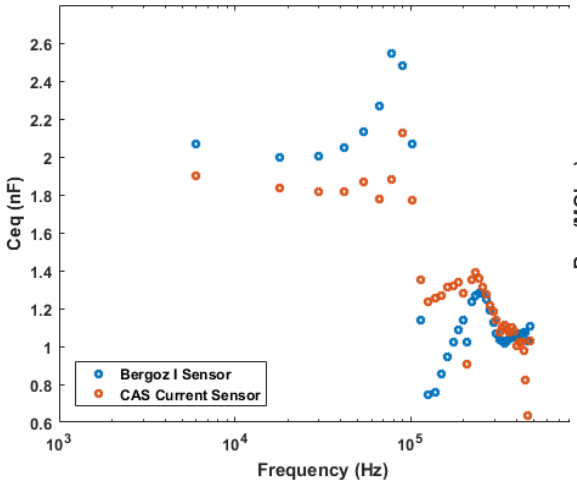

FIGURE C.8 C_{EQ} VS FREQUENCY, IDEAL SENSORS VS CHEAP SENSORS

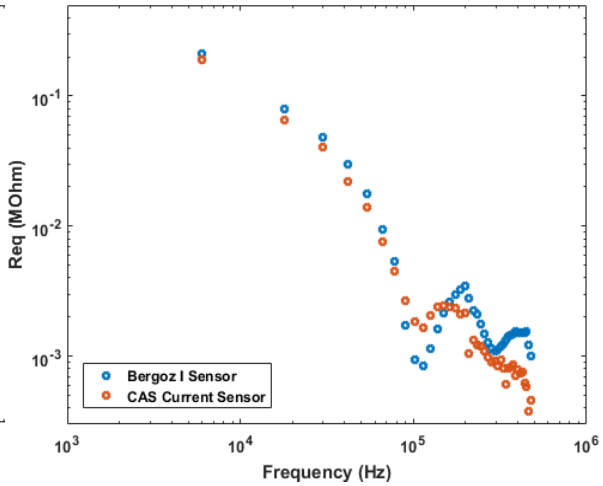

FIGURE C.9 R_{EQ} VS FREQUENCY, IDEAL SENSORS VS CHEAP SENSORS

To define the error margin of the sensor system, the deviation of C_{eq} from mean has been quantified using the same method as in Section 4.6.3. The system was set to measure the impedance of a stator without ageing present for 6 hours. The histogram of measured C_{eq} values are shown in Figure C.10. Ceq is extracted from an average for the first 4 harmonics between 6 kHz to 42 kHz. For comparison the histogram of Ceq values are plotted on the same scales for the ideal sensors in Figure C.11.

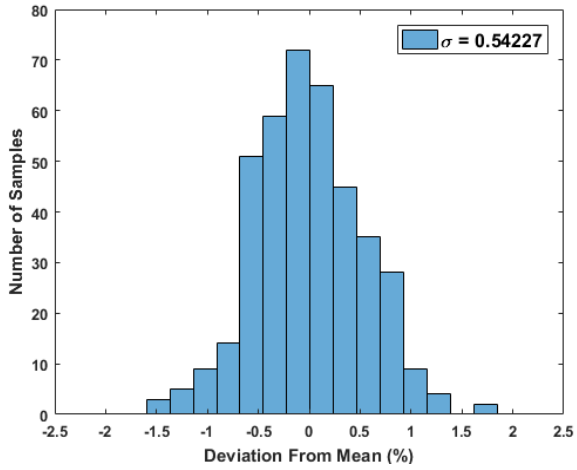

FIGURE C.10 C_{EQ} DEVIATION FROM MEAN VALUE FOR CHEAP SENSOR SYSTEM

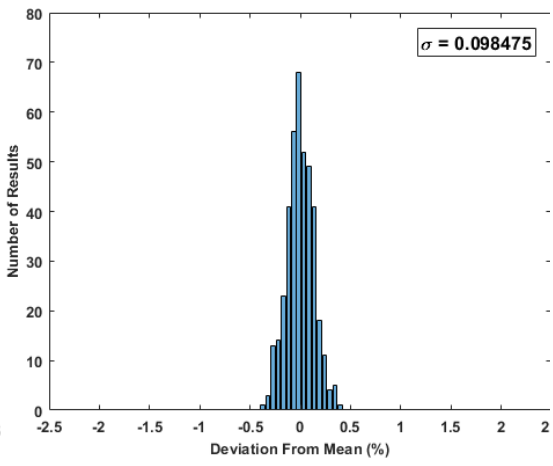

FIGURE C.11 C_{EQ} DEVIATION FROM MEAN VALUE USING IDEAL SENSORS

In Chapter 5, C_{eq} data is shown as the total capacitance obtained from measurement of capacitance at high frequencies starting at 342kHz and low frequencies up to 42kHz. The total capacitance is measured by using an average value of C_{eq} from multiple harmonics. Averageing across multiple harmonics uses the assumption that the noise figure at each harmonic is subjected to non-correlated white noise.

The effect of averageing multiple harmonics is shown in Figure C.12, where identical values with white noise have been averaged to obtain the standard deviation value for each data set. The standard deviation decreases predictably because with non-correlated noise, present on each harmonic, with identical signal-to-noise S/N ratios, mathematically, this is equivalent to simply increasing the length of measurement of a single harmonic.

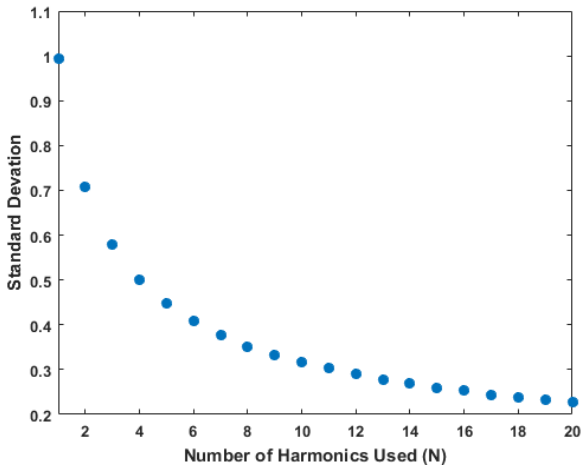

FIGURE C.12 MULTI-HARMONIC STANDARD DEVIATION EMULATION

Number of Harmonics	Standard Deviation
1	1.16
2	1.02
3	0.87
4	0.54
5	0.65
6	0.94

TABLE C-1 LOW COST SENSOR STANDARD DEVIATION VS NUMBER OF HARMONICS

In practice, the S/N ratio is maximum at the inverter switching frequency of 6 kHz, decreasing with increase of frequency. This sets a limit on the minimum standard deviation obtainable, with simple averageing of harmonics. Table C-1 shows the standard deviation vs the number of harmonics used in the averageing fit. It was experimentally determined that the minimum standard deviation of C_{eq} is obtained when the first 4 harmonics are used, increasing the number of harmonics used beyond this point decreases the precision of C_{eq} measurement.

At 6 kHz, using a single harmonic, the standard deviation for the low cost sensor is x11.5 times higher than that for the ideal sensors, this is improved by x2.1 by using multiple harmonics, returning 95% of C_{eq} values within ±1.08% of the mean value. Although this precision value is an order of magnitude worse than the ideal sensors and the sensors specified by the IEEE standards for measuring off-line C_{eq}, the trend of C_{eq} over time would still be useful to track the degradation rate of capacitance. It was shown in Section 5.3 that C_{eq} value changes by considerably more than that described in literature, a larger value of error may be acceptable in this case.

C.4 Long Term Results

The normalised results for long term Ceq monitoring using the low cost sensors are shown in Figure C.13, with Ceq measurement by the ideal sensors plotted alongside for comparison. A major linearity error was observed during the data processing, and although the relative Ceq decrease was correct between samples, it was necessary adjust the data by a constant factor 2.6 for all samples during normalisation as shown in Equation (C.1), to plot the low cost sensor data alongside the results obtained in Chapter 5. The compensation factor was obtained from observation of the average decrease of the three data end points, compared to the ideal measurement.

$$C\_norm(t) = 1 - 2.6 * (C_{start} - C(t)) \quad \textbf{(C.1)}$$

Figure C.13 shows that the low cost sensors portray, to some extent, the relative change of capacitance over time for samples, and that some larger features, such as the 'hump' in Sample 3 on day 5 is measurable using low cost sensors. However smaller features such as the distinct drop of Ceq for Sample 2 on day 14 are completely lost within the noise.

The long term data shows large deviations away from the Ceq measurement by the ideal sensors at times, however the noise also appears to be well correlated across multiple samples. Samples 1 and 2 show distinct spikes and plateaus in sync with each other, both samples were tested together in two separate ovens. Because there can be no possible interaction between samples and the large deviations are not observed in the ideal sensors and the processing system for both methods is identical, the error can only be due to the sensor hardware.

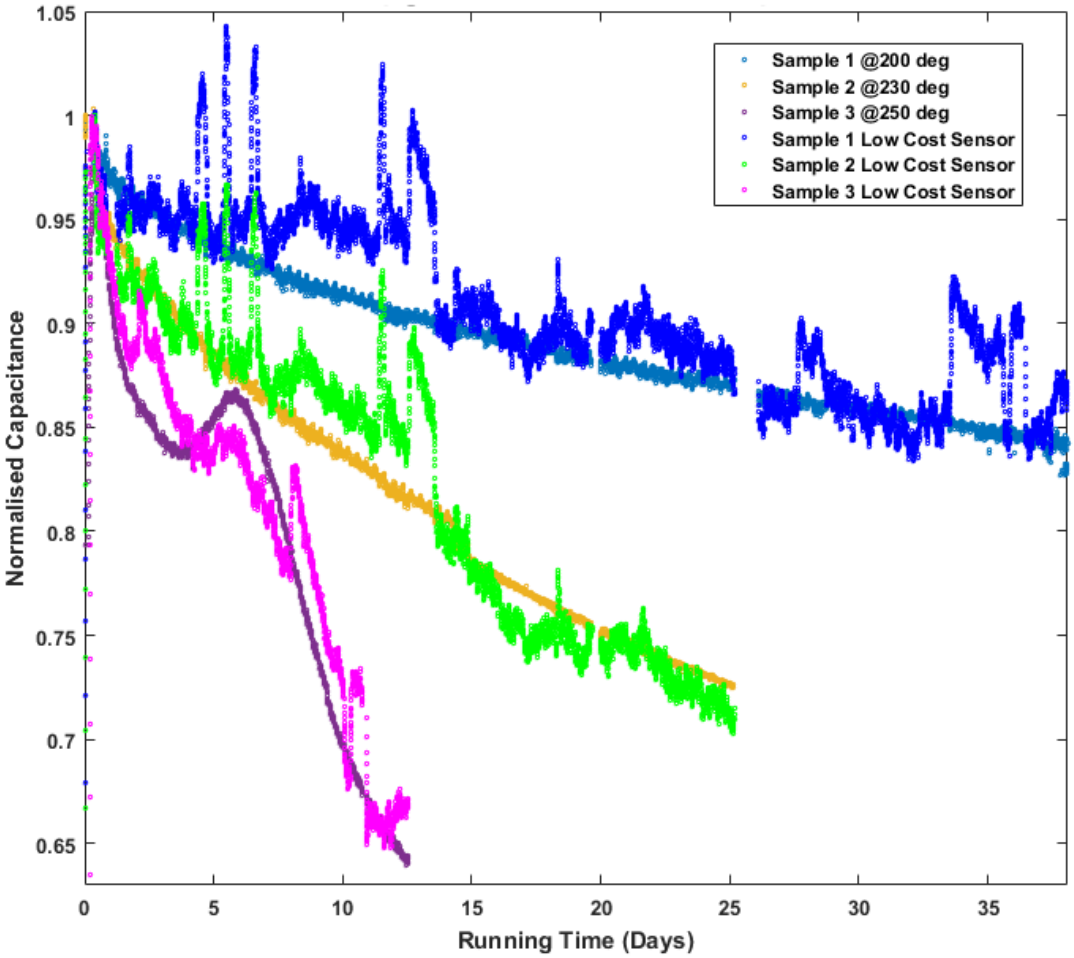

FIGURE C.13 NORMALISED C_{EQ} VALUES FOR CHEAP SENSORS (FILTERED RESULTS)

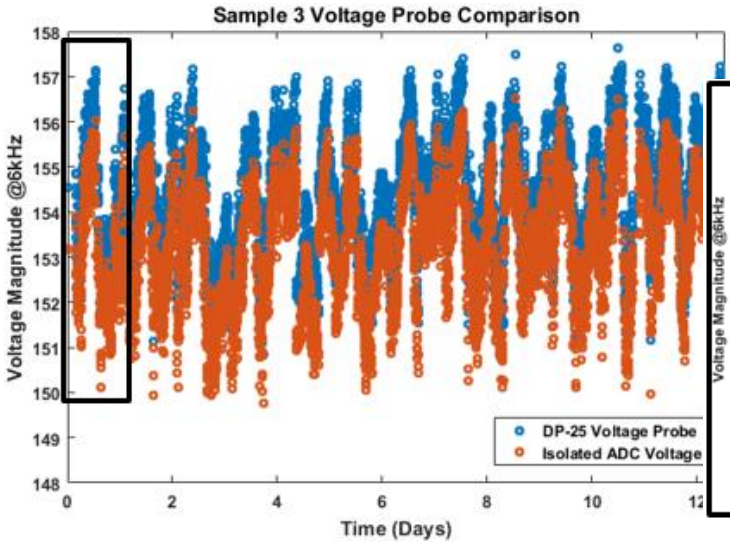

FIGURE C.14 SAMPLE 3 VOLTAGE MAGNITUDE COMPARISON @6KHZ

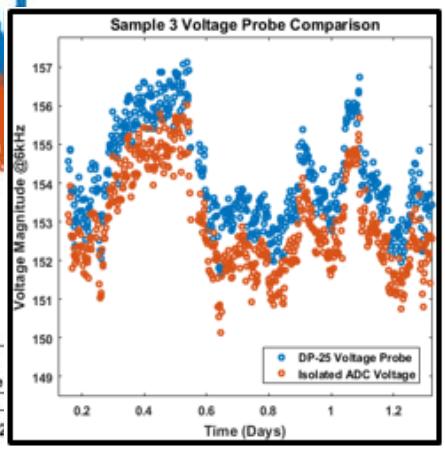

FIGURE C.15 SAMPLE 3 VOLTAGE MAGNIFIED

The correlated error observed in Figure C.13 can originate either from the isolated ADC voltage measurement system, or the CAS current sensor. During the experiment the voltage and current magnitude were recorded for each impedance harmonic for all the samples and both sensor systems. The voltage

harmonic at 6 kHz for Sample 3 is shown in Figure C.14 for the ideal sensor system and the low cost isolated ADC system. The 6 kHz harmonic varies a little during the experiment from a mean value of 153V (measured by DP-25 isolated voltage probe), however as can be seen in the magnified portion in Figure C.15, the isolated voltage tracks this variation as well as the DP-25 probe. It is therefore concluded that the error seen in Figure C.13 can only be due to variation in measured current.

The impact of current sensor instability is illustrated in Figure C.16 for Sample 3. The jumps observed on days 8, 10 and 11 completely mask the small drop of Ceq that was observed on day 9.4 by the ideal sensors.

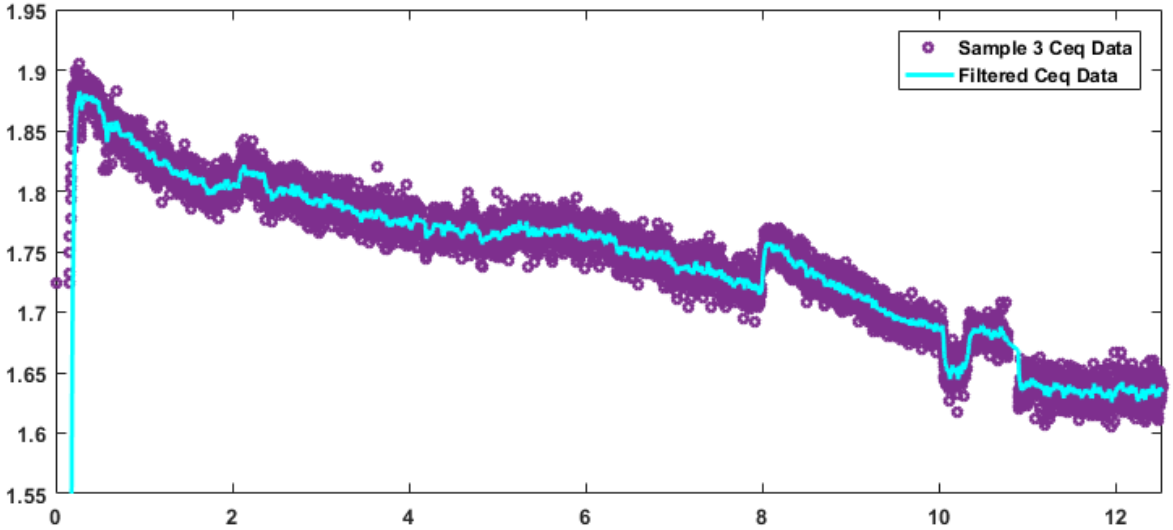

FIGURE C.16 C_{EQ} VALUE FOR SAMPLE 3 MEASURED BY LOW COST SENSORS

Data stability over time is emphasized when attempting to measure the dissipation values. It has been shown in the error analysis in Section 4.6.3 that the sensor accuracy required to monitor R_{eq} is an order of magnitude higher for the machine measured. This is drastically illustrated in the plot of the R_{ω} 'c' parameter as shown in Figure C.17. The low cost sensor system captures the rise of 'c' at the end of experiment, however it completely misses the prominent change between days 4 to 8, as well as returning a false signal on day 2 which is not present in the ideal measurement

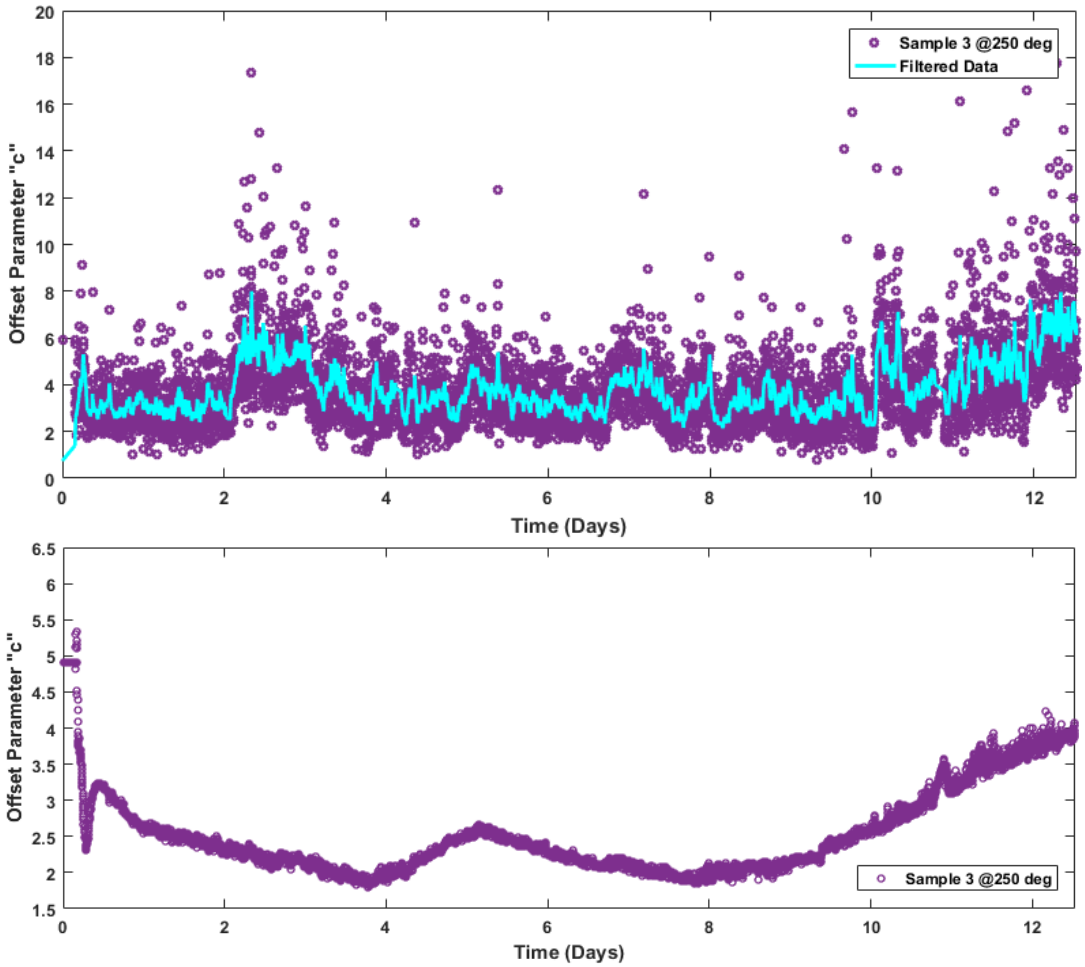

FIGURE C.17 RW 'C' PARAMETER MEASUREMENT COMPARISON

C.5 Conclusion

It has been shown that the low cost current sensor precision can be improved by averageing multiple harmonics due to its Gaussian noise characteristic. The sensor stability however limits the accuracy of the sensor system, to the level where important features can no longer be observed. It is suggested for future work that other sensors may also be experimented with, selecting a more appropriate trade-off between accuracy and bandwidth. Real-time calibration of the current sensor may also be attempted to reduce the influence of current sensor variability.

The low cost isolated ADC voltage sensor has been validated as a viable alternative to using isolated voltage probes, showing equivalent long term stability. The 5MHz bandwidth is adequate to measure insulation health as all major features are expected to be well below this frequency.

Appendix D

BUILD AND TEST OF THE MAIN EXPERIMENT

This Appendix contains the detailed circuit diagrams, photos of construction and design, and testing of the equipment used to conduct the accelerated ageing test in Chapter 5. This information is made available to be able to reconstruct the equipment built for the experiment as well as clarification of some of the minor design issues overcome in the creation of the monitoring system.

D.1 Relay Multiplex System

In Chapter 5, it was decided to test two samples in two ovens simultaneously, switching the power between the two ovens. This was accomplished with the relay system set out in Figure D.1. The main on-line monitoring system is always in place, in series relay 1, passing power through to the machines. The power to the machines is switched through relays 2 and 3, depending on which is to be measured on-line.

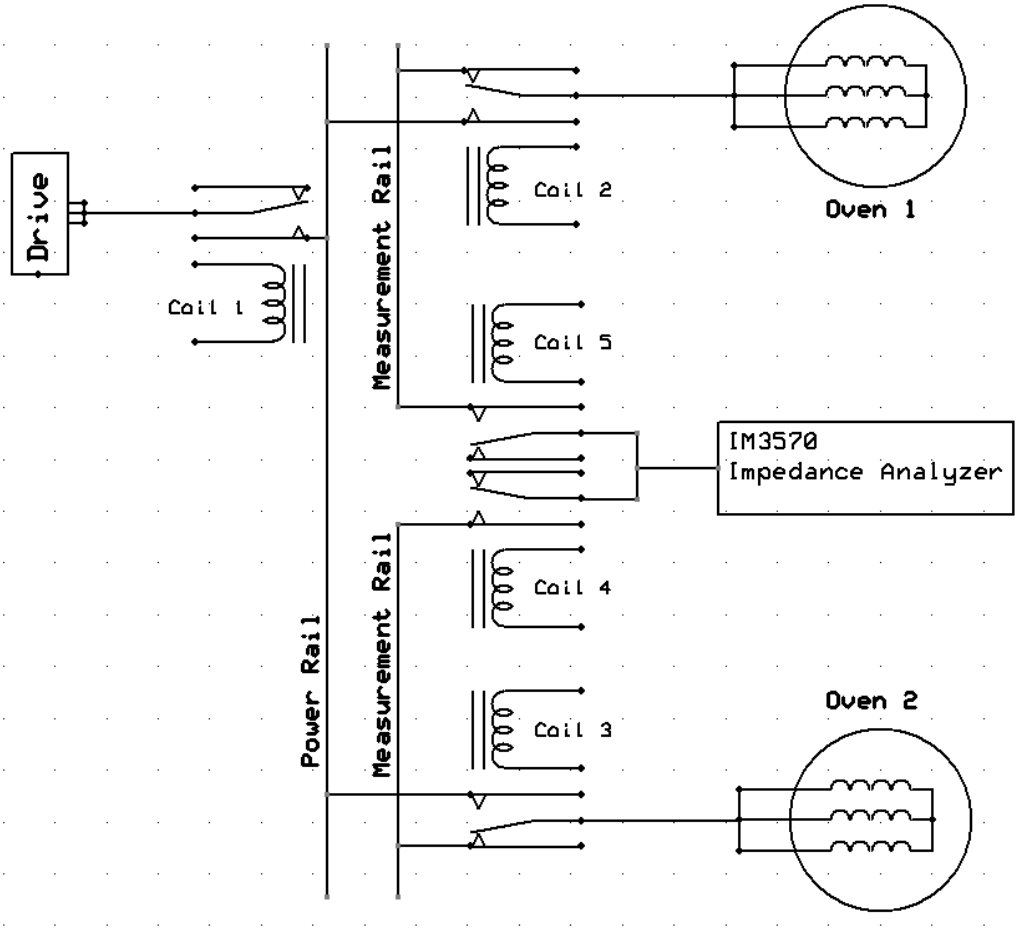

FIGURE D.1 RELAY SYSTEM CIRCUIT DIAGRAM

For daily off-line measurement, and safety, when the machines are not being operated, the default position of relays 2&3 returns them to the 'measurement' rail. To enable power to pass through to the machines, a physical 'run/measure' switch is in place, routing power to the relay drivers of either the 'power' relays or 'measure' relays. The switch arrangement is shown in Figure D.2.

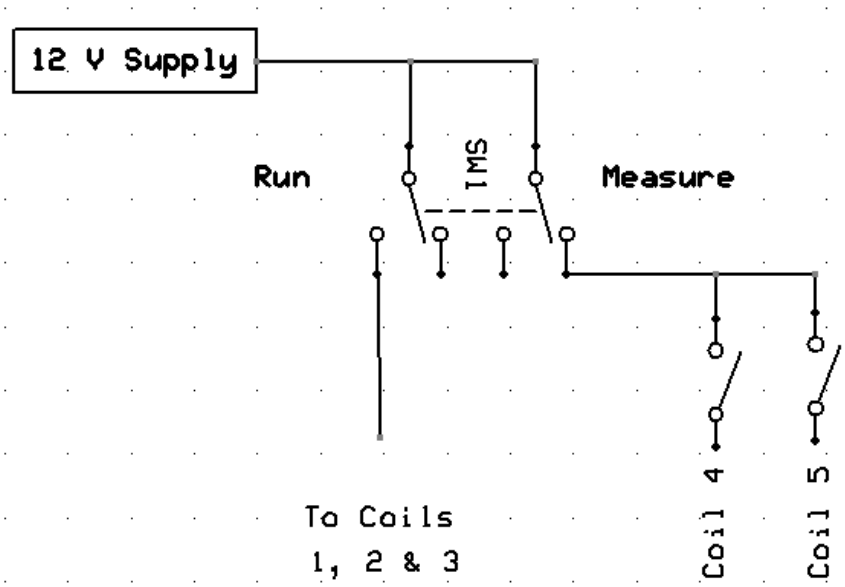

FIGURE D.2 SWITCHING BETWEEN RUN AND MEASURE MODES

The power to relay drivers for coils 2&3 does not pass directly from the supply 'run' switch shown in Figure D.2. For additional safety, the power must first pass through interlocks, placed on ovens 1&2, so that if the door of the oven is open, the power to the relay driving the corresponding sample is disabled. This is to prevent possibility of contact with live current, if one were to open the door to the oven and touch the sample.

D.2 System Layout

The system design for the insulation monitoring box begins with the front panel. Figure D.3 shows the I/O required for the experiment, from left to right, there is an input for the mains power to supply the measurement hardware, two Ethernet pass-through ports for the two Red Pitayas, a switch bank to enable stopping the drive and selecting the sample to test off-line using the Hioki instrument and the power I/O. Power comes in from the drive and is multiplexed to two samples in their respective ovens. Each oven has an interlock which disables the power to the respective oven selection relay so as to disable the possibility of contact with live windings while the oven door is open. To enable the drive, a cable passes from the front panel gland to the inverter drive enable mechanism.

FIGURE D.3 MEASUREMENT BOX FRONT PANEL

The major components used in the test are laid out as shown in Figure D.4. The major components include the pair of red pitayas used to conduct the experiments in Chapter 5 and Appendix C simultaneously, the differential voltage probe, the Bergoz current sensor, the isolated ADC, multiplex relays and relay driver board. Auxiliary systems such as power supplies and Bergoz sensor output conditioning hardware are mounted to the side of the box and the lid, as shown in Figure D.5.

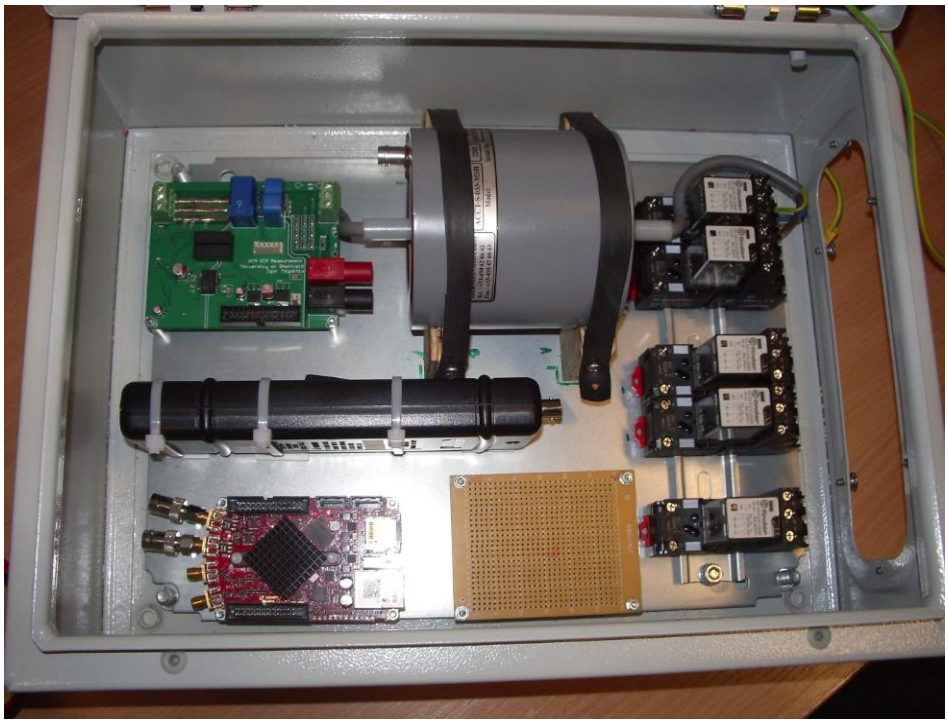

FIGURE D.4 INITIAL LAYOUT OF THE MONITORING SYSTEM

The most important part of the layout procedure is optimisation of the layout and wiring to minimize electromagnetic interference. The layout achieves the optimisation in three ways: routing of the inverter power, routing of the grounds and isolation of systems. It can be seen in Figure D.3 that power enters and leaves the box with the wires as close to each other as possible, inside the box, the power is routed in a narrow rectangle through the external ADC board the Bergoz sensor and the three relays at the top. The area is minimized and the

routing is as far from the Red Pitayas as possible. Power supply grounding is achieved by routing all supplies to a single star point as shown in Figure D.5, special care is taken to not allow any other ground paths

FIGURE D.5 STAR GROUNDING OF THE MEASUREMENT BOX

It is acknowledged that inside the box, there are three systems which are required to operate together; the current and voltage sensors, the relay multiplexing and the Red Pitaya acquisition and computing. To minimize the interaction of the grounds, especially with regard to the high speed ADCs on the Red Pitaya boards, the grounds of the systems were kept independent, with minimal inter-connection.

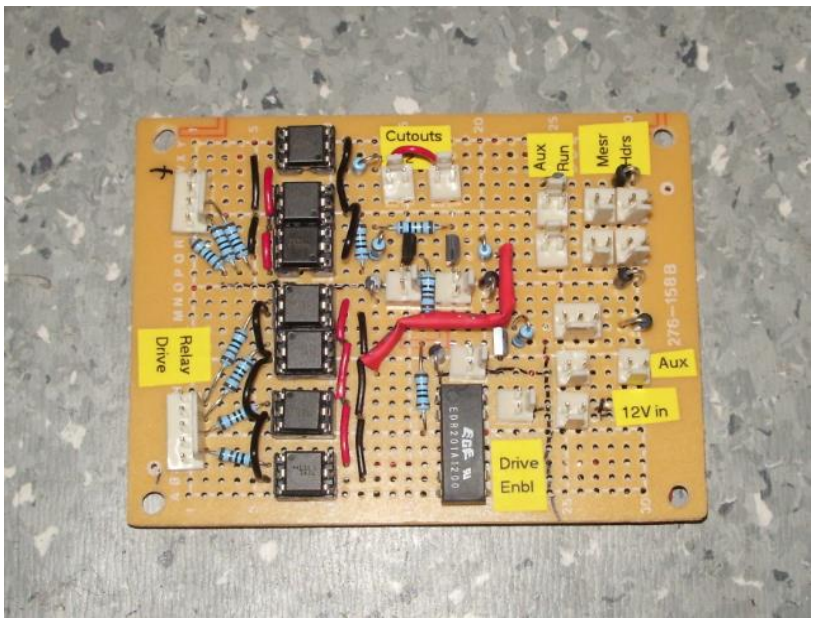

FIGURE D.6 RELAY DRIVER BOARD

The relay driver board in Figure D.6 contains a row of optical isolation between the Red Pitaya boards and the relay system. The isolated voltage probe, Bergoz current sensors, external ADC boards and Red Pitayas are on separate power supplies to each other. Overall there were minimal problems from EMC, except with regards to the digital signal from the external ADC board. Direct ground connection between the red pitaya grounds and the external ADC was required but not explicitly defined in the initial design. Data corruption was experienced, the problem was fixed by reinforcing the ground connection.

D.3 Turn on Procedure

To pass through the power to a sample, the following list of actions must be taken, these are in addition to checking that the drive is on and the emergency drive stop has not been pressed.

1. Press the 'Enable' switch on the drive (Hardware)
2. Ensure that oven doors are closed (Hardware)
3. Select the 'run' mode on the 'run/measure' switch (Hardware)
4. Enable the 'Power Pass' relay 1 in Figure D.1 (Software)
5. Enable the required oven using relay 2 or 3 in Figure D.1 (Software)
6. Power the 'Drive Enable' relay to start (Software)

If any of the above steps are not fulfilled, the drive power will not reach the test sample windings. If the oven door to a sample is opened, power is cut to the relay providing power to that sample. If the measure/run switch in Figure D.3 is switched to measure, or the emergency stop on the drive is pressed or the drive stop on the inverter is pushed, all of these actions will stop the inverter power.

D.4 Oven 1 Temperature

Initially, 200 °C target was set on Oven 1, to hold the temperature of Sample 1. It was found in practice though that although the temperature in Oven 2 was as set, the measured temperature of Oven 1 was actually between 202 – 203 degrees. The thermocouple used to measure temperature of Sample 1 is shown in Figure D.7, and the measured temperature is shown in Figure D.8. After discovering the true temperature of the sample, the calculations for expected sample lifetime were redone and the tables updated to reflect the measured sample temperature. The internal temperature of samples remained within 1 °C of the initial temperature, as illustrated by Figure D.9 temperature of Sample 5 containing thermocouples inside the windings.

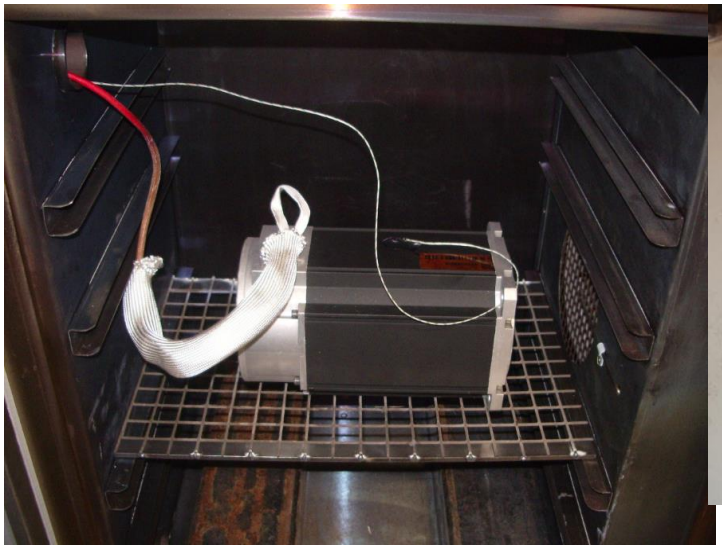

FIGURE D.7 SAMPLE 1 OVEN 1 TEMPERATURE MEASUREMENT

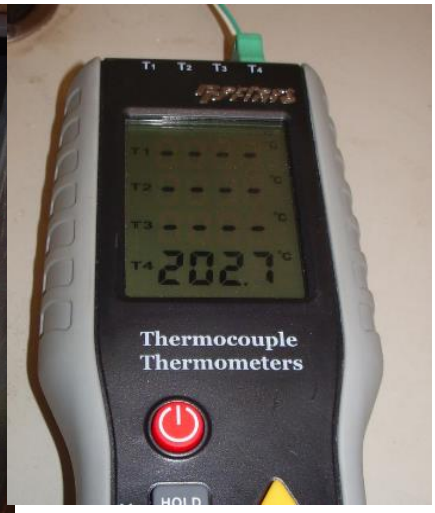

FIGURE D.8 TYPICAL SAMPLE 1 TEMPERATURE

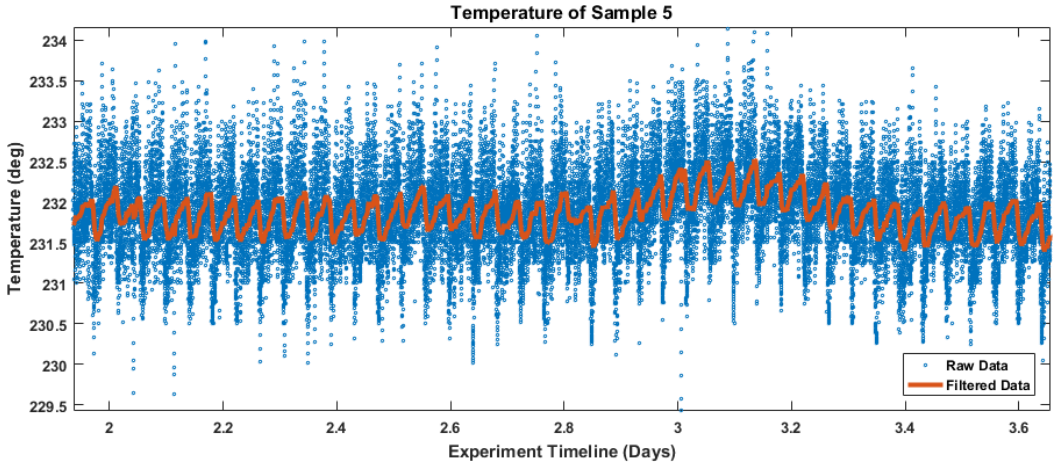

FIGURE D.9 SAMPLE 5 TEMPERATURE VARIATION OVER TIME

D.5 Full System

The wired internals of the measurement system are shown in Figure D.10. It is recommended based on experiences with the current build to allow more

space for wiring, as well as to include a ventilation fan for heat dissipation. The measurement system, inverter drive and two ovens are shown in Figure D.11. The test setup and hardware have been shown to work satisfactorily over a period of 32 weeks. Lessons learnt from the experience of building and testing the equipment have been invaluable to the author, and it is anticipated that the equipment constructed will continue testing machine insulation in many other experiments in the future.

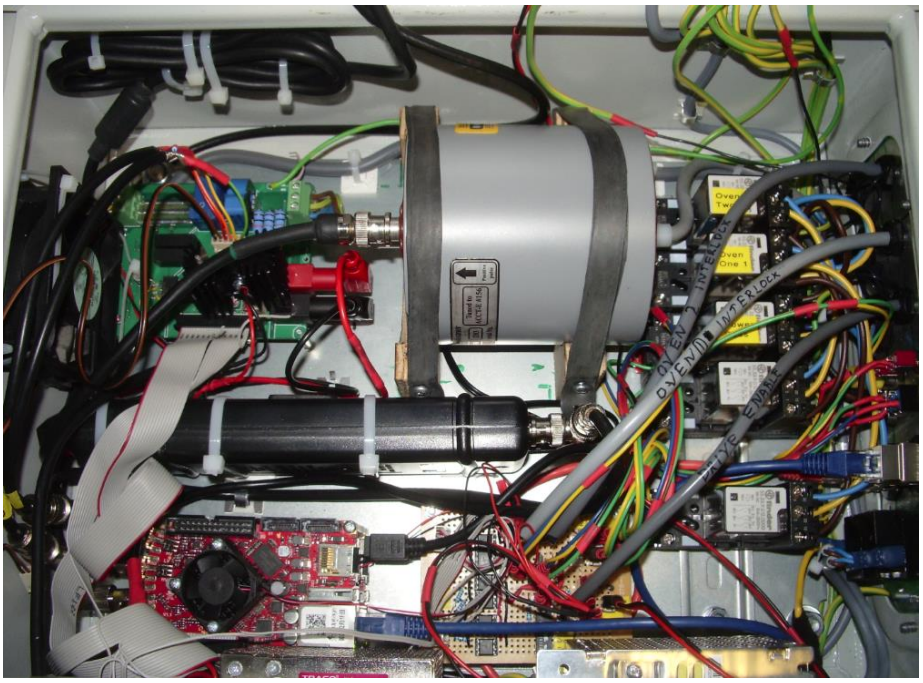

FIGURE D.10 FULLY WIRED SYSTEM BUILD

FIGURE D.11 LABORATORY LAYOUT

Table of Figures

List of Tables

Symbols Used

The symbols are listed in the same order as they are used in the thesis, with corresponding chapter and section identifiers for ease of navigation.

Chapter 1 Literature Review

Section 1.3

L_{10}	Bearing lifetime (number of revolutions)
a_{skf}	Experimentally derived life multiplier
C	Bearing dynamic load rating (N)
P	Equivalent dynamic load (N)
p	Bearing type coefficient (3 for ball bearings)

Section 1.4

Y	Winding insulation lifetime (Hours)
T	Temperature (°C)
P	An arbitrary physical property value
C	An arbitrary chemical reactant quantity
K	Chemical reaction rate
n	Order of chemical reaction (1 for the example shown)
C_0	Initial chemical reactant quantity
A	Pre-Exponential Arrhenius coefficient
E_a	Activation energy (J)
R	Universal gas constant (8.314 $J.mol^{-1}.K^{-1}$)
T	Temperature (Kelvin)
B	Constant combination $B=E_a/R$
L_{end}	Insulation lifetime at breakdown (Hours)
L_0	Nominal lifetime at T_0 (Hours)
T_0	The nominal temperature selected by the user (°C)
Q_{10}	Chemical rate acceleration per 10°C temperature rise
T_1	Temperature at reaction rake k_1
T_2	Temperature at reaction rate k_2
k_1	Reaction rate at temperature T_1, to calculate Q_{10}
k_2	Reaction rate at temperature T_2, to calculate Q_{10}
E	Voltage applied to insulation (V)
c	Experimentally derived constant
r	Experimentally derived constant
n	Experimentally derived constant
b	Experimentally derived constant

k_b	Boltzmann constant (1.38e-23 $m^2.kg.s^{-2}.K^{-1}$)
h	Planck constant (Js)
ΔG	Gibbs activation energy (J)
e	Charge of active particle (C)
λ	Entropy between healthy and failed states (J)

Chapter 2 Bearing Health

Section 2.2

F_{IR}	Frequency component of bearing inner race	(Hz)
F_{OR}	Frequency component of bearing outer race	(Hz)
F_C	Frequency component of bearing cage	(Hz)
F_B	Frequency component of bearing rolling elements	(Hz)
f_r	Rotor rotational frequency	(Hz)
n	Number of rolling elements	
BD	Ball Diameter (m)	
PD	Pitch diameter (m)	
β	Contact angle (rad)	

$f_{current}$	Frequency component of measured current	(Hz)
f_0	Fundamental machine current	(Hz)
$f_{vibration}$	Physical vibration frequency	(Hz)

Chapter 3 Insulation Failure

Section 3.3

C	Real capacitance value
k	Capacitor physical dimension constant
ε'_r	Real component of the dielectric constant
ε''_r	Imaginary component of the dielectric constant
Z	Impedance value

S	Complex power (VA)
V	Voltage (V)
ω	Frequency component (2*pi*f Hz)

C_{eq}	Equivalent capacitive element (F)
R_{eq}	Equivalent dissipative element (Ohm)

C_{sf0}	Model capacitance value (F)
C_{sf}	Capacitance representing C_{eq} at high frequency (F)
L_{ss}	Model inductance value (H)
R_s	Winding resistance value (Ohm)
R_{swh}	Winding dissipation value (Ohm)
R_ω	Dielectric dissipation value (Ohm)

C_{eq_lf}	Capacitance at low frequencies (F)
C_{eq_hf}	Equivalent capacitance above winding resonance point (F)

k_f	Experimentally derived adjustment factor

Chapter 4 Insulation Monitoring Technology

Section 4.1

C_{eq}	Equivalent capacitive component at ω (F)
R_{eq}	Equivalent dissipative component at ω (Ohm)
$\tan\delta$	Dissipation Factor (DF), expressed as % of dissipative current

Section 4.4

V_{cm}	Common mode voltage (V)
V_a	Phase A to neutral voltage (V)
V_b	Phase B to neutral voltage (V)
V_c	Phase C to neutral voltage (V)
V_{cm_rect}	Common mode voltage component from rectification (V)
V_p	Peak Voltage (V)
$V_{rectangle}$	An arbitrary rectangular waveform
a_0	DC component of the rectangular voltage
a_n	Harmonic magnitude of the rectangular waveform
V_+	Magnitude of rectangular waveform
t_{on}	Time spent at full magnitude (s)
T_s	Waveform period (s)
V_{dc}	DC bus voltage (V)
M	Modulation index
ω_0	Frequency of modulating wave
ω_s	Frequency of inverter switching ($1/T_s$)
θ_0	Phase of modulating wave (rad)
θ_s	Phase of switching waveform (rad)
J_0	First kind, Order 0 Bessel function
J_n	First kind, Order n Bessel functions

Section 4.5

I_{cm}	Common mode current	(A)
I_a	Phase A current	(A)
I_b	Phase B current	(A)
I_c	Phase C current	(A)
H	Magnetic field	(Am^{-1})

Section 4.6

C_{eq}	In this section, Ceq refers to the capacitive element in a parallel RC pair, transformed to from Z impedance data
R_{eq}	The resistive component of a parallel RC pair
Δf	FFT frequency resolution
N	Number of sample points
T_s	Sampling frequency time period
$\|V\|$	Voltage magnitude as measured by the voltage sensor
$\|I\|$	Current magnitude as measured by the current sensor
θ_i	Measured current phase value relative to a constant value
θ_v	Measured voltage phase value relative to a constant value

Chapter 5 Long Term Ageing Test

Section 5.3

$R_{(f)}$	R_ω line extrapolation
c	R_ω offset on an f vs R_{eq} log-log plot
m	R_ω gradient on an f vs R_{eq} log-log plot
f	Frequency (Hz)
$\tan\delta_{(50Hz)}$	Dissipation extrapolated to the value at 50Hz
$C_{(50Hz)}$	Capacitance extrapolated to the value at 50Hz
$R_{(50Hz)}$	Equivalent resistance extrapolated to the value at 50Hz
$C_{eq}(t)$	The value of low frequency capacitance with respect to time
t	Time of experiment
a	Constant to obtain $C_{eq}(t)$ with respect to t
b	Constant to obtain $C_{eq}(t)$ with respect to t
c	Constant to obtain $C_{eq}(t)$ with respect to t
C_i	Confidence interval value(s)
$\bar{x}$	Mean value of result
Z_i	Confidence parameter with respect to table of confidence levels
σ	Standard deviation of result
N	Number of points in the result

References

[1] "Report of Large Motor Reliability Survey of Industrial and Commercial Installations, Part I," *IEEE Transactions on Industry Applications,* Vols. IA-21, no. 4, pp. 853-864, 1985.

[2] "Report of Large Motor Reliability Survey of Industrial and Commercial Installations, Part II," *IEEE Transactions on Industry Applications,* Vols. IA-21, no. 4, pp. 865-872, 1985.

[3] "Report of Large Motor Reliability Survey of Industrial and Commercial Installations, Part III," *IEEE Transactions on Industry Applications,* Vols. IA-23, no. 1, pp. 153-158, 1987.

[4] W. H. Dickinson, "Report on reliability of electric equipment in industrial plants," *Transactions of the American Institute of Electrical Engineers,* vol. 8, no. 3, pp. 132-151, 1962.

[5] IEEE Committee Report, "Report on Reliability Survey of Industrial Plants, Part IV," *IEEE Transactions on Industry Applications,* Vols. IA-10, no. 4, pp. 456-462, 1974.

[6] P. F. Albrecht, J. C. Appiarius, R. M. McCoy, E. L. Owen and D. K. Sharma, "Assessment of the Reliability of Motors in Utility Applications - Updated," *IEEE Transactions on Energy Conversion,* Vols. EC-1, no. 1, pp. 39-46, March 1986.

[7] O. V. Thorsen and M. Dalva, "A Survey of Faults on Induction Motors in Offshore Oil Industry, Petrochemical Industry, Gas Terminals and Oil Refineries," *IEEE Transactions on Industry Applications,* vol. 31, no. 5, pp. 1186-1196, 1995.

[8] USA Department of Defence, "Capacitors, Inductors and Rotating Devices," in *MIL-HDBK-217F*, 1991, pp. 10.1-12.5 .

[9] P. J. Tavner and J. P. Hasson, "Predicting the design life of high integrity rotating electrical machines," in *Ninth International Conference on Electrical Machines and Drives*, Canterbury, 1999.

[10] J. G. McLeish, "Enhancing MIL-HDBK-217 reliability predictions with physics of failure methods," in *Annual Reliability and Maintainability Symposium*, San Jose, CA, 2010.

[11] G. Stone, "Advancements during the Past Quarter Century in On-line Monitoring of Motor and Generator Winding Insulation," in *IEEE Transactions on Dielectrics and Electrical Insulation*, 2002, pp. 746-750.

[12] A. Siddique, G. S. Yadava and B. Singh, "A review of stator fault monitoring techniques of induction motors," *IEEE Transactions on Energy Conversion,* vol. 20, no. 1, pp. 106-114, 2005.

[13] S. Grubic, J. M. Aller, B. Lu and T. G. Habetler, "A survey of testing and monitoring methods for stator insulation systems in induction machines," in *International Conference on Condition Monitoring and Diagnosis*, Beijing, 2008.

[14] G. Pascoli, W. Hribernik and G. Ujvari, "A Practical Investigation on the Correlation Between Aging and the Dissipation Factor Value of Mica Insulated Genrator Windings," in *International Conference on Condition Monitoring and Diagnosis*, Beijing, 2008.

[15] SKF, "SKF Bearing Calculator," [Online]. Available: http://webtools3.skf.com/BearingCalc/. [Accessed 27 4 2017].

[16] J. R. Stack, T. G. Habetler and R. G. Harley, "Fault Classification and Fault Signature Production for Rolling Element Bearings in Electric Machines," *IEEE Transactions on Industry Applications,* vol. 40, no. 3, pp. 735-739, 2004.

[17] SKF, "Technical Data for the 6204.Z Bearing," [Online]. Available: https://eshop.ntn-snr.com/en/6204-Z-649089.html. [Accessed 28 4 2017].

[18] J. R. Stack, T. G. Habetler and R. G. Harley, "Bearing fault detection via autoregressive stator current modeling," *IEEE Transactions on Industry Applications,* vol. 40, no. 3, pp. 740-747, 2004.

[19] L. Eren and M. J. Devaney, "Bearing Damage Detection via Wavelet Packet Decomposition of the Stator Current," *Instrumentation and Measurement,* vol. 53, no. 2, pp. 431-436, 2004.

[20] E. Sutrisno, H. Oh, A. S. S. Vasan and M. Pecht, "Estimation of remaining useful life of ball bearings using data driven methodologies," in *IEEE Conference on Prognostics and Health Management*, Denver, 2012.

[21] Artesis LLP, *MCM Motor Condition Monitor (Brochure),* Artesis LLP, 2017.

[22] Monitran Ltd, *MTN/VM220 High Performance Vibration Meter (Brochure),* Penn, UK: Monitran Ltd.

[23] T. W. Dakin, "Electrical Insulation Deterioration Treated as a Chemical Rate Phenomenon," *American Institute of Electrical Engineers, Transactions,* vol. 67, no. 1, pp. 113-122, 1948.

[24] ANSI/IEEE, IEEE Std 101-1987, Guide for the Statistical Analysis of Thermal Life Test Data, 1987, pp. 1-34.

[25] G. C. Stone, "The Statistics of Aging Models and Practical Reality," *IEEE Transactions on Electrical Insulation,* vol. 28, no. 5, pp. 716-728, 1993.

[26] H. Zhu, C. Morton and S. Cherukupalli, "Quality evaluation of stator coils and bars under thermal cycling stress," in *IEEE International Symposium on Electrical Insulation*, Toronto, Ont, 2006.

[27] H. Mitsui, Yoshida, I. Y. K and S. Kenjo, "Thermal Cyclic Degradation of Coil Insulation for Rotating Machines," *IEEE Transactions on Power Apparatus and Systems,* Vols. PAS-102, no. 1, pp. 67-73, 1983.

[28] Z. Huang, A. Reinap and M. Alaküla, "Degradation and fatigue of epoxy impregnated traction motors due to thermal and thermal induced mechanical stress - part I: Thermal mechanical simulation of single wire due to evenly distributed temperature," in *8th IET International Conference on Power Electronics, Machines and Drives*, Glasgow, 2016.

[29] Z. Huang, A. Reinap and M. Alaküla, "Degradation and fatigue of epoxy impregnated traction motors due to thermal and thermal induced mechanical stress - part II: Thermal mechanical simulation of multiple wires due to evenly and unevenly distributed temperature," in *8th IET International Conference on Power Electronics, Machines and Drives*, Glasgow, 2016.

[30] V. M. Montsinger, "Loading Transformers By Temperature," *Transactions of the American Institute of Electrical Engineers,* vol. 49, no. 2, pp. 776-790, 1930.

[31] D. Huger and D. Gerling, "An advanced lifetime prediction method for permanent magnet synchronous machines," in *International Conference on Electrical Machines (ICEM)*, Berlin, 2014.

[32] *IEEE Std 117-1974, Test Procedure for Evaluation of Systems of Insulating Materials for Random-Wound AC Electric Machinery,* American National Standard Institute (ANSI), 1992.

[33] C. Rusu-Zagar, P. Notingher, V. Navrapescu, G. Mares, G. Rusu-Zagar, T. Setnescu and R. Setnescu, "Method for Estimating the Lifetime of Electric Motors Insulation," in *International Symposium on Advanced Topics in Electrical Engineering*, Bucharest, 2013.

[34] *IEEE Std 98-2002, Standard for the Preparation of Test Procedures for the Thermal Evaluation of Solid Electrical Insulating Materials,* American National Standard Institute (ANSI), 2002.

[35] A. C. Gjerde, "Multifactor Ageing Models - Origins and Similarities," *Electrical Insulation Magazine,* vol. 13, no. 1, pp. 6-13, 1997.

[36] F. D. A. R. A. Guastavino and E. Torello, "Electrical aging test on twisted pair specimens under different environmental conditions," in *IEEE Conference on Electrical Insulation and Dielectric Phenomena*, Virginia Beach, VA, 2009.

[37] G. C. Montanari and L. Simoni, "Aging phenomenology and modeling," *IEEE Transactions on Electrical Insulation,* vol. 28, no. 5, pp. 755-776, 1993.

[38] S. Yang, A. Bryant, P. Mawby, D. Xiang, L. Ran and P. Tavner, "An Industry-Based Survey of Reliability in Power Electronic Converters," *IEEE Transactions on Industry Applications,* vol. 47, no. 3, pp. 1441-1451, 2011.

[39] G. Primavesi, "Aluminium Electrolytic Capacitors," in *Power Electronics in Traction (Digest No. 1997/324)*, 1997.

[40] C. Kulkarni, J. Celaya, G. Biswas and K. Goebel, "Accelerated Aging Experiments for Capacitor Health Monitoring and Prognostics," in *IEEE Autosetcon*, 2012.

[41] C. Kulkarni, G. Biswas, X. Koutsoukos, J. Celaya and K. Goebel, "Integrated Diagnostic/Prognostic Experimental Setup for Capacitor Degradation and Health Monitoring," in *Autosetcon*, 2011.

[42] X. Y. G. Z. Yuege Zhou, "Degradation Model and Maintenance Strategy of the Electrolytic Capacitors for Electronics Applications," in *Prognostics and System Health Management Conference*, Shenzhen, 2011.

[43] M. Vogelsberger, T. Wiesinger and H. Ertl, "Life-Cycle Monitoring and Voltage-Manahinh Unit for DC-Link Electrolytic Capacitors in PWM Converters," *IEEE Transactions on Power Electronics,* vol. 26, no. 2, pp. 493-503, 2011.

[44] J. Anderson, R. Cox and J. Noppakunkajorn, "An On-Line Fault Diagnosis Method for Power Electornic Drives," in *Electric Ship Technologies Symposium (ESTS)*, 2011.

[45] K. Abdennadher, P. Venet, G. Rojat, J. Retif and C. Rosset, "A Real Time Predictive Maintenance System of Aluminium Electrolytic Capacitors Used in Uninterrupter Power Supplies," in *Industry Applications Society Annual Meeting*, 2008.

[46] H. Pang and P. Bryan, "A Life Prediction Scheme for Electrolytic Capacitors in Power Converters Without Current Sensor," in *Applied Power Electronics Conference and Exposition (APEC)*, 2010.

[47] M. Gasperi, "Life Prediction Modeling of Bus Capacitors in AC Variable-Frequency Drives," *IEEE Transactions on Industry Applications,* vol. 41, no. 6, pp. 1430-1435, 2005.

[48] B. J. Hamrock and W. J. Anderson, "12. Rolling Bearing Fatigue Life," in *Rolling-Element Bearings*, NASA Reference Publication, 1983, pp. 32-36.

[49] T. C. ISO/TC, "Rolling Bearings - Damage and Failures - Terms, Characteristics and Causes," 2009.

[50] Barden Precision Bearings, *Bearing Failure: Causes and Cures,* Schaeffler.

[51] SKF, "Bearing Investigation," in *Railway Technical Handbook*, SKF, 2011, pp. 122-135.

[52] P. Alger and H. Samson, "Shaft Currents in Electric Machines," *American Institute of Electrical Engineers,* vol. XLII, no. 12, pp. 1325-1334, 1924.

[53] R. F. Schiferl, M. J. Melfi and J. S. Wang, "Inverter driven induction motor bearing current solutions," in *Industry Applications Society. Forty-Ninth Annual Conference*, 2002.

[54] D. Busse, J. Erdman, R. J. Kerkman, D. Schlegel and G. Skibinski, "Bearing Currents and Their Relationship to PWM Drives," in *IEEE IECON Conference*, Orlando, Florida, November 1995.

[55] D. F. Busse, J. M. Erdman, R. J. Kerkman, D. W. Schlegel and G. L. Skibinski, "An evaluation of the electrostatic shielded induction motor: a solution for rotor shaft voltage buildup and bearing current," *IEEE Transactions on Industry Applications,* vol. 33, no. 6, pp. 1563-1570, 1997.

[56] F. J. T. E. Ferreira, M. V. Cistelecan and A. T. d. Almeida, "Evaluation of Slot-Embedded Partial Electrostatic Shield for High-Frequency Bearing Current Mitigation in Inverter-Fed Induction Motors," *IEEE Transactions on Energy Conversion,* vol. 27, no. 2, pp. 382-390, 2012.

[57] A. Von Jouanne, H. Zhang and A. Wallace, "An Evaluation of Mitigation Techniques for Bearing Currents, EMI and Overvoltages in ASD Applications," *IEEE Transactions on Industry Applications,* vol. 34, no. 5, pp. 1113-1122, 1998.

[58] Omni Insturments, "MTN/1185 RMS Vibration Velocity Sensor," 2015. [Online]. Available: http://www.omniinstruments.co.uk/vibration-monitoring/accelerometers-for-general-vibration-monitoring-4-20ma-output/mtn1185-vibration-sensor-4-20ma.html. [Accessed 15 6 2017].

[59] M. Orman, P. Rzeszucinski, A. Tkaczyk, K. Krishnamoorthi, C. T. Pinto and M. Sulowicz, "Bearing fault detection with the use of acoustic signals recorded by a hand-held mobile phone," in *International Conference on*

Condition Assessment Techniques in Electrical Systems (CATCON), Bangalore, 2015.

[60] F. Duan, F. Elasha, M. Greaves and D. Mba, "Helicopter main gearbox bearing defect identification with acoustic emission techniques," in *IEEE International Conference on Prognostics and Health Management*, Ottawa, ON, 2016.

[61] A. Shahidi, L. A. Gupta, A. Kovacs and D. Peroulis, "Wireless temperature and vibration sensor for real-time bearing condition monitoring," in *IEEE MTT-S International Microwave Symposium Digest (MTT)*, Seattle, WA, 2013.

[62] C. Larsen and N. Branch, "Broadband waveguide vibration sensor for turbine bearing health monitoring," in *IEEE Aerospace Conference*, Big Sky, MT, 2013.

[63] D. Rossetti, Y. Zhang, S. Squartini and S. Collura, "Classification of bearing faults through time-frequency analysis and image processing," in *International Conference on Mechatronics - Mechatronika (ME)*, Prague, 2016.

[64] L. Szabó, D. Fodorean and A. Vasilache, "Bearing fault detection of electrical machines used in automotive applications," in *XXII International Conference on Electrical Machines (ICEM)*, Lausanne, 2016.

[65] Z. Huo, Y. Zhang, P. Francq, L. Shu and J. Huang, "Incipient Fault Diagnosis of Roller Bearing using Optimized Wavelet Transform based Multi-speed Vibration Signatures," *IEEE Access,* vol. PP, no. 99, p. 1, 2016.

[66] J. M. Robichaud and E. P, "Reference Standards for Vibration Monitoring and Analysis," Bretech Engineering Ltd, Saint John, NB, Canada, 2009.

[67] E. Sutrisno, H. Oh, A. S. S. Vasan and M. Pecht, "Estimation of remaining useful life of ball bearings using data driven methodologies," in *IEEE Conference on Prognostics and Health Management*, Denver, 2012.

[68] W. Zhou, B. Lu, T. G. Habetler and R. G. Harley, "Incipient Bearing Fault Detection via Motor Stator Current Noise Cancellation Using Wiener Filter," *IEEE Transactions on Industry Applications,* vol. 45, no. 4, pp. 1309-1317, 2009.

[69] H. Nejjari and M. Benbouzid, "Monitoring and Diagnosis of Induction Motors Electrical Faults Using a Currnt Park's Vectir Pattern Learning Approach," *IEEE Transactions on Industry Applications,* vol. LXVI, no. 3, pp. 730-735, 2000.

[70] J. Pyrhönen, T. Jokinen and V. Hrabovcová, “Chapter 8, Insulation of Electrical Machines,” in *Design of Rotating Electrical Machines*, Chichester, UK, John Wiley & Sons, Ltd, 2008, pp. 429-455.

[71] S. Y. Goh, J. Wale and D. Greenwood, “Thermal analysis for stator slot of permanent magnet machine,” in *International Conference on Electrical Machines (ICEM)*, Lausanne, 2016.

[72] P. Przybylek and H. Moscicka-Grzesiak, “The Influence of Water Content and Ageing Degree of Paper Insulation on its Mechanical Strength,” in *IEEE International Conference on Solid Dielectrics (ICSD)*, 2010.

[73] M. Duval, A. D. Pablo, I. Atanasova-Hoehlein and M. Grisaru, “Significance and detection of very low degree of polymerization of paper in transformers,” *IEEE Electrical Insulation Magazine,* vol. 33, no. 1, pp. 31-38, 2017.

[74] S. Diaham, M.-L. Locatelli and T. Lebey, “Improvement of Polyimide Electrical Properties During Short-Term of Thermal Aging,” in *Annual Report Conference on Electrical Insulation and Dielectric Phenomena*, 2008.

[75] W. Zhao, W. H. Siew, M. J. Given, Q. Li, J. He and E. Corr, “Thermoplastic materials aging under various stresses,” in *IEEE Electrical Insulation Conference (EIC)*, Montreal, 2016.

[76] K. Younsi, P. Neti, M. Shah, J. Zhou, J. Krahn, K. Weeber and D. Whitefield, “Online Capacitance and Dissipation Factor Monitoring of AC Motor Stator Insulation,” in *IEEE International Power Modulator and High Voltage Conference*, Atlanta, GA, 2010.

[77] M. S. M. a. A. Szatkowski, “Medium Voltage Cable Defects Revealed by Off-Line Partial Discharge Testing at Power Frequency,” *Electrical Insulation Magazine, IEEE ,* vol. XXII, no. 4, pp. 24-32, 2006.

[78] R&B Switchgear Group, R&B Switchgear Group, 2017. [Online]. Available: http://rbswitchgeargroup.com/partial-discharge/#. [Accessed 3 6 2017].

[79] P. Neti, P. Zhang, X. Qi, Y. Zhou, K. Younsi, M. Shah and K. Weeber, “Online Detection of Endwinding Contamination in Industrial Motors,” in *Electrical Insulation Conference (EIC)*, Annapolis, MD, 2011.

[80] Y. Toriyama, H. Okamoto, M. Kanazashi and K. Horii, “Degradation of Polyethylene by Partial Discharge,” *IEEE Transactions on Electrical Insulation,* Vols. EI-2, no. 2, pp. 83-92, 1967.

[81] I. Culbert, B. Lloyd and G. Stone, "Stator insulation problems caused by variable speed drives," in *Conference Record PCIC Europe*, Barcelona, 2009.

[82] J. Zhang and e. al, "Finite Element Analysis and Evaluation of Stator Insulation in High Voltage Synchronous Motor," *IEEE Transactions on Magnetics,* vol. 48, no. 2, pp. 955-958, 2012.

[83] S. Mahdavi and K. Hameyer, "High frequency equivalent circuit model of the stator winding in electrical machines," in *International Conference on Electrical Machines*, Marseille, 2012.

[84] D.-H. Hwang, K.-C. Lee, Y.-J. Kim, S.-W. Bae, D.-H. Kim and C.-G. Ro, "Voltage Stresses on Stator Windings of Induction Motors Driven by IGBT PWM Inverters," in *Industry Applications Conference*, Salt Lake City, UT, 2003.

[85] R. L. Nailen, "Transient Surges and Motor Protection," *IEEE Transactions on Industry Applications,* Vols. IA-15, no. 6, pp. 606-610, 1979.

[86] IEC Test Standards, *IEC TS 60034-18-41 Standard,* International Electrotechnical Commission, 2014.

[87] Baldor, "AC Inverter/Vector Duty Motors," 2014. [Online]. Available: http://www.baldor.com/brands/baldor-reliance/products/motors/ac-motors/variable-speed-ac/ac-inverter-vector-duty-motors. [Accessed 3 6 2017].

[88] J. P. Bellomo, P. Castelan and T. Lebey, "The effect of pulsed voltages on dielectric material properties," *IEEE Transactions on Dielectrics and Electrical Insulation,* vol. 6, no. 1, pp. 20-26, 1999.

[89] J. W. Aquilino, "Report of Transformer Reliability Survey - Industrial Plants and Commercial Buildings," *IEEE Transactions on Industry Applications,* Vols. IA-19, no. 5, pp. 858-866, 1983.

[90] G. C. Stone, I. Culbert, E. A. Boulter and H. Dhirani, "Chapter 8, Stator Failure Mechanisms and Repair," in *Rotating Machine Insulation Systems, in Electrical Insulation for Rotating Machines: Design, Evaluation, Aging, Testing, and Repair*, Hoboken, NJ, USA, John Wiley & Sons, Inc, 2014, pp. 137-178.

[91] G. Stone, E. Boulter, I. Culbert and H. Dhirani, Electrical Insulation For Rotating Machine Insulation Systems, Wiley-IEEE Press, 2004.

[92] *IEEE Std 43-2006, Recommended Practice for Testing Insulation Resistance of Electric Machinery,* American National Standard Institute (ANSI), 2006.

[93] S. Nategh, A. Krings, O. Wallmark and M. Leksell, "Evaluation of Impregnation Materials for Thermal Management of Liquid-Cooled Electric Machines," *IEEE Transactions on Industrial Electronics,* vol. 61, no. 11, pp. 5956-5965, 2014.

[94] H. K. D. C. M. Zhu and S. Cherukupalli, "Acoustic monitoring of stator winding delaminations during thermal cycling testing," *IEEE Transactions on Dielectrics and Electrical Insulation,* vol. 17, no. 5, pp. 1405-1410, 2010.

[95] R. Liang and e. al, "Determination of thermal and thermo-mechanical stresses in stator insulation of wind turbine generator based on online monitoring temperatures," in *IEEE International Conference on Dielectrics (ICD)*, Montpellier, 2016.

[96] R. Rothe and K. Hameyer, "Life expectancy calculation for electric vehicle traction motors regarding dynamic temperature and driving cycles," in *International Electric Machines & Drives Conference (IEMDC)*, Niagara Falls, 2011.

[97] Z. Huang, F. J. Márquez-Fernández, Y. Loayza, A. Reinap and M. Alaküla, "Dynamic thermal modeling and application of electrical machine in hybrid drives," in *International Conference on Electrical Machines (ICEM)*, Berlin, 2014.

[98] H. Solomon, "Fatigue of 60/40 Solder," *IEEE Transactions on Components, Hybrids, and Manufacturing Technology,* vol. 9, no. 4, pp. 423-432, 1986.

[99] Z. Ahmad, "Polymeric Dielectric Materials," in *Dielectric Material*, 2012, pp. 1-24.

[100] A. Ginart, I. Ali, J. Goldin, P. Kalgren and M. Roemer, "On-Line Motor Winding Early Diagnostic Based on Dynamic Leakage Current Monitoring," in *IEEE Aerospace Conference*, 2011.

[101] *IEEE Std 286-2000 (R2006), Recommended Practice for Measurement of Power Factor Tip-Up of Electric Machinery Stator Coil Insulation,* American National Standard Institute (ANSI), 2006.

[102] J. Clark, "Bonding in Carbonyl Compounds," Chemguide, 2009. [Online]. Available: http://www.chemguide.co.uk/basicorg/bonding/carbonyl.html#top. [Accessed 3 1 2016].

[103] G. C. Stone, I. Culbert, E. A. Boulter and H. Dhirani, "Chapter 12, Off-Line Rotor and Stator Winding Tests," in *Rotating Machine Insulation Systems, in Electrical Insulation for Rotating Machines: Design, Evaluation, Aging, Testing, and Repair*, Hoboken, NJ, USA, John Wiley & Sons, Inc, 2014, pp. 235-282.

[104] A. P. Nussbaumer, Mitteregger and T. M. Wolbank, “Online Detection of Insulation Degradation in Inverter Fed Drive Systems Base on High Frequency Current Sampling,” in *IECON 2011*, Melbourne, 2011.

[105] T. Sauerlaender and G. Duerbaum, “Energy based capacitance model for magnetic devices,” in *Sixteenth Annual IEEE Applied Power Electronics Conference and Exposition*, Anaheim, CA, 2001.

[106] B. Ackermann, A. Lewalter and E. Waffenschmidt, “Analytical modelling of winding capacitances and dielectric losses for planar transformers,” in *IEEE Workshop on Computers in Power Electronics*, 2004.

[107] K. Maki, H. Funato and L. Shao, “Motor modeling for EMC simulation by 3-D electromagnetic field analysis,” in *IEEE International Electric Machines and Drives Conference*, Miami, FL, 2009.

[108] B. Mirafzal, G. Skibinski, R. Tallam, D. Schlegel and R. Lukaszewski, “Universal Induction Motor Model With Low-to-High Frequency-Response Characteristics,” *IEEE Transactions on Industry Applications,* vol. 43, no. 5, pp. 1233-1246, 2007.

[109] M. A. Gries and B. Mirafzal, “Permanent Magnet Motor-Drive Frequency Response Characterization for Transient Phenomena and Conducte EMI Analysis,” in *Applied Power Electronics Conference and Exposition*, Austin, TX, 2008.

[110] P. Sarikprueck and P. Lumyong, “A study of phase to ground leakage current in 3-phase induction motor fed by switching voltage source,” in *International Conference on Electrical Machines and Systems*, Tokyo, 2009.

[111] A. R. Djordjevic, R. M. Biljie, V. D. Likar-Smiljanic and T. K. Sarkar, “Wideband frequency-domain characterization of FR-4 and time-domain causality,” *IEEE Transactions on Electromagnetic Compatibility,* vol. 43, no. 4, pp. 662-667, 2001.

[112] D. L. McKinnon, “Simulating insulation systems under various environmental conditions in the laboratory,” in *IEEE International Symposium on Electrical Insulation*, San Juan, 2012.

[113] Dapis, M. Wahyudi, D. A. Asfani, D. Fahmi and I. M. Y. Negara, “Accelerated ageing experiment for induction motor insulation due to humidity effect,” in *International Seminar on Intelligent Technology and Its Applications (ISITIA)*, Surabaya, 2015.

[114] M. K. W. Stranges, B. Mistry and R. Omranipour, “Sealed winding conformance testing,” *IEEE Industry Applications Magazine,* vol. 15, no. 1, pp. 35-38, 2009.

[115] E. A. Gonzalez, M. J. B. Castro, R. S. Presto, M. Radi and I. Petráš, "Fractional-order models in motor polarization index measurements," in *International Carpathian Control Conference (ICCC)*, Tatranska Lomnica, 2016.

[116] *IEEE Std 95-1977, Recommended Practice for Insulation Testing of Large AC Rotating Machinery With High Direct Voltage,* American National Standard Institute (ANSI), 1977.

[117] *IEEE Std 56-2016, Guide for Insulation Maintenance of Electric Machines,* American National Standard Institute (ANSI), 2016.

[118] *IEEE Std 433-1974, Recommended Practice for Insulation Testing of Large AC Rotating Machinery With High Voltage at Very Low Frequency,* American National Standard Institute (ANSI), 1974.

[119] Servizi s.r.l., *Cronmaster N65 Test Equipment User's Manual,* Venaria, Italy, 2013.

[120] J. Yang, S. B. Lee, J.-Y. Yoo, S. Lee, Y. Oh and C. Choi, "A Stator Winding Insulation Condition Monitoring Technique for Inverter-Fed Machines," *IEEE Transactions on Power Electronics,* vol. 22, no. 5, pp. 2026-2033, 2007.

[121] G. Pascoli, W. Hribernik and G. Ujvari, "A Practical Investigation on the Correlation Between Aging and the Dissipation Factor Value of Mica Insulated Genrator Windings," in *International Conference on Condition Monitoring and Diagnosis*, Beijing, 2008.

[122] R. Mills, C. Payne and K. Younsi, "Insulation cure monitoring on global VPI large AC motors," in *IEEE International Symposium on Electrical Insulation*, 2002.

[123] J. Yang, J. Cho, S. B. Lee, H. Jung and Y. Park, "An Inverter-Embedded Stator Winding Insulation Quality Assessment Technique for AC Machines," in *International Conference on Condition Monitoringand Diagnosis*, Bejing, China, 2008.

[124] C. Gerada, K. J. Bradley, M. Summer and P. Wheeler, "Operating induction motor drives with turn-to-turn faults," in *IEEE International Conference on Electric Machines and Drives*, Antonio, TX, 2005.

[125] *IEEE Std 522-1992, Guide for Testing Turn-to-Turn Insulation on Form-Wound Stator Coils for Alternating-Current Rotating Electric Machines,* American National Standard Institute (ANSI), 1992.

[126] Z. Gao, T. G. Habetler, R. G. Harley and R. S. Colby, "A Sensorless Adaptive Stator Winding Temperature Estimator for Mains-Fed Induction Machines

With Continuous-Operation Periodic Duty Cycles," *IEEE Transactions on Industry Applications,* vol. 44, no. 5, pp. 1533-1542, 2008.

[127] H. G. S. M. J. C. Greg C. Stone, "Application of Partial Discharge Testing to Motor and Generator Stator Winding Maintenance," *IEEE Transactions on Industry Applications,* vol. 32, no. 2, pp. 459-464, 1996.

[128] *IEEE Std 1434-2000, Trial-Use Guide to the Measurement of Partial Discharges in Rotating Machinery,* American National Standard Institute (ANSI), 2000.

[129] S. Campbell, G. Stone, H. Sedding, G. Klempner, W. McDermid and R. Bussey, "Practical On-Line Partial Discharge Tests for Turbine Generators and Motors," *IEEE Transactions on Energy Conversion,* vol. 9, no. 2, pp. 281-287, 1994.

[130] M. Kawada, Z. I. Kawasaki and K. Matsuura, "Insulation Diagnostic Technique to Assess the Conditition of Generator Winding by Measuring Microwave Associated with Dielectric Breakdown," *IEEE Transactions on Energy Conversion,* vol. 15, no. 1, pp. 19-23, 2000.

[131] H. C. Chen, B. Y. Chen, C. C. Kuo and M. H. Chao, "UHF micro-strip antenna design for partial discharge detection of gas insulated switch," in *7th Asia-Pacific International Conference on Lightning*, Chengdu, 2011.

[132] Phenix Technologies, *Partial Discharge Detector and Radio Interference Voltage Testing (Brochure Number 90503),* Phenix Technologies.

[133] HVPD, "On-line Partial Discharge (OLPD) Diagnostics for High Voltage Networks," HVPD, [Online]. Available: http://www.hvpd.co.uk/testing-and-monitoring-tools/. [Accessed 24 5 2017].

[134] G. Paoletti and A. Golubev, "Partial Discharge Theory and Applications to Electrical Equipment," in *IAS 34th Annual Meeting*, Phoenix Arizona, 2000.

[135] X. C. Y. C. J. S. a. H. X. M. I. Bo Yue, "Diagnosis of Stator Winding Insulation of Large Generator Based on Partial Discharge Measurement," *IEEE Transactions on Energy Conversion,* vol. 21, no. 2, pp. 387-395, 2006.

[136] A. Cavallini, E. Lindell, G. Montanari and M. Tozzi, "Off-Line PD Testing of Converter-Fed Wire-Wound Motors: When IECTS 60034-18-41 may fail ?," *IEEE Transactions on Dielectrics and Electrical Insulation,* vol. 17, no. 5, pp. 1385-1395, 2010.

[137] G. C. Stone and I. Culbert, "Partial discharge testing of random wound stators during short risetime voltage surges," in *IEEE Electrical Insulation Conference*, Montreal, QC, 2009.

[138] J. Yang, T.-j. Kang, B. Kim, S. B. Lee, Y.-W. Yoon, D. Kang, J. Cho and H. Kim, "Experimental Evaluation of Using the Surge PD Test as a Predictive Maintenance Tool for Monitoring Turn Insulation Quality in Random Wound AC Motor Stator Windings," *IEEE Transactions on Dielectrics and Electrical Insulation,* vol. 19, no. 1, pp. 53-60, 2012.

[139] A. Cavallini, D. Fabiani and G. C. Montanari, "A novel method to diagnose PWM-fed induction motors," *IEEE Transactions on Dielectrics and Electrical Insulation,* vol. 15, no. 5, pp. 1313-1321, 2008.

[140] M. Tozzi, A. Cavallini and G. C. Montanari, "Monitoring off-line and on-line PD under impulsive voltage on induction motors - Part 2: testing," *IEEE Electrical Insulation Magazine,* vol. 27, no. 1, pp. 14-21, 2011.

[141] D. Dorrell, W. Thomson and S. Roach, "Analysis of Airgap Flux, Current and Vibration Signals as a Function of the Combination of Static and Dynamic Airgap Eccentricity in 3-Phase Induction Motors," *IEEE Transactions on Industry Applications,* vol. 33, no. 1, pp. 24-34, 1997.

[142] J. Yun, J. Cho, S. B. Lee and J. Y. Yoo, "Online Detection of High-Resistance Connections in the Incoming Electrical Circuit for Induction Motors," *IEEE Transactions on Industry Applications,* vol. 45, no. 2, pp. 694-702, 2009.

[143] Z. A. Ping, Y. Juan and W. Ling, "Fault Detection of Stator Winding Interturn Short Circuit in PMSM Based on Wavelet Packet Analysis," in *Fifth International Conference on Measuring Technology and Mechatronics Automation*, Hong Kong, 2013.

[144] J. Quiroga, L. Liu and D. A. Cartes, "Fuzzy logic based fault detection of PMSM stator winding short under load fluctuation using negative sequence analysis," in *American Control Conference*, Seattle, WA, 2008.

[145] S. Grubic, J. Restrepo, J. M. Aller, B. Lu and T. G. Habetler, "A New Concept for Online Surge Testing for the Detection of Winding Insulation Deterioration in Low-Voltage Induction Machines," *IEEE Transactions on Industry Applications,* vol. 47, no. 5, pp. 2051-2057, 2011.

[146] A. P. Nussbaumer, Mitteregger and T. M. Wolbank, "Online Detection of Insulation Degradation in Inverter Fed Drive Systems Base on High Frequency Current Sampling," in *IECON 2011*, Melbourne, 2011.

[147] C. Zoeller, T. M. Wolbank and M. A. Vogelsberger, "Insulation condition monitoring of traction drives based on transient current signal resulting from differential and common mode excitation," in *IEEE International Electric Machines & Drives Conference (IEMDC)*, Coeur d'Alene, ID, 2015.

[148] C. Zoeller, M. A. Vogelsberger, W. Fahrner and T. M. Wolbank, "Influence of current transducer transfer properties on stator insulation condition monitoring of inverter-fed drives," in *International Symposium on Power*

Electronics, Electrical Drives, Automation and Motion (SPEEDAM), Anacapri, 2016.

[149] C. Zoeller, T. M. Wolbank and M. A. Vogelsberger, "Influence of parasitic capacitances of IGBT inverter on insulation condition monitoring of traction machines based on current signal transients analysis," in *European Conference on Power Electronics and Applications (EPE'16 ECCE Europe)*, Karlsruhe, 2016.

[150] P. Werynski, D. Roger, R. Corton and J. F. Brudny, "Proposition of a new method for in-service monitoring of the aging of stator winding insulation in AC motors," *IEEE Transactions on Energy Conversion,* vol. 21, no. 3, pp. 673-681, 2006.

[151] S. B. Lee and J. Yang, "An On-Line Groundwall and Phase to Phase Insulation Quality Assessment Technique for AC Machine Stator Windings," in *Industry Applications Conference*, 2005.

[152] P. Neti, K. Younsi and M. Shah, "A Novel High Sensitivity Differnetial Current Transformer for Online Health Monitoring of Industrial Motor Ground-Wall Insulation," in *IEEE Energy Conversion Congress and Exposition (ECCE)*, 2013.

[153] K. Younsi, P. Neti, M. Shah, J. Zhou, J. Krahn, K. Weeber and D. Whitefield, "Online Capacitance and Dissipation Factor Monitoring of AC Motor Stator Insulation," in *Power Modulator and High Voltage Conference (IPMHVC)*, 2010.

[154] P. Zhang, K. Younsi and P. Neti, "A Novel Online Stator Ground-Wall Insulation Monitoring Scheme for Inverter-Fed AC Motors," in *IEEE Energy Conversion Congress and Exposition (ECCE)*, 2013.

[155] A. S. Babel and E. G. Strangas, "Condition-based monitoring and prognostic health management of electric machine stator winding insulation," in *nternational Conference on Electrical Machines (ICEM)*, Berlin, 2014.

[156] J. Adabi, F. Zare, G. Ledwich and A. Ghosh, "Leakage current and common mode voltage issues in modern AC drive systems," in *Australasian Universities Power Engineering Conference*, Perth, WA, 2007.

[157] B. Sen, J. Wang and P. Lazari, "A High-Fidelity Computationally Efficient Transient Model of Interior Permanent-Magnet Machine With Stator Turn Fault," *IEEE Transactions on Industrial Electronics,* vol. 63, no. 2, pp. 773-783, 2016.

[158] A. Helgeson and U. Gafvert, "Dielectric response during curing of a resin-rich insulation system for rotating machines," in *Annual Report*

Conference on Electrical Insulation and Dielectric Phenomena, Austin, TX, 1999.

[159] S. Diaham, M.-L. Locatelli and T. Lebey, "Improvement of Polyimide Electrical Properties During Short-Term of Thermal Aging," in *Annual Report Conference on Electrical Insulation and Dielectric Phenomena*, 2008.

[160] M. Sumislawska, K. N. Gyftakis, D. F. Kavanagh, M. D. McCulloch, K. J. Burnham and D. A. Howey, "The Impact of Thermal Degradation on Properties of Electrical Machine Winding Insulation Material," *IEEE Transactions on Industry Applications,* vol. 52, no. 4, p. 29512960, 2016.

[161] K. N. Gyftakis, M. Sumislawska, D. F. Kavanagh, D. A. Howey and M. D. McCulloch, "Dielectric Characteristics of Electric Vehicle Traction Motor Winding Insulation Under Thermal Aging," *IEEE Transactions on Industry Applications,* vol. 52, no. 2, pp. 1398-1404, 2016.

[162] DuPont Teijin Films, *Mylar Polyester Film Electrical Properties (Datasheet H-32192-1),* DuPont, 2003.

[163] Huntsman, *Advanced Materials High Performance Components (Resin Brochure),* Huntsman Corporation, 2010.

[164] T. A. L. D. Grahame Holmes, "Pulse Width Modulation For Power Converters," IEEE Press, 2003, p. Appendix 1.

[165] K. Colombage, J. Wang, C. Gould and C. Liu, "PWM harmonic signature based islanding detection for a single-phase inverter with PWM frequency hopping," in *IEEE Energy Conversion Congress and Exposition (ECCE)*, Montreal, QC, 2015.

[166] B. J. Hamrock and W. J. Anderson, "12. Rolling BEaring Fatigue Life," in *Rolling-Element Bearings*, NASA Reference Publication, 1983, pp. 32-36.